Preparation and characterization of elastomeric polymers for soft grippers applications

SARAWADEE THAKASAME

A THESIS SUBMITTED IN PARTIAL FULFILLMENT OF
THE REQUIREMENTS FOR MASTER DEGREE OF SCIENCE
IN CHEMISTRY
FACULTY OF SCIENCE
BURAPHA UNIVERSITY
2024

COPYRIGHT OF BURAPHA UNIVERSITY

การเตรียมและศึกษาสมบัติของพอลิเมอร์ชนิดอีลาสโตเมอร์เพื่อการใช้งานเป็นกริปเปอร์ชนิดอ่อนนุ่ม

ศรวดี ท่าเกษม

วิทยานิพนธ์นี้เป็นส่วนหนึ่งของการศึกษาตามหลักสูตรวิทยาศาสตรมหาบัณฑิต
สาขาวิชาเคมี
คณะวิทยาศาสตร์ มหาวิทยาลัยบูรพา
2567
ลิขสิทธิ์เป็นของมหาวิทยาลัยบูรพา

Preparation and characterization of elastomeric polymers for soft grippers applications

SARAWADEE THAKASAME

A THESIS SUBMITTED IN PARTIAL FULFILLMENT OF
THE REQUIREMENTS FOR MASTER DEGREE OF SCIENCE
IN CHEMISTRY
FACULTY OF SCIENCE
BURAPHA UNIVERSITY
2024

COPYRIGHT OF BURAPHA UNIVERSITY

The Thesis of Sarawadee Thakasame has been approved by the examining committee to be partial fulfillment of the requirements for the Master Degree of Science in Chemistry of Burapha University

Advisory Committee

Principal advisor

S. Kaewpirom

(Associate Professor Dr. Supranee Kaewpirom)

Examining Committee

Principal examiner
(Assistant Professor Dr. Santhad Chuwongin)

T. Nongnual Member
(Assistant Professor Dr. Teeranan Nongnual)

S. Kaewpirom Member
(Associate Professor Dr. Supranee Kaewpirom)

T. Usavadee
Dean of the Faculty of Science
(Associate Professor Dr. Usavadee Tuntiwaranuruk)
October 21, 2024

This Thesis has been approved by Graduate School Burapha University to be partial fulfillment of the requirements for the Master Degree of Science in Chemistry of Burapha University

Witawat Jangiam Dean of Graduate School
(Associate Professor Dr. Witawat Jangiam)
5 Nov, 2024

1793587300 BUU iThesis 64910181 thesis / recv: 12102567 09:27:06 / seq: 30

This study was supported by a research funding from the Graduate School,

Burapha University.

64910181: MAJOR: CHEMISTRY; M.Sc. (CHEMISTRY)

KEYWORDS: ELECTROACTIVE ACTUATORS BENDING ANGLE GRAPHITE COMPOSITE ROBOTIC APPLICATIONS CALENDARING

SARAWADEE THAKASAME : PREPARATION AND CHARACTERIZATION OF ELASTOMERIC POLYMERS FOR SOFT GRIPPERS APPLICATIONS. ADVISORY COMMITTEE: SUPRANEE KAEWPIROM, 2024.

Electroactive actuator (ETA) systems are advanced devices that convert electrical energy into mechanical energy through electrothermal stimulation. These systems offer significant potential for applications in soft robotics, artificial muscles, and other advanced fields. This study developed a low-voltage-activated ETA comprising an electrically conductive layer and a polymer layer. The conductive layer was made from highly durable and flexible polyvinyl alcohol (PVA)/graphite (GH) composite, known for its exceptional electrical and thermal conductivity. Mechanical characterization showed a tensile elongation of 435.63% and a Young's modulus of 1.22×10^{6} MPa. This material was used to fabricate a PVA/GH/Gly composite film with a U-shaped configuration, alongside a polyimide (PI) film. A two-layer thin-film ETA was produced using a calendaring process, demonstrating high performance at low voltages over brief periods. The system with 50% weight of graphite exhibited the highest bending angle of 22.30º, with a film thickness of 147.87 µm, under 6 volts application for 120 seconds. It was found that blocking force increased progressively when the voltage was applied, peaking at 0.101 mN, the research findings validated the proposed graphite composite/Kapton tape system as a viable low-voltage-driven electroactive actuator. This breakthrough could pave the way for the development of advanced smart devices capable of efficiently converting electrical energy into mechanical motion.

ACKNOWLEDGEMENTS

Although my name is the only one on the cover of this dissertation, its completion would not have been possible without the support and contributions of numerous individuals. I would like to express my profound gratitude to Associate Professor Dr. Supranee Kaewpirom, my supervisor, for her invaluable guidance, encouragement, and the opportunity to conduct research in her laboratory. I am deeply appreciative of the many opportunities she provided, ranging from insightful advice and fostering holistic learning experiences in both academics and research to enabling my participation in research-to-market activities, which will be invaluable in my future endeavors.

I also extend my sincere thanks to Assistant Professor Dr. Santhad Chuwongin from the College of Advanced Manufacturing Innovation at King Mongkut's Institute of Technology Ladkrabang, and Assistant Professor Dr. Teeranan Nongnual from the Department of Chemistry at Burapha University, for their willingness to serve on my thesis committee and for their insightful feedback. This research was generously supported by the Scientific Innovation Service Unit, Faculty of Science, Burapha University (SIF-IN-64910181), and financially backed by the Thailand Science and Research Innovation Fund (10F640206). I would like to convey my heartfelt appreciation to Associate Professor Dr. Siridech Boonsang from the Department of Electrical Engineering at King Mongkut's Institute of Technology for his generous support in providing the essential equipment and tools necessary for my experiments, which allowed me to learn and utilize new instruments relevant to my research. I am also grateful to my family and friends in the polymer laboratory for their kindness, assistance, and unwavering encouragement throughout this journey. Finally, I owe my deepest gratitude to my family for their understanding, patience, and constant support, without which this dissertation would not have been possible.

Sarawadee Thakasame

TABLE OF CONTENTS

Page

ABSTRACT ..... D
ACKNOWLEDGEMENTS ..... E
TABLE OF CONTENTS ..... F
LIST OF TABLE ..... J
LIST OF FIGURES ..... K
CHAPTER 1 INTRODUCTION 42
1.1 Background 42
1.2 Objectives 43
1.3 Hypothesis 43
1.4 Scope of study 44
CHAPTER 2 THEORY AND LITERAURE REVIEWS 46
2.1 Gripper technologies 46
2.2 Soft robot 47
2.3 Conductive polymer composites 48
2.4 Electroactive polymers 49
2.5 Electrical conductivity and resistivity 50
2.6 Volume resistivity and conductivity 52
2.7 Graphite 53
2.8 Graphite oxide and reduced graphite oxide 55
2.9 Polyvinyl alcohol 57
2.10 Coefficient of thermal expansion 59
2.11 Polyimide 61
2.12 Polydimethylsiloxane 62
2.13 Polyvinyl chloride 63
2.14 Test methods 63

2.14.1 Fourier transform infrared spectrometer 63
2.14.2 Digital multimeter 65
2.14.3 Bending curvature 67
2.14.4 Tensile test.....70
2.14.5 Scanning electron microscopy.....73
2.14.6 Thermal camera.....74
2.15 Literature reviews 75
CHAPTER 3 RESEARCH METHODOLOGY 85
3.1 Chemical and Material.....85
3.1.1 Chemicals 85
3.1.2 Equipment 86
3.1.3 Instrument.....86
3.2 Experimental.....89
3.2.1 Preparation of conductive layer.....89
3.2.1.1 Preparation of graphite composite films by K-hand coating.....89
3.2.1.2 Preparation of graphite composite films by solution casting 90
3.2.2 Preparation of double-layer ETA 92
3.2.2.1 In-situ process.....92
PVA/GH/Gly.....92
PVA/GO/Gly and PVA/rGO/Gly 92
3.2.2.2 Two-step process.....93
3.2.3 Synthesis of graphite oxide 94
3.3 Characterization.....95
3.3.1 Chemical structure analysis.....95
3.3.2 Tensile measurement.....96
3.3.3 Morphological study of composite films.....96
3.3.4 Electrical conductivity.....96
3.3.6 Thickness.....99
3.3.7 Thermal images of ETA 99

3.3.8 Double-layer ETA model systems testing application 100
CHAPTER 4 RESULTS 101
4.1 Preparation of conductive composite films 101
4.1.1 K-hand coating method 101
4.1.2 Solution casting method 103
4.1.3 Preparation of Double-Layer ETA 107
4.1.3.1 Two-Step Process 107
4.1.3.2 In Situ Process 116
4.1.4 Synthesis of GO and rGO 123
4.1.5 Electrical conductivity of conductive layer 132
4.1.5.1 PVA/GH/Gly system 132
4.1.5.2 PVA/GO/Gly system 142
4.1.5.3 PVA/rGO/Gly system 144
4.1.6 Tensile Test 145
4.1.7 Bending angle 151
4.1.8 Blocking force 158
CHAPTER 5 DISCUSSION AND CONCLUSIONS 163
5.1 Discussion 163
5.1.1 Preparation of composite films 163
5.1.1.1 K-hand coating method 163
5.1.1.2 Solution casting method 163
5.1.2 Preparation of Double-Layer ETA 164
5.1.2.1 Two-Step Process 164
5.1.2.2 In Situ Process 165
5.1.3 Synthesis of GO and rGO 166
5.1.3.1 Synthesis of GO 166
5.1.3.2 FTIR of the conductive composite films 167
5.1.4 Electrical conductivity of conductive layer 168
5.1.4.1 PVA/GH/Gly system 168

5.1.4.2 PVA/GO/Gly System 169
5.1.4.3 PVA/rGO/Gly System 170
5.1.5 Tensile Test 170
5.1.6 Bending angle 171
5.1.7 Blocking force 172
5.2 Conclusions 173
5.3 Suggestions 173
APPENDIX A 175
APPENDIX B 203
REFERENCES 219
BIOGRAPHY 229

LIST OF TABLE

Page

Table 3-1 Weight and volume ratio of each polymer composite film formulation. 89

Table 3-2 Crosslink solution formulation. 90

Table 3-3 Sample name and formulations. 91

Table 4-1 Thickness and image of composite films prepared by K-hand coating technique. 102

Table 4-2 Thickness and image of glycerol plasticized composite films prepared by K-hand coating technique. 102

Table 4-3 Thickness and images of composite films prepared by solution casting technic. 104

Table 4-4 Thickness and image of double-layer ETA by two-step process. 108

Table 4-5 Coefficient of thermal expansion of the polymer.....111

Table 4-6 Thermal coefficient of expansion of conductive material. 112

Table 4-7 Thickness and images of actuator systems with various polymer layers: Kapton Tape, PVC Tape (3M), PVC Tape (Yazaki), and PP Tape (3M).....115

Table 4-8 Thicknesses and images of double-layer ETAs produced via the in-situ process.....117

Table 4-9 Thickness and image of PVA/rGO/Gly system by in-situ process. 122

Table 4-10 The SEM micrographs of GH, GO, and rGO fillers.....127

Table 4-11 The surface morphology of the composite films processed by non-calendaring was analyzed at magnifications of 100x and 2000x. 150

Table 4-12 The surface and cross-section morphology of the composite films processed by calendaring was analyzed at magnifications of 100x, 1000x, and 2000x. 151

Table 4-13 The thickness of the actuator layers calendaring and non-calendaring at a magnification of 250x. 153

LIST OF FIGURES

Page

Figure 2-1 One possible classification of the characteristics of soft grippers for different gripping technologies and object types 47

Figure 2-2 Schematic diagram of structure and mechanism of soft ETAs, (a) Initial state and (b) bending state 50

Figure 2-3 The two major allotropes of carbon are (a) sp^3-bonded diamond and (b) sp^2-bonded graphite. The sp^2-bonded allotrope is formable into three low-dimensional structures: (c) 2D sheets known as graphene, (d) 1D nanotubes, or (e) 0D buck balls (f)fullerite (g) C70, g) amorphous carbon, and (h) single-walled carbon nanotube ..53

Figure 2-4 Graphite powder 55

Figure 2-5 Steps of the synthesis of GO and rGO 57

Figure 2-6 Structural formula for PVA: (a) partially hydrolyzed; (b) fully hydrolyzed 58

Figure 2-7 Chemical structure of polyimide 61

Figure 2-8 Chemical structure of PDMS 62

Figure 2-9 Schematic of a Fourier transform infrared spectrometer 65

Figure 2-10 Agilent 34401A Digital Multimeter 66

Figure 2-11 Proper connections for measuring voltage, current and resistance 66

Figure 2-12 Wire Ohms measurements 67

Figure 2-13 Simple curve connects two lines with a smooth arc. 68

Figure 2-14 Compound curves 68

Figure 2-15 Reverse curves 69

Figure 2-16 Designation of arc definition and chord definition curves 69

Figure 2-17 Method for determining epinastic curvature. Petioles from control (a) and reoriented (b) bracts were excised and copied in a photocopier. 70

Figure 2-18 The shape of the specimen changes during tensile testing 71

Figure 2-19 A typical stress–strain curve for polymer film undergoing tensile strain testing 72

Figure 2-20 Schematic of a scanning electron microscope 74

Figure 2-21 Schematic diagram of infrared thermography camera 75

Figure 2-22 Schematic diagram of (a) CNTF/PDMS composite ETA fabrication process and (b) its bending process 76

Figure 2-23 Electrothermal bimorph actuators comprising an aligned MWCNT/epoxy composite and aluminum foil were fabricated.....77

Figure 2-24 Bending performance of the PI/AgNW/PDMS bimorph actuator. (a) Schematic of the electrothermal bimorph actuation mechanism. (b) The initial state, the bent state with maximum curvature and the recovered state of the U-shaped actuator.....77

Figure 2-25 a) Schematic cross-section of bilayer actuators made of paper and PP film. b) Fabrication processes of the electro resistive heater/sensory circuit on paper. c) Photograph of a U-shaped conductive film patterned on paper. d) Bending deformation of an actuator upon application of 30 V. e) SEM image on the surface of the hybrid film coated on the paper substrate 78

Figure 2-26 Application of the LRGO/Ag ETAs as a soft gripper. Consecutively captured images of grabbing a PDMS block: (a) approaching, (b) grasping, (c) lifting and moving, and (d) releasing 79

Figure 2-27 PBONF-reinforced CNT/PVA bilayer actuators. (a) Scheme indicating the definition of the bending angle α. (b) Photographs of the PBONF-reinforced CNT/PVA bilayer actuator at RH = 75% and RH = 86% 80

Figure 2-28 Diagram of the double-layer ETA. (a) Compose graphite paper and PI to fabricate flexible double-layer ETA. (b) Three specifications of graphite paper of sample A, B, C. (c) Bending the flexible actuator by hand. (d) The bend process of actuator of sample C when power on at 6 V 82

Figure 2-29 Bending principle of existing DEMES gripper using a bilayer unimorph consisting of a pre-stretched DEA on a passive structural layer 83

Figure 2-30 A soft fabric-based bimorph actuator.....84

Figure 3-1 The study flow chart.....88

Figure 3-2 A U-shape ETA prepared from In-situ process.....93

Figure 3-3 A U-shape ETA prepared from a conductive polymer composite and a polymer tape.....93
Figure 3-4 Synthesis process for graphite oxide.....94
Figure 3-5 Synthesis process for reduced graphite oxide.....95
Figure 3-6 FTIR instrument.....95
Figure 3-7 Testometric micro 350.....96
Figure 3-8 Digital multimeter (Agilent 34410).....97
Figure 3-9 Diagram of the electrical conductivity test.....98
Figure 3-10 Bending curvature measurement for electroactive actuator under applied DC voltage.....99
Figure 3-11 Thermal images of the bending movement of CNTF/PDMS composite ETA under different temperatures.....100
Figure 4-1 A flowchart outlining the procedure for preparing a conductive layer.....101
Figure 4-2 The double-layer ETA, showing its the flexibility.....107
Figure 4-3 Types of polymer layers are: PI PVC (3M) PVC (THAI-YAZAKI) PP (3M) and PDMS.....112
Figure 4-4 The actuator systems comprised of PVA/50GH/60Gly with various polymer tapes: (Kapton) (a), (3M PVC) (b), (PVC Yazaki) (c), and (3M PP) (d).....114
Figure 4-5 a) Types of PDMS Silicone b) The PVA/GH/Gly ETA incorporating PDMS as the polymer layer.....116
Figure 4-6 a-c). Molds used in the In-situ method.....117
Figure 4-7 Schematic of the actuator system, where the conductive layer and the polymer layer were prepared via the in-situ process.....119
Figure 4-8 The actuator of the PVA/GO/Gly system.....121
Figure 4-9 The actuator of the PVA/GO/Gly system.....122
Figure 4-10 FTIR spectra of GH, GO and rGO.....124
Figure 4-11 Digital images of a) GH b) GO and c) rGO.....124
Figure 4-12 Structure of graphite, graphite oxide and reduced graphite oxide.....124
Figure 4-13 FTIR spectra of PVA/8GO/60Gly, PVA/10GO/60Gly, PVA/15GO/60Gly, and PVA/20GO/60Gly.....129
Figure 4-14 FTIR spectra of PVA/8rGO/60Gly, PVA/10rGO/60Gly, PVA/15rGO/60Gly, and PVA/20rGO/60Gly.....130

Figure 4-15 FTIR spectra of PVA/50GH/6Gly, PVA/60GH/60Gly, PVA/70GH/60Gly, and PVA/80GH/60Gly. 131
Figure 4-16 Volume resistivity of PVA/50GH/60Gly. 133
Figure 4-17 Volume resistivity of PVA/60GH/60Gly. 133
Figure 4-18 Volume resistivity of PVA/70GH/60Gly. 134
Figure 4-19 Volume resistivity of PVA/80GH/60Gly. 134
Figure 4-20 Volume conductivity of PVA/50GH/60Gly 135
Figure 4-21 Volume conductivity of PVA/60GH/60Gly 135
Figure 4-22 Volume conductivity of PVA/70GH/60Gly 136
Figure 4-23 Volume conductivity of PVA/80GH/60Gly 136
Figure 4-24 Effect of graphite (GH) content on the volume resistivity of PVA/GH/Gly composite films. 138
Figure 4-25 Effect of graphite (GH) content on the volume conductivity of PVA/GH/Gly composite films. 138
Figure 4-26 Volume resistivity of non-calendared and calendared PVA/GH/Gly composite films. 141
Figure 4-27 Volume conductivity of non-calendared and calendared PVA/GH/Gly composite films. 142
Figure 4-28 Volume resistivity of PVA/GO/Gly composite films varied with the content of GO. 143
Figure 4-29 Volume conductivity of PVA/GO/Gly composite films varied with the content of GO. 143
Figure 4-30 Volume resistivity of PVA/rGO/Gly composite films varied with the content of rGO. 144
Figure 4-31 Volume conductivity of PVA/rGO/Gly composite films varied with the content of rGO. 145
Figure 4-32 Elongation at break of PVA/GH/Gly composites as a function of GH content (Data tested by ANOVA single factor statistical significance: $p < 0.05$, F cal = 4.1141 and F crit = 2.8164 which F cal > F crit means a significant difference)... 147
Figure 4-33 Young Modulus of PVA/GH/Gly composites as a function of GH content (Data tested by ANOVA single factor statistical significance: $p < 0.05$, F cal = 4.1141 and F crit = 2.8164 which F cal > F crit means a significant difference). 148

Figure 4-34 Tensile strength of PVA/GH/Gly composites as a function of GH content (Data tested by ANOVA single factor statistical significance: $p < 0.05$, F cal = 3.026 and F crit = 2.8164 which F cal > F crit means a significant difference). 149

Figure 4-35 Diagram of the actuator layers: layer 1 (Kapton tape), layer 2 (glue), layer 3 (PVA/GH composite). 152

Figure 4-36 Thickness of (a) layers 1 (Kapton tape), (b) layers 2 (glue), and (c) layers 3 (graphite film) for graphite content of 50%, 60%, 70%, and 80% wt. 155

Figure 4-37 Apply a potential of 6 V to the sample and remove a potential of 0 V..156

Figure 4-38 Thickness and bending angle for non-calendaring and calendaring actuators at 6 V. 157

Figure 4-39 Blocking force setup. 160

Figure 4-40 Blocking force of the calendaring actuator when power is on (2 min) and off (2 min) at 6 V of PVA/50GH/60Gly. 160

Figure 4-41 Blocking force of the calendaring actuator when power is on (2 min) and off (2 min) at 6 V of PVA/60GH/60Gly. 161

Figure 4-42 Blocking force of the calendaring actuator when power is on (2 min) and off (2 min) at 6 V of PVA/70GH/60Gly. 161

Figure 4-43 Blocking force of the calendaring actuator when power is on (2 min) and off (2 min) at 6 V of PVA/80GH/60Gly. 162

ต้นฉบับไม่ปรากฏหน้า 1-41

CHAPTER 1
INTRODUCTION

1.1 Background

Soft robotic grippers are grippers that can hold objects of various shapes and sizes as well as different object categories that are mainly fragile and highly deformable. They have unique properties compared with the traditional rigid robotics, such as lightweight, low cost, easy fabrication, and simple to control (Arachchige, Chen, Walker, & Godage, 2021; Gong et al., 2018; J.Boylan, 1996). Being able picking and placing of delicate objects without harmful them, and flexibility to operate in complicated environments, as compared to their rigid counterparts, are some other benefits they offer (Zaidi, Maselli, Laschi, & Cianchetti, 2021). A major part of soft robots, can be driven by a number of ways that are grouped into four types: tendon length variation, smart materials (including dielectric materials, electro-active polymers and heat sensitive materials), chemical reactions, and pneumatic/hydraulic transmissions. Smart materials can respond to electricity or electric field and exhibit a large strain in angular or linear motions (Li, Chen, Yang, & Li, 2019). Electroactive polymers (EAPs) have the ability to undergo a large amount of strain or physical deformation when subjected to an external electric field. Among them, polymeric based electrothermal actuators (ETA) use joule heating to drive the thermal expansion of a polymeric substrate (Sun, Leaker, Lee, Nam, & Naguib, 2019). They are soft, flexible materials that could convert electrical energy to mechanical energy and thus impart a force. Owing to their easy fabrication process, low cost and high performance, ETA received increasing attention into numerous applications (Aouraghe, Mengjie, Qiu, & Fujun, 2021; G. Chen et al., 2020). ETAs can create large bending displacement when operated by a DC voltage, which is a great advantage to many applications including robotics. However, their disadvantages include the need to maintain electrolyte and difficulty to sustain constant displacement under activation of a DC voltage (except for conductive polymers) (Y. Bar-Cohen, & Anderson, I. A., 2019).

Electroactive actuator consists of two important parts: conductive and polymer layers. The conductive layer is high thermal conductivity and outstanding mechanical performance and have been widely used in soft ETAs as the flexible heater to introduce temperature change by joule heating and thermal conductivity. Some examples of conductive layers are carbon nanomaterials, including carbon nanotube (CNT), carbon black, graphite and graphene (F.-P. Du, Tang, C.-Y., Xie, X.-L., Zhou, X.-P., & Tan, L., 2009; Seo et al., 2014; Tian et al., 2021). Besides, the polymer layer is a flexible polymer substrate gaining popularity in advantages of getting larger deformation and insulated, without necessity of additional insulation around the heater. The ideal polymer layers are polymer materials with large coefficient of thermal expansion (CTE), small Young's modulus, good flexibility, extraordinary durability against repeated deformation and resistance to high temperature, such as polydimethylsiloxane (PDMS) elastomer and polyimide (PI) (Tian et al., 2021).

In this study, double-layer ETA model systems were developed. Conductive layers were prepared from various composites, e.g., PVA/graphite, PVA/graphene oxide (GO), PVA/reduced graphene oxide (RGO), PDMS/graphite. Polymer layers were selected from highly flexible polymers with large CTE such as PI, PVC and PP. The performance of the ETA model systems was investigated via of their bending displacement.

1.2 Objectives

To study the possibility of applying conductive polymer composite films and selected polymer films with high CTE in electroactive actuator model systems for robotic soft gripper application.

1.3 Hypothesis

1. Conductive polymer composite films can be used as conductive layers in ETA model systems.

2. Polymer layer with a high CTE can expand easily after joule heating.

3. Bending performance of electroactive actuators (ETA) model systems depends on the electrical conductivity of their conductive layers.

4. Bending displacement of ETA model systems depends on the applied voltages.

1.4 Scope of study

1. Preparation of polymer conductive composite films from PVA/graphite, PVA/GO PVA/RGO, PDMS/graphite composite.

2. Measurement of the resistance, resistivity and electrical conductivity of the conductive layers in the ETA model systems.

3. Study of the effect of crosslinking and glycerol plasticizer on the physical, chemical, mechanical and electrical of the polymer conductive composite films.

4. Determination of the optimum conditions for the preparation of a conductive layer and the selection of suitable polymer layers.

4.1 Method for preparing composite film.

4.2 Mixing time.

4.3 Pouring volume.

4.4 Types of conductive fillers e.g., graphite, GO and RGO composite were prepared.

4.5 Curing time.

4.6 Size of conductive composite films and polymer tape.

5. Study of the effect of the thickness of composite films, polymer tape and ETA model systems on their bending performance.

6. Chemical structure of graphite, GO, RGO and conductive composite film samples using attenuated total reflection - Fourier transform infrared (ATR-FTIR) technique.

7. Surface morphology of ETA model systems and tensile fractured surface morphology of polymer composite films using a scanning electron microscopy (SEM).

8. Measurement of the temperature generated from the ETA and its distribution observed from the thermal images of ETA model systems using a thermal camera.

9. Study of the potential applications of ETA model systems as soft robotic grippers.

CHAPTER 2
THEORY AND LITERAURE REVIEWS

2.1 Gripper technologies

Soft gripping are categorized into three technologies: i) actuation, ii) controlled stiffness and iii) controlled adhesion. These three categories are not exclusive and many devices make use of combinations of two technology classes to reach their high performance. The preferred technology and materials for a given task depend on properties of the object being manipulated, the operating environment (e.g., wet, dry, clean), required force, required speed, permissible power consumption and weight, biocompatibility, as well as system constraints including the integration or use of external sensors, and control methods.

Figure 2-1 provides a qualitative overview of the suitability of the three different gripper technologies for different object shapes (e.g., flat objects are easy to pick up using controlled adhesion). Gripping by actuation consists of bending gripper fingers or elements around the object, as we do with our fingers when picking up an egg or glass of water. The bending shape can be actively controlled, or one can exploit contact with the object to induce deformation. Of the many approaches, those with external electromagnetic motors and fluidic elastomer actuators (FEAs) are the most mature, with many devices shown in past 30 years. These techniques work well in air and in water, and are not overly sensitive to surface conditions or surface energy. There remain many challenges for gripping by actuation, including obtaining sufficient forces, controlling force and force distribution, especially for handling deformable objects. Flat objects are not suited to this method (Shintake, Cacucciolo, Floreano, & Shea, 2018).

Gripping using controlled stiffness exploits the large change in rigidity of some materials or material combinations to hold an object. An actuator is required to envelop the object with part of the gripper, but as the gripper is in the soft state, the actuation force can be very low, allowing very gentle objects to be caged. Important examples are phase change materials such as shape memory polymers and low-melting point alloys, granular jamming, and electrorheological

(ER)/magnetorheological (MR) fluids. Such grippers can be fast and allow tuning of the stiffness to a desired level. Limitations are the range of stiffness change that can be achieved, and for thermal systems the time constants can be long.

Gripping using controlled adhesion, like variable stiffness, requires an actuation method to partly envelop the object. Controlled adhesion by electro adhesion or dry adhesive relies on surface forces at the interface between gripper and object. This operating principle is a major advantage when manipulating very delicate objects, as it avoids the high compressive forces required in gripping by actuation, because one can obtain high shear forces without exerting large overall normal forces on object. Controlled adhesion is also ideal for flat objects or objects that cannot be enveloped. Limitations include requiring clean and relatively smooth and dry surfaces.

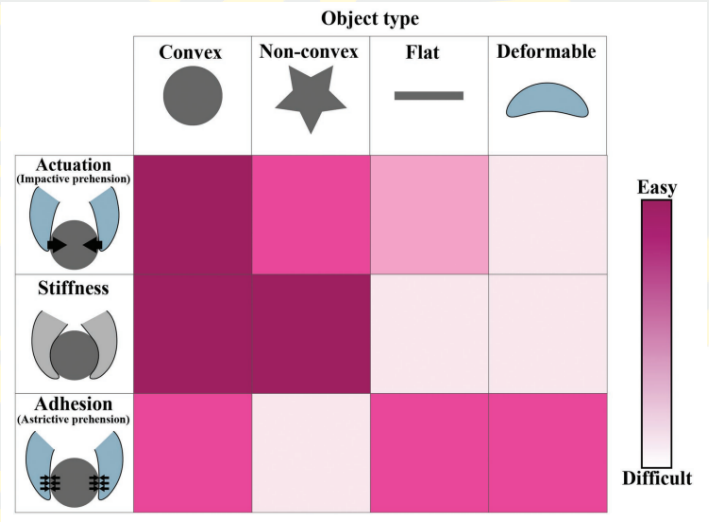

Figure 2-1 One possible classification of the characteristics of soft grippers for different gripping technologies and object types (Shintake et al., 2018).

2.2 Soft robot

Soft robots have distinguishable potential and advantages compared to traditional rigid robots, such as flexibility, high environmental adaptability, shock-absorbing properties, and high degrees of freedom. Therefore, the application areas of soft robots have involved human–machine interaction, locomotion and exploration, manipulation, medical and surgical applications, rehabilitation, and

wearable robots. Soft robotic grippers are one of the research areas in the field of soft robots. Scholars have created various soft robotic grippers with different drive modes, including pneumatic actuation, cable driven actuation, shape memory alloys actuation, and electroactive polymers actuation (D. Wang, Wu, Zhang, & Du, 2021).

Soft robots contain little or no rigid material and have been designed to perform a wide variety of robotic tasks, from bio-inspired crawling and peristalsis to pick-and-place gripping. Their unique promise for enabling inherently safe and adaptive contact with both solid and soft surfaces has made these emerging systems attractive for wearable and field robotics. There are many designs of soft robotic grippers, for example, the four-fingered gripper and six-pointed star gripper (Zhou, 2015). Part of soft robots can be driven by an amount of ways that are gathered into four types: tendon length variation, smart materials (including dielectric materials, electro-active polymers and heat sensitive materials), chemical reactions, and pneumatic/hydraulic transmissions. Smart materials can respond to electricity or electric field and exhibit a large strain in angular or linear motions (Li et al., 2019).

2.3 Conductive polymer composites

Conductive polymer composites (CPCs) are obtained by mixing an insulating polymer matrix with conductive fillers such as carbon black (CB), carbon fibers (CF), carbon nanotube (CNT), graphene (Gr) or any relevant filler particles which produce a good conducting pathway through the polymer matrix. CPCs exhibit several interesting features such as high electrical conductivity, light weight, corrosion resistant and good mechanical properties performance (Mohd Radzuan, Sulong, & Sahari, 2017).

Conductive polymer composites have come to existence since the 1950s with a resistivity between metallic conductor (10^{-7} Ω.m) and insulating materials (10^{15} Ω.m), which can find their applications in many fields such as floor heating elements, electronic equipment, important strategic materials such as electromagnetic interference (EMI) shielding, and semi-conducting materials for dissipation of static electricity (W. Zhang, Dehghani-Sanij, A. A., & Blackburn, R. S. , 2007).

By adding conductive fillers to polymers, materials can be designed with specific properties tailored to each application. In order for composites materials to be used for conductive applications, conductive materials have a surface resistivity of less than 10^5 Ω/square, dissipative materials have a surface resistivity from 10^5 to 10^{12} Ω/square and insulative materials have a surface resistivity greater than 10^{12} Ω/square. For many articles in ESD-protected environments, the optimal surface resistivity is in the range 10^6 to 10^9 Ω/square (Narkis, 1999). The electrical conductivity of a composite material is related to the filler volume fraction, size, shape and structure. A polymeric composite consisting of an insulating polymer matrix and conductive fillers becomes electrically conductive as the filler content exceeds a certain critical filler volume fraction. This transition-like change in conductivity is generally attributed to percolation phenomena. The transition occurs in the percolation threshold concentration of fillers in the polymeric matrix (Naficy & Garmabi, 2007), which is a consequence of the formation of a continuous electrical path through the composite material.

2.4 Electroactive polymers

Electroactive polymers (EAPs) are polymers that undergo shape and/or dimensional change in response to an applied electrical field. EAPs are a subset of electro responsive polymers (ERPs), which exhibit electrically coupled responses in general (H. Wang, Chen, Lau, & Ren, 2016).

Electrothermal actuators (ETAs) are a new generation of active materials that can produce different motions from thermal expansion induced by Joule heating (Sun et al., 2019).

The convenience and the practicality of electrical stimulation and the recent improvement in capabilities made EAPs one of the most attractive materials among the activatable polymers. EAP materials benefit from many of the appealing characteristics of their being polymers, e.g. lightweight, inexpensive, fracture tolerant and pliable. Moreover, they can be configured into almost any conceivable shape, and their properties can be tailored to suit a broad range of requirements. These capabilities and the significant changes in shape or size under electrical

stimulation while being able to endure many cycles of actuation are inspiring many applications. Practitioners in biomimetics are particularly excited about these materials since they can be used to mimic the movements of animals and insects. Potentially, mechanisms actuated by EAPs will enable engineers to create devices previously imaginable only in science fiction (Y. Bar-Cohen, 2007). ETAs have an electrically conductive heating layer that provides Joule heat during the actuation. Similarly, in photothermal actuators, an active layer containing light absorbing material converts light into heat. Normally, soft actuators exhibit only basic deformations such as expansion, contraction, bending, or folding. In recent years, there has been an increasing trend in the research of soft actuators that achieve complex and programmable deformations (Cao & Dong, 2021).

A typical soft ETA is composed of two material layers with a great difference in coefficient of thermal expansion (CTE), as shown in Figure 2-2. When applied with voltages, the conductive layer with a lower CTE generates the joule heat to heat up the whole ETA. On account of the difference in CTE, the substrate with higher CTE will expand more, yielding a bending deformation to the lower-CTE layer. The deformation here is usually expressed in bending curvature and angular and vertical displacement at the end of the ETA (Tian et al., 2021).

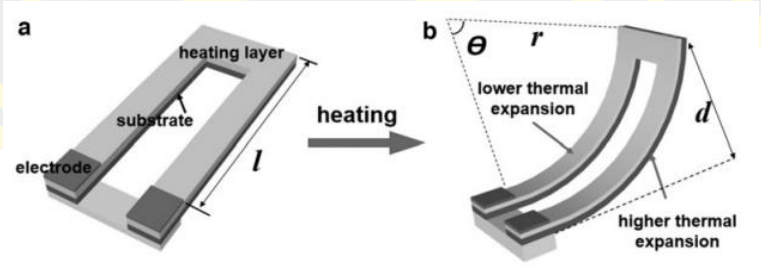

Figure 2-2 Schematic diagram of structure and mechanism of soft ETAs, (a) Initial state and (b) bending state (Tian, Li, Tian, Yang, & Ren, 2021).

2.5 Electrical conductivity and resistivity

The electrical conductivity of a composite is usually characterized by its necessity on the filler volume fraction. At low filler loadings, the conductivity of the composite is still very close to that of the pure polymer matrix. At some critical

loading, called the percolation threshold, the conductivity increases several orders of magnitude with very little increase in the filler amount (Clingerman, King, Schulz, & Meyers, 2002).

Electrical resistivity and conductivity are important properties for materials. Different materials have different conductivity and resistivity. Electrical conductivity is based on electrical transport properties. These can be measured with multiple techniques by using a variety of instruments. If electricity easily flows through a material, that material has high conductivity. Copper and aluminum are well known materials that have high conductivity. Conclusively, electrical conductivity is the measure of how easily electricity flows through a material.

The electrical resistivity of a material is a number describing how much that material resists the flow of electricity. Resistivity is measured in units of ohmmeters (Ω m). If electricity can flow easily through a material, that material has low resistivity. If electricity has great difficulty flowing through a material, that material has high resistivity. The electrical wires in overhead power lines and buildings are made of copper or aluminum. This is because copper and aluminum are materials with very low resistivities (about 20 n Ω m), allowing electric power to flow very easily. If these wires were made of high resistivity materials like some types of plastics which can have resistivities about 1 E Ω m (1×10^{18} Ω m), very little electric power would flow. Electrical resistivity is represented by the Greek letter r. Electrical conductivity is represented by the Greek letter s, and is defined as the inverse of the resistivity. This means a high resistivity is the same as a low conductivity, and a low resistivity is the same as a high conductivity: Conductivity and resistivity are inversely proportional to each other. When conductivity is low, resistivity is high. When resistivity is low, conductivity is high. The equation is as follows:

$$\sigma = \frac{1}{\rho} \qquad (1)$$

Where resistivity is represented by ρ and is measured in ohm-meters (Ω m) conductivity is represented by σ and is measured in siemens per meter (S/m) (Raheem, 2007).

The electrical conductivity of a composite is usually characterized by its necessity on the filler volume fraction. At low filler loadings, the conductivity of the composite is still very close to that of the pure polymer matrix. At some critical loading, called the percolation threshold, the conductivity increases several orders of magnitude with very little increase in the filler amount (Clingerman et al., 2002).

2.6 Volume resistivity and conductivity

Volume resistivity represents the electrical resistance through a cube of insulating material. As measured in Ohm-centimeters, it demonstrates the electrical resistance through a one-centimeter cube of the sample. Similarly, when using Ohm-inches, it indicates the electrical resistance through a one-inch cube of the material. Electronic devices contain a variety of chemicals meant to insulate or conduct. Volume resistivity testing for these chemicals ensures electricity travels through these components as intended. Volume resistivity in conductive pastes and other electronic components can indicate contamination if the desired level of resistivity or conductivity isn't achieved. This value is measured according to ASTM D257. It is dependent on temperature, frequency, and voltage and will vary with the conditioning of the material (Rodriguez, 1982). Volume resistivity can be calculated using the equation:

$$\rho_v = \frac{A}{T} R_v \qquad (2)$$

When A: the effective area of the measuring electrode for the particular arrangement employed with A = (a + g) (b + g) for rectangular specimen, a, b = lengths of the sides of rectangular electrodes and g = gab between electrode,

T: average thickness of the specimen,

R_v: measured volume resistance in ohms (Ω).

Since the films have a uniform thickness, a property that is often measured is the sheet resistance. This property is also called sheet resistivity, surface resistivity or surface resistance. Resistivity is the inverse of conductivity. Volume resistivity is also called bulk resistivity because it is a measure of the resistivity across a defined

thickness. As mentioned earlier, resistivity is the inverse of conductivity. Since volume resistivity is measured in ohms-cm, volume conductivity is one-over-ohm-cm (1/Ω-cm) and is measured in S/cm, Therefore, a volume resistivity of 500 ohm-cm is equal to a volume conductivity of 1/500 or 0.002 S/cm (Perabo, 2013).

2.7 Graphite

Atomic carbon forms two primary structures, which are based upon sp^3 (diamond) or sp^2 (graphite) chemical bonding (Figure 2-3). Of these, diamond is the less stable form and will transform into graphite when heated (Figure 2-3 (a)). The sp^2-graphitic structure currently dominates the world of carbon nanomaterials as it forms the full spectrum of low-dimensional geometries. For example, in its most compact stable form, sp^2 -carbon arranges into a zero-dimensional (0D) structure known as a buckyball (Figure 2-3 (e)). By inserting rows of atoms around the equator of this buckyball, a one-dimensional (1D) carbon nanotube emerges (Figure 2-3 (h)). Finally, if this carbon nanotube is "unzipped" along its length, we have a flat, two-dimensional (2D) sheet known as graphene (Figure 2-3 (c)).

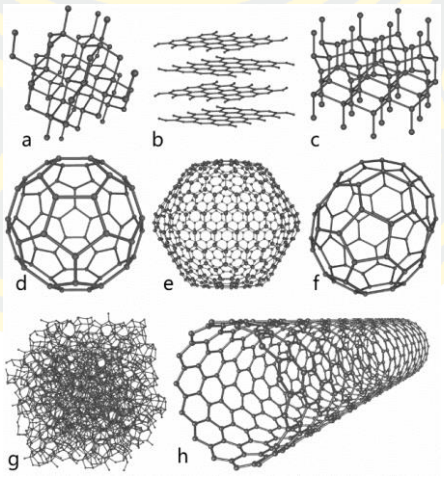

Figure 2-3 The two major allotropes of carbon are (a) sp^3-bonded diamond and (b) sp^2-bonded graphite. The sp^2-bonded allotrope is formable into three low-dimensional structures: (c) 2D sheets known as graphene, (d) 1D nanotubes, or (e) 0D buck balls (f)fullerite (g) C70, g) amorphous carbon, and (h) single-walled carbon nanotube (Kaur, 2018).

Graphite is anisotropic, being a good electrical and thermal conductor within the layers (due to the in-plane metallic bonding) and a poor electrical and thermal conductor perpendicular to the layers (due to the weak van der Waals forces between the layers). The conductivities depend on for example the degree of graphitization, that is how close the material is to perfect graphite (Granberg, 2021).

Graphite, well known as graphene-based filler, is naturally and is reported as the best conductive filler for its excellent conductive properties and well dispersion in polymer matrix (Abdullah, 2017). Graphite, like diamond, is a crystalline form of carbon. Graphite and diamond are natural allotropes of carbon (i.e. different molecular forms of the same element) that arise from the way the carbon atoms are joined together and arranged to form regular structures. In diamond, each carbon atom is bound to four other carbon atoms by strong covalent bonds in a regular isometric structure that gives rise to the hardest known mineral. In graphite, carbon atoms are bonded to only three other carbon atoms to form strong, two dimensional layers, that are extremely stable, but where each layer is only weakly linked to adjacent layers by van der Waal's forces. The resulting hexagonal layered structure forms one of the softest minerals. The presence of an unpaired valence electron makes graphite an excellent electrical conductor within the plane of the layers.

Graphite is inert towards most chemicals and has a high melting point of ~3,550 °C, but in the presence of oxygen will begin to oxidize at temperatures >300 °C and can be induced to sustain burning above 650 °C, given suitable conditions; the rate of thermal oxidation is slow but increases with increasing temperature. Thermal conductivity in graphite is anisotropic but is very high in the direction parallel to the plane of the layers. The calculated crystal density of graphite 2.266 g/cm^3 but the measured specific gravity is typically between 2.20–2.30 depending on purity; high values are due mostly to impurities; low values are associated with trapped porosity. Graphite is soft, greasy to the feel and is flexible and sectile, but not elastic (John Keeling, 2017). Graphite powder (Figure 2-4) is one of the most commonly used conductive fillers due to its low cost, excellent conductivity, and chemical stability (W. He et al., 2021).

Figure 2-4 Graphite powder ("Graphite Powder," 2022).

2.8 Graphite oxide and reduced graphite oxide

Graphite oxide (GO) has attracted the recurring interest of the chemical community since it was first synthesized in 1855 by Brodie (Dimiev, Kosynkin, Alemany, Chaguine, & Tour, 2012). Numerous studies were done throughout the decades to reveal its structure. Several models of the structure of GO have been developed, which often partially exclude each other. The earliest model was developed in 1939, while a more recent model was published in 2006. Despite the effort of many chemists, the structure of GO has remained elusive. Graphite oxide (GrO) is a layered material produced by the oxidation of graphite. In contrast to pristine graphite, the GrO sheets, known as graphene oxide, are heavily oxygenated, bearing hydroxyl and epoxide functional groups on their basal planes, in addition to carbonyl and carboxyl groups presumable located at the sheet edges. Nevertheless, there are certain features that still remain unknown among which stands out the chemical structure.

In recent years, new interest in GO was sparked after it was found that GO can serve as the precursor for chemically converted graphene (CCG), which can be effectively used in fabrication of, for example, transparent conductive films and field effect transistors. GO and its functionalized derivatives have been investigated for applications in optoelectronics, biodevices, drug delivery systems and composites. One of the interesting properties of GO is its propensity to spontaneously exfoliate in

aqueous solutions into monolayer sheets. This is the only known method to readily introduce a monolayer carbon lattice into hydrophilic media (Dimiev et al., 2012; Ernesto Hernández-Hernández, 2020).

The reduction of graphene oxide is considered to be an attractive route to obtain graphene-like behavior. Chemical, thermal or photo-thermal reduction methods are used to obtain reduced graphene oxide structures. However, rGO cannot reach the pristine graphene structure. Even after severe reduction rGO still contains residual oxygen and structural defects originated in the chemical oxidation synthesis of GO. Chemical reducing agents used for rGO synthesis are often inorganic agents such as NaB or organics, such as phenyl hydrazine hydrate or hydroxylamine. Thermal reduction occurs in an inert or reducing atmosphere at temperatures between 300°C -2000°C. Finally, the photothermal-reduction of GO can be done with a direct laser beam at wavelengths under 390 nm (energy > 3.2 eV). The studies show that thermal reduction methods are advantageous compared to chemical reduction methods. Not only a lower level of reduction is achieved by chemical reduction methods but also the reducing agents used in methods are highly toxic. The thermal reduction methods have the upper hand due to their high level of reduction and relatively environmentally friendly process. The carbon to oxygen ratio of the resulting product is an important feature. The higher the C/O ratio the closer the properties of rGO to the properties of pristine graphene. The reduction process causes drastic changes in the structural properties, mechanical strength, stability, dispersibility, and reactivity of GO. These changes are directly related to the elimination of the oxygen containing compounds in the GO structure and restoration of the sp^2 structure after the reduction process (Gürsel, 2022).

GO prepared by Hummer's method consists of a-few-layer carbon platelets decorated with oxygen containing functional groups. The removal of some oxygen-based groups by reducing agents or thermal treatment can yield rGO. The main process is as follows. GO is exfoliated via ultrasonication and then reduced by hydrazine hydrate, a strong reducing agent, for 2 h. Since hydrazine is toxic, alternative reagents such as $NaBH_4$, ascorbic acid, and HI can be used. Among these, ascorbic acid is essential for the scalable production of rGO. The chemical procedure to obtain rGO using ascorbic acid as a reducing agent is shown in Figure 2-5.

This reaction does not produce toxic gases. rGO has been proven to be a good candidate for various applications such as field effect transistors (FET), solar cells, energy applications and production of composite paper-like materials due to its abundant atomic defects (Razaq et al., 2022).

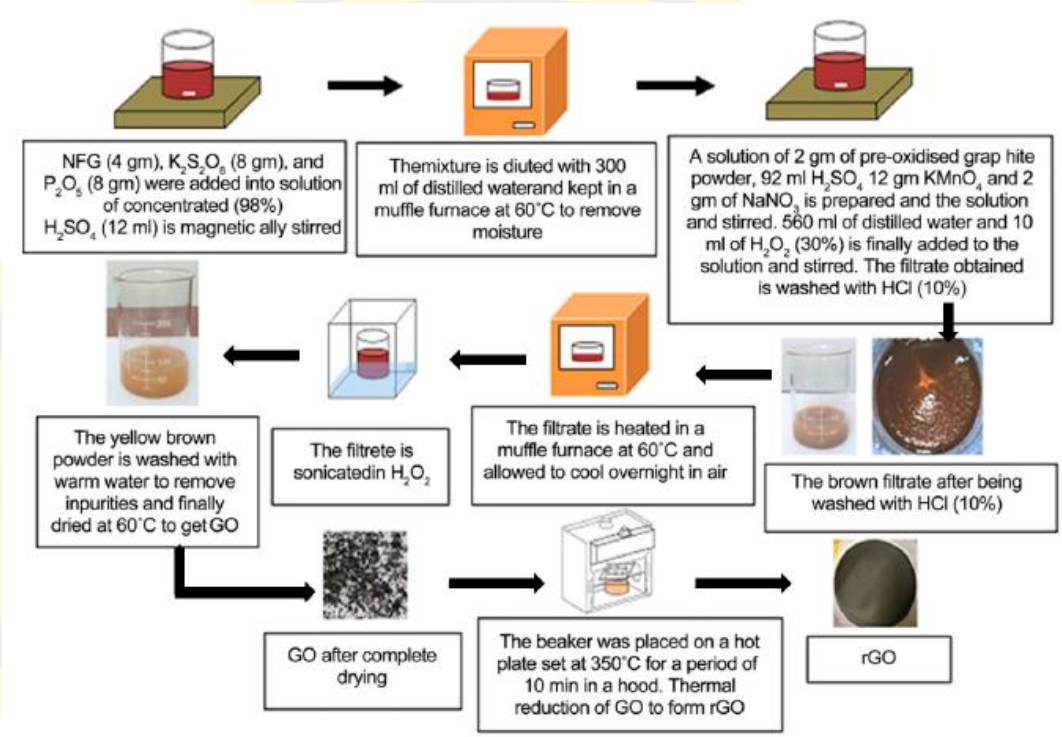

Figure 2-5 Steps of the synthesis of GO and rGO (Razaq et al., 2022).

2.9 Polyvinyl alcohol

Polyvinyl alcohol (PVA) is a well-known synthetic polymer that is attracting attention for the production of biodegradable plastic materials. The main chains of the vinyl polymer are joined only by carbon-carbon linkages, similar to typical plastics such as polyethylene, polypropylene and polystyrene. The major uses of PVA include textiles, paper coating, warp sizing, adhesives and films. PVA is a water-soluble polymer. Among the vinyl polymers produced industrially, PVA is the only one known to be mineralized by microorganisms but its natural biodegradation rate is slow (Duangkhaetita Kanjanasopa, 2018).

PVA are synthetic polymers used since the early 1930s in a wide range of industrial, commercial, medical and food applications including resins, lacquers,

surgical threads and food-contact applications. The physical characteristics of PVA are dependent on its method of preparation from the hydrolysis, or partial hydrolysis, of polyvinyl acetate. PVA, is generally classified into two groups, partially hydrolyzed (a) and fully hydrolyzed (b). (Figure 2-6) Varying the length of the initial vinyl acetate polymer and the degree of hydrolysis under alkaline or acidic conditions yields PVA products of differing molecular weights (20,000–400,000), solubility, flexibility, tensile strength and adhesiveness. Various properties are measured to characterize PVA such as pH, viscosity, loss on drying, melting point, refractive index, heavy metals and residue on ignition. These properties vary based on molecular weight and% hydrolysis for the grade of PVA (DeMerlis & Schoneker, 2003).

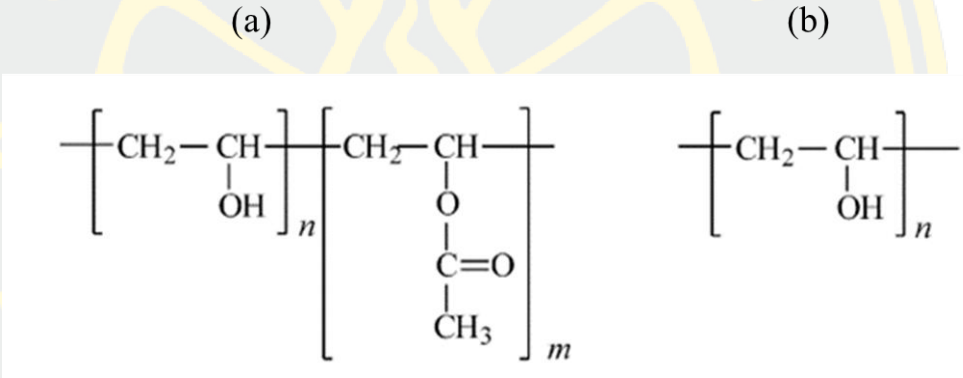

Figure 2-6 Structural formula for PVA: (a) partially hydrolyzed; (b) fully hydrolyzed (Chahal, Kumar, & Hussian, 2019).

PVA is hydrophilic, semi-crystalline, biocompatible and nontoxic polymer, which contains many hydroxyl groups and comprises the shape memory features (Pirahmadi, Kokabi, & Alamdarnejad, 2020). PVA is a thermoplastic polymer that is obtained by the hydrolysis of poly(vinyl acetate) (PVAc) and not by polymerization processes like some other synthetic polymers. After hydrolysis, PVA still contains 1–2 mol% of acetyl groups. Its degree of polymerization (DP) depends primarily on the size of the PVAc macromolecular chain.

The transformation of PVAc into PVA is obtained by the base catalyzed alcoholysis or by the acid-initiated hydrolysis. PVA is the most polar synthetic polymer, it is odorless, nontoxic, biocompatible, and soluble in water, acids, and high polar solvents. Its molecular weight (MW) depends on PVAc MW and the degree of

hydrolysis (Feldman, 2020). This polymer is widely used by blending with other polymer compounds, such as biopolymers and other polymers with hydrophilic properties; it is utilized for various industrial applications to enhance the mechanical properties of films because of its compatible structure and hydrophilic properties (Gaaz et al., 2015).

2.10 Coefficient of thermal expansion

The coefficient of thermal expansion (CTE) is an important material property that indicates the dimensional stability of a material under temperature variations. Because elastomers are frequently subjected to thermal loading, the CTE of an elastomer has been a key consideration in their various applications (Lee, Kim, & Kim, 2016).

CTE is a property reflecting dimensional stability of a material under changing thermal conditions. Among several formal definitions of the CTE, one of the most popular is the linear CTE (CLTE):

$$\text{CLTE} = \frac{1}{\text{L (T)}} \left(\frac{\partial \text{L}}{\partial \text{T}}\right)_{\text{p}}, \tag{3}$$

where L (T) is the length of the material at temperature T, ∂L is the change in length given ∂T difference in temperature at constant pressure p.

The higher the CTE value is the more a given material expands with increasing temperature. CTE is an industrially crucial property since mismatches in thermal expansivities between different materials lead to internal stress and eventually to a failure, of a manufactured part. The main factors influencing the CTE of a polymer are cohesive forces between molecules, topological and geometrical arrangement of atoms, chain stiffness and bond flexibility. Quantitatively, it was only possible, until now, to roughly relate the CTE of amorphous polymers to other measured macroscopic properties, such as the glass transition temperature (T_g) or van der Waals volume (V_W) (Gracheva, Lambard, Samitsu, Sodeyama, & Nakata, 2021).

According to Awasthi and co-workers (Aman Awasthi, 2018), the coefficient of thermal expansion is the rate at which the size of a material changes with respect to temperature change. Size considerations can be made by changes in length, area or volume, and so there are coefficients derivable for linear, area and volume expansions.

With an assumed constant pressure, linear expansion, area expansion and volume expansion can be written more simply as;

$$\left.\begin{aligned} \alpha_L &= \frac{1}{L}\frac{dL}{dT} \\ \alpha_A &= \frac{1}{A}\frac{dA}{dT} \\ \alpha_V &= \frac{1}{A}\frac{dV}{dT} \end{aligned}\right\} \quad (3.1)$$

Where L, A and V are length, area and volume, respectively, and T is temperature. The unit of measurement for thermal expansion coefficients is the inverse of temperature, $°C^{-1}$ or K^{-1}. However, extra dimensions such as cm/cm or mm^2/mm^2 are added to the unit so that it can be inferred whether the coefficient is linear, area or volumetric.

When materials are heated, the molecules of that material start to agitate more and the average distance between them increases which translates into expansion of its dimensions. Measurements are made with a thermomechanical analyzer consisting of a specimen holder and a probe that transmits changes in length to a transducer that translates movements of the probe into an electrical signal. A composite film of 5 mm × 5 mm, with a thickness of approximately 65 µm, is subjected to dynamic TMA test using Thermo Mechanical Analyser TMA 40, Mettler Toledo. The test temperatures ranged from 40 to 200 °C and the heating rate of 10 °C/min. A constant load of 0.02 N is to be applied on the probe. The change in the dimension to corresponding temperature observed and recorded. The obtained TMA plot (the displacement vs temperature) is evaluated for the coefficient of linear thermal

expansion (CLTE) in the temperature range from the ambient to the maximum temperature after which the material shows softening (Prof. Tushar S Kulkarni, 2012).

2.11 Polyimide

Polyimide (PI) is a family of high-performance polymers with imide-containing heterocyclic rings (Figure 2-7). PIs were first reported in 1908 by Bogert and Renshaw (Zhuang, Seong, & Lee, 2019). Their excellent overall properties include thermo-oxidative stability, unique electrical properties and high radiation- and solvent-resistance. With high mechanical strength, they have been used for advanced applications in aviation, aerospace, micro-electronics, gas separation, pervaporation membranes, fuel cells, batteries, electronic memory devices, shape memory devices, optical devices, biomedical applications, sensors, aerogels and polymer matrices in composites/hybrid materials (Zhuang et al., 2019). PI is an insulating layer for semiconductor devices, because of their outstanding chemical and physical properties, such as excellent mechanical strength, high thermal stability, good dielectric properties, radiation and solvent resistance. To achieve the usage in electronic devices, PI films would be coated with other materials such as conductive metals, silicon or glass substrate (Z.-H. Wang, Chen, Yang, Zhao, & Yang, 2018).

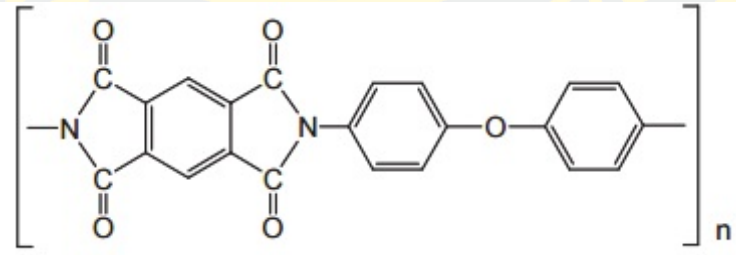

Figure 2-7 Chemical structure of polyimide (Satoshi Yoda, 2003).

PI is a promising material in the semiconductor and microelectronic industries due to its excellent mechanical properties and outstanding thermal stability at elevated temperatures. PI is generally used as a coating material on silicon wafers as insulators or substrates of copper-clad laminates. These electronic devices usually serve in circumstances experiencing a wide temperature range. The mismatch in the CTE between the PI film and substrate will give rise to a thermal stress concentration,

which leads to cracking or peeling of the PI film. When components' sizes become smaller and approach the nanoscale, subtle differences in the CTE critically affect the performance of the electronic system. Thus, high performance PI films with a CTE less than 10 ppm $^{o}C^{-1}$ in the glassy temperature region are highly desirable for the applications discussed above (Liu et al., 2018).

2.12 Polydimethylsiloxane

Polydimethylsiloxane (PDMS) is regarded as one of the most important biomaterials that show a high potential for an extensive range of applications, including biomedical devices and wound dressing, due to their broad spectrum of desirable properties including unique flexibility, low glass transition temperature, superior thermal and oxidative stabilities, remarkable biocompatibility, high oxygen permeability and very low toxicity (Lin et al., 2019).

PDMS is an organosilicon polymer (Figure 2.8) that is synthesized from dimethyl siloxane oligomers with vinyl-terminated end groups, dimethylvinylated and trimethylated silica filler, a platinum catalyst, a cross-linking agent, dimethylmethylhydrogen siloxane and an inhibitor, tetramethyltetravinyl cyclotetrasiloxane.

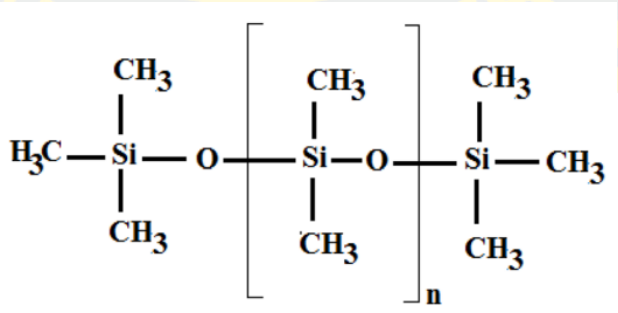

Figure 2-8 Chemical structure of PDMS
(Hamouni, Arous, Abdessemed, Nezzal, & Van der Bruggen, 2019).

Once cured, the polymer has a CTE of 3.1×10^{-4} K^{-1}. The Young modulus of PDMS can range between 0.7 and 3.5 MPa, depending on the mixing ratio, curing temperature and baking time. The Young modulus of PDMS is lower than silicon-

based or metallic materials and allows for it to undergo large elastic deformations during its removal from a master template with micro- or nanoscale features (Wes W Tooley, 2011).

2.13 Polyvinyl chloride

Polyvinyl chloride (PVC) is extraordinarily useful as a commercial material. Among the thermoplastics, it ranks second only to polyolefins in total worldwide production volume due to its high stiffness, flame retardancy, chemical resistance and low cost. However, the disadvantages of rigid PVC, such as low notch impact strength and low heat resistance, have restricted its application (Chuayjuljit, Thongraar, & Saravari, 2008).

PVC is a versatile thermoplastic material that is used in the production of hundreds of products that consumers encounter in everyday life and many more that are encountered less frequently but are nevertheless very important in construction, electronics, healthcare and other applications. Its low cost and desired mechanical and physical properties make its use widespread. Both, flexible and rigid products can be made from PVC. Researches have shown that the possibility of substitute material for PVC is very less and even if there are some, they are neither as efficient nor economic. Products made from PVC are usually chemical resistant and have negligible effect of weather and abrasion. Hence, they are not harmful to human health. Moreover, chlorine content makes the material highly flame retardant (Ansar Khan, 2016).

2.14 Test methods

2.14.1 Fourier transform infrared spectrometer

FTIR spectroscopy is a technique used to obtain the absorption or emission infrared spectrum of a solid, liquid or gas. The FTIR spectrometer simultaneously collects high-resolution information over a wide spectral range (between 4000 and 400 cm^{-1}), a distinct advantage over a dispersive spectrometer, which estimates power over a narrow range of frequencies at once. The aim of spectroscopy techniques (FTIR or bright perceptible (UV–Vis) spectroscopy) is to quantify how

much light a sample absorbs at each frequency. The most direct approach, the “dispersive spectroscopy” method, consists of focusing a monochromatic light beam at a sample, measuring the amount of absorbed light, and recalculating it for each frequency.

In infrared spectroscopy, IR radiation is passed through a sample. Some of the infrared radiation is absorbed by the sample and some of it is passed through (transmitted). The resulting spectrum represents the molecular absorption and transmission, making a molecular fingerprint of the sample. Like a fingerprint no two unique molecular structures produce the same infrared spectrum. This makes infrared spectroscopy useful for several types of analysis.

Fourier transform spectroscopy is a less instinctive approach for obtaining similar data. Rather than focusing a monochromatic (single frequency) light emission at the sample, this strategy might focus a bar, or array, which contains numerous frequencies of light at once and measures how much of that beam is absorbed by the sample (Fadlelmoula, Pinho, Carvalho, Catarino, & Minas, 2022).

The normal instrumental process is as follows:

1. The Source: Infrared energy is emitted from a glowing black-body source. This beam passes through an aperture which controls the amount of energy presented to the sample (and, ultimately, to the detector).

2. The Interferometer: The beam enters the interferometer where the spectral encoding takes place. The resulting interferogram signal then exits the interferometer.

3. The Sample: The beam enters the sample compartment where it is transmitted through or reflected off of the surface of the sample, depending on the type of analysis being accomplished. This is where specific frequencies of energy, which are uniquely characteristic of the sample, are absorbed.

4. The Detector: The beam finally passes to the detector for final measurement. The detectors used are specially designed to measure the special interferogram signal.

5. The Computer: The measured signal is digitized and sent to the computer where the Fourier transformation takes place. The final infrared spectrum is then

presented to the user for interpretation and any further manipulation ("Introduction to Fourier Transform Infrared Spectrometry.," 2001).

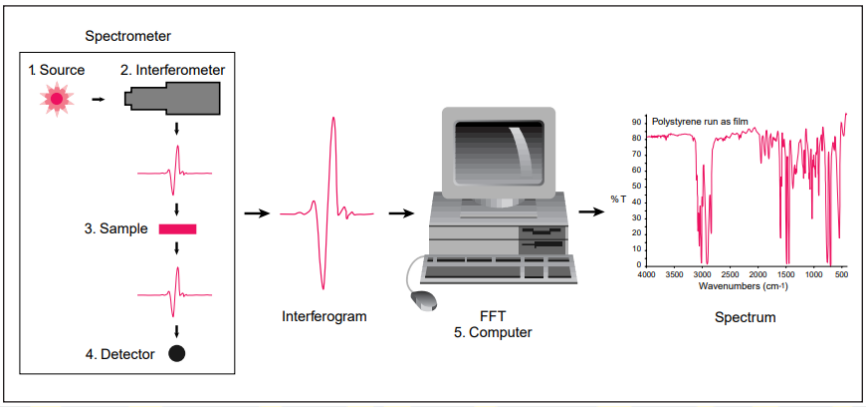

Figure 2-9 Schematic of a Fourier transform infrared spectrometer (Dr. Gurumurthy.B. R and Dinesh Bhatia, 2017).

2.14.2 Digital multimeter

Multimeter is a significant device for sensing or measuring electronic parameters (e.g., voltage, current, resistance) and is crucial to the fields of science and technology. Moreover, it usually appears in our daily life, e.g., factory, school laboratory, home tools, and so on. Although the digital multimeter has been widely used for several eras due to the considerations of precision and cost, the analog multimeter is still preferable in many applications, in particular, for monitoring promptly varying values and easy understanding. The disadvantage of the traditional analog multimeter (abbreviated as A-meter for short) is the lack of data communication interface within it to allow further data processing. Therefore, reading an A-meter usually relies on human eyes with two obvious problems-inefficiency and easy fatigue-while visual inspection onto an A-meter is needed for a long period of time (Figure 2-10). The Agilent 34401A is a digital multimeter, or DMM, which means that it displays measurements in a digital form rather than a needle moving across a dial (facstaff.bucknell.edu, 2014). It's called a multimeter because it can make a variety of measurements and replace a collection of different single-function meters. The measurements that will be most important are voltage, current, and resistance. The voltage and current measurements can be for either a.c. or d.c. signals.

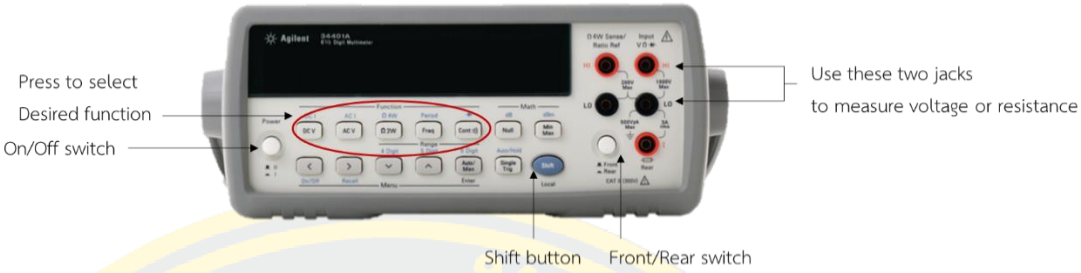

Figure 2-10 Agilent 34401A Digital Multimeter ("Agilent 34401A Digital Multimeter ", 2022).

The test leads must also be connected to the circuit differently for different kinds of measurements, as shown in Figure 2-11.

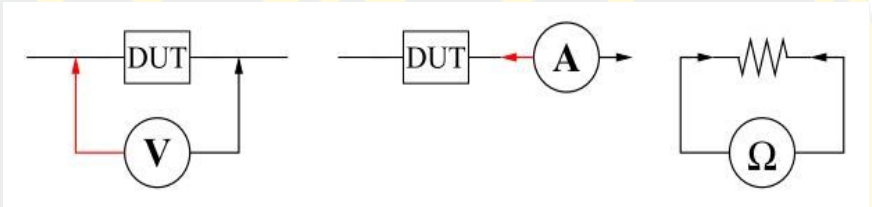

Figure 2-11 Proper connections for measuring voltage, current and resistance (Mathewscompany., 2016).

The multimeter offers two resistance measurements: 2-wire and 4-wire ohms. For both methods, the test current flows from the input HI (Hisense) terminal, through the resistor being measured. For 2-wire ohms, the voltage drops across the resistor being measured is sensed interior to the multimeter. Therefore, test lead resistance is also measured. For 4-wire ohms, separate "sense" connections are required. Because no current flows in the sense leads, the resistance in these leads does not give a measurement error. The errors mentioned earlier in this chapter for DC voltage measurements also apply to resistance measurements. The 4-wire ohms method provides the most accurate way to measure small resistances because it reduces test lead and contact resistances. This is often used in automated test applications where resistive and/or long cable, numerous connections, or switches exist between the multimeter and the device under test (DUT). The optional connections for 4-wire ohms measurements are shown below, as shown in Figure 2-12 ("Resistance Measurement Considerations,").

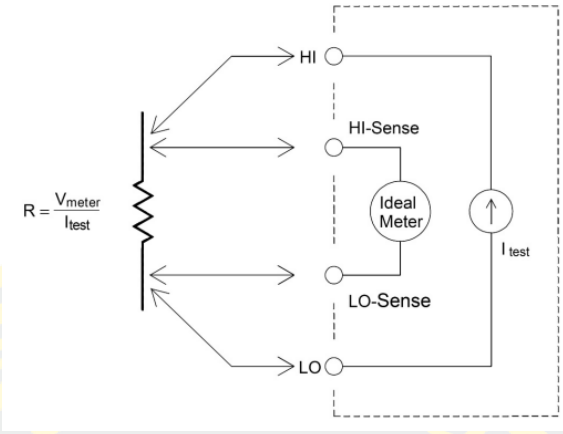

Figure 2-12 Wire Ohms measurements ("Resistance Measurement Considerations,").

2.14.3 Bending curvature

Curves are regular bends provided in the lines of communication like roads, railways etc. and also in canals to bring about the gradual change of direction. The rate of change of the angle through which the tangent to a curve turns in moving along the curve and which for a circle is equal to the reciprocal of the radius (Priyanka). Curves provided in the horizontal plane to have the gradual change in direction are known as horizontal curves, whereas those provided in the vertical plane to obtain the gradual change in grade are known as vertical curves. Curves are laid out on the ground along the center line of the work. They may be circular or parabolic and are classified inti three main categories:

(i) Simple

A simple curve consists of a single arc of a circle connecting two straights. It has radius of the same magnitude throughout as show in Figure 2-13.

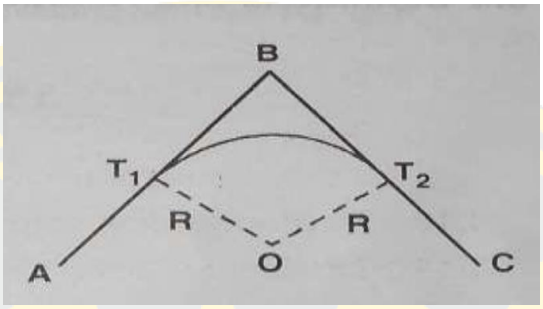

Figure 2-13 Simple curve connects two lines with a smooth arc.

(ii) Compound

A compound curve consists of two or more simple curves having different radii bending in the same direction and lying on the same side of the common tangent. Their centres lie on the same side of the curve (Figure 2-14).

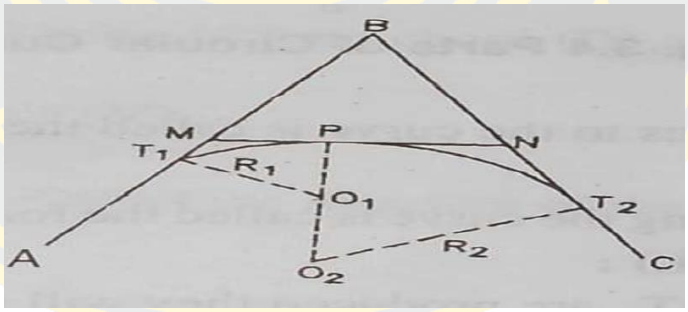

Figure 2-14 Compound curves (G.I.T., 2006).

(iii) Reverse

A reverse or serpentine curve is made up of two arcs having equal or different radii bending in opposite directions with a common tangent at their junction. Their centres lie of opposite sides of the curve (Figure 2-15).

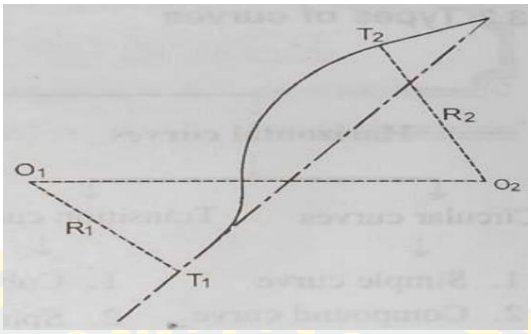

Figure 2-15 Reverse curves (G.I.T., 2006).

A curve may be designated either by the radius or by the angle subtended at the centre by a chord of particular length. A curve is designated by an angle called the degree of the curve (D). By arc definition, the central angle subtended by a circular arc of 30 m (100-ft) and by Chord definition, the angle at the center of a circular arc subtended by a chord of 30 m (100 ft) (Figure 2-16).

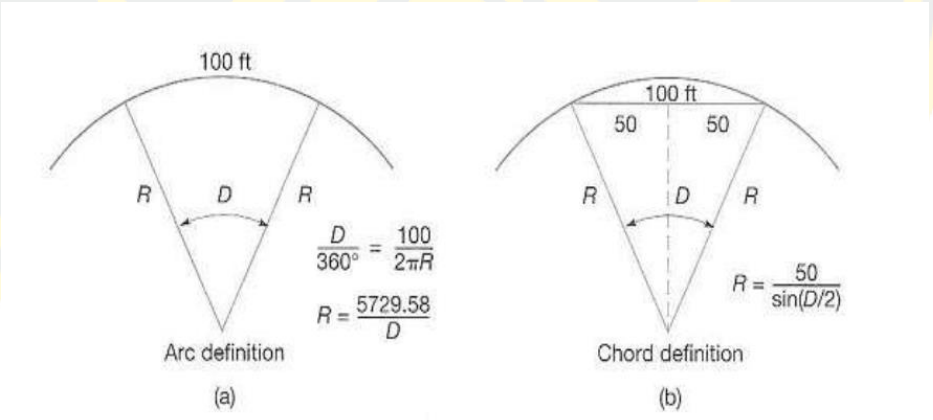

Figure 2-16 Designation of arc definition and chord definition curves (G.I.T., 2006).

Epinasty curvature is the angle between tangents to the curvature of the ends of the petioles (θ) was used as a measure of epinasty and can be determined by the angle, measured using a point of contact, similar to the stem of a leaf, for each of the curve angles touching each point (Michael S. Reid, 1981) as show in Figure 2-17.

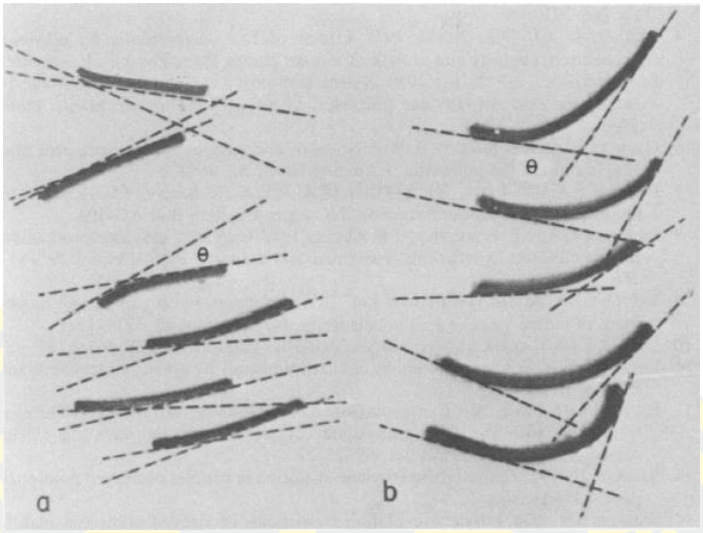

Figure 2-17 Method for determining epinastic curvature. Petioles from control (a) and reoriented (b) bracts were excised and copied in a photocopier. (Michael S. Reid, 1981).

2.14.4 Tensile test

One of the most common mechanical stress– strain tests is performed using tension. The tension test can be used to ascertain several mechanical properties of materials that are important in design. In the tension test, a specimen is deformed with a tensile load that is applied uniaxially along the long axis of a specimen, usually until a fracture occurs. The output of a tensile test is recorded as a load or force versus elongation. The load and elongation are normalized to the respective parameters of engineering stress and engineering strain. Figure 2-18 shows the uniaxial tensile test sample and the tensile testing machine that is used to obtain a stress–strain curve. Figure 2-18 shows the changes in shape of the specimen during tensile testing.

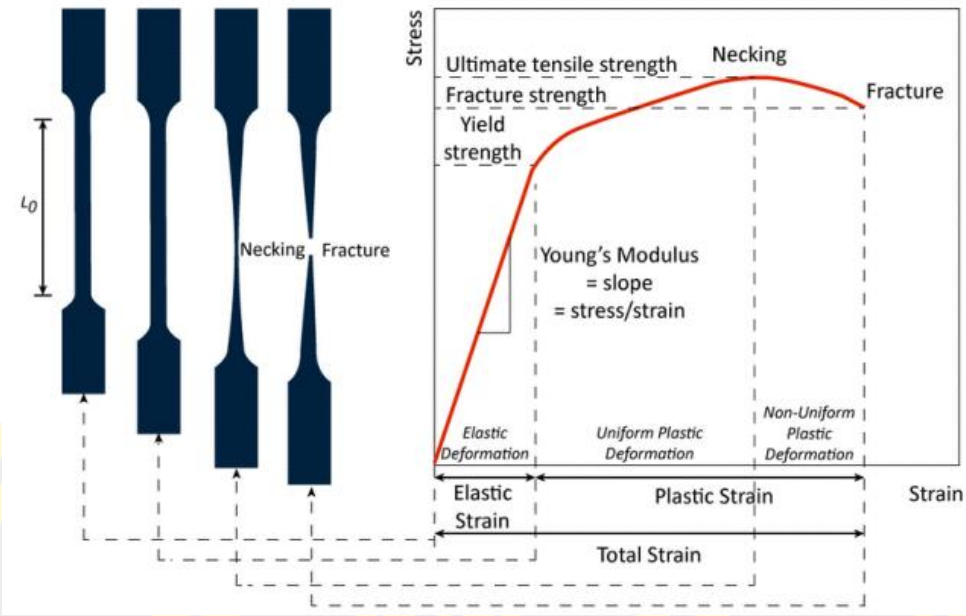

Figure 2-18 The shape of the specimen changes during tensile testing (Yalcin, 2017).

Engineering stress σ is defined by equation 4.

$$\sigma = \frac{F}{A_0} \quad (4),$$

where F is the instantaneous load applied perpendicular to the specimen cross-section and A_0 is the original cross-sectional area before any load is applied. Engineering strain ϵ is defined by equation 5.

$$\epsilon = \frac{l_i - l_0}{l_0} = \frac{\Delta L}{l_0} \quad (5),$$

where l_0 is the original length before any load is applied and Δl is the deformation elongation or change in length at some instant, as referenced to the original length (Ridwan, Prabowo, Muhayat, Putranto, & Sohn, 2020).

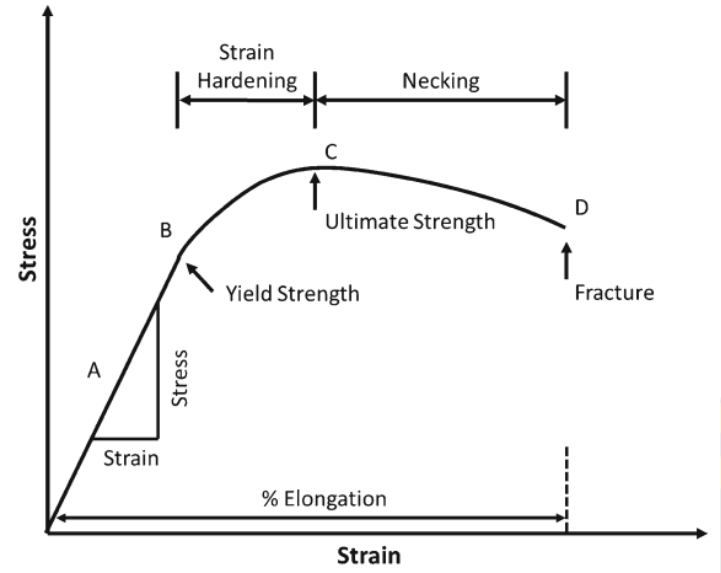

Figure 2-19 A typical stress–strain curve for polymer film undergoing tensile strain testing (Lim & Hoag, 2013).

An idealized stress–strain curve for polymer film tensile testing is shown in Figure 2-19. In this scenario, the strain is applied to the polymer film by moving the grips at a constant rate until fracture of the film occurs. In Figure. 2-19, regions A–B, B–C, and C–D represent the elastic deformation, plastic strain hardening deformation and necking regions, respectively. The points B and D represent the yield point and fracture point (film breaking point), respectively. These regions are well known in the literature and a description can be found in any reference on the strength of materials.

The maximum tensile strength of a film is the maximum stress that a film can withstand being stretched before necking or failing. Plasticizers can increase the free volume between the polymer chains leading to greater chain mobility and film flexibility plasticized polymer would, therefore, be less resilient and would deform at a lower force than without the plasticizer. Hence, lower tensile strength is expected with the addition of plasticizer. Similarly, the elongation is expected to be higher with the addition of plasticizer. The Young's modulus is the slope of the linear section on the stress–strain curve where the film undergoes the elastic deformation, and because there is greater chain mobility with the addition of a plasticizer there is less resistance to deformation hence a lower Yong's modulus is expected (Lim & Hoag, 2013).

2.14.5 Scanning electron microscopy

The scanning electron microscope (SEM) uses a focused beam of high-energy electrons to generate a variety of signals at the surface of solid specimens. The signals that derive from electron-sample interactions reveal information about the sample including external morphology (texture), chemical composition and crystalline structure and orientation of materials making up the sample. In most applications, data are collected over a selected area of the surface of the sample and a 2-dimensional image is generated that displays spatial variations in these properties. Areas ranging from approximately 1 cm to 5 microns in width can be imaged in a scanning mode using conventional SEM techniques (magnification ranging from 20X to approximately 30,000X, spatial resolution of 50 to 100 nm) (Swapp, 2017). The SEM is also capable of performing analyses of selected point locations on the sample; this approach is especially useful in qualitatively or semi-quantitatively determining chemical compositions (using EDS), crystalline structure and crystal orientations (using EBSD). The design and function of the SEM is very similar to the EPMA and considerable overlap in capabilities exists between the two instruments.

As show in Figure 2-20, electrons are produced at the top of the column, accelerated down and passed through a combination of lenses and apertures to produce a focused beam of electrons which hits the surface of the sample. The sample is mounted on a stage in the chamber area and, unless the microscope is designed to operate at low vacuums, both the column and the chamber are evacuated by a combination of pumps. The level of the vacuum will depend on the design of the microscope.

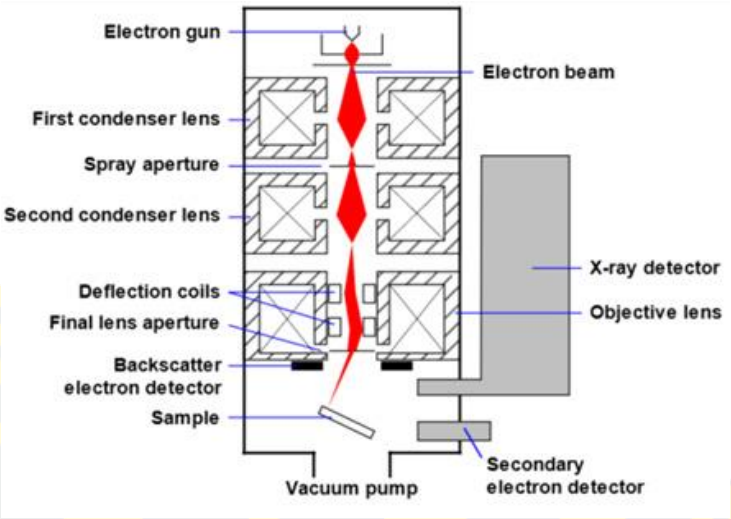

Figure 2-20 Schematic of a scanning electron microscope (Doug, 2022).

The position of the electron beam on the sample is controlled by scan coils situated above the objective lens. These coils allow the beam to be scanned over the surface of the sample. This beam rostering or scanning, as the name of the microscope suggests, enables information about a defined area on the sample to be collected. As a result of the electron-sample interaction, a number of signals are produced. These signals are then detected by appropriate detectors.

2.14.6 Thermal camera

Thermal imaging is the method of detecting long IR range of electromagnetic spectrum which is invisible to the human eye by means of special and sophisticated cameras called as infrared imagers. The long-wave IR falls between 8 µm - 15 µm and provides thermal data or heat map of the captured scene in quantified form representing temperature data of the same. Thermal imaging does not need ambient light to capture thermal image as its working principle is based solely on sensing thermal emissions of the scene to be imaged. The temperature map thus obtained is represented through application of pseudo color palette for visualization purposes which is done by software application in the form of firmware inside the infrared imager or on an application in a computer system. The detector technology, IR Optics used, combined with the software functions are parameters that decide the cost of the thermal imaging system (Figure 2-21) (Shazia Shaikh, 2019).

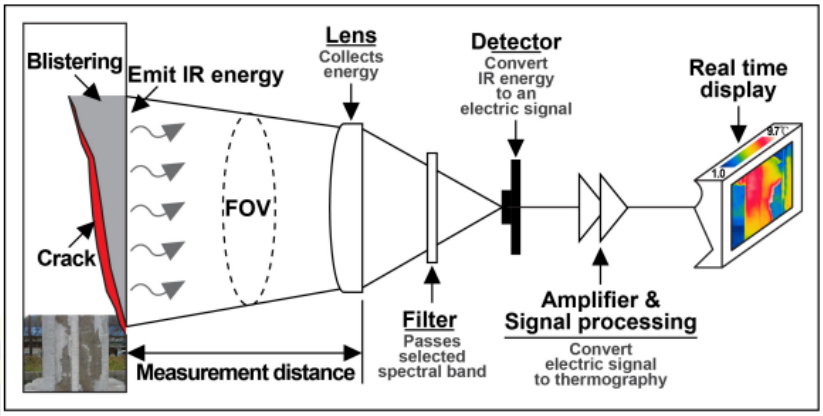

Figure 2-21 Schematic diagram of infrared thermography camera (Young Hoon Jo, 2013).

2.15 Literature reviews

Aouraghe and co-workers (Aouraghe et al., 2021) created an ETA device that can convert electrical energy into mechanical energy when stimulated by electro-heating. This actuator has a two-layer structure (Figure 2-22) consisting of a layer with good electrical conductivity and the other layer with good thermal expansion. Carbon nanotube film (CNTF) is a strong and flexible material was used as a conductive layer. The film with the thickness of ~ 11±1.5 μm was prepared using floating catalyst chemical vapor deposition method (FCCDV). Another layer of the actuator was polydimethylsiloxane (PDMS)with a high coefficient of thermal expansion (9.3×10^{-4} $°C^{-1}$) and low Young's modulus (2.07 MPa). At a low driving voltage of 8 V, CNTF/PDMS composite ETA exhibited abending angle of ~324° and high electro heating performance of 351°C within 12 s. With altering the driving voltages, the actuation movement and the produced heat could be regulated. After 20 cycles, the values were almost the same. The displacement of the system was affected by both the thickness of PDMS and the applied voltage. The soft gripper of the robot, built from CNTF/PDMS composite actuators, could lift and crab an object equal to 1.3 and 5.3 times its weight, respectively.

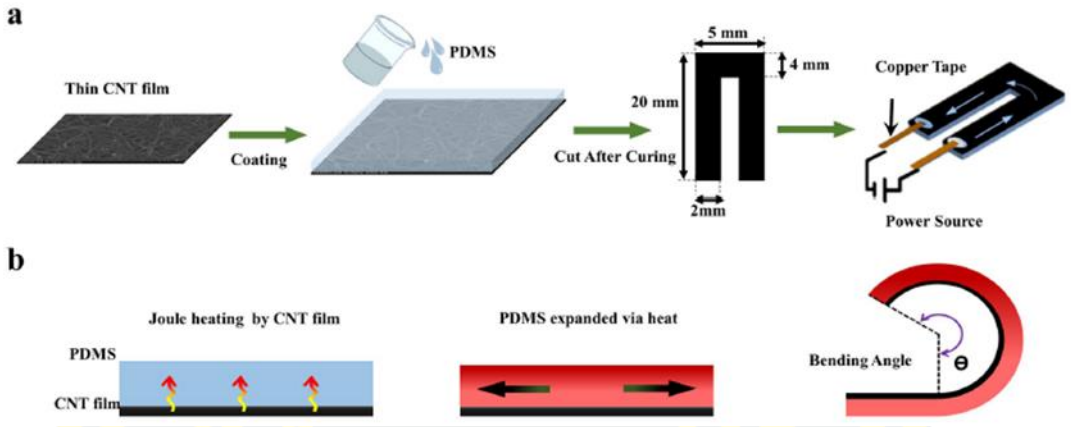

Figure 2-22 Schematic diagram of (a) CNTF/PDMS composite ETA fabrication process and (b) its bending process (Aouraghe et al., 2021).

Shirasu and co-workers (Shirasu et al., 2017) fabricated U-shaped bimorph actuators using the bimorph actuator containing aligned MWCNT/polymer composites and aligned MWCNT-reinforced epoxy composite/aluminum laminates, containing 9, 14, and 27 vol.% MWCNTs. The length and width dimensions of the entire sample were 20 ×5 mm^2. An ultrathin gold coating (50 nm thick) was sputtered onto the surface of the composite layer of the U-shaped samples to decrease the contact resistance between the composite layer and the copper electrodes and to uniform heat distribution in the composite layer during electrical heating. The edge of the sample was masked during deposition by a polyimide tape to prevent electrical shorting between the ultrathin gold layer and the aluminum layer (Figure 2-23). With altering the driving voltages, the actuation movement was being heated and shrinks along its length. The bending displacement and force output of the bimorph actuators with a free length of 16 mm reached 7.6–10.0 mm and 0.8–7.8 mN under a DC voltage of 5.2–6.0 V. In order to control the bending displacement and force output of the bimorph actuator, it was effective to design the Young's modulus and CTE of the composite layer by controlling the MWCNT volume fraction and the dimensional parameters.

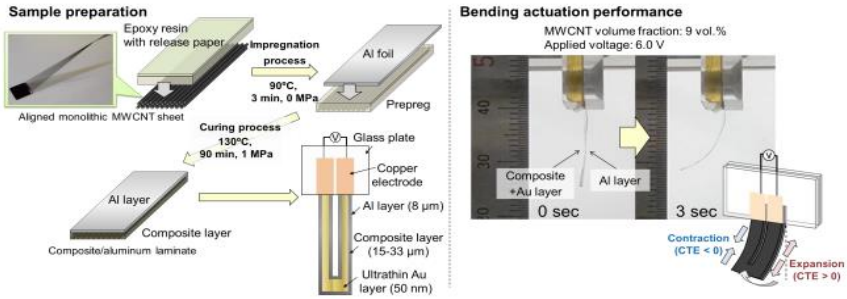

Figure 2-23 Electrothermal bimorph actuators comprising an aligned MWCNT/epoxy composite and aluminum foil were fabricated (Shirasu et al., 2017).

Yao and co-workers (Yao, Cui, Cui, & Zhu, 2017) prepared highly conductive and flexible AgNW/PDMS actuators. Low-voltage and extremely flexible electrothermal bimorph actuators were fabricated in a simple, efficient and scalable process. The bimorph actuators were made of flexible silver nanowire (AgNW) based heaters, which exhibited a fast heating rate of 18 ºC/s and stable heating performance under large bending. AgNW/PDMS actuators can achieve a very large bending angle of 720º or curvature of 2.6 cm^{-1} and can generate high temperature of ~160 °C in 30 s with maximum heating rate of 18 °C s^{-1} under a low driven voltage of 0.2 V sq^{-1} (4.5 V). Actuator structures with large curvature can be achieved by designing the actuator into different configurations (Figure 2-24). The potential applications of used soft actuator in soft robotics were demonstrated as self walkers and soft grippers.

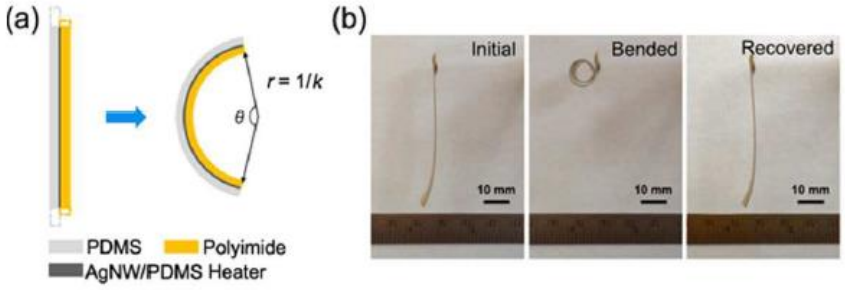

Figure 2-24 Bending performance of the PI/AgNW/PDMS bimorph actuator. (a) Schematic of the electrothermal bimorph actuation mechanism. (b) The initial state, the bent state with maximum curvature and the recovered state of the U-shaped actuator (Yao et al., 2017).

Amjadi and co-workers (Amjadi & Sitti, 2018) fabricated multiresponsive actuators, composed of normal copy paper and polypropylene (PP) film. Coppy paper gave its high coefficient of hygroscopic expansion (CHE) approxirately ≈ 0.1 C^{-1} and plus a low coefficient of thermal expansion of 10 ppm K^{-1}, and PP film showed its high CTE of about 137.5 ppm K^{-1} and negligible CHE. When 30 V was applied to an actuator, the conductive film immediately responded to mechanical actuation. Bilayer actuators operated based on the large hygroscopic shrinkage of paper and simultaneously major thermal expansion of the PP film upon increasing their temperature (Figure 2-25). High-performance self-sensing actuators can not only sense the self-actuation sate but also recognize the touch of soft and hard objects. Moreover, multiresponsive actuators can track their dynamic motion upon external stimuli like light irradiation.

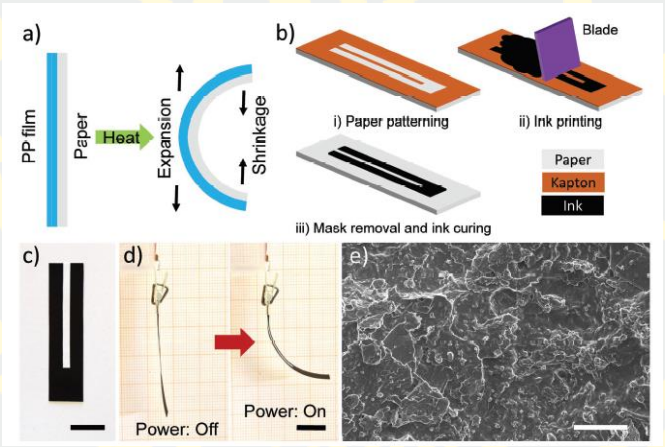

Figure 2-25 a) Schematic cross-section of bilayer actuators made of paper and PP film. b) Fabrication processes of the electro resistive heater/sensory circuit on paper. c) Photograph of a U-shaped conductive film patterned on paper. d) Bending deformation of an actuator upon application of 30 V. e) SEM image on the surface of the hybrid film coated on the paper substrate (Amjadi & Sitti, 2018).

As shown in Figure 2-26, Wang and co-workers (Z.-H. Wang et al., 2018) prepared low-voltage, large-strain flexible electrothermal actuators (ETAs) from laser reduced graphene oxide (LRGO)/Ag particle/PI. LRGO/Ag particle ETAs under a driving voltage of 28 V, the actuator obtained a bending angle of 192º within 6 s.

Besides, the bending deformation could be precisely controlled by the driving voltage ranging from 10º to 192º. The electrothermal performance of the devices maximum heating rate reaches 30 $^{o}Cs^{-1}$ while the maximum operating temperature is about 80 ºC. Because of the significant thermal expansion difference between LRGO and PI, the actuator achieves a large-strain deformation at a relatively low temperature.

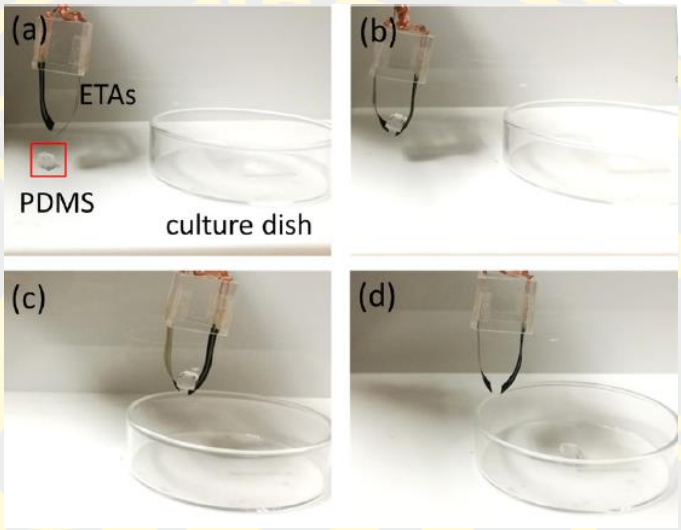

Figure 2-26 Application of the LRGO/Ag ETAs as a soft gripper. Consecutively captured images of grabbing a PDMS block: (a) approaching, (b) grasping, (c) lifting and moving, and (d) releasing (Z.-H. Wang et al., 2018).

Chen and co-workers (M. Chen et al., 2017) fabricated a moisture-responsive soft actuator with a CNT/poly(vinyl alcohol) (PVA) bilayer structure. The PBONF-reinforced CNT/PVA bilayer actuators can unsymmetrically adsorb and desorb water, resulting in a reversible deformation (Figure 2-27). The actuators show a pronounced increase of conductivity due to the deformation induced by the moisture change, which allows the integration of a moisture-sensitive actuator and a humidity sensor.

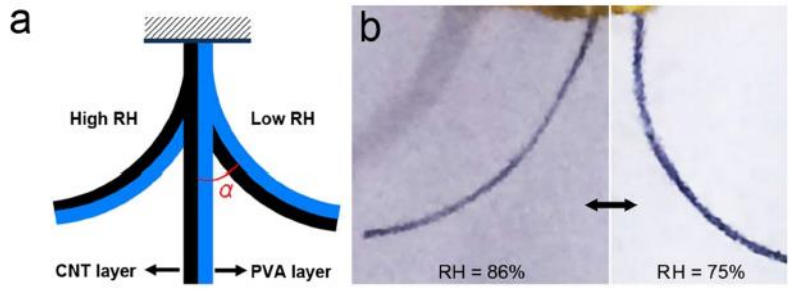

Figure 2-27 PBONF-reinforced CNT/PVA bilayer actuators. (a) Scheme indicating the definition of the bending angle α. (b) Photographs of the PBONF-reinforced CNT/PVA bilayer actuator at RH = 75% and RH = 86% (M. Chen et al., 2017).

Miura and co-workers (Miura et al., 2020) fabricated a ferroelectric polymer-based printed soft sensor to sense and measure the dynamic shear forces generated during a slippage event. Soft sensor was fabricated on a poly(ethylene naphthalate) (PEN) film substrate and affixed to a glass carrier. Several passivation layers consisting of PEN, polyimide (PI) and polyvinyl chloride (PVC) were placed onto the device. This ferroelectric-based sensor demonstrated good ferroelectric characteristics, providing ferroelectricity of 8.2 $\mu C \cdot cm^{-2}$ after annealing at 140 °C. This study experimentally demonstrated the effectiveness of the proposed printable high-sensitivity tactile sensor, which could serve as part of a wearable robotic e-skin. The sensor could facilitate the production of a system to detect and prevent the slippage of objects from robotic grippers.

Dai and co-workers (Dai et al., 2009) fabricated a new ionic polymer–metal composites (IPMC) membranes based on a polymer blend consisting of PVA and poly(2-acrylamido-2-methyl-1-propanesulfonic acid) (PAMPS). PVA, a polyhydroxy polymer, is used commonly in medical applications because of its biocompatibility. PAMPS is a better ionic conductor which is partially hydrated due to its inherent sulfonic acid groups in the structure. The properties of the blend membranes were characterized by measuring their water uptake (WU), ion exchange capacity (IEC) and ionic conductivity (σ) which were inherently controlled by the amount of PAMPS added. Membrane showed the bending of >100° and maintained bending under constant pressure. The thickness of PVA/PAMPS (1/1) membranes increases, the tip force increases accordingly. In addition, the generative tip force driven with different

applied voltage was also measured. It was found that the tip force was proportional to the applied voltage for PVA/PAMPS (1/1) membranes. The actuation of all IPMC strip followed the frequency of the input potential. The phase angle of the tip displacement with respect to operating voltage for actuators based Nafion and PVA/PAMPS membrane was quite similar.

Salavagione and co-workers (Horacio J. Salavagione, Gómez, & Martínez, 2009) prepared poly(vinylalcohol)/reduced graphite oxide (PVA/RGO) nanocomposites by reducing graphite oxide in the presence of the polymer matrix and coagulating the system with 2-propanol. Graphite oxide (GO) was obtained using Hummer's method. The conductivity of the PVA/RGO nanocomposites as a function of the filler loading has been measured by the four-probe method. The FTIR spectra this is a strong band centered at 1628 cm^{-1} in the spectrum of the GO and although may also be due to adsorbed water, it contains a significant contribution from the skeletal vibration of non-oxidized graphitic domains. In addition, some interesting changes in the relative intensities of the characteristics bands of PVA in the 1200-1000 cm^{-1} region can be observed. These bands are attributed to the C-O of doubly H-bonded OH in crystalline regions (1144 cm^{-1}) and C-O unbonded in amorphous zones (1096 cm^{-1}). The changes in crystallinity suggested by FTIR results, some changes it the crystallization and crystalline parameters of the esterified products can be expected. Indeed, significant changes in the crystalline parameters have been observed in reduced GO/PVA (RGO-PVA) nanocomposites, where an almost amorphous material was obtained for 10 wt % of filler.

Du and co-workers (F.-P. Du, Tang, C.-Y., Xie, X.-L., Zhou, X.-P., & Tan, L., 2009) proposed ionic polymer membrane cast from the mixture of poly(sodium 4-styrenesulfonate-co-acrylic acid) (PSA) and polyvinyl alcohol (PVA) was used as an electromechanical actuator. Particular, a thin layer of PSA with a thickness of 12 nm is uniformly grafted on the surfaces of MWNTs. PSAg-MWNTs with different weight fractions (0, 5, 10, and 20 wt%) was dispersed in an aqueous mixture of 10 wt % PSA and 20 wt % PVA. The water-soluble PSA-g-MWNTs can be homogeneously dispersed in the PSA/PVA membrane with a loading ratio of up to 20 wt %. An external bias of (1.5 V is applied upon a repeated square wave (frequency of 0.25 Hz). The maximum displacement of the PSA/PVA membrane is 20 mm, and various

loadings of PSA-g-MWNTs leads to a slight but noticeable decrease in the displacement, where they are 18, 16, and 14 mm for PSA-g-MWNTs loading of 5, 10, and 20 wt%. The conductivity of PSA-g-MWNTs-loading (wt%) 0, 5, 10, and 20 equaled 7.53×10^{-13} 4.91×10^{-9} 5.09×10^{-8}, and 1.44×10^{-4} S cm^{-1}, respectively.

Fan and co-workers (Fan et al., 2020) proposed three kinds of flexible double layer electrothermal actuators (ETAs) made of "U"-shaped graphite paper and polyimide (PI) film. The bending angle of the actuator can reach 248.6º and the bending curvature can reach 1.23 cm^{-1} at 6 V in ten seconds (Figure 2-28). Furthermore, they exhibited excellent driving performance and high durability. Two ETAs were assembled into a flexible smart gripper and the gripper can achieve the desired driving performance while applying a low voltage.

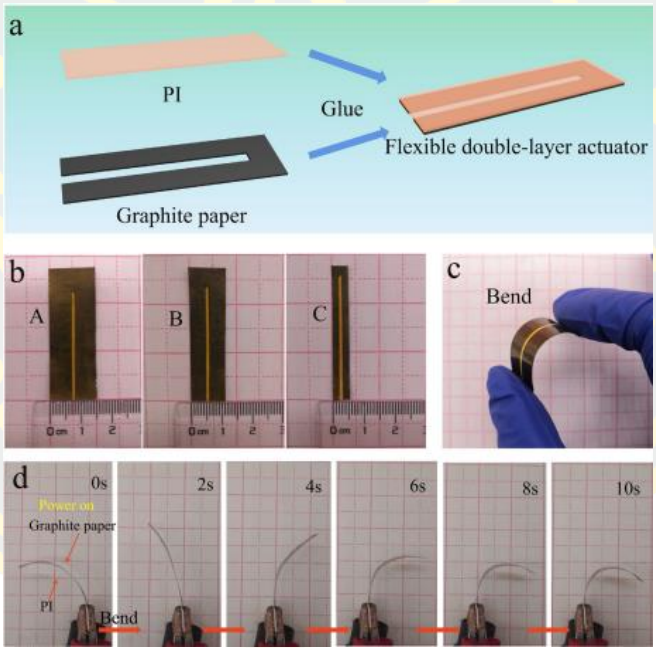

Figure 2-28 Diagram of the double-layer ETA. (a) Compose graphite paper and PI to fabricate flexible double-layer ETA. (b) Three specifications of graphite paper of sample A, B, C. (c) Bending the flexible actuator by hand. (d) The bend process of actuator of sample C when power on at 6 V (Fan et al., 2020).

Henga and co-workers (Kim-Rui Henga, 2017). developed a new design of DEA unimorph consists of a flexible frame holding at a DEA on the discrete support by a stiffer spine-like flexure of 380μm thick PVC sheet (Figure 2-29). This dielectric

elastomer unimorph of 3 grams produced a maximum voltage induced bending of close to 90° and a maximum voltage-induced blocked force of up to 168 mN. Given their higher stiffness and large actuation, these 3-D shaped and strengthened DEA unimorphs made stronger grippers for passive grasping and active pinching. Such dielectric elastomeric unimorphs made normally close grippers capable of grasping a payload 5-6 times the gripper weight.

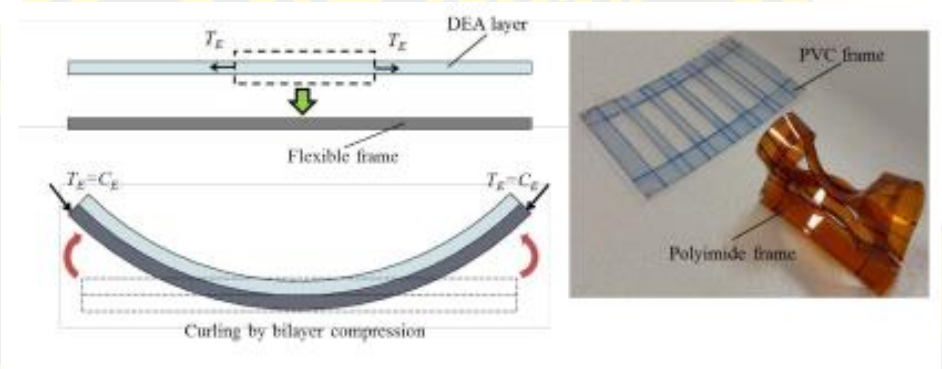

Figure 2-29 Bending principle of existing DEMES gripper using a bilayer unimorph consisting of a pre-stretched DEA on a passive structural layer (Kim-Rui Henga, 2017).

Yuan and co-workers (Yuan, Ma, Fan, Liu, & Ding, 2012) investigated the fabrication and electrical properties of a composite with a host polymer of ethylene vinyl acetate (EVA) and fillers of reduced graphene oxide (RGO) and polyaniline (PANI) (donated as RGO/PANI/EVA composite). During mixing of RGO in EVA, poor dispersion and localization of RGO in the polymer matrix lead to the non-linear relation between the conductivity and the RGO concentration. The conductivity of the composite with the RGO concentration of 1.0, 2.0, 4.0, and 6.0 wt%, were 1.1×10^{-9}, 6.2×10^{-7}, 5.1×10^{-4}, and 2.7×10^{-3} S cm^{-1}, respectively. In order to improve the dispersion of RGO in the EVA matrix, in situ polymerization of aniline monomer in the presence of RGO was adopted, due to the functional groups can favor the chemical grafting of PANI polymers to the RGO surface in the in situ polymerization, which may assist in the preparation of well-dispersed graphene-based polymer composites. The conductivity of the polymer matrix (5%PANI/94%EVA and 5%PANI/93%EVA and) were 3.1×10^{-7} and 5.6×10^{-5} S cm^{-1}, corresponding to the

RGO concentration of 1.0 and 2.0wt%, respectively. Therefore, the PANI chains may link the individual RGO sheets and result in a high-conductivity network.

Yin and co-workers (Yin et al., 2020) developed a soft fabric-based bimorph actuator by laminating a biaxially oriented polypropylene (BOPP) film and a conductive fabric at room temperature (Figure 2-30). The speedy and cost-effective production method facilitated mass production of the actuating fabrics of very large size. The fabric-based actuator can be controlled wirelessly, possessing an extremely fast response (0.27 s) with a large bending deformation (angle of 100°), more than twice faster than previously reported bimorph actuators. On the other hand, a large arc bending with a curvature of 0.75 cm^{-1} in 1.6 s and 0.55 cm^{-1} in 3 s, was achieved by light radiation and magnetic stimulus, respectively. Various wireless controlled prototypes are demonstrated, including a soft gripper, soft kickers and artificial blooming flowers, illustrating a new way to mass produce cost-effective bimorph actuators via a simple, green and fast approach for applications in robots, wearable, and functional textiles.

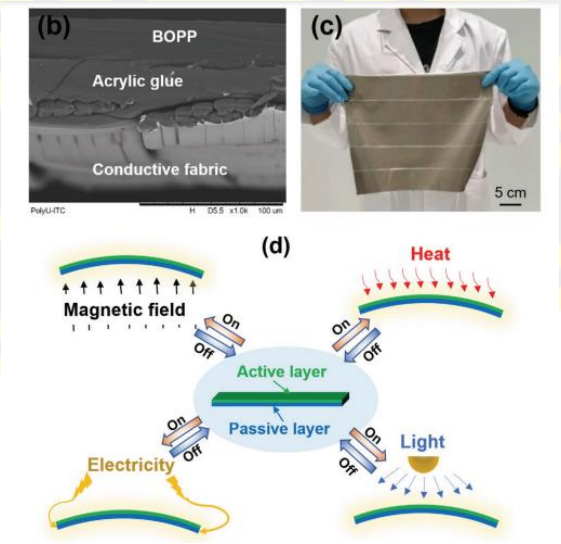

Figure 2-30 A soft fabric-based bimorph actuator (Yin et al., 2020).

CHAPTER 3
RESEARCH METHODOLOGY

In this study, double-layer ETA model systems consisting of a conductive layer and a polymer layer were prepared from various polymer composites, e.g., PVA/graphite, PVA/GO, PVA/rGO, and PDMS/graphite and various polymer layers selected from PI, PVC, or PP. The thickness, morphology, chemical and physical properties, conductivity and bending curvature of the proposed model systems were characterized Figure 3-1.

3.1 Chemical and Material

3.1.1 Chemicals

1. Graphite powder, Mw 12.01 g/mol, particle size < 50 µm.

2. Polyvinyl alcohol (PVA), Mw 89,000-98,000 g/mol, 99+% hydrolyzed, aldrich.

3. Glycerol ($C_3H_8O_3$), 92.09%, Density 1.2570 g/mL, AR grade, Ajax Finechem.

4. Methanol (CH_3OH), Mw 32.04 g/mol, HPLC grade, Fisher Chemical.

5. Acetic acid (CH_3COOH), Mw 60.05 g/mol, density 1.05 g/cm^3, AR grade, ACS, Ph Eur USP, Scharlau.

6. Glutaraldehyde ($C_5H_8O_2$) 25%, aqueous solution, Mw. 100.12 g/mol, density (d. 20º/4 ºC) 1.055 – 1.065, Lobacheime.

7. Sulfuric acid (H_2SO_4) 95-97%, Mw 98.08 g/mol, AR grade, QRec.

8. Sodium nitrate ($NaNO_3$) 99%, Mw 84.99 g/mol, AR grade, QRec.

9. Potassium permanganate ($KMnO_4$), Mw 158.034 g/mol, AR grade, QRec.

10. Hydrogen peroxide (H_2O_2) 35%, Mw 34.01 g/mol, extra pure, QRec.

3.1.2 Equipment

1. Dropper.
2. Analytical balance, Satrorius, BSA224S.
3. Micropipette 100-1,000 µL ONiLAB.
4. Micrometer, Macoh, 0-25 mm, 0.01 mm.
5. Petri dish (size 90mm x 15mm).
6. Forceps.
7. Alligator clips red and black.
8. Battery box.
9. Battery.
10. Switch “B” single pole 6A 250V chang CH501.
11. Wire (red-black).
12. PVC Plastic electrical insulation tape, black, Yazaki.
13. Protractor No.990 INCA.
14. Polyimide or Kapton tape, 3M.
15. Polyimide tape, 75 micron, Bushi tape.
16. Vinyl electrical tape, super 33+, 3M.
17. PVC plastic electrical insulation tape, red, Yazaki.
18. Silicone rubber (PDMS) provided by Rung Art Co., Ltd., Thailand, formula RA-320

3.1.3 Instrument

1. Attenuated total reflectance Fourier transform infrared spectroscopy (ATR-FTIR).
2. Spin coater, Ossila UK.
3. Spectrophotometer, Perkin Elmer model system 2000.
4. K-Hand coater, Short K-bar no.200, RK print coat instruments model 30-15.
5. Micropipette 100-1000 µL, Onilab.
6. Micrometer, macoh outside micrometer 0-25 mm resolution 0.01 mm.
7. Analytical balance, Satrorius, BSA224S.

8. Oven, binder model FED 240.

9. Hotplate stirrer, C-MAC HS7, IKA, Germany.

10. Digital multimeter, Agilent 34410A, Agilent Technologies (Thailand) Ltd.

11. DC power supply DRP-303D, Digital.

12. Analog multimeter, SUNWA YX-360TR E-B.

13. Scanning electron microscope (SEM), LEO, LEO1450VP.

14. Tensile tester, Testometric (Micro 350), Testometric Co., Ltd.

15. Digital camera.

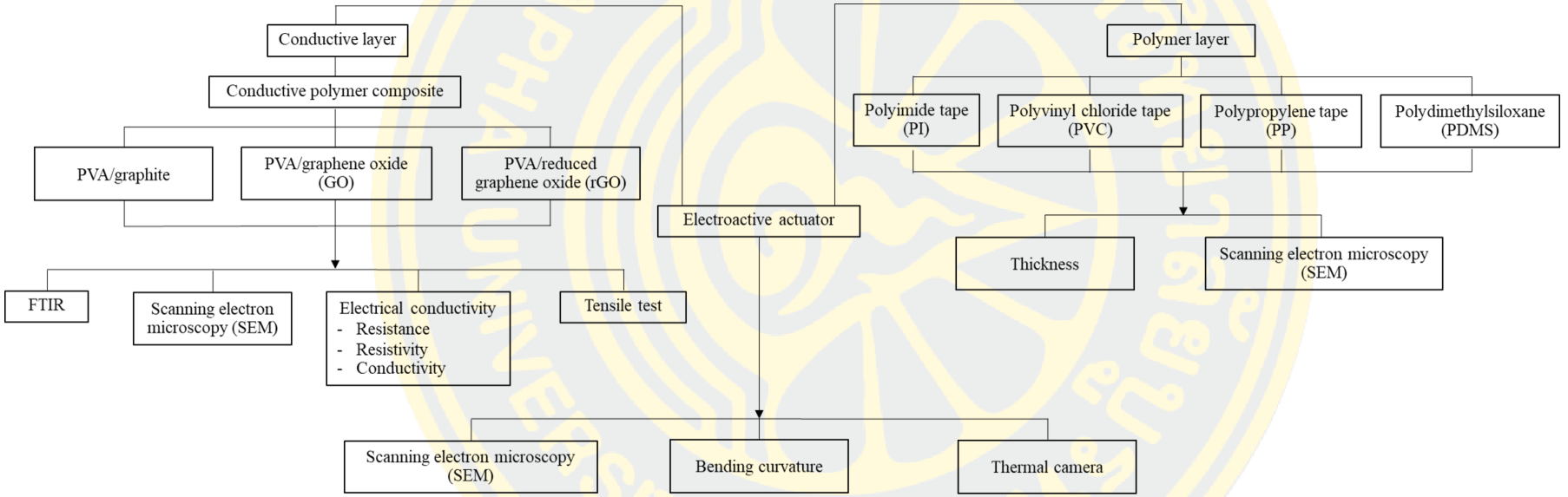

Figure 3-1 The study flow chart.

3.2 Experimental

3.2.1 Preparation of conductive layer

The process of preparing composite film, using polyvinyl alcohol as a matrix, was studied by varying the concentrations of glycerol solutions, graphite content, composite solution mixing time and solution casting volume.

3.2.1.1 Preparation of graphite composite films by K-hand coating

A 10%w/v polyvinyl alcohol solution was prepared by dissolution PVA in distilled water. The solution was stirred at 90 ºC with continuous stirring for 2 h. After allowed to cool to room temperature, glycerol (Gly), 30%w/v with respect to PVA weight, was added into a 10 mL of the prepared polymer solution and the solution was stirred for another 2 min. Graphite (GH) was then added into the solution at the various concentrations of 60, 70, and 80%w/w. After thoroughly mixing, the crosslinking solution was added, as shown in Table 3.1, and the mixture, was stirred for 15 min. The formulation of crosslink solution is shown in the Table 3.2. The mixture was coated onto an aluminum foil (2×2 cm^2) using K-hand coater with a short K-bar No.200, and baked in a hot air oven at 70 ºC for 1 hour. After drying, the film was removed from the aluminum foil.

Table 3-1 Weight and volume ratio of each polymer composite film formulation**.**

Sample	Graphite (g)	Glycerol (mL)
PVA/60GH	0.6	-
PVA/70GH	0.7	-
PVA/80GH	0.8	-
PVA/60GH/Gly	0.6	0.3
PVA/70GH/Gly	0.7	0.3
PVA/80GH/Gly	0.8	0.3

Table 3-2 Crosslink solution formulation.

Solution	Volume (mL)
50%w/v Methanol	1.2
10%w/v Acetic acid	0.8
1.2%w/v Glutaraldehyde	0.4
10%w/v Sulfuric acid	0.4

3.2.1.2 Preparation of graphite composite films by solution casting

A 10% w/v PVA solution was prepared, and glycerol was added to it, followed by stirring for 2 minutes. Graphite was then added with continuous stirring for 10 minutes until the mixture became homogeneous. The crosslinking solution was subsequently added, and the mixture was stirred for an additional 15 minutes. Sample names and formulations are shown in Table 3.3. The mixture was poured into a Petri dish and left at room temperature for 5 minutes to reduce air bubbles before being baked in a hot air oven at 70 ºC for 4 hours. Afterward, the PVA/graphite composite film was removed. The film thickness and electrical conductivity were measured.

Table 3-3 Sample name and formulations.

Sample	PVA (g)	Glycerol (mL)	Graphite (g)
PVA/10GH/22Gly	1.5	0.33	0.10
PVA/10GH/24Gly	1.5	0.36	0.10
PVA/10GH/26Gly	1.5	0.39	0.10
PVA/10GH/28Gly	1.5	0.42	0.10
PVA/10GH/30Gly	1.5	0.45	0.10
PVA/50GH/40Gly	1.5	0.45	0.45
PVA/50GH/50Gly	1.5	0.60	0.75
PVA/50GH/60Gly	1.5	0.75	0.75
PVA/50GH/70Gly	1.5	0.90	0.75
PVA/60GH/30Gly	1.5	1.05	0.75
PVA/60GH/40Gly	1.5	0.45	0.90
PVA/60GH/50Gly	1.5	0.60	0.90
PVA/60GH/60Gly	1.5	0.75	0.90
PVA/60GH/70Gly	1.5	0.90	0.90
PVA/70GH/30Gly	1.5	1.05	0.90
PVA/70GH/40Gly	1.5	0.45	1.05
PVA/70GH/50Gly	1.5	0.60	1.05
PVA/70GH/60Gly	1.5	0.75	1.05
PVA/70GH/70Gly	1.5	0.90	1.05
PVA/80GH/30Gly	1.5	1.05	1.05
PVA/80GH/40Gly	1.5	0.45	1.20
PVA/80GH/50Gly	1.5	0.60	1.20
PVA/80GH/60Gly	1.5	0.75	1.20
PVA/80GH/70Gly	1.5	0.90	1.20
PVA/80GH/80Gly	1.5	1.05	1.20

3.2.2 Preparation of double-layer ETA

3.2.2.1 In-situ process

PVA/GH/Gly

Kapton tape with the size of 0.5×5.0 cm^2 was attached to the of 5.8×5.8 cm^2 mold with double side adhesive tape (Figure 2-32). The double sided adhesive tape with the dimension of was 0.1×4.0 cm^2 was attached on top of the Kapton tape. The prepared polymer composite solutions, (with the volume of 3 and 4 mL) namely, PVA/50-80GH/60Gly, as show in Table 3.3, was poured into the plastic mold, covering the tape surface. Air bubbles was reduced by leauiny the solution at room temperature for 5 min and the system was baked in a hot air oven at 60 ºC for 2 h. Later, the middle with double sided adhesive tape was removed from the Kapton tape.

PVA/GO/Gly and PVA/rGO/Gly

Composite solutions of PVA/GO/Gly and PVA/rGO/Gly at concentrations of 8%, 10%, 15%, and 20% wt were prepared. A 10% wt PVA solution was first prepared by adding 4 mL of deionized (DI) water and stirring the mixture with a magnetic stirrer at 60°C for 2 hours. Then, 60% wt glycerol was added, and the mixture was mixed for 2 minutes. The mixture was allowed to cool to room temperature, then the crosslinking agent was added and stirred for 12 minutes. The mixture was poured into pre-prepared molds (with a groove size of 0.5 × 5 cm^2, polymer tape of 0.5 × 4 cm^2, and a red PVC tape of 0.1 × 5 cm^2 in the center to form a U-shape) and excess solution was removed. The sample was dried in a hot air oven at 60°C for 2 hours. The central tape was removed, and the Electroactive Actuator (ETA) was extracted from the mold.

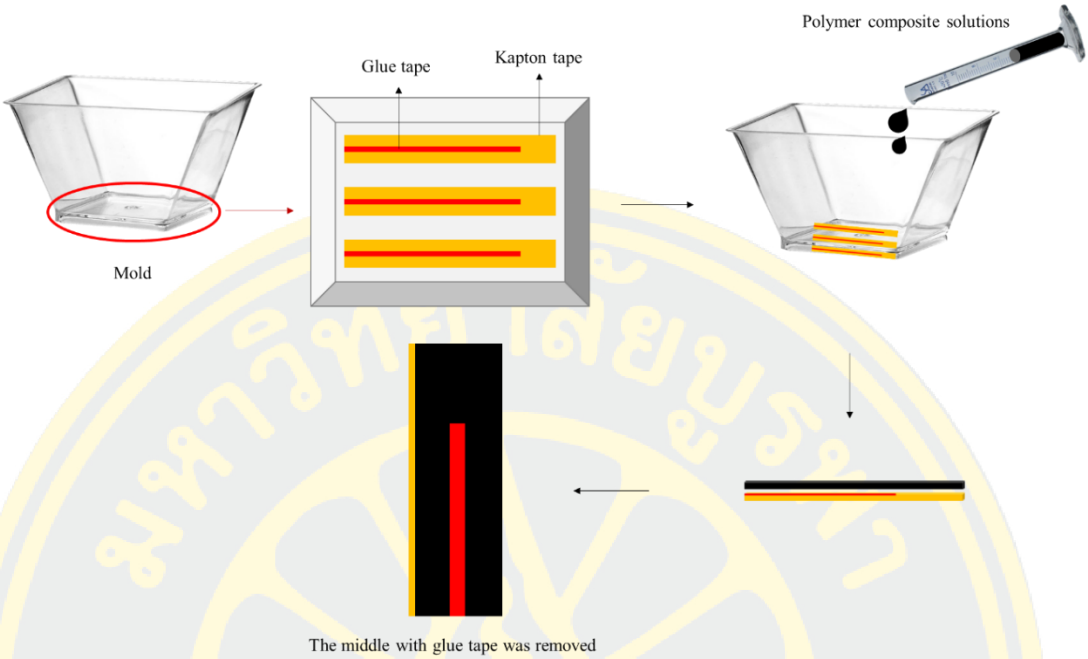

Figure 3-2 A U-shape ETA prepared from In-situ process.

3.2.2.2 Two-step process

A graphite composite film (obtained from 3.2.2) was cut into 0.5×5.0 cm^2 rectangular sheet. The area of 0.1×4.0 cm^2 at the middle of the composite film was then chopped off and the film became U-shape (Figure 2-33). The U-shaped composite film was then, attached on the top of the polymer tape with size of 0.5×4.0 cm^2, and then the U-shaped ETA was obtained.

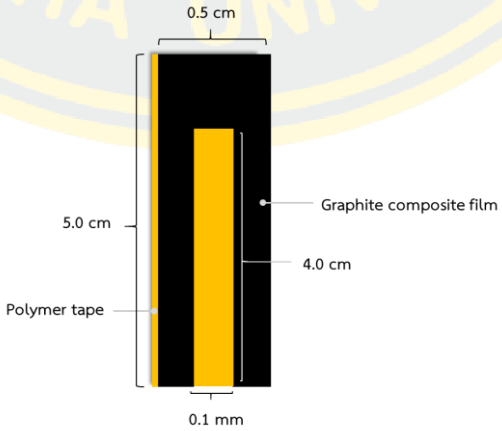

Figure 3-3 A U-shape ETA prepared from a conductive polymer composite and a polymer tape.

3.2.3 Synthesis of graphite oxide

Graphite oxide (GO) had been synthesized using Hummer's method (Salavagione et al., 2009). 2 g of graphite was mixed with 1 g of $NaNO_3$ and 50 mL of conc. H_2SO_4, and the mixture was cooled down to 0 ºC. Then, 6 g of $KMnO_4$ was slowly added while maintaining the temperature below 5 ºC. The cooling bath was removed, and the suspension was maintained for 0.5 h. After that, 100 mL of water was added, and the temperature increased to 90 ºC. The mixture was further diluted with 300 mL of water, treated with 50 mL of 5% H_2O_2, filtered, and washed with hot water until neutral. The dark brown GO powder was dried in a vacuum oven at 60 ºC for 4 h (Figures 2-34).

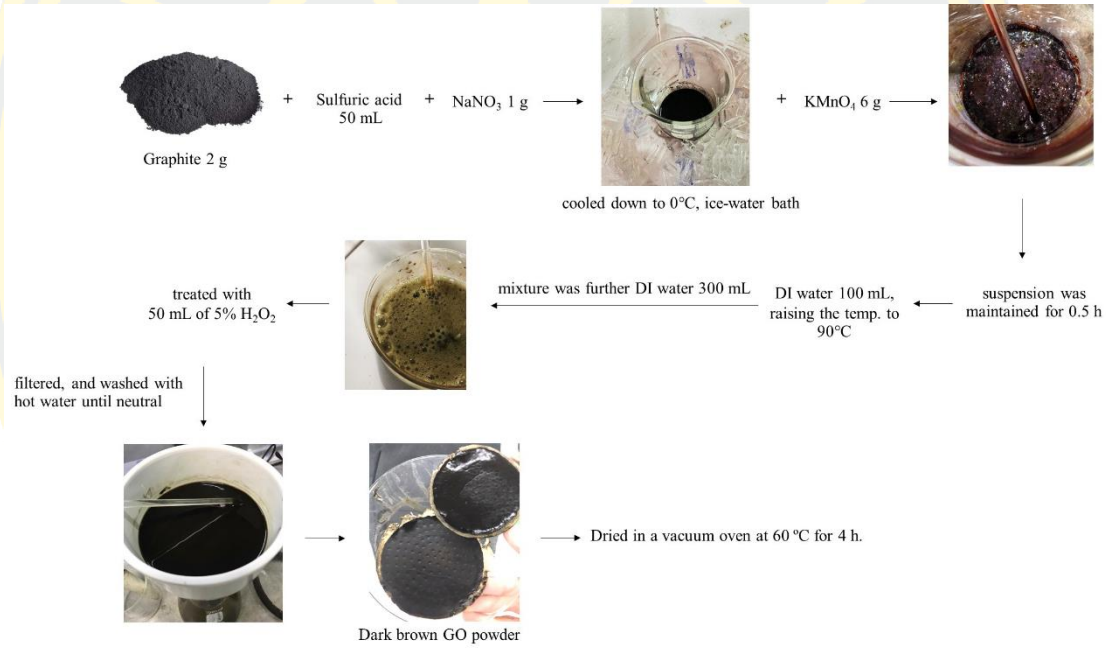

Figure 3-4 Synthesis process for graphite oxide.

3.2.4 Synthesis of reduced graphite oxide

Reduced graphite oxide was synthesized by first taking 400 mg of the GO powder prepared in section 3.2.4 and combining it with 400 mL of distilled water and 4 g of ascorbic acid (AA). The mixture was stirred using a magnetic stirrer for 30 minutes at 60°C. It was subsequently centrifuged at 4000 rpm for 40 minutes to remove any excess materials. Following this, 30% hydrogen peroxide was introduced, and the mixture was stirred again with a magnetic stirrer for 30 minutes at 60°C, resulting in the formation of a black product. The product was then subjected to

washing with ethanol and deionized water three times each and was finally dried in a hot air oven at 120°C for 24 hours (Habte, A. T., & Ayele, D. W. et al., 2019) (Figures 2-35).

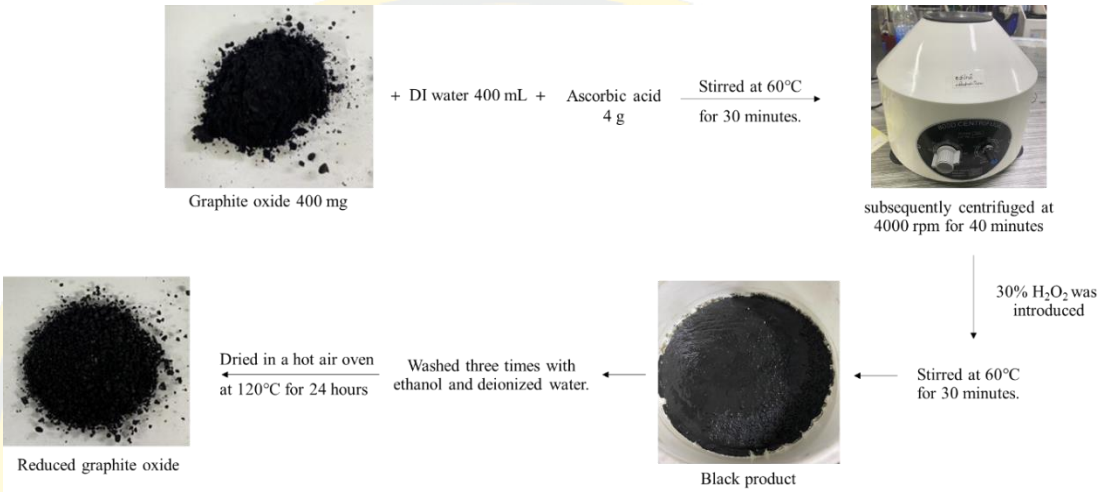

Figure 3-5 Synthesis process for reduced graphite oxide.

3.3 Characterization

3.3.1 Chemical structure analysis

The functional groups in the graphite, GO, RGO and conductive composite films were analyzed using of attenuated total reflection - Fourier transform infrared (ATR-FTIR) technique. The number of scans was 12 and the maximum resolution to collect data was 4 cm^{-1} at the wavenumber ranged from 400 to 4,000 cm^{-1}.

Figure 3-6 FTIR instrument.

3.3.2 Tensile measurement

Tensile test was carried out using Testometric micro 350, as showed in Figure 2-35. A polymer composite film was in rectangular shape with a dimension of 0.5 × 5.0 cm^2. The gauge length, the pulling speed and the load cell were 30 mm, 10 mm/min and 500 N, respectively. The sample is stretched at a constant speed until failure. The averaged values and standard deviations of the elongation at break, Young's modulus and tensile strength were reported.

Figure 3-7 Testometric micro 350.

3.3.3 Morphological study of composite films

The surface morphology of the graphite composites as well as the ETA actuators was examined using scanning electron microscopy (SEM). The samples were coated with gold under a vacuum. The examination used an accelerating voltage of 10 kV with the magnification of 100x, 250x, and 2000x.

3.3.4 Electrical conductivity

Electrical conductivity measurement of the PVA/graphite composite films was performed with a digital multimeter (Agilent 34410) (Figure 2-36) at room temperature, using two copper electrode pads. Two 1.0×2.2 cm^2 copper sheets were placed on a 3.5×5.0 cm^2 PVA/graphite composite film, allowing a 1.5 cm space between the two pads (Figure 2-37). The red-black probe was pressed between the copper electrodes at a distance of 1.3 cm. Each measurement was performed for 50 s

before the resistance was read. The corresponding volume resistivity (ρ_v) and volume conductivity (σ_v) was calculated using equation 3.1 and 3.2, respectively, according to ASTM D257-90 (Skov, 2016).

$$\rho_v = \frac{A}{T} \times R_v \quad (3.1)$$

When $A = (a + g)(b + g)$

R_v is the electrical resistivity (Ω),
A is the electrode surface area (cm^2),
T is the average thickness (cm),
g is the dimension of the digital multimeter probe (cm),
a, b is the length of the rectangular electrode (cm).

$$\sigma = \frac{1}{\rho} \quad (3.2),$$

When ρ and σ are the resistivity (Ω·m) and the electrical conductivity (S/m), respectively (Zainab, 2007).

Figure 3-8 Digital multimeter (Agilent 34410).

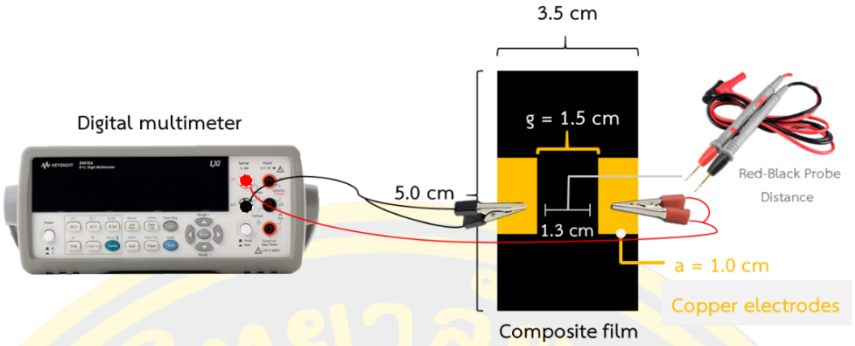

Figure 3-9 Diagram of the electrical conductivity test.

3.3.5 Bending curvature

The experiment was carried out to measure the bending angle of the actuator model systems. The electric potential of 6, 21, and 30 V was given to the samples by DC power supply DRP303D. The video was taken for 4 minutes, while the DC voltage was applied at the first 2 minutes and the DC voltage was taken off in the last 2 minutes. Then the curvature was measured with a circle protractor No.990 INCA to obtain the degree of bending of the actuator. In Figure 2-38, the bending curvature of the actuator was measured after the electric potential was applied and the picture of the bending actuator was taken. In the picture, tangent lines to the curve at the reference points L1 and L2 were drawn. The angle at the intersection between the two tangent lines was measured using a protractor No.990 INCA. According to Aouraghe and co-workers (Aouraghe et al., 2021), under driving DC voltage, curvature followed the plane of the intersecting line is deflected and changes in bending angle can be measured.

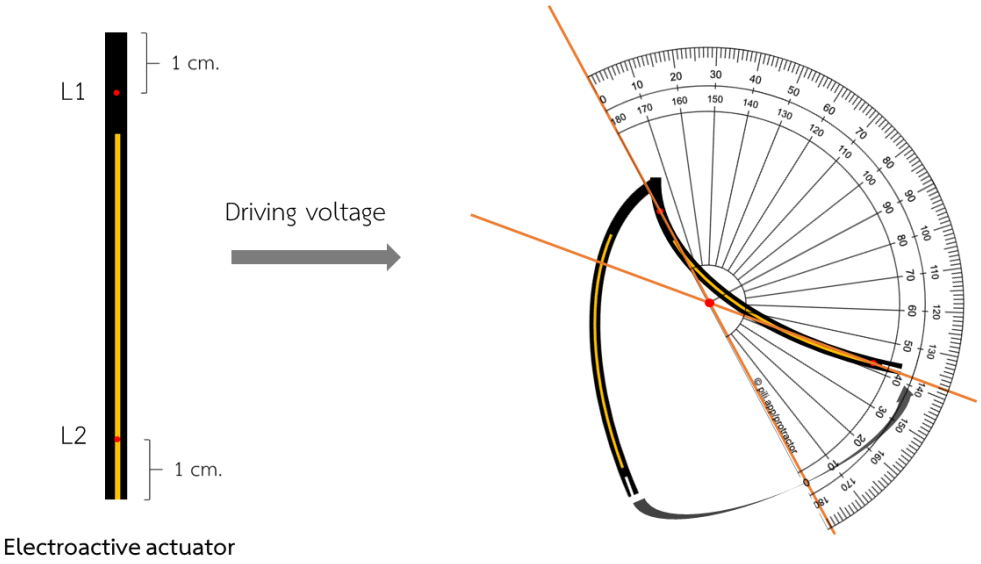

Figure 3-10 Bending curvature measurement for electroactive actuator under applied DC voltage.

3.3.6 Thickness

The thickness of the graphite composite film, polymer tape and the ETA model system was measured by a micrometer (0-25 × 0.01 mm) and SEM images of cross sectional area of the actuator.

3.3.7 Thermal images of ETA

Thermal camera was utilized to measure the temperature generated from then ETA under different voltages. On a colour thermographic display, warmer components or regions will show up as reds, oranges and yellows, while cooler parts will typically be shown as purples and blues (green usually indicates areas that are roughly at room temperature). Because they measure infrared radiation, and not visible light, thermal cameras are also useful for identifying heat sources in very dark or otherwise obscured environments.

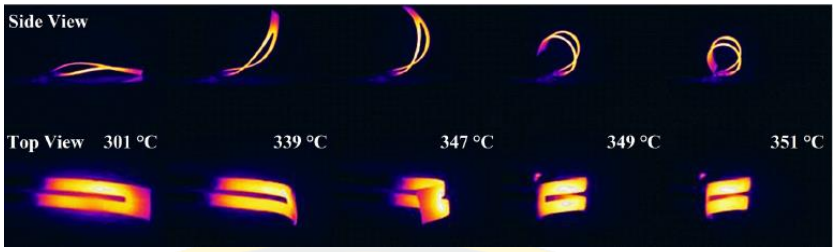

Figure 3-11 Thermal images of the bending movement of CNTF/PDMS composite ETA under different temperatures (Aouraghe et al., 2021).

3.3.8 Double-layer ETA model systems testing application

To demonstrate the potential applications of the proposed actuator under driving voltage, the applied voltage of 6, 9, 15, 21, and 30 V was applied to the proposed ETA and the bending movement was measured. If ETA exhibits both high thermal response under driving voltage and reach its steady state bending angle within few seconds, it can be demonstrated that the proposed ETA shows excellent potential of holding and crabbing objects and can be used as soft grippers. Two actuators were used to made a flexible smart gripper in parallel form, and the flexible smart gripper was connected to the DC power supply. The flexible smart gripper was placed above a foamed plastic block and the DC power supply was adjusted to 6 V. The weight of the actuator and the weight of the foamed plastic block were weighed. After power on, if the flexible smart gripper clamps the foamed plastic block, lifts and moves it to reach the top of the Petri-dish, and then the foamed plastic block will fall into the Petri-dish after power off. The experiment of moving foamed plastics block with a flexible smart gripper will prove that the gripper can achieve the desired driving performance when applying a low voltage (Fan et al., 2020).

CHAPTER 4
RESULTS

4.1 Preparation of conductive composite films

Conductive films had been fabricated from polyvinyl alcohol, incorporating glycerol as a plasticizer and graphite, in varying concentrations, as a conductive filler. An investigation into the influence of mixing time and volume was conducted to establish optimal parameters for film production. Two distinct methodologies, namely K-hand coating and solution casting, were employed. The outcomes of these experiments are depicted in Figure 4.1.

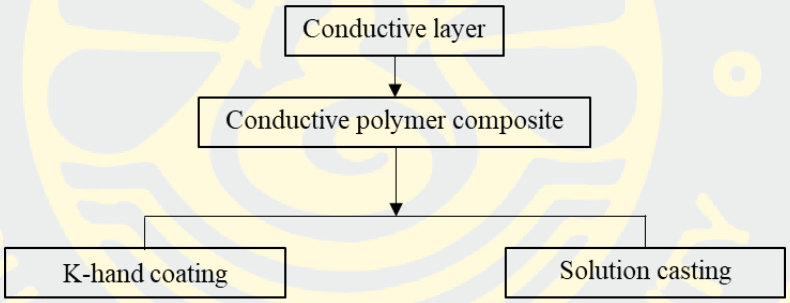

Figure 4-1 A flowchart outlining the procedure for preparing a conductive layer.

4.1.1 K-hand coating method

The experiments conducted on the preparation of compostable polyvinyl alcohol films, both with and without the addition of glycerol as a plasticizer, as detailed in Tables 4.1 and 4.2 using the K-hand coating technique with K-Bar No. 200 Gray, as described in Section 3.2.1.1. It had been noted that the composite films without the glycerol plasticizer were black, difficult to remove from the aluminum foil mold, prone to breakage, and exhibited thicknesses ranging from 0.052 to 0.059 mm. Surprisingly, the composites with GH content of glycerol plasticizer were also black but were easier to remove from the aluminum foil mold, with thicknesses ranging from 0.057 to 0.062 mm. It had been observed that the film thickness

increased with higher graphite concentrations, and the addition of glycerol resulted in an increase in film thickness.

Table 4-1 Thickness and image of composite films prepared by K-hand coating technique.

Sample	Thickness (mm)±SD	Image	Physical appearance
PVA/60GH	0.052±0.01		Black in color, difficult to detach from the substrate, and susceptible to fracturing easily.
PVA/70GH	0.059±0.02		Black in color, difficult to detach from the substrate, and susceptible to fracturing easily.
PVA/80GH	0.056±0.01		Black in color, difficult to detach from the substrate, and susceptible to fracturing easily.

PVA, Polyvinyl alcohol; GH, Graphite

Table 4-2 Thickness and image of glycerol plasticized composite films prepared by K-hand coating technique.

Sample	Thickness (mm)±SD	Image	Physical appearance
PVA/60GH/30Gly	0.057±0.00		Black in color and easy to detach from the substrate.
PVA/70GH/30Gly	0.060±0.01		Black in color and easy to detach from the substrate.
PVA/80GH/30Gly	0.062±0.00	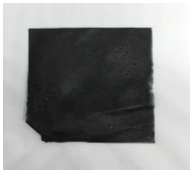	Black in color and easy to detach from the substrate.

PVA, Polyvinyl alcohol; GH, Graphite; Gly, Glycerol

4.1.2 Solution casting method

Conductive films were fabricated through solution casting of 15 mL solutions, wherein graphite content (50%, 60%, 70%, and 80% by weight of PVA) and glycerol content (30%, 40%, 50%, 60%, and 70% by weight of PVA) were systematically varied. The methodology employed for this process was previously outlined in Section 3.2.1.2. It was observed that variation in graphite and glycerol concentrations exerted negligible influence on the thickness of the composite films. The values are tabulated in Table 4.3. (Nemet, Soso, & Lazic, 2010), had indicated that films formulated in the absence of a plasticizer displayed extreme fragility and were prone to fracture upon handling. It was postulated that the polar hydroxyl groups (-OH) situated along the plasticizer chains facilitated the establishment of hydrogen bonds between the polymer and the plasticizer. These newly formed polymer-plasticizer hydrogen bonds were believed to have superseded the pre-existing intermolecular interactions within the biopolymer film. Owing to its compact molecular structure and pronounced polarity, glycerol had emerged as the preeminent plasticizing agent in the field.

Table 4-3 Thickness and images of composite films prepared by solution casting technic.

Sample	Thickness (mm)±SD	Image	Physical appearance
PVA/50GH/30Gly	0.104±0.01		Black color, ease easy to detach from the substrate, and dimensional stability.
PVA/60GH/30Gly	0.187±0.01		Black color, easy to detach from the substrate, and dimensional stability.
PVA/70GH/30Gly	0.160±0.01		Black color, easy to detach from the substrate, and dimensional stability.
PVA/80GH/30Gly	0.134±0.03		Black color, easy to detach from the substrate, and dimensional stability.
PVA/50GH/40Gly	0.230±0.02		Black color, easy to detach from the substrate, and dimensional stability.
PVA/60GH/40Gly	0.250±0.02		Black color, easy to detach from the substrate, and dimensional stability.
PVA/70GH/40Gly	0.254±0.01		Black color, easy to detach from the substrate, and dimensional stability.

Sample	Thickness (mm)±SD	Image	Physical appearance
PVA/80GH/40Gly	0.226±0.01		Black color, easy to detach from the substrate, and dimensional stability.
PVA/50GH/50Gly	0.199±0.01		Black color, easy to detach from the substrate, and dimensional stability.
PVA/60GH/50Gly	0.183±0.01		Black color, easy to detach from the substrate, and dimensional stability.
PVA/70GH/50Gly	0.245±0.02		Black color, easy to detach from the substrate, and dimensional stability.
PVA/80GH/50Gly	0.310±0.01		Black color, easy to detach from the substrate, and dimensional stability.
PVA/50GH/60Gly	0.219±0.02		Black color, easy to detach from the substrate, and dimensional stability.
PVA/60GH/60Gly	0.182±0.01		Black color, easy to detach from the substrate, and dimensional stability.

Sample	Thickness (mm)±SD	Image	Physical appearance
PVA/70GH/60Gly	0.235±0.01		Black color, easy to detach from the substrate, and dimensional stability.
PVA/80GH/60Gly	0.255±0.01		Black color, easy to detach from the substrate, and dimensional stability.
PVA/50GH/70Gly	0.231±0.01		Black color, easy to detach from the substrate, and dimensional stability.
PVA/60GH/70Gly	0.165±0.01		Black color, easy to detach from the substrate, and dimensional stability.
PVA/70GH/70Gly	0.246±0.01		Black color, easy to detach from the substrate, and dimensional stability.
PVA/80GH/70Gly	0.240±0.01		Black color, easy to detach from the substrate, and dimensional stability.

4.1.3 Preparation of Double-Layer ETA

4.1.3.1 Two-Step Process

The conductive layer (layer 1) of the ETA was constructed from a PVA/GH/Gly solution wherein glycerol concentrations were systematically varied at 30%, 40%, 50%, 60%, and 70% by weight. The PVA solution was poured into molds and subsequently cured within a hot air oven. Thereafter, the resulting samples was fashioned into U-shaped pieces, measuring 0.5 x 5 cm^2, as depicted in Figure 4-2. These pieces was then affixed to the adhesive surface of Kapton tape (layer 2), measuring 0.5 x 4 cm^2. The thickness of the fabricated ETA spanned a range from 0.121 to 0.387 mm.

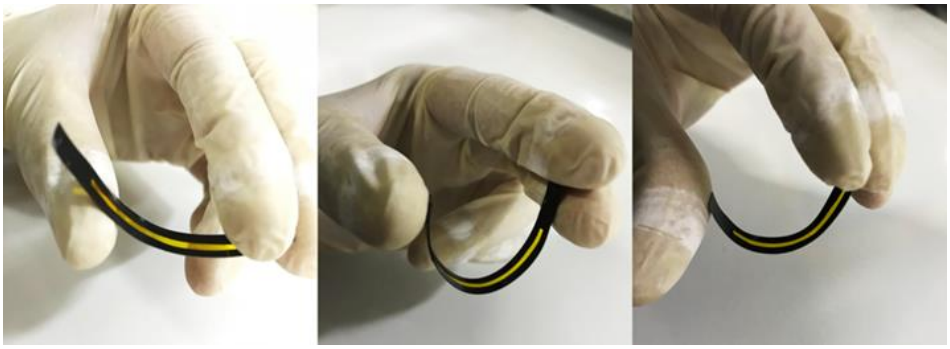

Figure 4-2 The double-layer ETA, showing its the flexibility.

It had been observed that glycerol concentration exerted a significant influence on the thickness of the conductive layer. An increase in glycerol content generally resulted in thicker films, a critical factor in optimizing the layer's conductive properties. This variation in thickness underscored the direct correlation between glycerol concentration and the structural and functional characteristics of the conductive layer. This relationship facilitated the fine-tuning of material properties for specific applications, such as enhancing flexibility, conductivity, and mechanical strength in the final product (Arham, 2018).

Table 4-4 Thickness and image of double-layer ETA by two-step process.

Sample	Thickness (mm)±SD	Image
PVA/50GH/40Gly	0.307±0.00	
PVA/60GH/40Gly	0.358±0.01	
PVA/70GH/40Gly	0.384±0.01	
PVA/80GH/40Gly	0.334±0.02	

Sample	Thickness (mm)±SD	Image
PVA/50GH/50Gly	0.321±0.01	
PVA/60GH/50Gly	0.312±0.01	
PVA/70GH/50Gly	0.340±0.02	
PVA/80GH/50Gly	0.356±0.01	
PVA/50GH/60Gly	0.301±0.01	
PVA/60GH/60Gly	0.284±0.05	

Sample	Thickness (mm)±SD	Image
PVA/70GH/60Gly	0.361±0.02	
PVA/80GH/60Gly	0.387±0.02	
PVA/50GH/70Gly	0.307±0.02	
PVA/60GH/70Gly	0.3210±0.02	
PVA/70GH/70Gly	0.323±0.02	
PVA/80GH/70Gly	0.367±0.02	

PVA/GH/Gly system

The preparation of conductive composite films involved the application of three distinct polymer materials as overlays: Kapton Tape (3M) with a thickness of 0.034 mm, PVC Tape (3M) with a thickness of 0.140 mm, PVC Tape (THAI-YAZAKI) with a thickness of 0.119 mm, and PP Tape (3M) with a thickness of 0.022 mm (as illustrated in Figure 4-3). Each layer had dimensions of 0.5 × 5.5 cm^2 (layer 2), as depicted in Figures 3.6-3.8. The actuator exhibited a range of coefficient of thermal expansion (CTE) values. A comparative analysis of the polymer layers revealed that Kapton shows the lowest CTE value, followed by PVC (3M), PVC (THAI-YAZAKI), PP, and PDMS in ascending order. The conductive layers, comprising GH, GO, and rGO, demonstrated significant influence on the actuator's response to electrical potential, resulting in deformation and bending. CTE values for the conductive fillers were tabulated in Table 4.6. The composite films show uniformity, a black

Table 4-5 Coefficient of thermal expansion of the polymer

Polymer tape	CTE* (ppm/°C)	Thickness (mm)
DuPont™ Kapton® polyimide film (3M)*	20.0-30.0	0.034
Polyvinyl chloride (3M)*	50.4	0.140
Polyvinyl chloride (THAI-YAZAKI)**	70.0-250.0	0.119
PDMS***	300.0	0.012
PP****	135.65	0.022

Official Information from the Manufacturer:

* (DuPont™, 2022)

** List of Thermal Expansion Coefficients (CTE) for Natural and Engineered Materials © 2024 MSE Supplies LLC

*** (Dow, 1995-2024)

**** (Davis, 2003)

Table 4-6 Thermal coefficient of expansion of conductive material.

Material	CTE (ppm /°C)	Electrical conductivity (S/cm)
GH	8 (Marques, F. C. et al. 2019)	0.073×10^{-8} (Akhileshwar P. et al. 2021)
GO	-341.15 (Gao, D. et al. 2020)	4.570×10^{-8} (Jaafar, E., et al. 2018)
rGO	-274.15 and -245.15 (Nyanor, P. et al. 2019)	4.210×10^{-5} (Jaafar, E., et al. 2018)

Figure 4-3 Types of polymer layers are: PI PVC (3M) PVC (THAI-YAZAKI) PP (3M) and PDMS.

ETA was prepared using five different polymer layers: Kapton tape (3M), PVC (3M), PVC (THAI-Yazaki), PDMS, and PP, with their respective thicknesses and CTE values shown in Table 4.5. The CTE values, listed from lowest to highest, are as follows: Kapton > PVC (3M) > PVC (THAI-YAZAKI) > PP > PDMS. The ETA thicknesses derived from each mentioned polymer layer are 0.235±0.04, 0.404±0.02, 0.361±0.04, and 0.0080±0.02 mm, respectively, with the conductive layer of PVA/50GH/Gly. In this study, Kapton tape had been chosen for further investigation due to its minimal thickness and lowest CTE compared to the other tapes. The best conductive filler layer had been graphite, known for its high CTE but low electrical conductivity. In the study by (Fan et al., 2020) graphite paper and PI film had been combined to create actuators due to their excellent performance. Three kinds of flexible double-layer ETAs had been made by combining graphite paper and PI film. The CTE of the graphite paper had been 2.7×10^{-6} °C^{-1}, and the CTE of the PI film had been 2.5×10^{-5} °C^{-1}. The graphite paper and PI film had

different CTE values, and the graphite paper had demonstrated excellent electrothermal performance, resulting in flexible double-layer ETAs with good driving performance at low voltage. (Sachyani et al., 2017) developed electro-thermal actuators (ETAs) based on carbon nanotubes (CNT). The performed actuation was due to different coefficients of thermal expansion (CTEs) in their bi-layer structure. Despite their advantages, their movement had been limited. This study had improved CNT-based actuators' deflection by reducing CNT layer resistance and introduced a novel tri-layer actuator achieving a record 300° deflection by adding a photopolymerizable polymer layer. In the research conducted by (Yao et al., 2017) a silver nanowire (AgNW) based bimorph actuator achieved a bending angle of 720° and curvature of 2.6 cm^{-1} at an ultra-low voltage of 0.2 V sq^{-1} (4.5 V). This performance was due to the AgNW heater's high conductivity, mechanical robustness, and the significant thermal expansion difference between PDMS and polyimide tape. Fabricated with a simple, low-cost process, the actuator had enabled controllable patterns and been demonstrated in a walking device and a soft gripper. (Fahmy Taha, Ashraf, & Caesarendra, 2020) had indicated that GO and rGO exhibited higher electrical conductivity than GH. Consequently, in this present study, the conductive systems based on GH, GO and rGO were investigated in terms of their electrical conductivity. With their lower cost compared to Kapton tape, PVC (3M) and PVC (Yazaki) were tested for their performance compared with Kapton tape. However, no significant difference was found, despite having slightly higher thickness and CTE values. Therefore, PDMS and PP were chosen for further investigation due to their higher CTE values compared to Kapton tape.

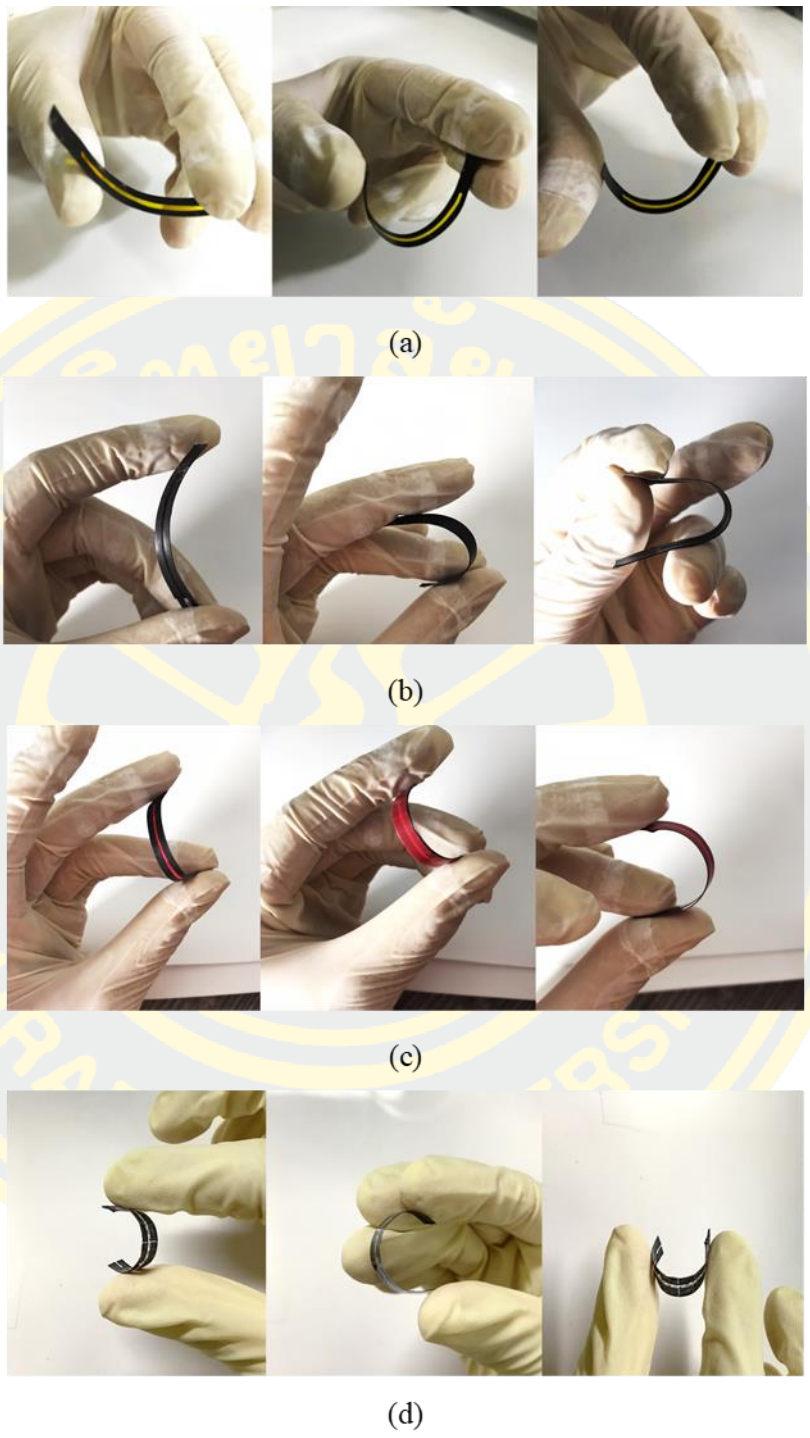

Figure 4-4 The actuator systems comprised of PVA/50GH/60Gly with various polymer tapes: (Kapton) (a), (3M PVC) (b), (PVC Yazaki) (c), and (3M PP) (d).

Table 4-7 Thickness and images of actuator systems with various polymer layers: Kapton Tape, PVC Tape (3M), PVC Tape (Yazaki), and PP Tape (3M).

Sample	Volume (mL)	Tape	Thickness (mm)±SD	Image
PVA/50GH/60Gly	15	Kapton	0.235±0.04	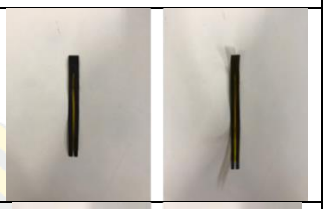
PVA/50GH/60Gly	15	3M PVA	0.404±0.02	
PVA/50GH/60Gly	15	Yazaki PVA	0.361±0.04	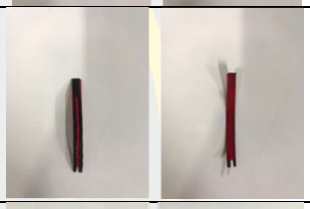
PVA/50GH/60Gly	15	PP	0.0080±0.02	

PDMS formulations RA-320, RA-330, and RA-420, popular in the biomedical field due to their biocompatibility, similarity to human soft tissue, chemical inertness, gas permeability, low shrinkage (<2%) upon curing, surface conformity (<10 nm), and ease of fabrication (Lee et al., 2016), were processed into the polymer layer of the prepared actuators. These formulations were prepared by blending 2%wt of silicone rubber accelerator. Among them, the RA-320 formulation, as shown in Figure 4-7a, exhibited a homogeneous texture, flexibility, and minimal air bubbles, making it seemingly the most suitable polymer layer for an actuator. However, as shown in Figure 4-7b, the actuator with the RA-320 PDMS polymer layer was extremely thin, with thicknesses ranging from 0.0015 to 0.0023 mm. This resulted in the PDMS formulation being unsuitable for fabricating ETA. The PDMS layer prepared under

optimal conditions was too thin to maintain its shape and contained air bubbles, which hindered its effectiveness as an actuator.

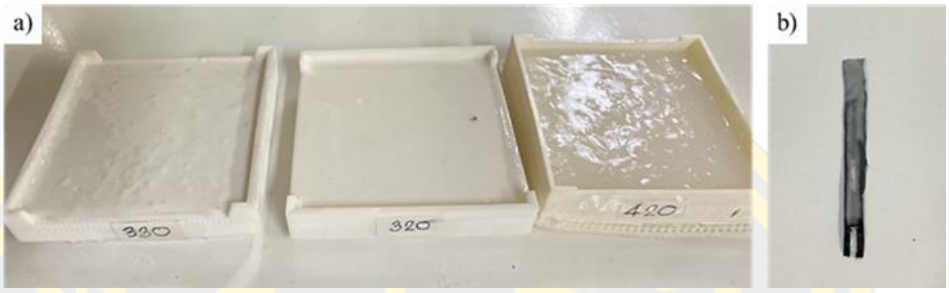

Figure 4-5 a) Types of PDMS Silicone b) The PVA/GH/Gly ETA incorporating PDMS as the polymer layer.

4.1.3.2 In Situ Process

The PVA/GH/Gly actuator was prepared as outlined in Section 3.2.2.1, using varying volumes of composite solution—specifically 3 mL and 4 mL. The composite film was fabricated within a mold, as shown in Figure 4-6, with Kapton tape and PVC tape secured to the mold. Afterward, the actuator was detached from the mold, with the red PVC tape peeled off. The actuator took on a U-shape, with the U-shaped portion serving as the conductive layer of the composite film, and was cut to dimensions of 0.5 × 4 cm. The resulting composite film was black and was easily removed from the mold. The experiment demonstrated a clear correlation between the volume of the composite solution and the thickness of the composite film. Films made with 3 mL of solution had thicknesses in the range 0.111–0.124 mm, while those made with 4 mL of solution had thicknesses in the range 0.123–0.134 mm, as shown in Table 4.8. These findings established a direct correlation between the volume of the composite solution and the film thickness, with increasing volume resulting in increased thickness.

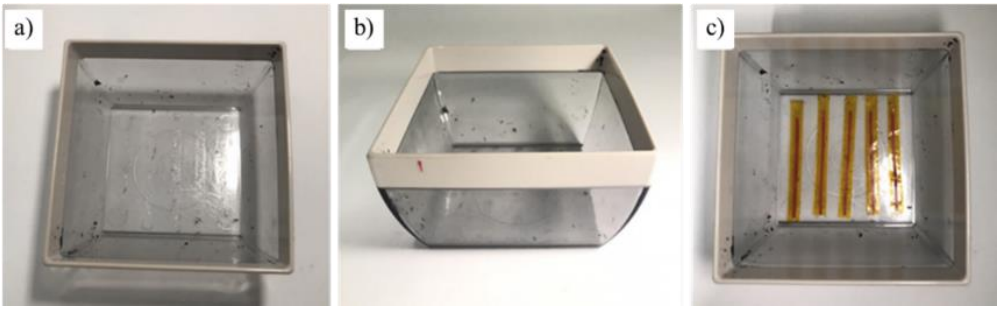

Figure 4-6 a-c). Molds used in the In-situ method.

Table 4-8 Thicknesses and images of double-layer ETAs produced via the in-situ process.

Sample	Volume (mL)	Thickness (mm)±SD	Image
PVA/50GH/60Gly	3	0.124±0.01	
PVA/60GH/60Gly	3	0.111±0.01	
PVA/70GH/60Gly	3	0.114±0.00	
PVA/80GH/60Gly	3	0.122±0.00	

Sample	Volume (mL)	Thickness (mm) ±SD	Image
PVA/50GH/60Gly	4	0.128±0.02	
PVA/60GH/60Gly	4	0.123±0.01	
PVA/70GH/60Gly	4	0.134±0.01	
PVA/80GH/60Gly	4	0.124±0.00	

The conductive layers were prepared using four distinct methods: K-hand coating, solution casting, in-situ process, and two-step process. Among these methods, the in-situ process was distinguished by its ability to produce exceptionally thin samples compared to the other approaches. Additionally, the in-situ process uniquely allowed the conductive and polymer layers to be positioned in close proximity, forming a dual-layer assembly. Due to its capability to produce the thinnest samples, ensure the closest proximity between the conductive and polymer layers, and offer a comprehensive, time-efficient preparation in a single step, the in-situ u process was selected as the optimal method for further analysis of various properties.

Preparation of actuator systems using the in-situ process method

The in-situ preparation of four electroactive actuator systems (PVA/GH/Gly, PVA/GO/Gly, PVA/rGO/Gly, and PDMS/GH/Gly) is depicted in Figure 4-7.

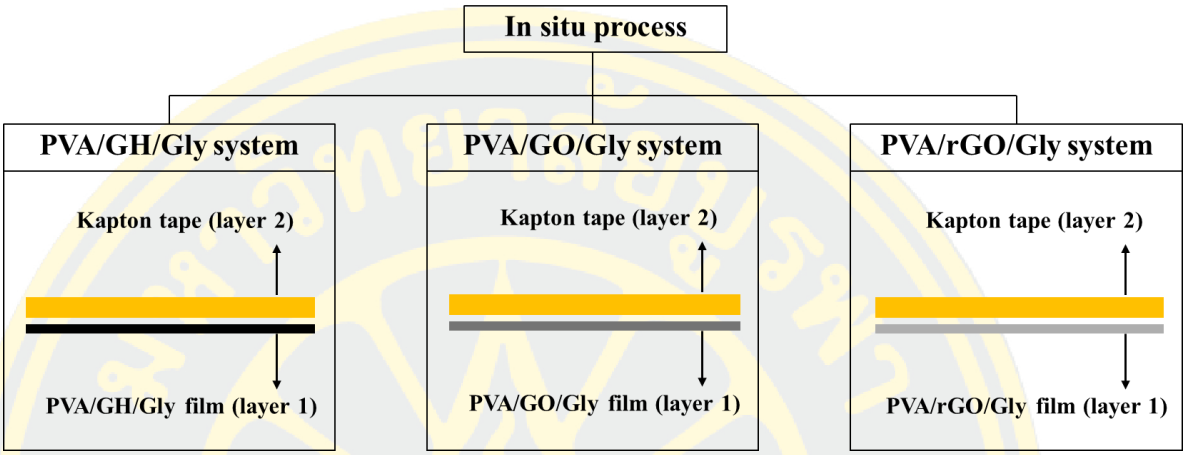

Figure 4-7 Schematic of the actuator system, where the conductive layer and the polymer layer were prepared via the in-situ process.

PVA/GH/Gly system

An electroactive actuator had been successfully prepared using a PVA/GH/Gly mixed solution as the conductive layer and Kapton tape as the polymer layer; the percentage of glycerol had not shown any significant influence on the actuator.

PVA/GO/Gly system

The electroactive actuator was prepared using PVA/GO/Gly, with the preparation steps outlined in Section 3.2.2.1. The glycerol percentage was fixed at 30% wt relative to the weight of PVA, and the amounts of graphite oxide were varied at 8, 10, 15, and 20% wt. The actuator is shown in Figure 4-8. The preparation process is detailed in Section 3.2.3, where the synthesis of GO is described using a modified Hummers' method from pure GH powder. The amount of graphite oxide affected the thickness and morphology of the films, as noted in the research by (Cobos, Fernandez, & Fernandez, 2018) Additionally, a comparative study highlighted several advantages of the PVA/graphene nanocomposite film prepared using a green method, including environmental friendliness, production of the

smallest graphitic domains by ascorbic acid, suitability of ascorbic acid-reduced GO for biomedical applications, and prevention of graphene agglomeration in the PVA matrix. The table showing the thickness and morphology of the PVA/GO/Gly films indicates that as the GO content increased, GO agglomeration in the PVA matrix occurred. The highest GO content of 20% wt showed dense agglomeration, while the 8% wt sample exhibited the greatest thickness, possibly due to better dispersion of GO particles (Table 4.9). The in-situ reduction of GO dispersed in a polymer matrix was identified as one of the most effective strategies for achieving stable dispersions of GO.

Table 4.9 Thickness and image of PVA/GO/Gly system by in-situ process.

Sample	Thickness (mm)±SD	Image
PVA/8GO/60Gly	0.210±0.21	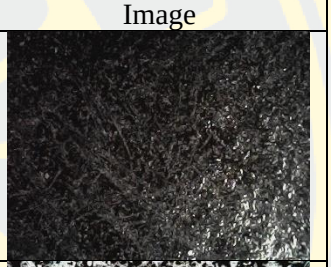
PVA/10GO/60Gly	0.136±0.03	
PVA/15GO/60Gly	0.143±0.01	
PVA/20GO/60Gly	0.178±0.01	

Figure 4-8 The actuator of the PVA/GO/Gly system.

PVA/rGO/Gly system

The electroactive actuator was prepared using 30% wt glycerol relative to the weight of PVA. The rGO content had affected the thickness of the actuator. The increased thickness was observed as the amount of rGO increased, as well as the increased agglomeration with denser particles (Table 4.10). After the chemical reduction of GO, the rGO became thinner and spread out more as a sheet (Srihata, Jamnongkan, Rattanasak, Boonsang, & Kaewpirom, 2016). (Horacio J. Salavagione et al., 2009), synthesized PVA/rGO by reducing graphite oxide in the presence of the polymer matrix and coagulating the system. Different levels of rGO content were prepared, specifically 0.5, 1, 1.5, 2, 5, 7.5, and 10% filler. The agglomerates exhibited distinctive characteristics, except when the rGO content was 8%, which resulted in the highest thickness. This might be due to the lower amount of rGO filler causing the particles to be more dispersed, resulting in the greatest thickness.

Table 4-9 Thickness and image of PVA/rGO/Gly system by in-situ process.

Sample	Thickness (mm)±SD	Image
PVA/8rGO/60Gly	0.203±0.02	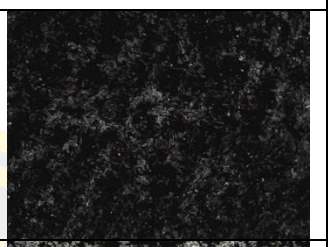
PVA/10rGO/60Gly	0.137±0.01	
PVA/15rGO/60Gly	0.143±0.01	
PVA/20rGO/60Gly	0.172±0.01	

Figure 4-9 The actuator of the PVA/GO/Gly system.

4.1.4 Synthesis of GO and rGO

Synthesis of graphite oxide and reduction of graphite oxide had been carried out using graphite powder. Figures 4-10 to 4-11 show the infrared spectra of graphite powder (GH), graphite oxide (GO), and reduced graphite oxide (rGO). It was evident that there was no functional groups and significant peaks on the surface of graphite, whereas in GO, functional groups such as hydroxyl, carbonyl, carboxyl, and epoxy groups were detected, as shown by the broad bands at wavenumbers 3342 cm^{-1} (O-H stretching vibrations), 1736 cm^{-1} (C=O group), 1217 cm^{-1} (C-O stretching), and 1035 cm^{-1} (C-O alkoxy stretching), respectively. The low quantity of carboxyl and carbonyl groups had made GO suitable for the production of highly conductive and defect-free graphene-like materials via reduction (Morimoto, Kubo, & Nishina, 2016). These findings were consistent with previous research by (Bera, Gupta, & Maji, 2018) and (Razi-Asrami, Ghasemi, Amiri, & Sadeghi, 2017). The decrease in intensity was attributed to the decomposition of these groups during thermal treatment (Ruidíaz-Martínez et al., 2020). As for the spectra of reduced graphite oxide, the disappearance of the OH group was observed, with peaks at 1737 cm^{-1} (C=O stretching), 1528 cm^{-1} (C=C stretching), 1366 cm^{-1} (C-OH stretching), and 1217 cm^{-1} (C-O stretching), respectively (Gong et al., 2018). RGO had been identified as a nanomaterial obtained by the chemical reduction of graphene oxide, with fewer oxygen groups and properties closer to those of graphene (Manousi, Rosenberg, Deliyanni, Zachariadis, & Samanidou, 2020).

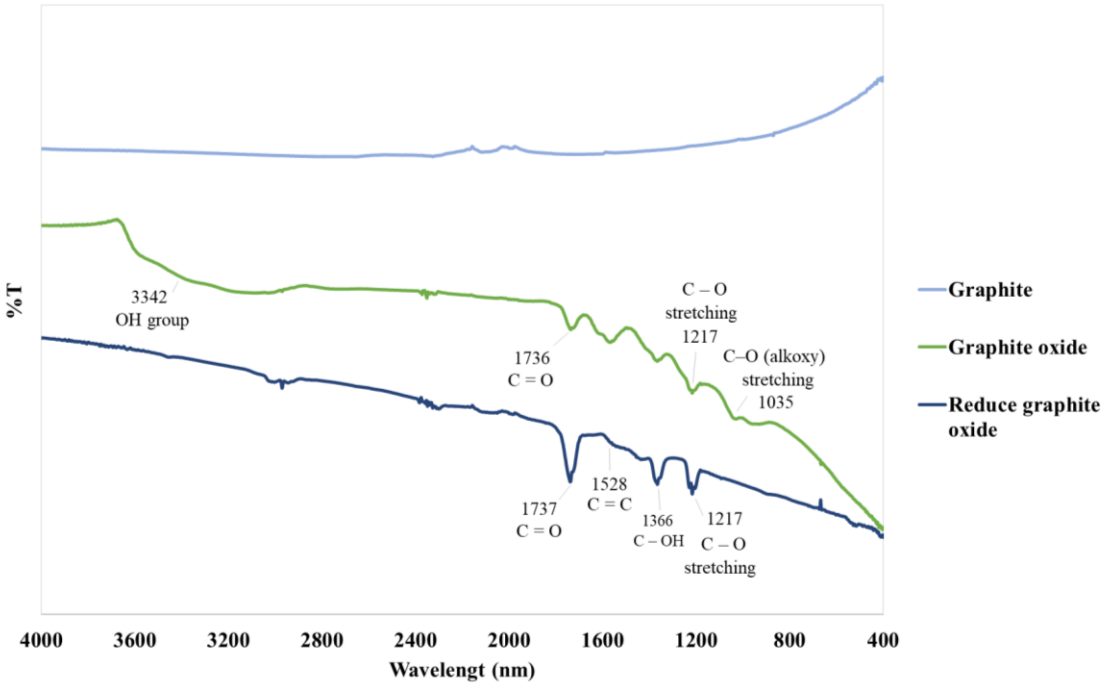

Figure 4-10 FTIR spectra of GH, GO and rGO.

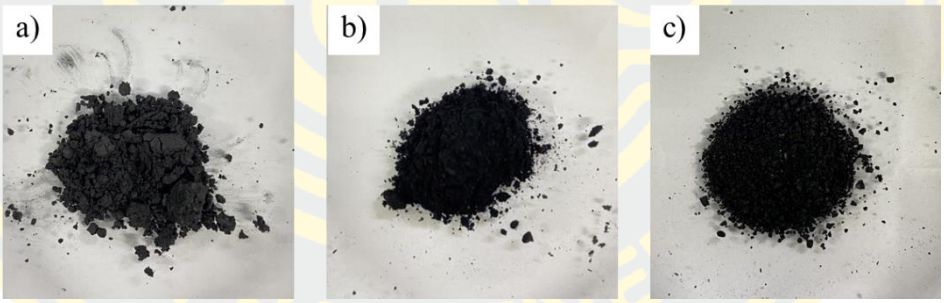

Figure 4-11 Digital images of a) GH b) GO and c) rGO.

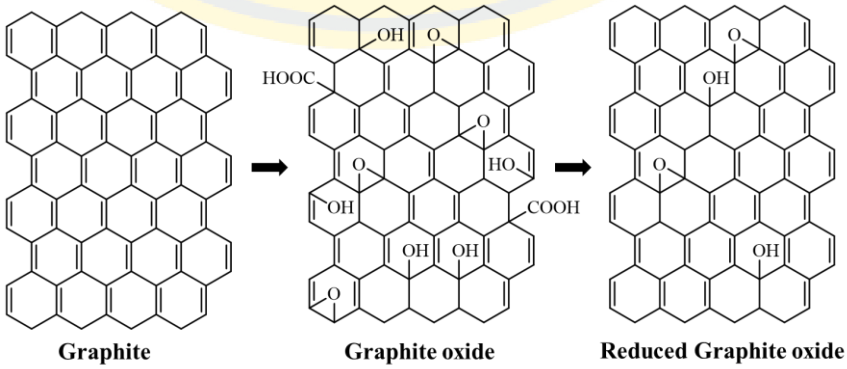

Figure 4-12 Structure of graphite, graphite oxide and reduced graphite oxide.

As shown in Figure 4-11a), graphite is a finely powdered solid with a smooth texture. It is lightweight and dark gray to nearly black, with a capability to absorb light (Y. He et al., 2013). Graphite oxide also existed in solid form, resembling a powder, but it appeared darker than graphite. It was not as lightweight as graphite and possessed a less smooth texture. This could be observed in Figure 4-11b). The solid graphite oxide appeared dark black and glossy, unlike graphite. It was not as lightweight as graphite and exhibited a more uneven surface compared to pristine graphite, as illustrated in Figure 4-11c) (Pei & Cheng, 2012).

From Table 4.10, the morphological characteristics of the three types of fillers graphite (GH), graphite oxide (GO), and reduced graphite oxide (rGO) were studied using SEM techniques. GO and rGO was synthesized and observed at magnifications of 100x, 500x, 1000x, 3000x, and 5000x. GH, composed of layered atomic carbon structures, appears black and consists of particles with smooth surfaces (Immanuel & Sivasubramanian, 2020). GO was prepared using sulfuric acid, resulting in a more expanded and disordered lattice. This expansion and disorder are observed as wrinkled surfaces, with folds and rough areas compared to the smooth layers of graphite. These observations can be attributed to the formation of oxygen-containing functional groups and structural defects in the GO. rGO was prepared using ascorbic acid, which acts as a reducing agent. This resulted in a more complex structure with smoother surfaces than graphite oxide but not as smooth as graphite. This indicates partial reduction and restoration of graphene layers. The surface is rougher, with a porous structure formed by the release of gases during the reduction process. The exfoliation and creation of pores between graphene layers can be observed at magnifications of 3000x and 5000x, showing that rGO has a complex surface with stacked layers (Mission et al., 2018). Graphite and rGO suspensions were visualized to compare their structures. Images of multi-layered rGO, suspension films, and graphite flakes were created. The removal of covalently bound oxygen addends from GO had been achieved thermally, chemically, or through a combination of both methods, resulting in reduced GO (rGO) that had still contained many defects. During the reduction process from GO to rGO, the surface of the sample became corrugated due to the release of oxygen-containing groups (Mohan, Brown, Jayaraman, &

Bhattacharyya, 2015). Using different conditions during oxidation and reduction processes was not significantly affected the morphology of each rGO sample. However, in all cases, it is possible to obtain a product with a porous structure (Sieradzka, Ślusarczyk, Biniaś, & Fryczkowski, 2021).

Table 4-10 The SEM micrographs of GH, GO, and rGO fillers.

Sample	Magnification				
	100x	500x	1000x	3000x	5000x
GH	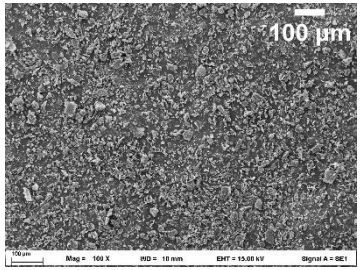	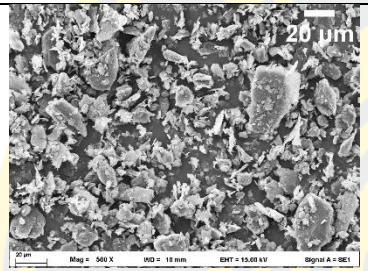	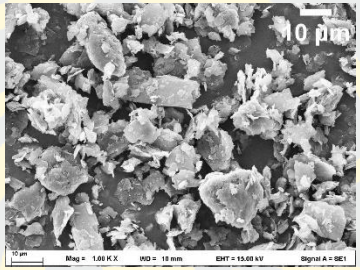	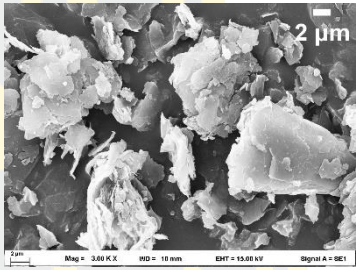	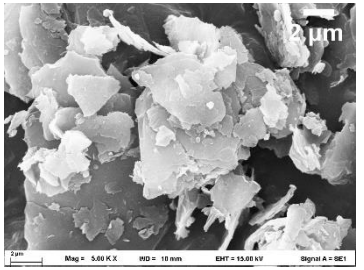
GO	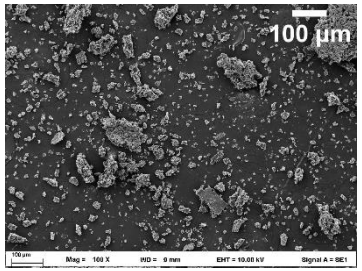	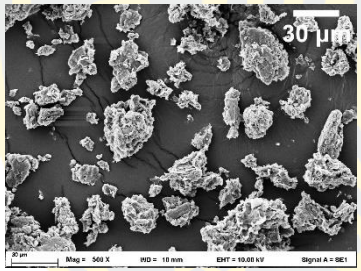	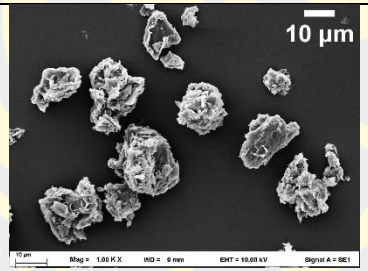	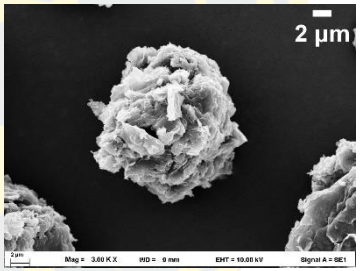	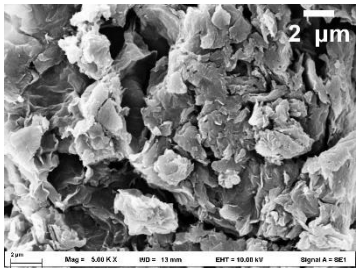
rGO	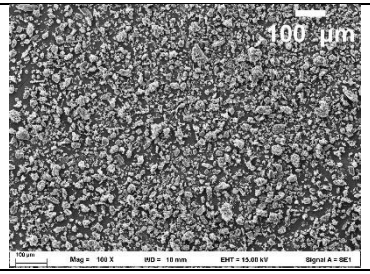	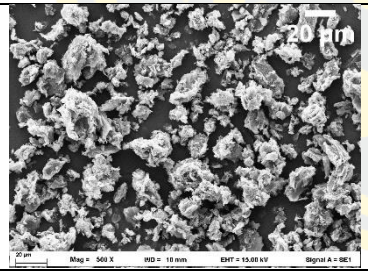	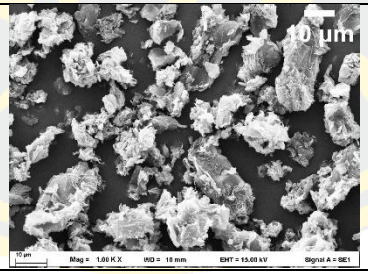	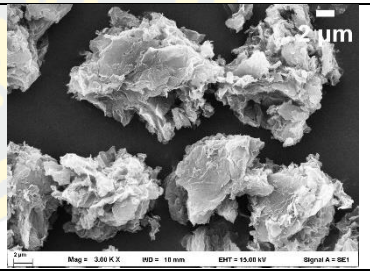	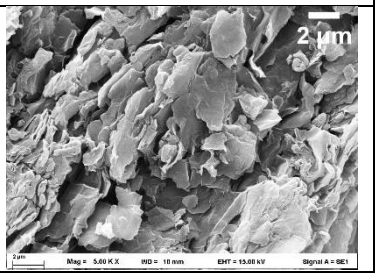

Conductive composite films

FTIR spectra of prepared conductive composite films are shown in Figure 4-13. It can be seen from results that as the amount of GO increased, the –OH stretching vibration band had shifted from 3270 to 3281 cm^{-1} and became broader. The C–OH stretching vibration band shifted from 1085 to 1090 cm^{-1} (Jing et al., 2021). Additionally, the characteristic absorption peak of CH_2 stretching shifted from 2914 to 2918 cm^{-1}, and the characteristic absorption peak of –CH/CH_2 deformation vibrations shifted from 1323 to 1417 cm^{-1}. The hydrogen bonds that formed between the GO and PVA enhanced the mechanical properties of the composite film. The GO acted as a "binder," linking different PVA chains and improved the overall toughness and rigidity of the composite material. These findings is consistent with the results proposed by (Georgiou, Koutsioukis, & Georgakilas, 2021). They reported that functional groups of GO/PVA composite were characterized by a broad band at 3300 cm^{-1} (O–H stretching), a peak at 2940 cm^{-1} (C–H stretching), and a peak at 1640 cm^{-1} attributed to the aromatic C=C stretching vibration of the graphene-based material. Other signals that had typically appeared in the FTIR spectrum of GO included a strong broad band at 3420 cm^{-1} (OH stretch), a peak at 1400 cm^{-1} (C=C aromatic ring), and two peaks at 1255 cm^{-1} and 1060 cm^{-1} assigned to the phenolic (C–O) group.

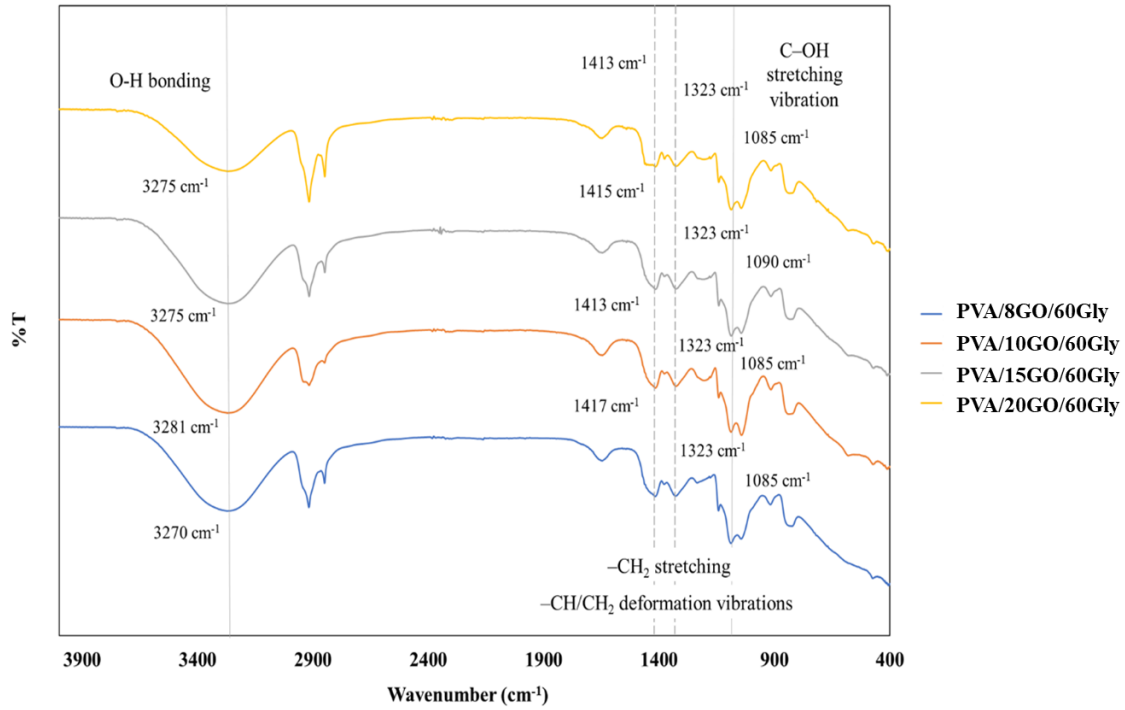

Figure 4-13 FTIR spectra of PVA/8GO/60Gly, PVA/10GO/60Gly, PVA/15GO/60Gly, and PVA/20GO/60Gly.

From the analysis of the conductive films prepared using PVA/rGO/Gly, the infrared spectrum, as shown in Figure 4-14, indicated that after the reduction step, the bands in the range of 3258 to 3270 cm^{-1} diminished relative to the other bands due to the removal of OH groups from the graphenic surface of rGO. Additionally, the characteristic absorption peak of CH_2 stretching shifted from 2914 to 2918 cm^{-1}, and the characteristic absorption peak of $–CH/CH_2$ deformation vibrations shifted from 1322 to 1417 cm^{-1}. The multiple bands around 1081 to 1086 cm^{-1} associated with C–O stretching were also evidenced (Georgiou et al., 2021).

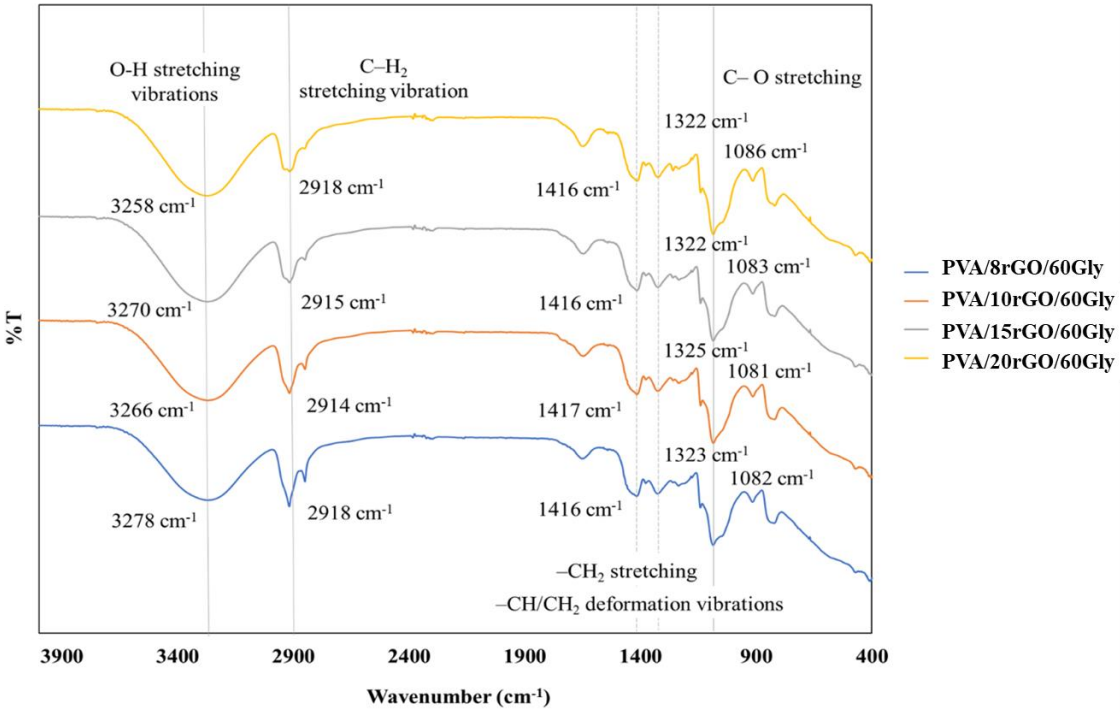

Figure 4-14 FTIR spectra of PVA/8rGO/60Gly, PVA/10rGO/60Gly, PVA/15rGO/60Gly, and PVA/20rGO/60Gly.

Fourier transform infrared (FTIR) spectroscopy was also used to investigate the chemical structure of conductive layer PVA/GH/Gly composite films with different graphite contents of 50, 60, 70, and 80% wt (Figure 4-15). The FTIR spectrum of PVA shows distinct vibrations in the range 2939 to 2946 cm^{-1} (stretching vibration of C–H), 1734 to 17410 cm^{-1} (C=O of the carbonyl group), 1376 to 1377 cm^{-1} and 1452 to 1453 cm^{-1} (bending and wagging of CH_2 groups). The band in the range 3261 to 3262 cm^{-1} indicates O–H stretching vibration of both PVA and Glycerol. FTIR analysis also confirmed the presence of PVA within the composite films. Peaks at 2936 cm^{-1} and 1725 cm^{-1} corresponded to the stretching vibrations of C-H and carbonyl C=O groups, respectively, characteristic of PVA. Similarly, the observed peaks at 1430 cm^{-1} and 1375 cm^{-1} could be attributed to the bending and wagging of CH_2 groups within the PVA structure. Additionally, peaks at 1250 cm^{-1} and 850 cm^{-1} supported the presence of C-O and C-C stretching vibrations, further corroborating the successful incorporation of PVA. These findings aligned with the work of (Salim,

Hany, Elshahawy, & Oraby, 2022) who reported the development of solid polymer electrolytes utilizing PVA as a key component. (Jamali, Shaikh, & Chandio, 2023) improved the flexibility of a PVA membrane through the addition of glycerol, followed by functional group analysis. FTIR spectrum of the PVA membrane showed a significant absorption band at 3262 cm^{-1}, indicating the presence of O–H stretching vibrations. Unlike GO and rGO, graphite exhibited no prominent functional groups in the FTIR spectra.

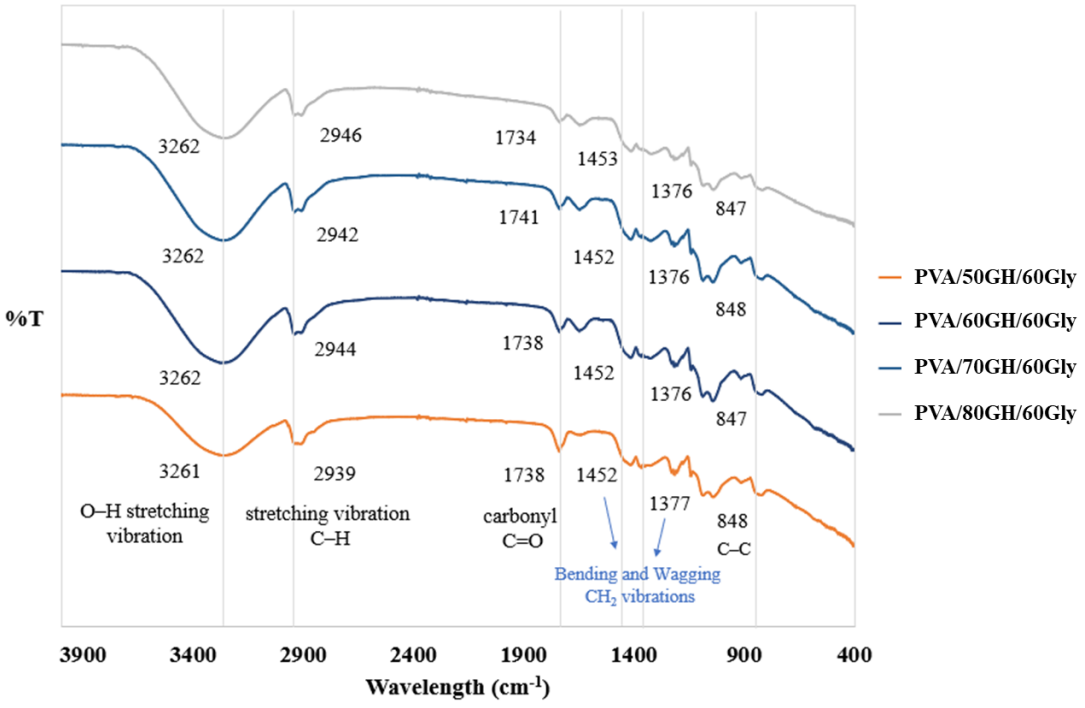

Figure 4-15 FTIR spectra of PVA/50GH/6Gly, PVA/60GH/60Gly, PVA/70GH/60Gly, and PVA/80GH/60Gly.

4.1.5 Electrical conductivity of conductive layer

4.1.5.1 PVA/GH/Gly system

Electrical resistance of the prepared conductive films was measured using a Digital Multimeter, following the procedure described in Section 3.3.4. Vaseline petroleum gel was applied as adhesive interface layer. The conductive films PVA/50GH/60Gly, PVA/60GH/60Gly, PVA/70GH/60Gly, and PVA/80GH/60Gly, tested with and without the application of Vaseline, exhibited a reduction in electrical resistance. The resistivity values were 3.36×10^{9}, 8.95×10^{8}, 2.36×10^{6}, and 2.37×10^{6} Ω·cm, and the electrical conductivity values were 3.29×10^{-12}, 3.90×10^{-9}, 4.19×10^{-9}, and 4.12×10^{-9} S/m. This was attributed to the fact that in both cases, the copper electrodes made closer contact with the samples, minimizing gaps and reducing resistance in all samples (S. M. Zainab, Junaid, Xu, & Malik, 2020). Consequently, the conductivity values increased (Figures 4-16 to 4-19). Since electrical resistance values are inversely proportional to conductivity values, higher resistance led to lower conductivity, and lower resistance corresponds to higher conductivity (Heaney, 2003). It was indicated from the above results that the amount of graphite affected electrical conductivity of the films. This is consistent with the results reported by (F. P. Du, Tang, C. Y., Xie, X. L., Zhou, X. P., & Tan, L., 2009) that the conductivity values for PSA-g-MWNTs-loading with of 0, 5, 10, and 20 Wt% graphite were as 7.53×10^{-13}, 4.91×10^{-9}, 5.09×10^{-8}, and 1.44×10^{-4} S cm^{-1}, respectively. These values also increased with the increasing amount of MWNTs.

The effect of glycerol on electrical resistance and electrical conductivity of the composite films is demonstrated in the Figure 4-16 to 4-19. Glycerol, a highly permissive additive, had effectively increased the dielectric constant and reduced the modulus of elasticity in composite materials (A.L., 2016). As shown in the Figure 4-20 to 4-23, the electrical conductivity of composite films had increased with the graphite concentration.

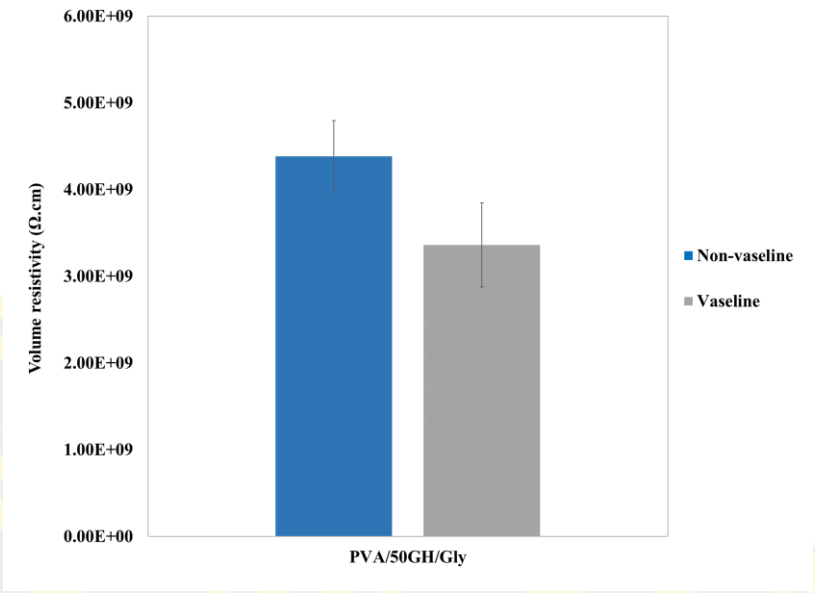

Figure 4-16 Volume resistivity of PVA/50GH/60Gly.

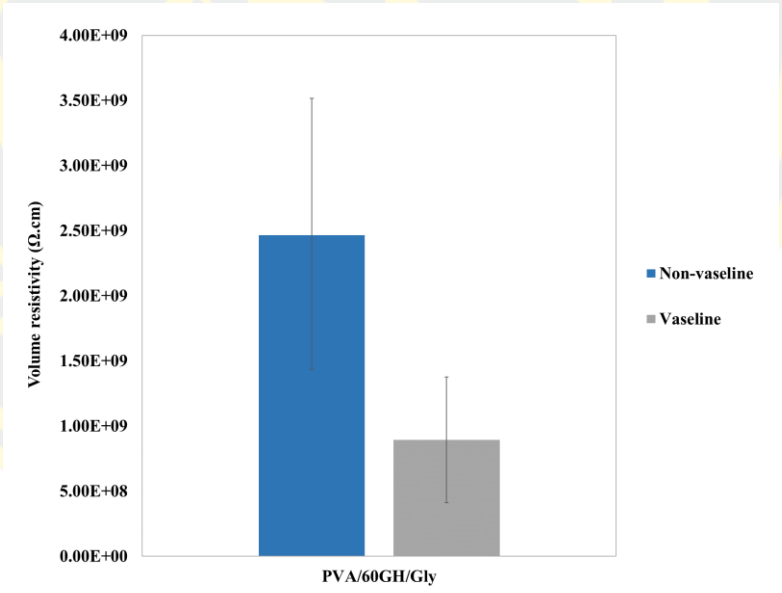

Figure 4-17 Volume resistivity of PVA/60GH/60Gly.

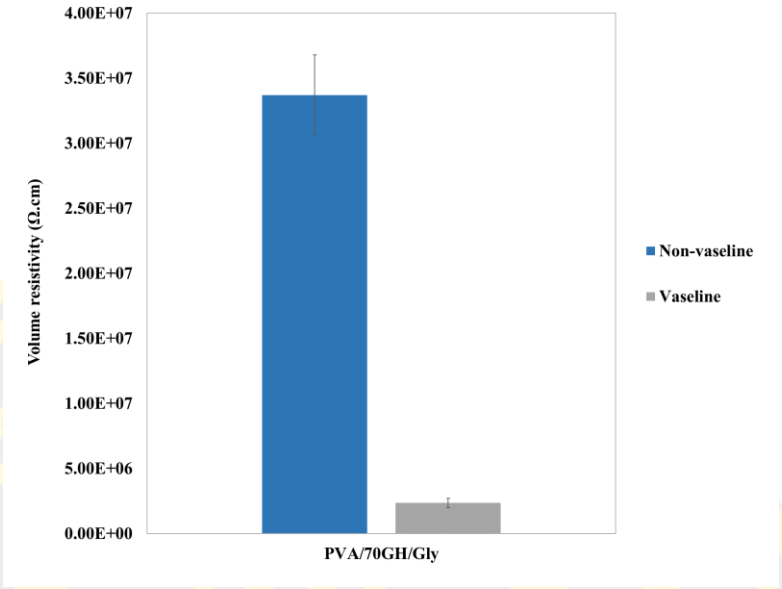

Figure 4-18 Volume resistivity of PVA/70GH/60Gly.

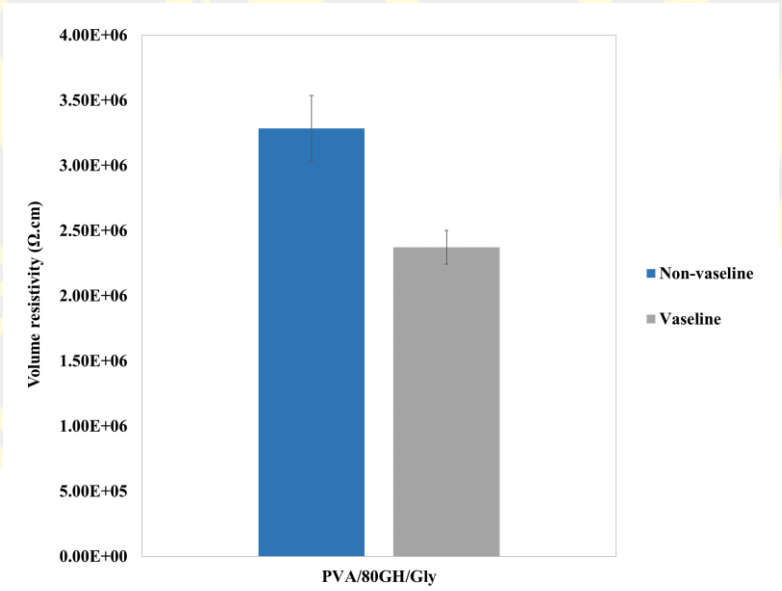

Figure 4-19 Volume resistivity of PVA/80GH/60Gly.

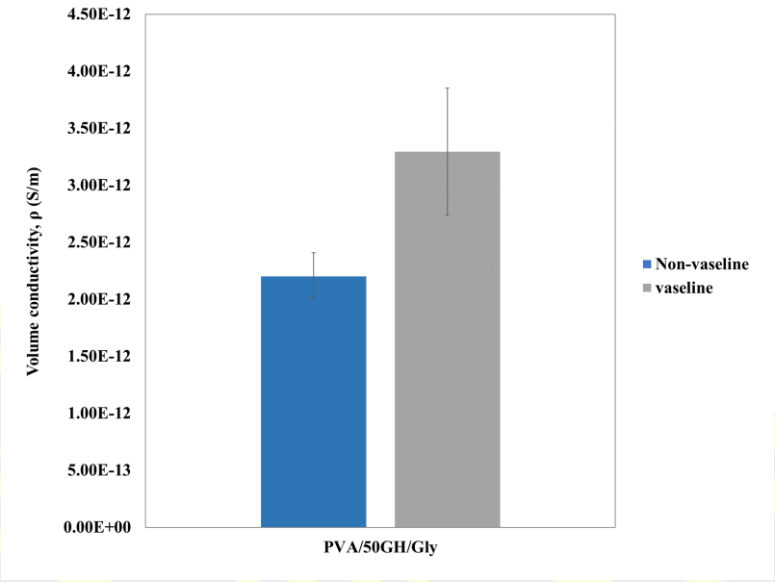

Figure 4-20 Volume conductivity of PVA/50GH/60Gly.

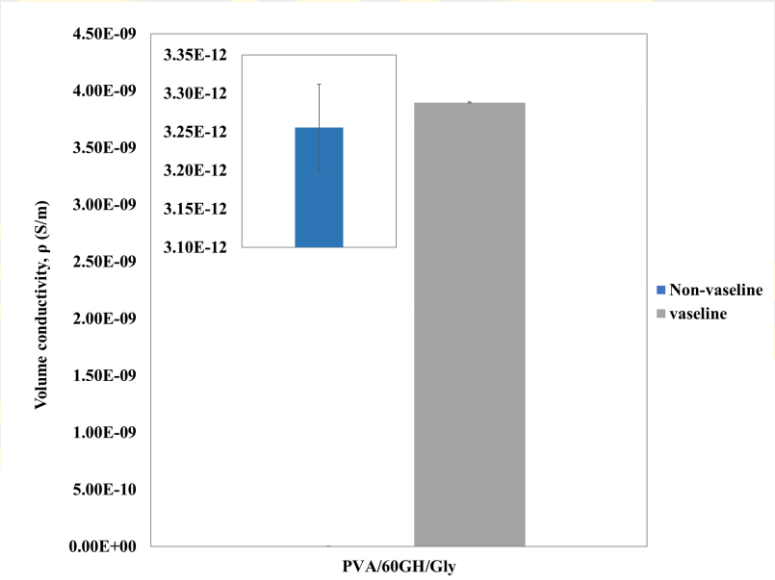

Figure 4-21 Volume conductivity of PVA/60GH/60Gly.

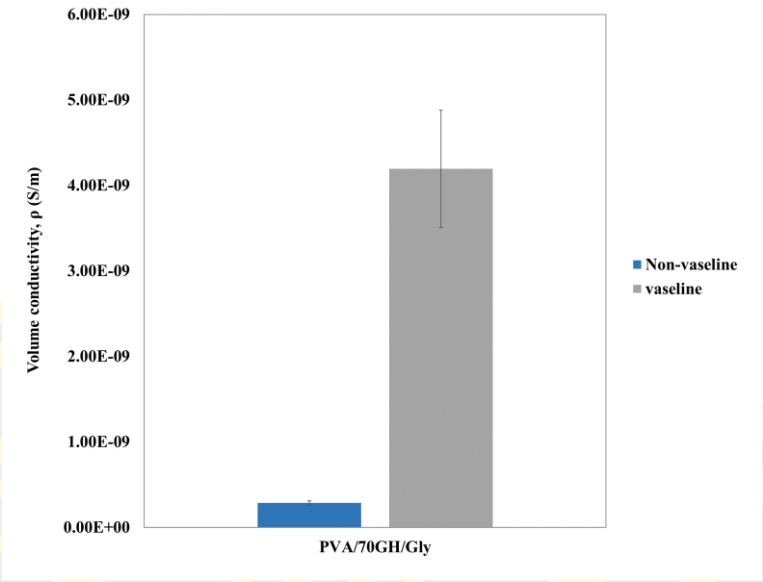

Figure 4-22 Volume conductivity of PVA/70GH/60Gly.

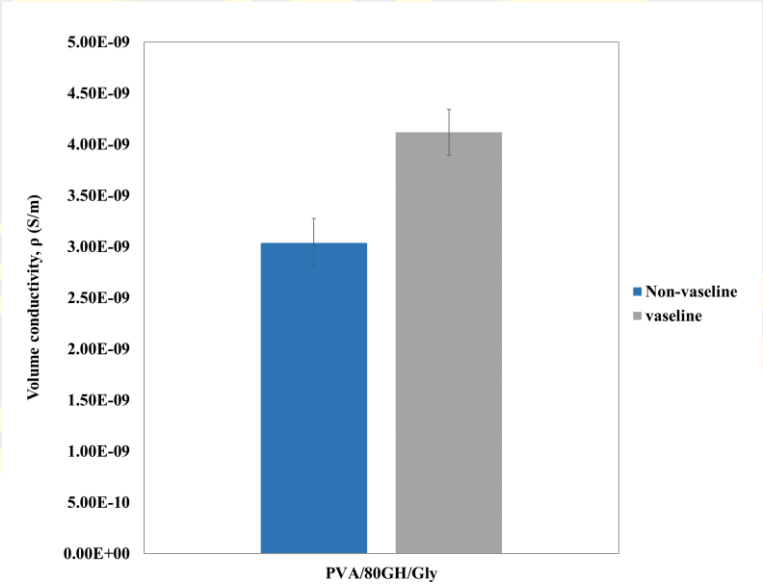

Figure 4-23 Volume conductivity of PVA/80GH/60Gly.

Effect of graphite content

From Figures 4-24 and 4-25, when the graphite content in the composite films increased from 50%wt to 80%wt, the volume resistivity of the PVA/GH/Gly composite films decreased significantly. This indicated an enhancement in the electrical conductivity of the composite films. The volume conductivity of the composite films, varying with different graphite content, also increased as the graphite content increased. This improvement in electrical conductivity of the composite films resulted from the increased number of conductive pathways within the films. The effective dispersion of graphite particles in the PVA matrix led to better connectivity between the particles, facilitating easier electron movement. The measured electrical conductivity values for the composite films containing 50, 60, 70 and 80wt% graphite are 6.43×10^{-5}, 1.04×10^{-4}, 3.39×10^{-4}, and 4.15×10^{-4} S/cm, respectively. These values corresponds with the results proposed by (F. P. Du, Tang, C. Y., Xie, X. L., Zhou, X. P., & Tan, L., 2009), that the electrical conductivity of PSA-g-MWNTs-loading with 0, 5, 10, and 20, wt% of showed the electrical conductivity values of 7.53×10^{-13}, 4.91×10^{-9}, 5.09×10^{-8}, and 1.44×10^{-4} S/cm, respectively.

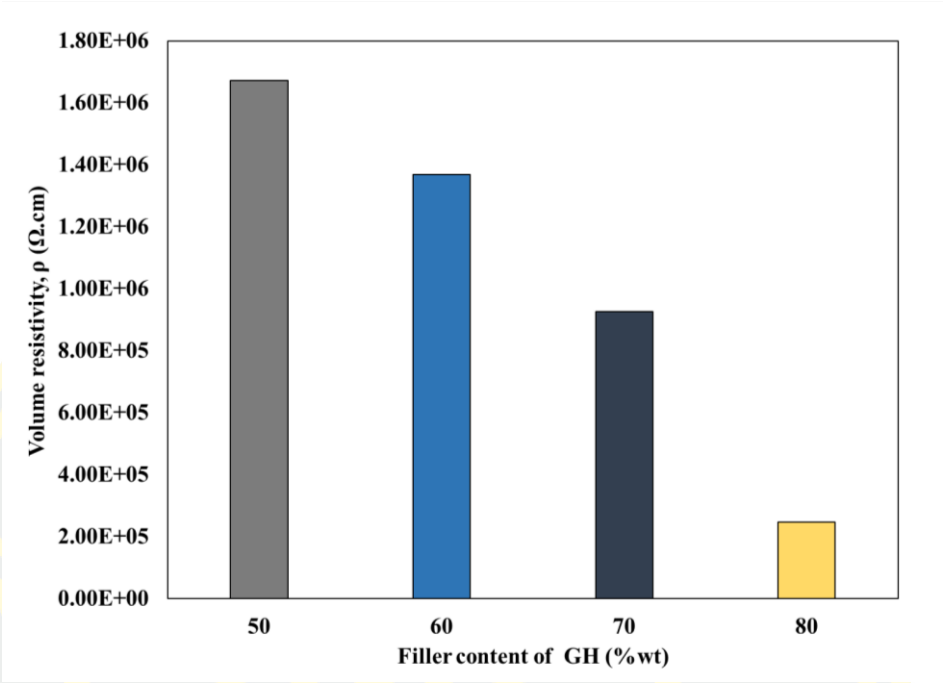

Figure 4-24 Effect of graphite (GH) content on the volume resistivity of PVA/GH/Gly composite films.

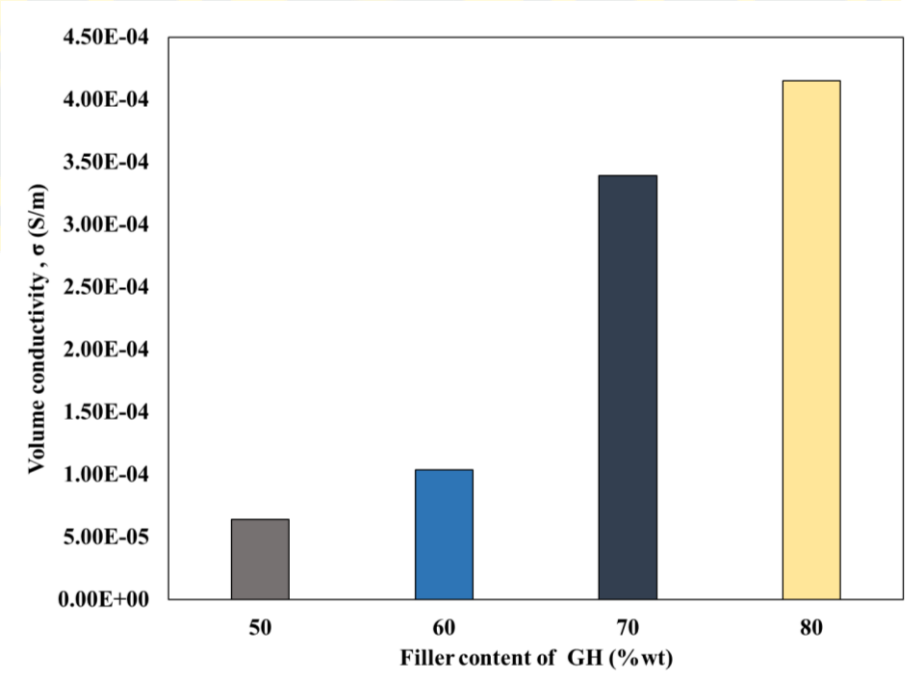

Figure 4-25 Effect of graphite (GH) content on the volume conductivity of PVA/GH/Gly composite films.

Effect of calendaring

Figure 4-26 and 4-27 display the surface resistivity and surface conductivity of the PVA/graphite composite films, both non-calendaring and calendaring, as a function of graphite content. When the concentration of graphite increased from 50 to 80%wt, the volume resistivity of the non-calendaring graphite composite film significantly increased from 2.16×10^{9} to 3.13×10^{9} Ω.cm. Besides, the corresponding volume conductivity significantly decreased from 4.63×10^{-12} to 3.20×10^{-12} S/m. This was due to the poor distribution of graphite particles in the PVA matrix, as well as voids that hindered electron movement. With calendaring, the PVA/graphite composite film with 60%wt graphite shows a volume resistivity of 1.43×10^{9} Ω.cm. The value decreased to 1.11×10^{9} Ω.cm when the graphite content increased to 80%wt. This was because the voids and gaps between graphite particles reduced. As a result, the graphite network formed, enabling electron movement. Scanning electron micrographs in Table 4.12 also confirmed the reduction of voids and gaps after calendaring. Similar finding was presented by (Leng, Li, Wang, Zhang, & Zhou, 2022) confirming that the square resistance of the coating containing 60%wt graphite reduced from 829 kΩ to 14 kΩ when the graphite content reached 100%wt. According to (Ma, Siddiqui, Marom, & Kim, 2010), rolling caused the composite particle voids to decrease and the void gaps to be reduced. The corresponding volume conductivity had also been shown in Figure 4-27. Due to the relationship between resistivity and conductivity, a material that possess high conductivity shows low resistivity, and vice versa. The electrical conductivity of the composites increased when graphite content increased. Hanif et al. revealed that the conductivity of the composite films increased by two orders of magnitude when graphite content increased from 15%wt (2.44×10^{-6} S/cm) to 30%wt (9.44×10^{-5} S/cm). Moreover, (Alo & Otunniyi, 2020) confirmed that the conductivity of PE/epoxy/graphite composites increased from 0.20 S/cm at 30%wt graphite to 4.12 S/cm at 80%wt graphite. In this present study, when calendaring had been applied, the composite containing 50%wt graphite showed the lowest electrical resistivity of 8.03×10^{8} Ω.cm and the highest conductivity of 1.24×10^{-11} S/m.

The high conductivity may be due to the well-dispersed graphite particles in the PVA matrix. By extruding, graphite particles in the composites had become denser, resulting in better electrical conductivity. Then, the calendaring method was used to process the composite film. According to (Ma et al., 2010), calendaring not only decreased number of voids between particles, but also reduced the void gaps. In summary calendaring offers a two-fold benefit for enhancing the performance of the composite film. Firstly, it likely brings the conductive layer and Kapton tape closer together, promoting strong adhesion between the two layers. This improved interface could translate to a higher bending angle, allowing the device to withstand greater mechanical strain. Secondly, calendaring might also reduce porosity within the PVA/graphite composite. By minimizing these pores, the material becomes less susceptible to electrical leakage, potentially enabling efficient current flow within the device.

In Figures 4-26 – 4-27, the electrical properties of the calendared actuator were investigated to understand the impact of the calendaring process. Figure 4-26 shows the electrical resistivity of the unrolled actuator. Surprisingly, the composites with GH content of 50, 60, 70, and 80 wt% showed the electrical conductivity of 2.160×10^{9}, 2.495×10^{9}, 2.852×10^{9}, and 3.130×10^{9} Ω·cm. (Figure 4-27) Notably, the calendared actuator exhibited significantly lower resistivity values, ranging from 8.03×10^{8} to 1.43×10^{9} Ω·cm. Besides, unrolled actuator displayed electrical conductivity values of 1.24×10^{-11}, 6.99×10^{-12}, 8.16×10^{-12}, and 9.01×10^{-12} S/m. After calendaring, these values increased to 4.63×10^{-12}, 4.01×10^{-12}, 3.51×10^{-12}, and 3.20×10^{-12} S/m, respectively. This enhancement in conductivity can be attributed to the calendaring process bringing the graphite particles and the free space within the matrix closer together. This improved proximity likely facilitates the transfer of electrical conductivity between the internal conductive particles.

In the percolation threshold model, low graphite content results in dispersed particles within the insulating polymer, leading to minimal interparticle contact and consequently reduced conductivity. As the graphite content increases, a continuous conductive network is formed, enhancing conductivity (Phuchaduek, Jamnongkan, Rattanasak, Boonsang, & Kaewpirom, 2015). However, excessive graphite content

can lead to particle agglomeration, creating gaps that impede the efficiency of the conductive network.

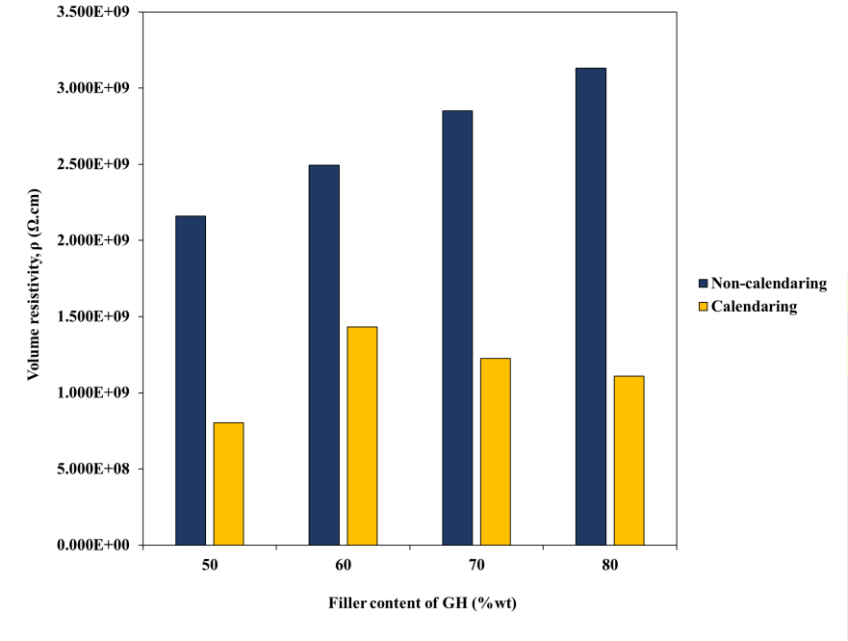

Figure 4-26 Volume resistivity of non-calendared and calendared PVA/GH/Gly composite films.

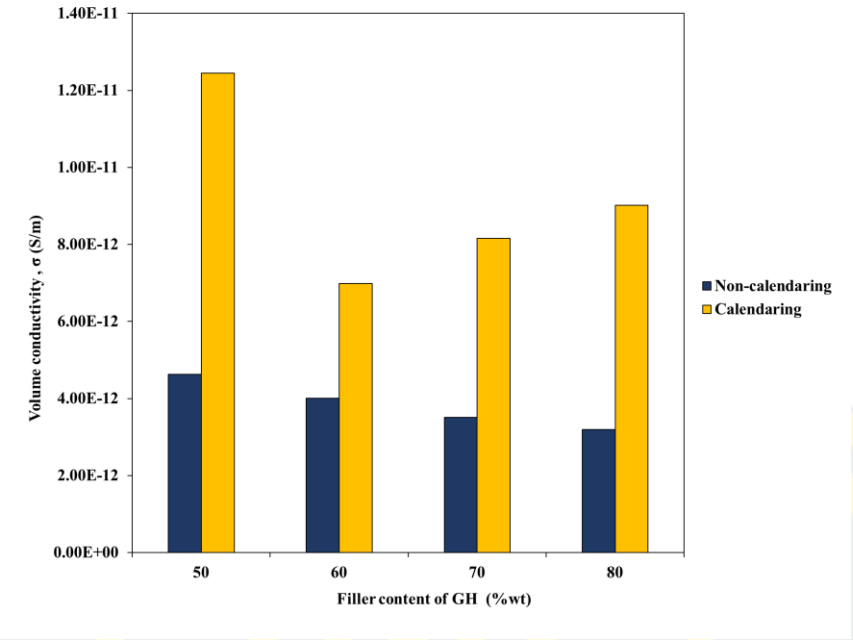

Figure 4-27 Volume conductivity of non-calendared and calendared PVA/GH/Gly composite films.

4.1.5.2 PVA/GO/Gly system

From Figures 4-28 and 4-29, the test results had shown that the PVA/GO/Gly actuators with different graphite oxide contents of 8, 10, 15, and 20%wt exhibited a significant decrease in electrical resistivity as the graphite oxide content increased. The values are 3.77×10^{8}, 3.47×10^{8}, 2.56×10^{8}, and 1.66×10^{8} Ω.cm. Correspondingly, the electrical conductivity values are 2.66×10^{-7}, 3.62×10^{-7}, 3.97×10^{-7}, and 6.04×10^{-7} S/m, The similar results was reported by (Suma & Sangappa, 2024) who prepared composite films by mixing PVA with GO at different concentrations of 0.1, 0.2, 0.3, 0.4, and 0.5%wt. They found that the electrical conductivity of the composites were in the range 3.0×10^{-5} to 2.5×10^{-4} S/cm. However, these values were lower than that proposed by (Song, Zhang, Lin, & Chen, 2013), The reported electrical resistivity values of the composites containing graphite oxide at concentrations of 0.2, 0.4, 0.6, 0.8, and 1%wt were in the range of 3.00×10^{17} to 9.00×10^{17} Ω.cm. This discrepancy might be due to the large particle size of the synthesized graphite oxide, which, when used to prepare the composite film, resulted in poor dispersion, leading to inadequate

film coverage or particle clumping, and thus insufficient electrical conductivity during testing.

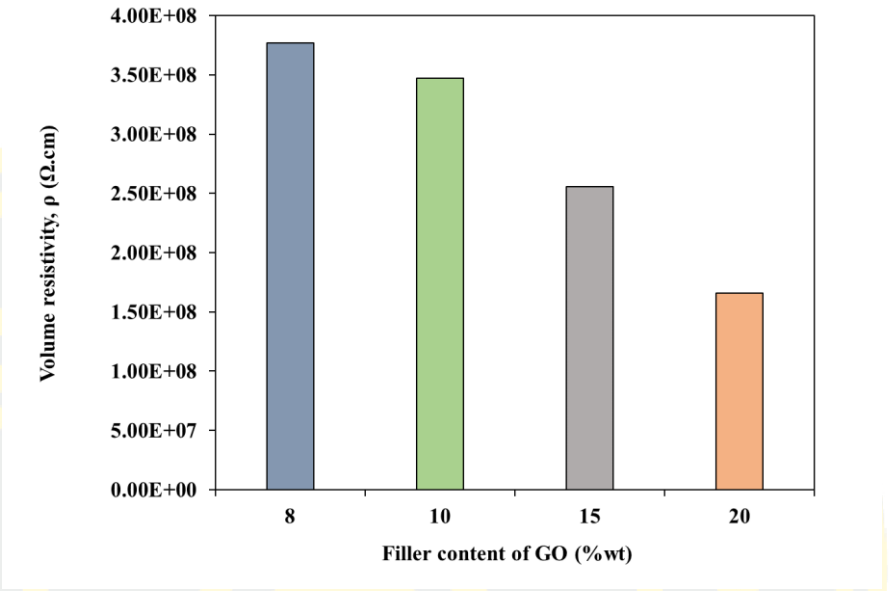

Figure 4-28 Volume resistivity of PVA/GO/Gly composite films varied with the content of GO.

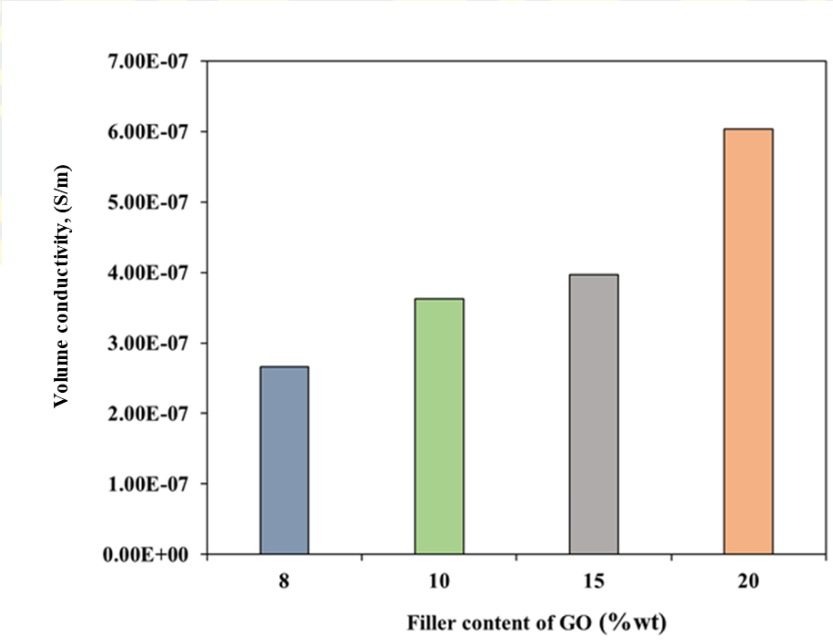

Figure 4-29 Volume conductivity of PVA/GO/Gly composite films varied with the content of GO.

4.1.5.3 PVA/rGO/Gly system

Electrical volume resistivity and conductivity of PVA/rGO/Gly actuators containing different amounts of reduced graphite oxide of 8, 10, 15, and 20%wt are shown in Figure 4-30 and 4-31, respectively. The electrical resistivity decreased significantly with the increase in graphite oxide content. The composites containing 8, 10, 15, and 20 %wt of graphite oxide showed the volume resistivity of 2.60×10^{8}, 3.36×10^{8}, 2.27×10^{8}, and 7.03×10^{8} Ω.cm. and, the electrical conductivity of 3.86×10^{-7}, 3.06×10^{-7}, 6.34×10^{-7}, and 1.47×10^{-7} S/m. This suggested that an appropriate amount of rGO (15%) helped to form an efficient percolation network, resulting in the highest electrical conductivity. However, at concentrations of 8, 10, and 20%wt, the electrical resistivity increased with the amount of reduced graphite oxide. This is inversely proportional to the electrical conductivity. At 20%wt, the excess rGO might have caused the conductive layer to become too thick, interfering with the flow of electric charges and thereby reducing the conductivity compared to the 15%wt concentration.

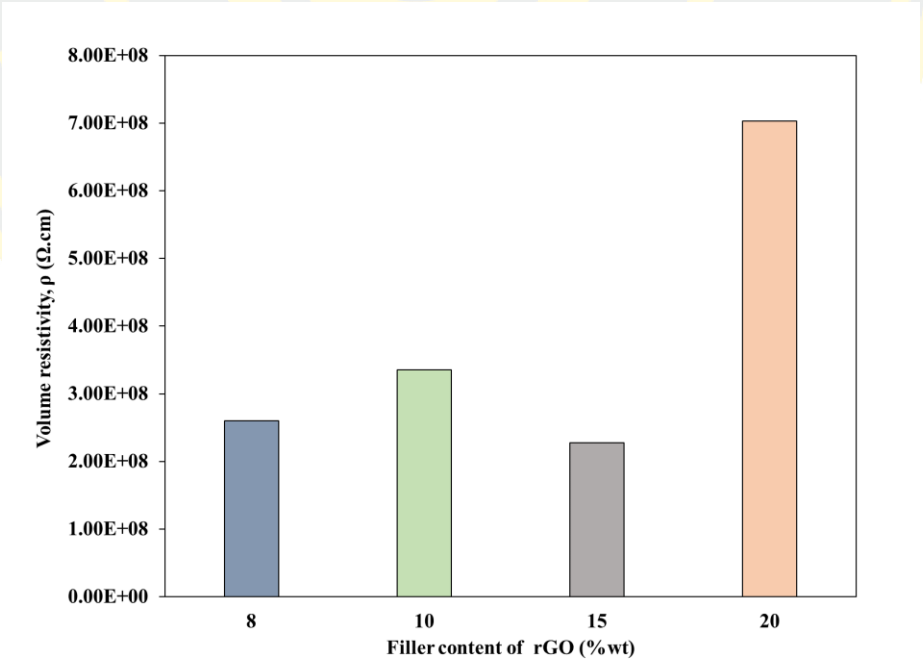

Figure 4-30 Volume resistivity of PVA/rGO/Gly composite films varied with the content of rGO.

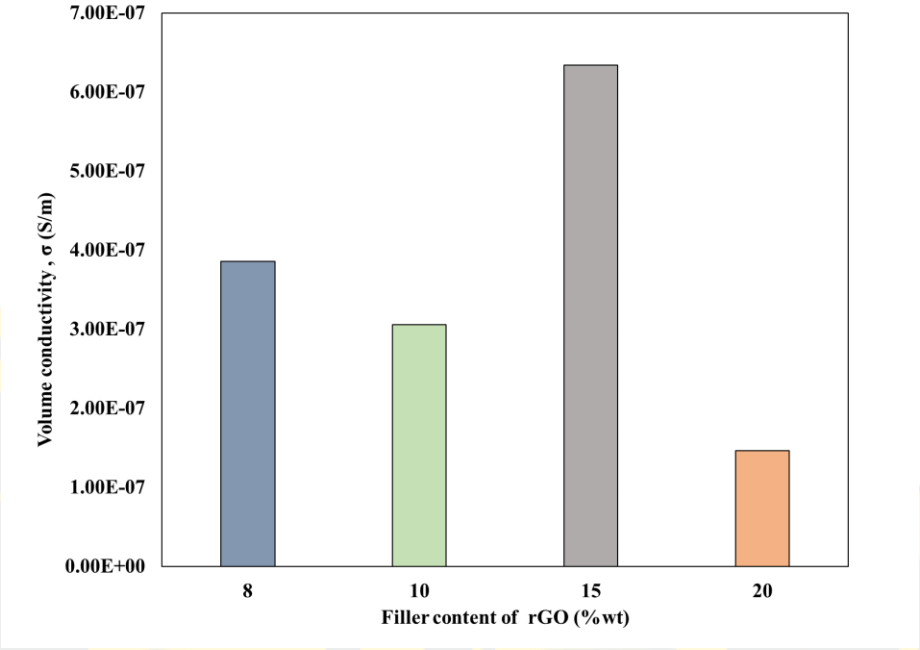

Figure 4-31 Volume conductivity of PVA/rGO/Gly composite films varied with the content of rGO.

Therefore, the PVA/GH/Gly system has been chosen for further study, due to its highest electrical conductivity and promising trend with increasing graphite content. This system was subsequently experimented on for its mechanical properties, especially its, flexibility, and other related characteristics.

4.1.6 Tensile Test

To our knowledge, electroactive actuators (ETAs) demonstrate the ability to deform while remaining functional, ensuring safety for human interaction. Their flexibility and adaptability enable innovative robotic movements and the development of nuanced structures. ETAs are energy-efficient, highly flexible, lightweight, and easy to fabricate (Xu, Faul, Taghavi, & Rossiter, 2023). They exhibit favorable performance due to good mechanical strength and low Young's modulus, as reported by (Xing et al., 2014) and (Ozdemir et al., 2015). Notable advantages include high actuation strains, wide frequency bandwidths, rapid response, low weight, easy

miniaturization, and flexibility (Tan, Wang, Gao, Huang, & Lee, 2024). Studying the tensile strength and flexibility of electrically conductive films is essential, ensuring durability, efficiency, safety, and material development, thereby leading to reliable and versatile actuators. From the analysis of various composite systems, it was found in our study that PVA/GH exhibited the highest electrical conductivity. Therefore, this composite was selected for testing its mechanical properties. By considering maximum stress values, Young's modulus, and the percentage of elongation at break, the mechanical performance of the composite films were assessed, as shown in Figures 4-28 to 4-30.

In Figure 4-32, it was observed that the elongation at break of the composite films with varying graphite filler content showed significant difference at $p<0.05$. Graphite, characterized by its atoms bound by strong covalent bonds in an orderly isometric structure, forms a rigid mineral (J. Keeling, 2017). The increased graphite content introduced greater heterogeneity within the PVA matrix, as reflected in the morphology observed using SEM techniques (Table 4.11). Higher graphite concentrations resulted in increased roughness and brittleness, inversely affecting the composite's strength. This finding was consistent with the results revealed by (Hanif, 2019). In their study Hydroxyethyl cellulose (HEC) composite films with graphite contents ranging from 0 to 35 wt% were developed. They found that the films' flexibility decreased with increased graphite content due to graphite's high stiffness and aspect ratio compared to the HEC matrix. Conversely, the modulus of elasticity increased with increased graphite content. The tensile strength consistently decreased at a 35 wt% graphite concentration, likely due to insufficient interaction between graphite particles and the matrix molecules.

Figure 4-33 depicts the Young's Modulus of graphite ranging from 4.1 to 27.6 GPa (J.Boylan, 1996), indicating its high stiffness. Incorporating high amounts of graphite into the composite films had increased the rigidity of the films. This was in line with the findings of (Ramesh, 2009), who observed that the Young's modulus of cast aluminium alloy 6061 (AL6061) /graphite particulate composites increased by approximately 9% as graphite content rose from 0% to 4%. This increase was accompanied by improvements in ductility, ultimate tensile strength (UTS), and

compressive strength, likely due to graphite particles acting as barriers to dislocations. The tensile strength of the composites was also showed the similar trend as elongation. (Figure 4-34) This reduction is likely resulted from clustering phenomena observed in the SEM images (Table 4.11). Graphite can be able to intercalate between the PVA polymer chains, disrupting the intermolecular forces that had held the polymer matrix together. This disruption had weakened the overall mechanical strength of the composite, making it more susceptible to breakage under stress. At higher graphite contents (80%), the graphite particles began to agglomerate, forming larger, less evenly distributed structures, which had further compromised the composite's mechanical integrity.

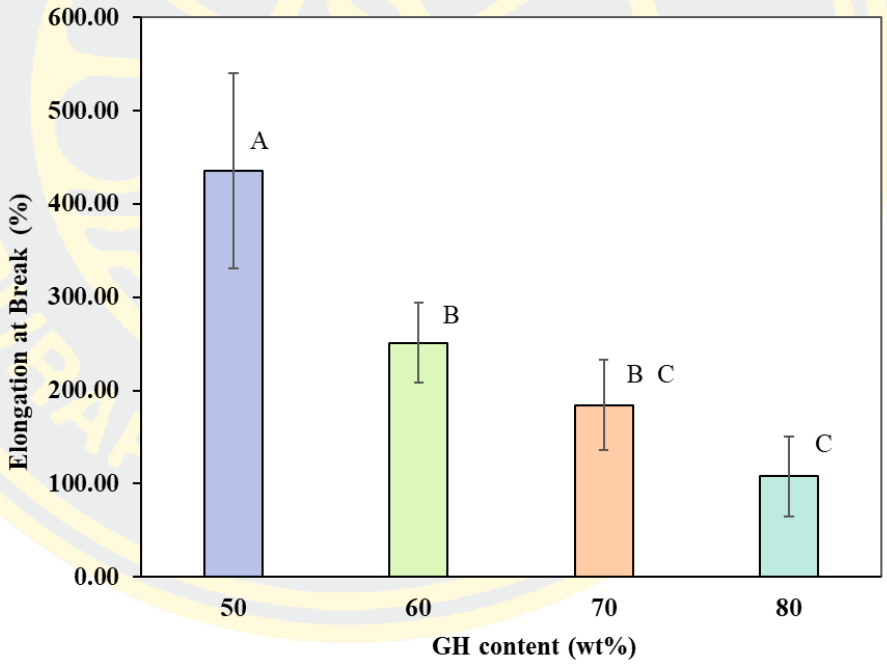

Figure 4-32 Elongation at break of PVA/GH/Gly composites as a function of GH content (Data tested by ANOVA single factor statistical significance: $p < 0.05$, F cal = 4.1141 and F crit = 2.8164 which F cal > F crit means a significant difference).

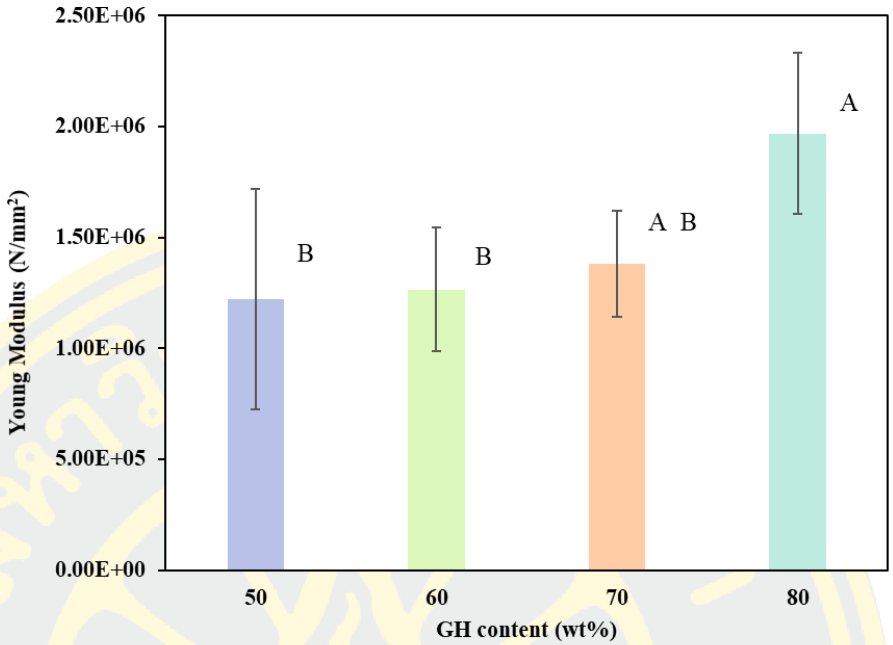

Figure 4-33 Young Modulus of PVA/GH/Gly composites as a function of GH content (Data tested by ANOVA single factor statistical significance: $p < 0.05$, F cal = 4.1141 and F crit = 2.8164 which F cal > F crit means a significant difference).

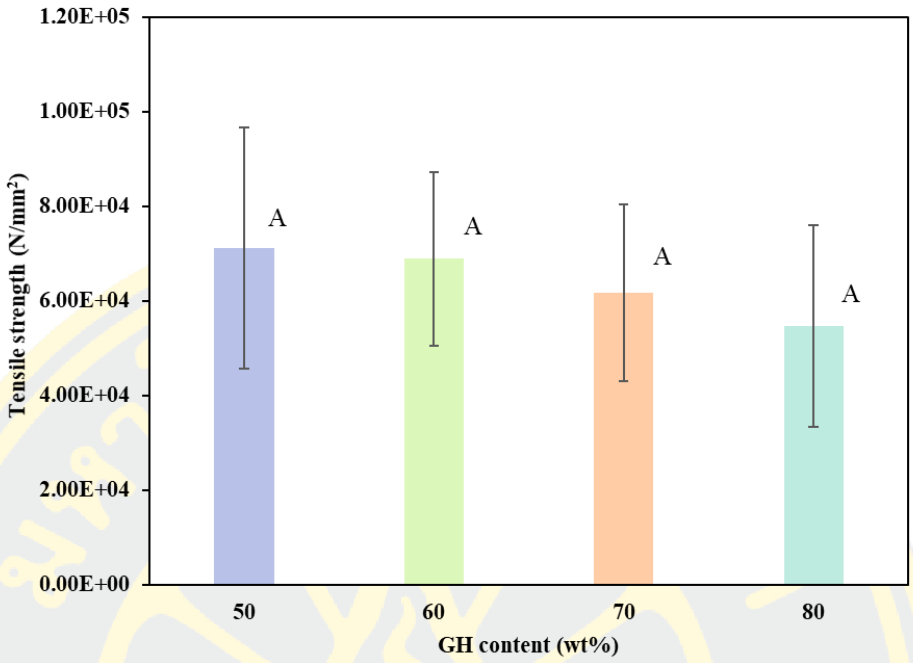

Figure 4-34 Tensile strength of PVA/GH/Gly composites as a function of GH content (Data tested by ANOVA single factor statistical significance: $p < 0.05$, F cal = 3.026 and F crit = 2.8164 which F cal > F crit means a significant difference).

The surface morphology of the conductive composite film samples is illustrated in Tables 4-11. The increase in filler content within the composite films led to particle agglomeration, resulting in rough and uneven films. This morphology is associated with the electrical conductivity of the films; higher filler content improves conductivity due to the enhanced connectivity between particles. From Table 4-12, it was observed that the surface and cross-sectional morphology of calendared conductive films, as compared to non-calendared conductive films, exhibited wrinkles and improved packing density. This enhanced packing led to better particle contact and distribution, thereby resulting in improved electrical conductivity. The morphological changes observed in the calendared films indicated a more uniform structure, which contributed to the increased efficiency in electrical performance.

Table 4-11 The surface morphology of the composite films processed by non-calendaring was analyzed at magnifications of 100x and 2000x.

Sample	Magnification	
	100x	2000x
PVA/50GH/60Gly	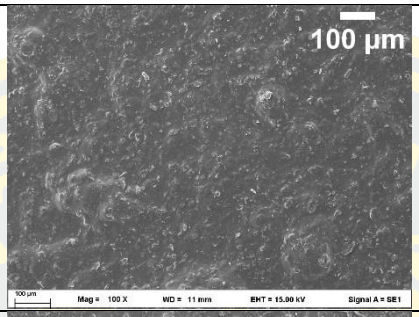	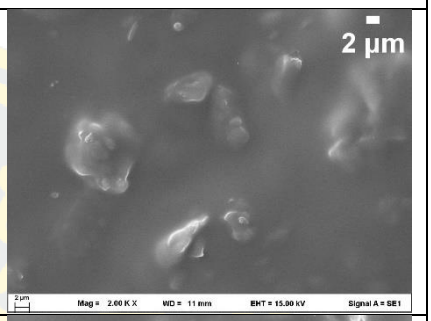
PVA/60GH/60Gly	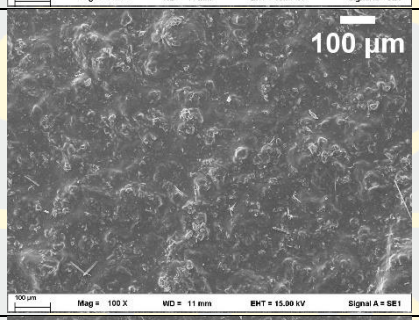	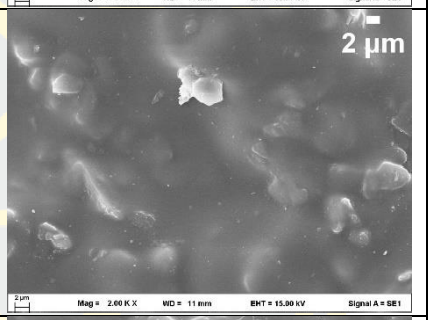
PVA/70GH/60Gly	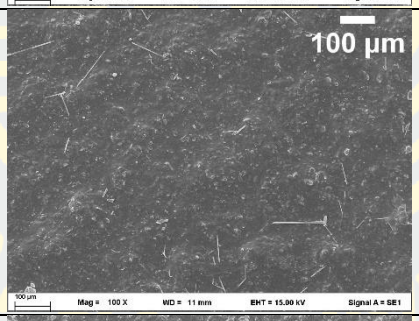	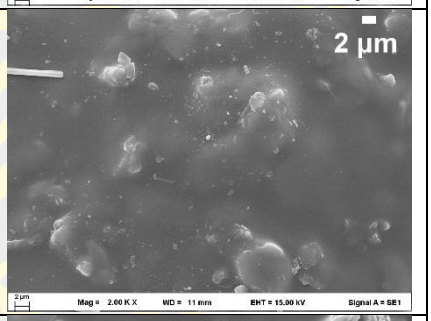
PVA/80GH/60Gly	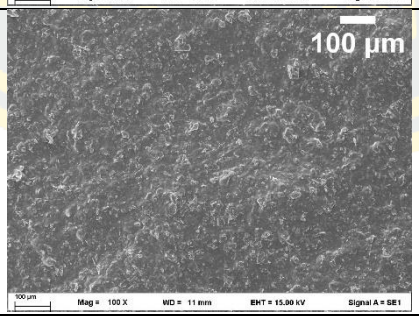	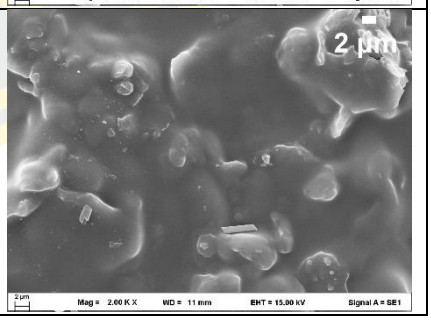

Table 4-12 The surface and cross-section morphology of the composite films processed by calendaring was analyzed at magnifications of 100x, 1000x, and 2000x.

Sample	Surface		Cross-section
	100x	2000x	1000x
PVA/50GH/60Gly	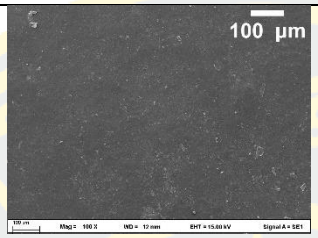	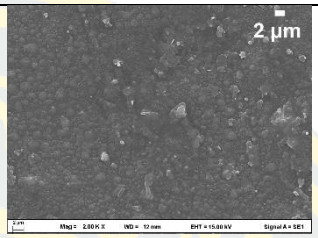	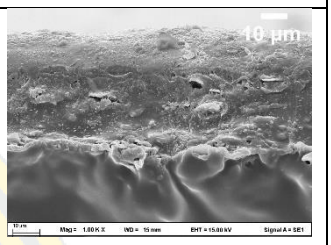
PVA/60GH/60Gly	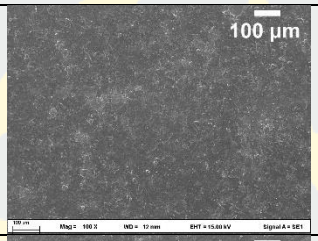	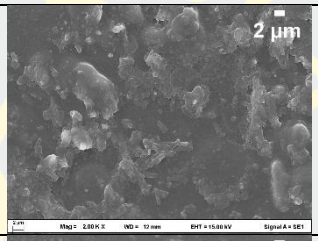	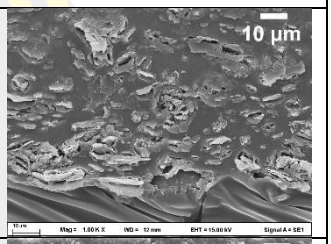
PVA/70GH/60Gly	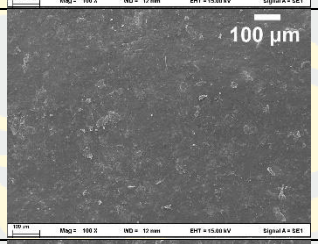	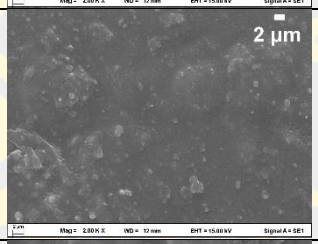	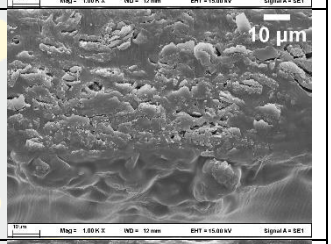
PVA/80GH/60Gly	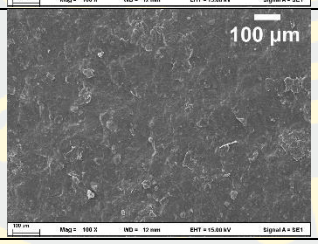	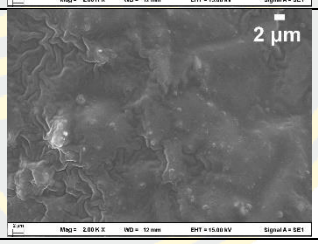	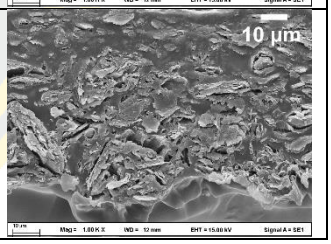

4.1.7 Bending angle

The electroactive actuator had comprised three layers: a polymer layer (Kapton tape), an adhesive layer, and a conductive layer (graphite composite film), as shown in Figure 4-35. The polymer, designed in a U-shape, provides both flexibility and insulation, while the adhesive layer securely bonds the layers together. The conductive layer enables the actuator to bend or deform in response to electrical stimuli, making it ideal for applications in soft robotics and flexible sensors. The prepared actuators were subjected to thickness measurement, as illustrated in Figure 4-36, utilizing SEM techniques for both non-calendaring and calendaring

processes. In Table 4.13, the cross-sectional images revealed that the overall thickness of the actuator reduced following the calendaring process.

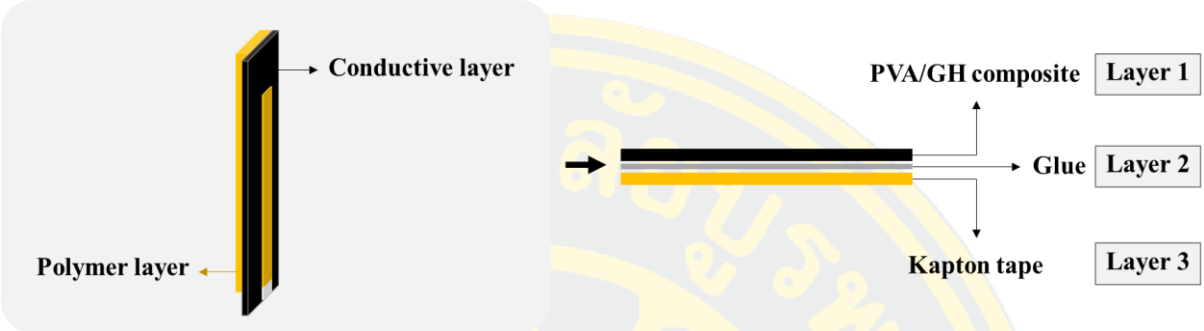

Figure 4-35 Diagram of the actuator layers: layer 1 (Kapton tape), layer 2 (glue), layer 3 (PVA/GH composite).

When actuators with graphite concentrations ranging from 50% to 80% by weight had been processed through calendaring, variations in the thickness of each layer were observed, as illustrated in Figure 4-36. Figure 4-36 (a) shows that the thickness of the polymer tape layer decreased across all formulations after calendaring. Figure 4-36 (b) indicates that the adhesive layer increased in thickness following calendaring. In contrast, Figure 4-36 (c) demonstrates that the thickness of the graphite composite layer had generally decreased with graphite content (50%, 70%, and 80% by weight), except for the 60%wt concentration, which showed increased thickness. These thickness variations was attributed to the behavior of the material under compression. Higher graphite concentrations tended to compress more, leading to a reduction in thickness, Additionally, the distribution of graphite particles played a significant role in how the material responded to pressure, thereby affecting the final thickness.

Table 4-13 The thickness of the actuator layers calendaring and non-calendaring at a magnification of 250x.

Sample	Non-Calendaring	Calendaring
PVA/50GH/60Gly	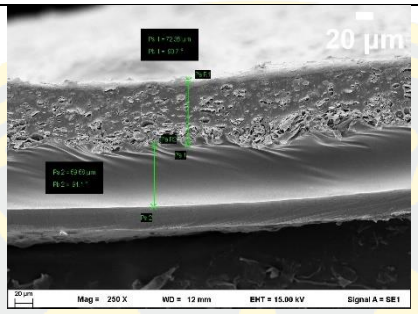	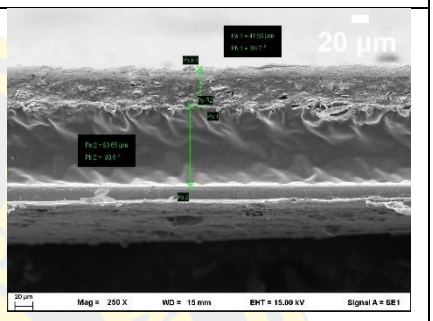
PVA/60GH/60Gly	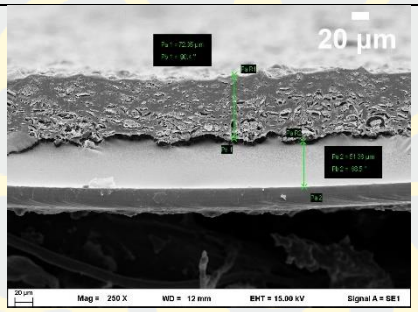	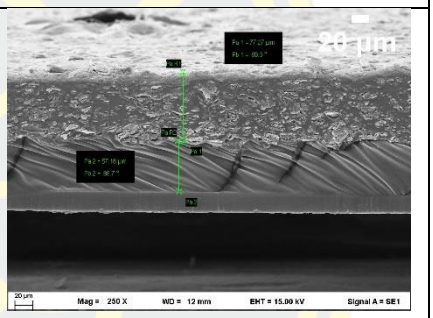
PVA/70GH/60Gly	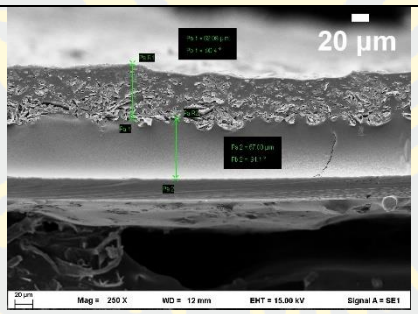	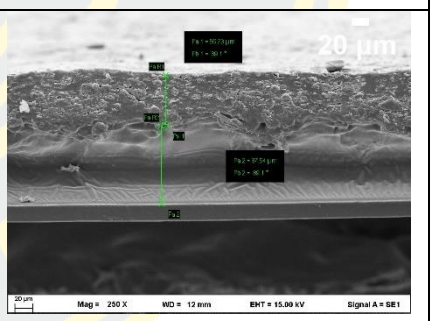
PVA/80GH/60Gly	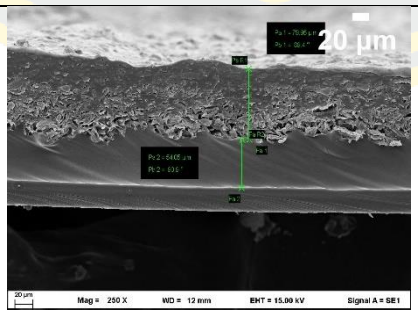	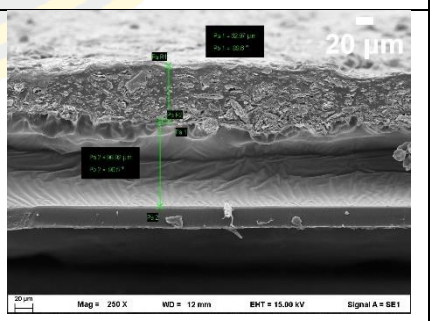

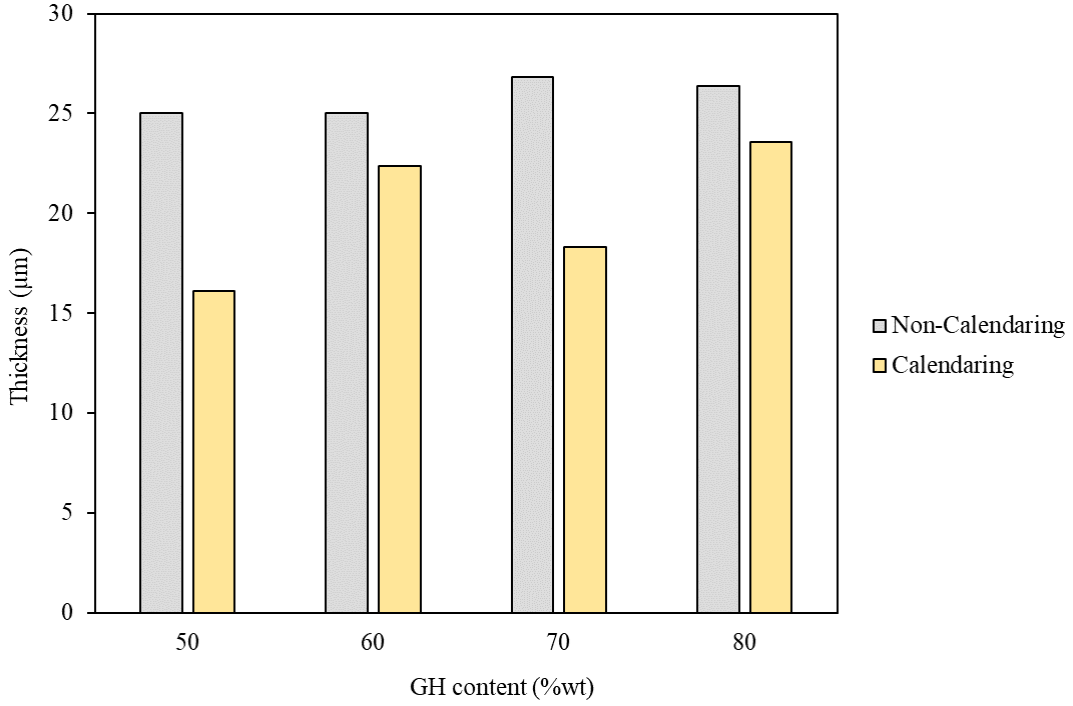
30
25
20
15
10
5
0
Thickness (µm)
50
60
70
80
GH content (%wt)
Non-Calendaring
Calendaring

(a)

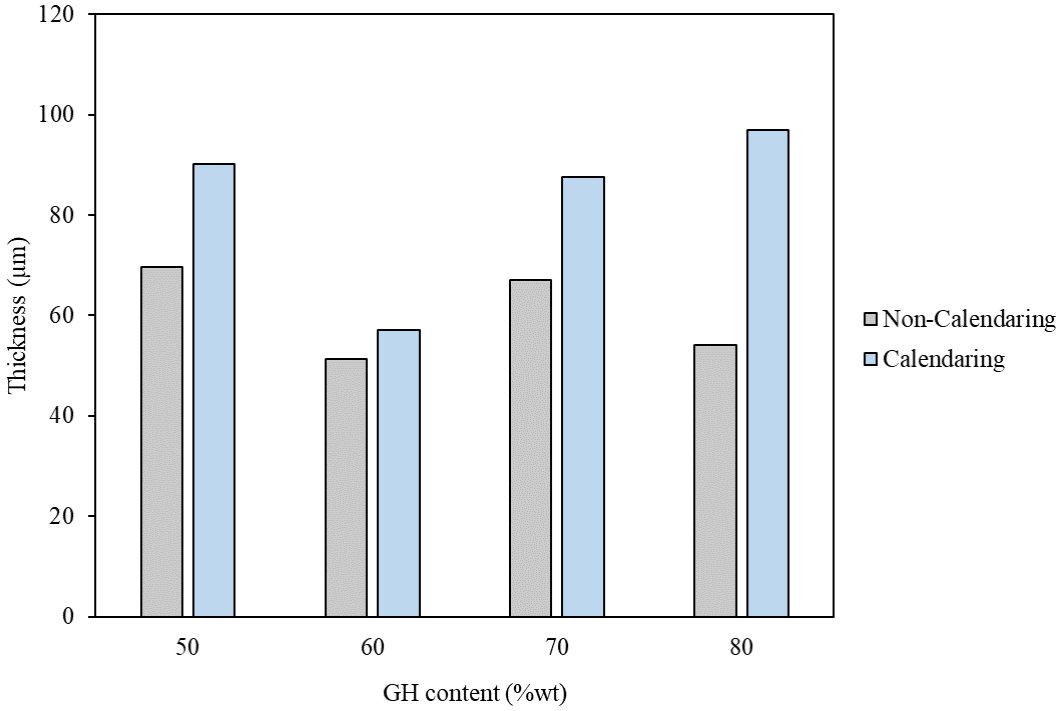
120
100
80
60
40
20
0
Thickness (µm)
50
60
70
80
GH content (%wt)
Non-Calendaring
Calendaring

(b)

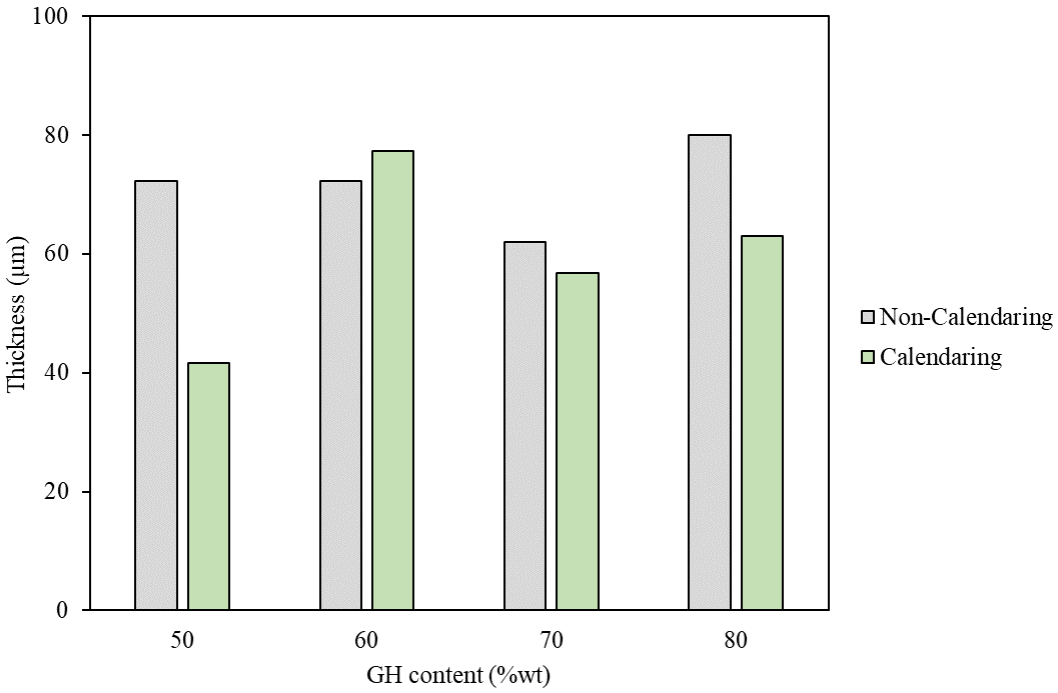

(c)

Figure 4-36 Thickness of (a) layers 1 (Kapton tape), (b) layers 2 (glue), and (c) layers 3 (graphite film) for graphite content of 50%, 60%, 70%, and 80% wt.

Bending ability of the model actuator was tested and the data are shown in Figure 4-33. As shown in Figure 4-37, when a voltage of 6 volts was applied to the actuator from 0 seconds to 240 seconds, the actuator bended. The extent and direction of the bending depended on the duration and consistency of the applied voltage, thereby demonstrating the actuator's ability to convert electrical energy into mechanical motion.

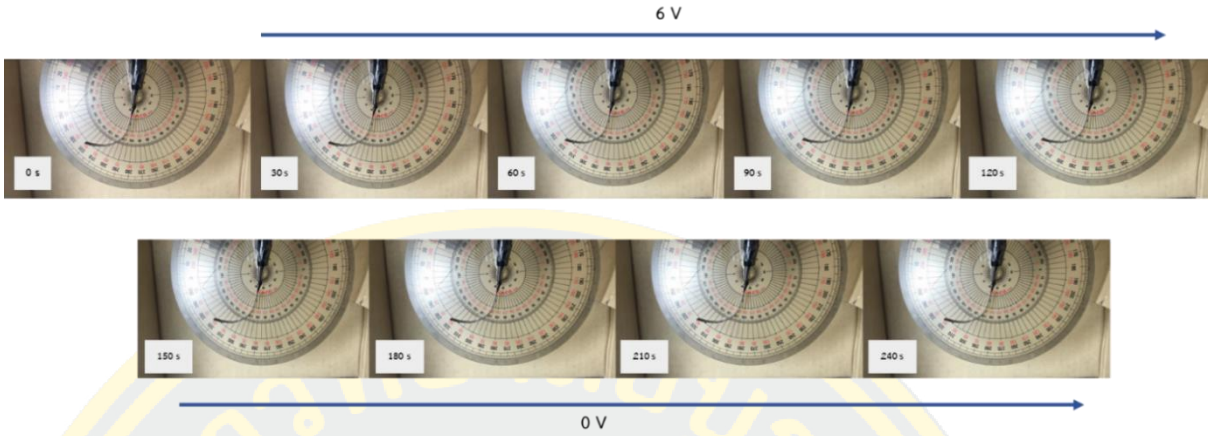

Figure 4-37 Apply a potential of 6 V to the sample and remove a potential of 0 V. https://drive.google.com/drive/folders/1NufJzU38v49wdg_dTc_RR3mz4aBtugLD

Figure 4-38 illustrates the relationship between thickness and bending angle of the model ETA under a low voltage of 6 V. With graphite contents of 50%, 60%, 70%, and 80%wt, the non-calendaring systems exhibited bending angles of 14.30º, 15.40º, 11.70º, and 14.00º, respectively. Besides, the calendaring systems showed bending angles of 22.30º, 18.60º, 15.30º, and 15.00º, respectively. The actuator with 50%wt graphite exhibited the greatest bending angle of 22.30º after calendaring, corresponding to the thinnest thickness of 147.87 µm. This was due to calendaring likely narrowed the gap between the conductive layer and Kapton tape, allowing the two layers to bond more tightly, resulting in a higher bending angle. Additionally, calendaring led to a reduction in porosity within the PVA/graphite composite, thereby decreasing the number of pores and improving electrical conductivity (Ma et al., 2010).

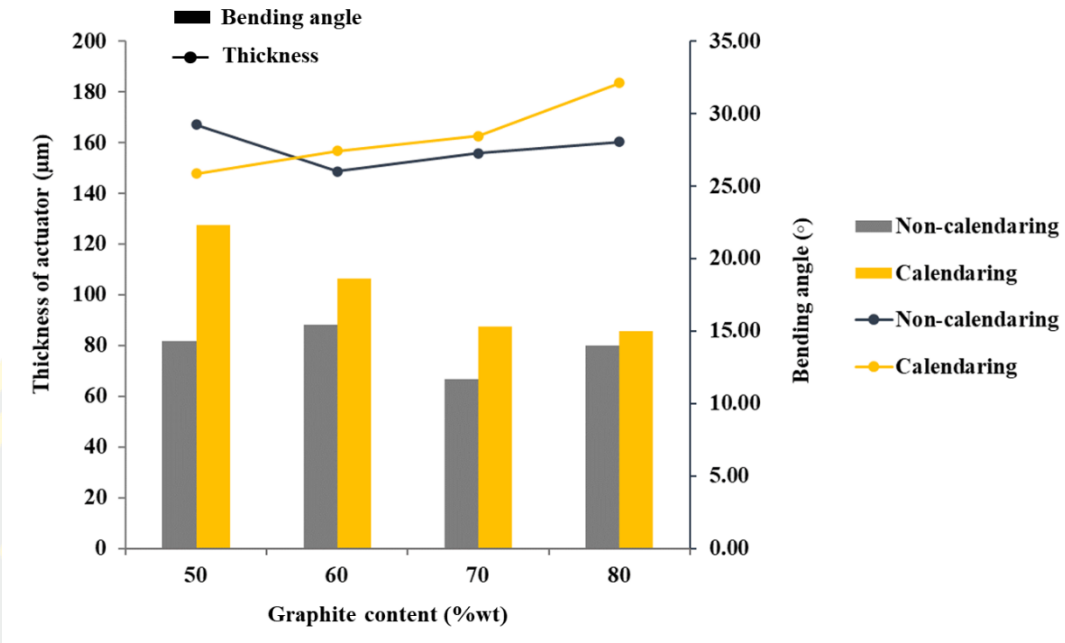

Figure 4-38 Thickness and bending angle for non-calendaring and calendaring actuators at 6 V.

This reduction might be attributed to the increased weight of the graphite, which made the material heavier and more difficult to bend or move. Although the electrical conductivity increased with the increased graphite concentration, the impact of the increased weight outweighed the benefits of improved conductivity, resulting in a reduced bending angle instead of an increase.

The study of the temperature characteristics of actuators in this context is based on the principle of applying an electric current to the actuator. When the current passes through the conductive layer, it generates heat due to the conversion of electrical potential energy into thermal energy. This heat causes the polymer layer within the actuator to expand, leading to the bending or flexing of the actuator. Therefore, measuring the temperature that occurs after applying the electrical potential is crucial for analyzing the actuator's performance, as a higher temperature directly influences the polymer's expansion and the resulting bending angle of the actuator.

In this study, the bending angle obtained from the experiment was very small, which is due to the low temperature generated during the bending process. In other words, the temperature within the actuator during operation did not high enough to cause any significant expansion of the polymer, resulting in a small bending angle. According to (Aouraghe et al., 2021), actuators made from CNTF/PDMS (Carbon Nanotube Film/Polydimethylsiloxane) composite and PI (Polyimide) tape were able to reach temperatures as high as 351°C. Such a high temperature led to significant expansion of the polymer, resulting in a more pronounced bending angle. The small bending angle observed in the current study suggested that the heat conduction within the conductive layer might be insufficient or the conversion of electrical energy into heat might not be occurring as efficiently as it should.

4.1.8 Blocking force

The blocking force, defined as the equivalent force required to keep the actuator tip in a fixed position, was measured in both axial and vertical configurations (Fan et al., 2020); (Amjadi & Sitti, 2016). The blocking force could not be measured directly; therefore, an electronic balance was utilized for indirect measurement. During this process, both ends of the graphite composite film in the actuator were connected to a DC power supply. The electric current induced displacement or bending in the film, which caused the bent section to exert pressure on the weighing

platform of the electronic balance. In Figure 4-39, the model actuator was subjected to an electric potential of 6 V and tested for a total duration of 4 minutes. During the initial 2 minutes (120 seconds), the electric potential was applied continuously, and the subsequent 2 minutes involved turning off the electric potential source. The maximum value recorded on the electronic scale during the 2 minutes of electric potential application was converted to blocking force, as illustrated in Figures 4-40 to 4-43. The blocking force of the actuators processed by rolling, with graphite concentrations of 50%, 60%, 70%, and 80% by weight, was analyzed. For the actuator with 50% by weight graphite, the blocking force increased over time, reaching a maximum of 0.101 mN at 120 seconds. After turning off the electric potential, the blocking force initially decreased rapidly but then gradually increased, even without applied voltage. This behavior aligned with findings from (Tian et al., 2021) who indicated that the lower coefficient of thermal expansion (CTE) conductive layer generates Joule heating when voltage is applied, warming the entire electroactive actuator (ETA). Materials with higher CTE expand more, causing bending in the lower CTE layer, resulting in curvature and angular displacement. Upon removal of the electric potential, the cessation of Joule heating halts further bending. For the actuators with 60%, 70%, and 80% by weight graphite, similar testing conditions revealed that the blocking force behavior varied. At 60% by weight graphite, the blocking force slightly decreased at 120 seconds and continued to decline over time. Conversely, for 70% and 80% by weight graphite, the blocking force increased with time, even after the electric potential was removed, continuing to rise until 240 seconds. This increase may be attributed to residual stresses in the actuators due to the rigidity of graphite. Further investigation is necessary to confirm this hypothesis.

Additionally, the actuator may have retained electric charges due to the properties of the PVA and graphite mixture. Although PVA does not inherently possess thermal storage properties, it can exhibit charge storage behavior (Liew, Ramesh, & Arof, 2014). The temporary increase in blocking force after the electric potential was turned off could be due to the release of these stored charges. Furthermore, graphite's significant heat storage capacity and improved thermal

conductivity (Z. Zhang & Fang, 2006) might contribute to increased blocking force due to thermal expansion effects, as heat generated during the application of electric potential remains in the system even after the potential is removed.

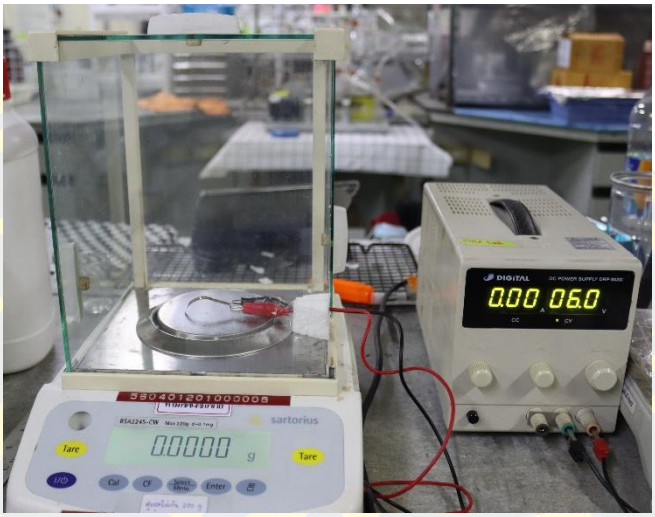

Figure 4-39 Blocking force setup.

(https://drive.google.com/drive/folders/159EehMdcaAI6xCll6zxXfBlLPDz9AmxO)

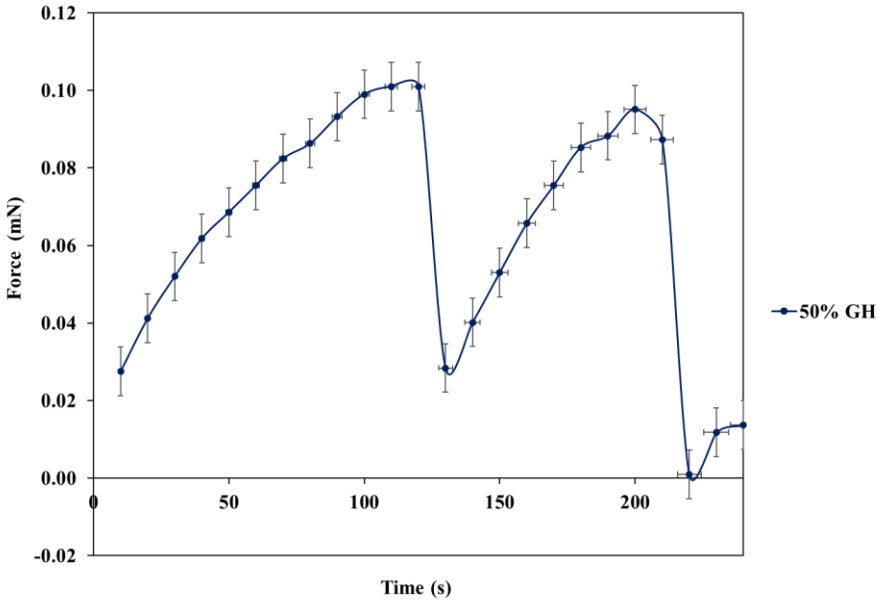

Figure 4-40 Blocking force of the calendaring actuator when power is on (2 min) and off (2 min) at 6 V of PVA/50GH/60Gly.

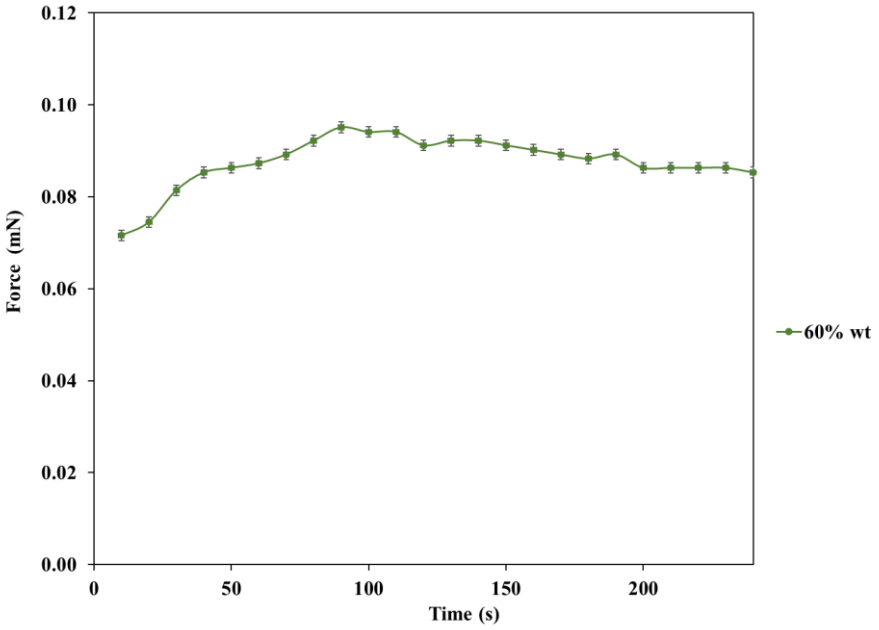

Figure 4-41 Blocking force of the calendaring actuator when power is on (2 min) and off (2 min) at 6 V of PVA/60GH/60Gly.

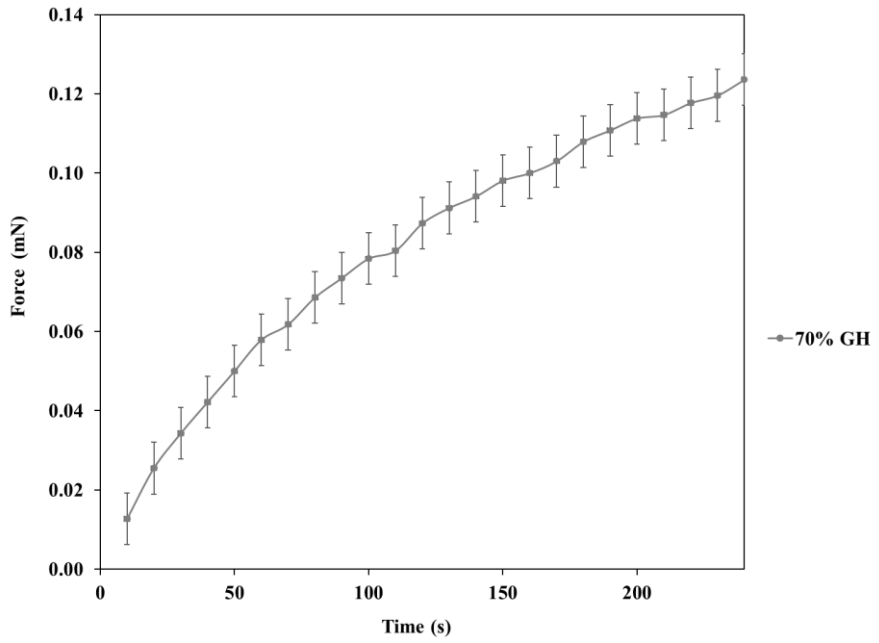

Figure 4-42 Blocking force of the calendaring actuator when power is on (2 min) and off (2 min) at 6 V of PVA/70GH/60Gly.

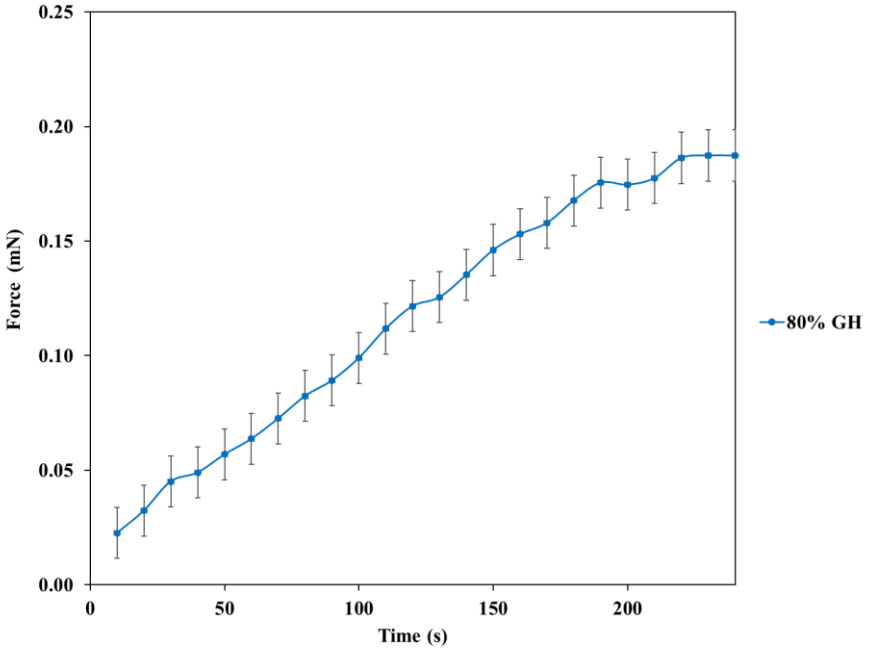

Figure 4-43 Blocking force of the calendaring actuator when power is on (2 min) and off (2 min) at 6 V of PVA/80GH/60Gly.

CHAPTER 5
DISCUSSION AND CONCLUSIONS

5.1 Discussion

5.1.1 Preparation of composite films

5.1.1.1 K-hand coating method

Compostable polyvinyl alcohol (PVA) films were prepared with and without the incorporation of glycerol as a plasticizer (Nemet et al., 2010). The films produced without glycerol were black in color, difficult to remove from the aluminum foil mold, susceptible to breakage, and their thicknesses ranged from 0.052 to 0.059 mm. In contrast, films containing glycerol, although similarly black, were more readily removed from the mold and exhibited thicknesses ranging from 0.057 to 0.062 mm. The film thickness increased with increased graphite concentrations. Moreover, the addition of glycerol also contributed to an increase in film thickness. The study showed that adding glycerol to PVA films improved the flexibility of the films, making them easier to remove from molds and less likely to break, while slightly increasing thickness. Both glycerol and higher graphite concentrations contributed to this thickness increase, suggesting they enhance the films' mechanical properties for better practical use.

5.1.1.2 Solution casting method

Conductive films were made using solution casting with various concentrations of graphite (50%–80% by weight of PVA) and glycerol (30%–70% by weight of PVA). Changes in these concentrations had minimal effect on film thickness. Films without glycerol were very fragile, whereas those with glycerol were more flexible and thicker. Glycerol was found to be the most effective plasticizer due to its polar hydroxyl groups, which enhance hydrogen bonding and improve film properties. The findings suggest that variations in graphite and glycerol concentrations had minimal impact on the thickness of the composite films. This differs from earlier research (Nemet et al., 2010), which showed that films without plasticizers were highly fragile. Hence, in this present study the presence of

glycerol improved the films' flexibility by forming hydrogen bonds between its hydroxyl groups and the polymer, replacing the original intermolecular interactions. Glycerol’s compact structure and strong polarity make it an effective plasticizer, enhancing mechanical properties without significantly affecting film thickness.

5.1.2 Preparation of Double-Layer ETA

5.1.2.1 Two-Step Process

The conductive layer (Layer 1) of the ETA was created using a PVA/GH/Gly solution with glycerol concentrations varying from 30% to 70% by weight. The PVA solution was poured into molds and cured in a hot air oven, resulting in U-shaped pieces measuring 0.5 x 5 cm^2, which were then affixed to Kapton tape (Layer 2) measuring 0.5 x 4 cm^2. The thickness of the ETA ranged from 0.121 to 0.387 mm, with glycerol concentration significantly impacting this thickness—higher glycerol content generally led to thicker films. This relationship underscores the critical role of glycerol in optimizing the structural and functional properties of the conductive layer, enhancing flexibility, conductivity, and mechanical strength for specific applications, thereby improving the overall performance of the ETA (Arham, 2018).

PVA/GH/Gly system

Conductive composite films were prepared using Kapton Tape (3M), PVC Tape (3M), PVC Tape (THAI-YAZAKI), and PP Tape (3M). Kapton exhibited the lowest coefficient of thermal expansion (CTE), followed by PVC (3M), PVC (THAI-YAZAKI), PP, and PDMS. ETAs were constructed by compositing a PVA/50GH/Gly conductive layer with these polymer layers. The thicknesses of the ETAs were 0.235±0.04 mm (Kapton), 0.404±0.02 mm (PVC 3M), 0.361±0.04 mm (PVC THAI-YAZAKI), and 0.080±0.02 mm (PDMS). Kapton was selected for further investigation due to its optimal thickness and CTE values (20.0-30.0 ppm/°C) (DuPont™, 2022). Graphite was identified as the most effective conductive filler, despite its high CTE and low conductivity.

5.1.2.2 In Situ Process

PVA/GH/Gly actuators were fabricated using 3 mL and 4 mL composite solutions, with molds secured by Kapton and PVC tapes. The resulting films were black and easily removed from the molds. Film thickness increased with solution volume: 3 mL solutions produced films with thicknesses of 0.111–0.124 mm, while 4 mL solutions produced films with thicknesses of 0.123–0.134 mm. Among the methods tested—K-hand coating, solution casting, in-situ process, and two-step process—the in-situ process was found to be the most effective. It produced the thinnest samples and allowed for close alignment of conductive and polymer layers. Consequently, the in-situ process was selected for further investigations due to its efficiency and ability to produce optimal film characteristics.

This research examines the in-situ preparation and characterization of four electroactive actuator systems: PVA/GH/Gly, PVA/GO/Gly, PVA/rGO/Gly, and PDMS/GH/Gly. The key findings are:

PVA/GH/Gly System: An electroactive actuator was successfully fabricated with PVA/GH/Gly as the conductive layer and Kapton tape as the polymer layer. The actuator's performance was not significantly influenced by variations in glycerol concentration, indicating stability across different glycerol levels.

PVA/GO/Gly System: With glycerol fixed at 60% wt relative to PVA, the GO content was varied between 8% and 20% wt. The film thickness and morphology were significantly influenced by the GO concentration. The 8% GO sample demonstrated the greatest thickness due to better dispersion, while the 20% GO sample exhibited dense agglomeration. The study also emphasized the advantages of using a green preparation method, such as environmental benefits and reduced graphene agglomeration (Cobos et al., 2018).

PVA/rGO/Gly System: The electroactive actuator was prepared with 60% wt glycerol relative to the weight of PVA. The results indicated that the rGO content significantly influenced the thickness of the actuator. As the amount of rGO increased, a corresponding increase in thickness was observed, along with enhanced agglomeration of denser particles (Srihata et al., 2016). Following the chemical

reduction of GO, the rGO particles exhibited a thinner and more sheet-like morphology. (Horacio Javier Salavagione, Martínez, & Gómez, 2009), various levels of rGO content (0.5, 1, 1.5, 2, 5, 7.5, and 10%) were tested, revealing that the sample with 8% rGO achieved the highest thickness. This phenomenon may be attributed to better particle dispersion at this concentration, underscoring the importance of optimizing rGO content to enhance the properties of the electroactive actuators.

5.1.3 Synthesis of GO and rGO

5.1.3.1 Synthesis of GO

Graphite oxide (GO) was synthesized and subsequently reduced to reduced graphite oxide (rGO) using graphite powder. The presence of significant functional groups on GO, including hydroxyl, carbonyl, carboxyl, and epoxy groups, was revealed by infrared spectroscopy. These groups were indicated by broad bands at wavenumbers 3342 cm^{-1} (O-H stretching), 1736 cm^{-1} (C=O group), 1217 cm^{-1} (C-O stretching), and 1035 cm^{-1} (C-O alkoxy stretching). No significant functional groups or peaks were observed in the initial graphite powder. The suitability of GO for producing highly conductive, defect-free graphene-like materials through reduction was attributed to the low quantity of carboxyl and carbonyl groups present (Morimoto et al., 2016). A decrease in the intensity of these functional group peaks was observed during the thermal treatment process, which was attributed to their decomposition (Ruidíaz-Martínez et al., 2020).

In the FTIR spectra of reduced graphite oxide (rGO), the disappearance of the OH group was observed, along with peaks at 1737 cm^{-1} (C=O stretching), 1528 cm^{-1} (C=C stretching), 1366 cm^{-1} (C-OH stretching), and 1217 cm^{-1} (C-O stretching) (Gong et al., 2018). RGO is recognized as a nanomaterial derived from the chemical reduction of graphene oxide, featuring a reduced number of oxygen groups and properties that are more akin to those of graphene (Manousi et al., 2020).

The morphological characteristics of graphite (GH), graphite oxide (GO), and reduced graphite oxide (rGO) were studied using SEM techniques. Graphite was observed as a finely powdered solid with a smooth texture, lightweight nature, and dark gray to nearly black color (Immanuel & Sivasubramanian, 2020). In contrast, GO was found to be darker, less smooth, with a more uneven and wrinkled surface

due to the formation of oxygen-containing functional groups and structural defects during its synthesis using sulfuric acid.

Reduced graphite oxide (rGO), which was synthesized using ascorbic acid as a reducing agent, exhibited a more complex structure with smoother surfaces than GO but not as smooth as graphite. The surface of rGO was observed to be rough and porous, formed by the release of gases during the reduction process (Mission et al., 2018). This partial reduction led to the restoration of graphene layers, with exfoliation and pore creation visible at higher magnifications. The process of reducing GO to rGO caused the surface to become corrugated due to the release of oxygen-containing groups (Mohan et al., 2015). Despite variations in oxidation and reduction conditions, a porous structure was consistently observed in rGO.

5.1.3.2 FTIR of the conductive composite films

FTIR spectra of the conductive composite films were analyzed. As the amount of GO increased, the –OH stretching vibration band was observed to shift from 3270 to 3281 cm^{-1} and become broader. The C–OH stretching vibration band shifted from 1085 to 1090 cm^{-1} (Jing et al., 2021). Additionally, the CH_2 stretching peak shifted from 2914 to 2918 cm^{-1}, and the –CH/CH_2 deformation vibration peak shifted from 1323 to 1417 cm^{-1}. The formation of hydrogen bonds between GO and PVA was found to enhance the mechanical properties of the composite film. GO was identified as acting as a "binder," linking different PVA chains and improving the toughness and rigidity of the material (Georgiou et al., 2021). In the PVA/rGO/Gly films, a reduction in the bands within the range of 3258 to 3270 cm^{-1} was noted, indicating the removal of OH groups from the rGO surface. Shifts in the CH_2 stretching and –CH/CH_2 deformation peaks were observed, and multiple bands around 1081 to 1086 cm^{-1} associated with C–O stretching were detected. FTIR spectroscopy of PVA/GH/Gly composite films with different graphite contents revealed distinct vibrations. Peaks corresponding to C–H stretching, carbonyl C=O stretching, and CH_2 bending and wagging were identified. The presence of PVA was confirmed, with peaks at 2936 cm^{-1} and 1725 cm^{-1} indicating C-H and carbonyl C=O groups, respectively. Peaks at 1250 cm^{-1} and 850 cm^{-1} further supported the incorporation of PVA. The flexibility of PVA membranes was improved by glycerol addition, and a

significant absorption band at 3262 cm^{-1} indicated O–H stretching vibrations. In contrast, graphite did not exhibit prominent functional groups in the FTIR spectra (Jamali et al., 2023).

5.1.4 Electrical conductivity of conductive layer

5.1.4.1 PVA/GH/Gly system

The electrical resistance of the conductive films was measured using a digital multimeter, with Vaseline petroleum gel applied as an adhesive interface layer. The resistivity values of PVA/50GH/60Gly, PVA/60GH/60Gly, PVA/70GH/60Gly, and PVA/80GH/60Gly films were found to be 3.36×10^{9}, 8.95×10^{8}, 2.36×10^{6}, and 2.37×10^{6} Ω·cm, respectively. The corresponding electrical conductivity values were 3.29×10^{-12}, 3.90×10^{-9}, 4.19×10^{-9}, and 4.12×10^{-9} S/m, respectively. Improved contact between the copper electrodes and the samples was achieved by applying Vaseline, which reduced resistance and increased conductivity (S. M. Zainab et al., 2020). It was observed that the electrical conductivity of the films was significantly affected by the amount of graphite, with higher graphite content leading to reduced resistance and increased conductivity (Heaney, 2003). The effect of glycerol was also noted, with an increase in electrical conductivity observed as the graphite concentration increased. This enhancement was attributed to glycerol's impact on increasing the dielectric constant and reducing the modulus of elasticity.

Effect of Graphite Content

As the graphite content in the composite films increased from 50% wt to 80% wt, a significant decrease in volume resistivity was observed. This decrease indicated an enhancement in the electrical conductivity of the composite films. The volume conductivity of the films also increased with higher graphite content. This improvement in conductivity was attributed to the increased number of conductive pathways within the films. Better dispersion of graphite particles in the PVA matrix facilitated improved connectivity between particles, which allowed for easier electron movement. The electrical conductivity values measured for the composite films with 50%, 60%, 70%, and 80% wt graphite were 6.43×10^{-5}, 1.04×10^{-4}, 3.39×10^{-4}, and 4.15×10^{-4} S/cm, respectively. In line with the research by (F. P. Du, Tang, C. Y., Xie, X. L., Zhou, X. P., & Tan, L., 2009), the electrical conductivity values of

PSA-g-MWNTs increased with the increasing loading of MWNTs at 0, 5, 10, and 20 wt%.

Effect of Calendaring

The surface resistivity and conductivity of PVA/graphite composite films were assessed with and without calendaring, across varying graphite contents. For non-calendared films, the volume resistivity increased from 2.16×10^{9} Ω·cm to 3.13×10^{9} Ω·cm and the volume conductivity decreased from 4.63×10^{-12} S/m to 3.20×10^{-12} S/m as graphite content rose from 50% to 80% wt. This increase in resistivity and decrease in conductivity were attributed to inadequate graphite particle distribution and voids that impeded electron movement.

In contrast, calendaring improved the films' electrical properties. The volume resistivity of calendared films decreased from 1.43×10^{9} Ω·cm to 1.11×10^{9} Ω·cm with increasing graphite content from 60% to 80% wt, due to reduced voids and enhanced particle connectivity. Scanning electron micrographs confirmed the reduction of voids and gaps after calendaring (Leng et al., 2022). Calendared films showed increased conductivity and reduced resistivity, with resistivity values ranging from 8.03×10^{8} to 1.43×10^{9} Ω·cm and conductivity values ranging from 4.63×10^{-12} to 3.20×10^{-12} S/m. The improved conductivity was attributed to better particle contact and reduced electrical leakage due to the calendaring process (Ma et al., 2010).

5.1.4.2 PVA/GO/Gly System

The test results revealed that the electrical resistivity of PVA/GO/Gly actuators decreased significantly with increasing graphite oxide content, with values of 3.77×10^{8}, 3.47×10^{8}, 2.56×10^{8}, and 1.66×10^{8} Ω·cm for 8%, 10%, 15%, and 20%wt graphite oxide, respectively. The corresponding electrical conductivity values were 2.66×10^{-7}, 3.62×10^{-7}, 3.97×10^{-7}, and 6.04×10^{-7} S/m. The observed discrepancy was attributed to the large particle size of the synthesized graphite oxide, which led to poor dispersion, inadequate film coverage, or particle clumping, resulting in insufficient electrical conductivity. Therefore, increasing the amount of graphite oxide enhances the electrical conductivity of the conductive composite film (Suma & Sangappa, 2024).

5.1.4.3 PVA/rGO/Gly System

The electrical volume resistivity and conductivity of PVA/rGO/Gly actuators containing 8%, 10%, 15%, and 20% wt reduced graphite oxide (rGO) were measured. It was observed that the electrical resistivity decreased with increasing rGO content. The volume resistivity values were 2.60×10^{8}, 3.36×10^{8}, 2.27×10^{8}, and 7.03×10^{8} Ω·cm, while the electrical conductivity values were 3.86×10^{-7}, 3.06×10^{-7}, 6.34×10^{-7}, and 1.47×10^{-7} S/m for 8%, 10%, 15%, and 20% wt rGO, respectively. The results indicated that a 15% rGO content formed an efficient percolation network, resulting in the highest electrical conductivity. Conversely, at 8%, 10%, and 20% wt, the electrical resistivity increased with rGO content, which is inversely proportional to electrical conductivity. At 20% wt, the excess rGO may have led to a thick conductive layer that hindered charge flow, reducing conductivity compared to the 15% wt concentration. The test results demonstrated that increasing graphite oxide content in PVA/GO/Gly actuators significantly reduced electrical resistivity and increased electrical conductivity. Similar trends were observed in previous studies (Suma & Sangappa, 2024). However, the results differed from those of (Song et al., 2013), likely due to the larger particle size of the synthesized graphite oxide, which caused poor dispersion and inadequate coverage, leading to lower conductivity in the tested films. This suggests that particle size plays a crucial role in determining the electrical properties of composite films.

The PVA/GH/Gly system was chosen for further investigation due to its superior electrical conductivity and promising trends with increased graphite content. Further tests focused on its mechanical properties.

5.1.5 Tensile Test

The tensile test results of electroactive actuators (ETAs) demonstrated that these devices can deform while maintaining functionality, ensuring safety in human interaction. Ideal ETAs are energy-efficient, highly flexible, lightweight, and easy to fabricate, with favorable mechanical properties such as high tensile strength and low Young's modulus. Key advantages identified include high actuation strains, wide frequency bandwidths, rapid response, low weight, easy miniaturization, and flexibility (Xu et al., 2023). In this study, the PVA/GH composite was selected for

mechanical property testing due to its superior electrical conductivity. Mechanical performance was evaluated by examining maximum stress values, Young's modulus, and the percentage of elongation at break. It was observed that variations in graphite filler content did not significantly affect elongation at break ($p<0.05$). However, the addition of rigid graphite increased the brittleness of the films (J. Keeling, 2017). Graphite's high stiffness and aspect ratio decreased the flexibility of the films while increasing their modulus of elasticity (J.Boylan, 1996). However, tensile strength consistently decreased at higher graphite concentrations, likely due to inadequate interaction between graphite particles and matrix molecules. Tensile strength showed a slight reduction with increased graphite content (Ramesh, 2009). Graphite can intercalate between the PVA polymer chains, disrupting intermolecular forces within the polymer matrix. This disruption weakened the overall mechanical strength of the composite, making it more prone to breakage under stress. At higher graphite concentrations (80%), the graphite particles began to agglomerate into larger, less dispersed structures, further compromising the composite's mechanical integrity.

The incorporation of higher amounts of graphite increased the rigidity of the composite films, improving ductility, ultimate tensile strength (UTS), and compressive strength, possibly due to graphite particles acting as barriers to dislocations. Surface morphology analysis revealed that increased filler content within the composite films resulted in rough and uneven films due to particle agglomeration. While higher filler content enhanced electrical conductivity by improving particle connectivity, calendared films, compared to non-calendared ones, exhibited better packing density and uniformity. These morphological changes were associated with improved particle contact and distribution, leading to enhanced electrical performance.

5.1.6 Bending angle

The bending angle results indicated that the electroactive actuators (ETAs) demonstrated varying performances based on graphite content and the calendaring process. The calendaring process was found to significantly reduce the overall thickness of the actuators. With 50%wt graphite, the system with a thickness of 147.87 µm exhibited the highest bending angle of 22.30º. This improvement was

likely due to the reduced gap between the conductive layer and Kapton tape, which enhanced bonding and reduced porosity, thereby improving electrical conductivity (Ma et al., 2010). However, despite the increase in electrical conductivity with higher graphite concentrations, the increased weight of the material led to a reduction in bending angle, as the material became heavier and more difficult to bend.

Additionally, the temperature characteristics of the actuators were found to play a crucial role in their bending performance. The small bending angles observed in this study were attributed to the low temperatures generated during operation, which were insufficient to cause significant expansion of the polymer layer. This suggested that the heat conduction within the conductive layer may not have been adequate, or the conversion of electrical energy into heat was not as efficient as required for optimal bending performance. Normally, this is because the temperature characteristics of actuators depend on electric current, which generates heat in the conductive layer, causing the polymer to expand and enabling bending (Aouraghe et al., 2021).

5.1.7 Blocking force

The blocking force of the electroactive actuator was indirectly measured using an electronic balance while applying 6 V for 2 minutes, followed by 2 minutes without voltage. In summary, the blocking force was influenced by graphite concentration, the actuator containing 50%wt graphite showed an increasing blocking force over time, peaking at 0.101 mN at 120 seconds before decreasing after the electric potential was turned off. This behavior aligns with Joule heating theory, where bending occurs due to the lower coefficient of thermal expansion (CTE) of the conductive layer.

In contrast, the actuator with 60%wt graphite experienced a slight decline in blocking force, while those with 70% and 80%wt graphite exhibited an increase even after the voltage was removed, likely due to residual stresses from the rigidity of graphite (Z. Zhang & Fang, 2006). Thus, the actuator with 50%wt graphite demonstrated the best performance in blocking force and bending behavior, confirming the influence of Joule heating on the bending mechanism related to the CTE of the conductive layer (Tian et al., 2021).

5.2 Conclusions

1. The preparation of conductive polymer composite films and polymer films using the PVA/GH/Gly system and Kapton tape was successfully achieved.

2. The model electroactive actuator (ETA), with a thickness of 147.87 µm, prepared using PVA/50GH/Gly followed by calendaring, showed a maximum bending angle of 22.30º when a 6 V potential was applied for 240 seconds.

3. The prototype system has not yet demonstrated effective performance as a gripper. The bending angle observed in the experiments was small due to the insufficient internal temperature of the actuator, which was not high enough to induce significant expansion of the polymer. This indicates that the heat conduction and conversion of electrical energy into heat were not sufficiently effective.

5.3 Suggestions

1. During the preparation of the conductive composite solution composed of PVA, graphite, and glycerol, subsequently cross-linked with glutaraldehyde, the solution should be allowed to cool prior to mixing in order to prevent accelerated cross-linking. Molds should be prepared in advance to accommodate the ongoing cross-linking of the solution throughout the ETA system preparation process.

2. During the synthesis of GO and rGO, extreme caution must be observed when utilizing concentrated sulfuric acid (H_2SO_4) and potassium permanganate ($KMnO_4$) due to their strong oxidizing properties. Hydrogen peroxide (H_2O_2) should be handled with care to prevent potential explosions upon contact with organic materials. Additionally, the oxidation of graphite to produce GO should be meticulously controlled to manage the substantial heat released and to avert uncontrolled or violent reactions.

3. Electrical circuits should be assembled with precision to prevent the occurrence of short circuits. Inappropriate connections or the use of substandard conductive materials can result in short circuits, which may cause damage to the circuit or pose fire hazards.

4. It is essential to ensure that electric current is distributed uniformly across the sample. Uneven distribution can lead to localized heat accumulation, potentially resulting in damage to the material or changes in its electrical properties.

APPENDIX A

Experimental data

Table 1 Thickness of PVA/GH and PVA/GH/Gly

Sample	Thickness (mm)			Average thickness (mm)
	1	2	3	
PVA/Graphite-60-1	0.0900	0.0500	0.0590	0.0663
PVA/Graphite-60-2	0.0490	0.0420	0.0480	0.0463
PVA/Graphite-60-3	0.0500	0.0390	0.0410	0.0433
PVA/Graphite-70-1	0.0800	0.1090	0.0500	0.0797
PVA/Graphite-70-2	0.0680	0.0580	0.0110	0.0457
PVA/Graphite-70-3	0.0480	0.0550	0.0488	0.0506
PVA/Graphite-80-1	0.0420	0.0520	0.0640	0.0527
PVA/Graphite-80-2	0.0820	0.0580	0.0540	0.0647
PVA/Graphite-80-3	0.0380	0.0520	0.0610	0.0503
PVA/Graphite-60/Glycerol-1	0.0700	0.0580	0.0420	0.0567
PVA/Graphite-60/Glycerol-2	0.0750	0.0380	0.0580	0.0570
PVA/Graphite-60/Glycerol-3	0.0580	0.0650	0.0520	0.0583
PVA/Graphite-70/Glycerol-1	0.0820	0.0690	0.0490	0.0667
PVA/Graphite-70/Glycerol-2	0.0620	0.0500	0.0420	0.0513
PVA/Graphite-70/Glycerol-3	0.0690	0.0500	0.0450	0.0547
PVA/Graphite-80/Glycerol-1	0.0520	0.0690	0.0700	0.0637
PVA/Graphite-80/Glycerol-2	0.0620	0.0600	0.0500	0.0573
PVA/Graphite-80/Glycerol-3	0.0700	0.0590	0.0700	0.0663

Table 2 Thickness of PVA/GH/Gly

Sample	Thickness (mm)			Average
	1	2	3	
10GH/PVA/20Gly-1	0.199	0.180	0.150	0.176
10GH/PVA/22Gly-1	0.212	0.200	0.161	0.191
10GH/PVA/24Gly-1	0.181	0.240	0.276	0.232
10GH/PVA/26Gly-1	0.201	0.221	0.250	0.224
10GH/PVA/28Gly-1	0.232	0.240	0.240	0.237
10GH/PVA/30Gly-1	0.283	0.252	0.242	0.259
10GH/PVA/30Gly-2	0.200	0.225	0.300	0.242
10GH/PVA/30Gly-3	0.270	0.296	0.280	0.282
50GH/PVA/30Gly-1	0.219	0.218	0.182	0.206
50GH/PVA/30Gly-2	0.175	0.198	0.220	0.198
50GH/PVA/30Gly-3	0.198	0.160	0.175	0.178
50GH/PVA/30Gly-4	0.280	0.280	0.320	0.293
50GH/PVA/30Gly-5	0.350	0.320	0.270	0.313
60GH/PVA/30Gly-1	0.185	0.232	0.291	0.236
60GH/PVA/30Gly-2	0.180	0.190	0.191	0.187
60GH/PVA/30Gly-3	0.260	0.280	0.250	0.263
60GH/PVA/30Gly-4	0.321	0.311	0.322	0.318
60GH/PVA/30Gly-5	0.422	0.422	0.308	0.384
70GH/PVA/30Gly-1	0.310	0.185	0.130	0.208
70GH/PVA/30Gly-2	0.175	0.178	0.190	0.181
70GH/PVA/30Gly-3	0.350	0.340	0.240	0.310
70GH/PVA/30Gly-4	0.231	0.248	0.369	0.283

Sample	Thickness (mm)			Average
	1	2	3	
70GH/PVA/30Gly-5	0.280	0.271	0.280	0.277
80GH/PVA/30Gly-1	0.150	0.148	0.138	0.145
80GH/PVA/30Gly-2	0.165	0.150	0.120	0.145
80GH/PVA/30Gly-3	0.165	0.149	0.130	0.148
80GH/PVA/30Gly-4	0.312	0.339	0.250	0.300
80GH/PVA/30Gly-5	0.360	0.321	0.315	0.332
50GH/PVA/40Gly-1	0.275	0.275	0.270	0.273
50GH/PVA/40Gly-2	0.340	0.275	0.240	0.285
50GH/PVA/40Gly-3	0.270	0.310	0.320	0.300
50GH/PVA/40Gly-4	0.359	0.330	0.320	0.336
50GH/PVA/40Gly-5	0.390	0.294	0.330	0.338
60GH/PVA/40Gly-1	0.290	0.285	0.275	0.283
60GH/PVA/40Gly-2	0.390	0.380	0.429	0.400
60GH/PVA/40Gly-3	0.328	0.340	0.410	0.359
60GH/PVA/40Gly-4	0.450	0.440	0.280	0.390
60GH/PVA/40Gly-5	0.340	0.360	0.369	0.356
70GH/PVA/40Gly-1	0.280	0.250	0.325	0.285
70GH/PVA/40Gly-2	0.475	0.430	0.450	0.452
70GH/PVA/40Gly-3	0.435	0.419	0.389	0.414
70GH/PVA/40Gly-4	0.390	0.412	0.380	0.394
70GH/PVA/40Gly-5	0.352	0.390	0.379	0.374
80GH/PVA/40Gly-1	0.265	0.252	0.300	0.272
80GH/PVA/40Gly-2	0.330	0.350	0.309	0.330

Sample	Thickness (mm)			Average
	1	2	3	
80GH/PVA/40Gly-3	0.369	0.305	0.364	0.346
80GH/PVA/40Gly-4	0.380	0.400	0.395	0.392
80GH/PVA/40Gly-5	0.345	0.330	0.320	0.332
50GH/PVA/50Gly-1	0.280	0.290	0.279	0.283
50GH/PVA/50Gly-2	0.370	0.361	0.410	0.380
50GH/PVA/50Gly-3	0.680	0.680	0.685	0.682
50GH/PVA/50Gly-4	0.329	0.335	0.312	0.325
50GH/PVA/50Gly-5	0.270	0.221	0.189	0.227
60GH/PVA/50Gly-1	0.301	0.279	0.300	0.293
60GH/PVA/50Gly-2	0.252	0.260	0.289	0.267
60GH/PVA/50Gly-3	0.290	0.278	0.245	0.271
60GH/PVA/50Gly-4	0.420	0.421	0.376	0.406
60GH/PVA/50Gly-5	0.320	0.310	0.340	0.323
70GH/PVA/50Gly-1	0.352	0.316	0.330	0.333
70GH/PVA/50Gly-2	0.360	0.408	0.421	0.396
70GH/PVA/50Gly-3	0.315	0.312	0.300	0.309
70GH/PVA/50Gly-4	0.320	0.340	0.340	0.333
70GH/PVA/50Gly-5	0.330	0.320	0.329	0.326
80GH/PVA/50Gly-1	0.421	0.405	0.375	0.400
80GH/PVA/50Gly-2	0.300	0.300	0.330	0.310
80GH/PVA/50Gly-3	0.430	0.451	0.470	0.450
80GH/PVA/50Gly-4	0.309	0.321	0.361	0.330
80GH/PVA/50Gly-5	0.259	0.305	0.310	0.291

Sample	Thickness (mm)			Average
	1	2	3	
50GH/PVA/60Gly-1	0.310	0.330	0.310	0.317
50GH/PVA/60Gly-2	0.230	0.282	0.302	0.271
50GH/PVA/60Gly-3	0.290	0.271	0.298	0.286
50GH/PVA/60Gly-4	0.259	0.269	0.270	0.266
50GH/PVA/60Gly-5	0.390	0.378	0.320	0.363
60GH/PVA/60Gly-1	0.240	0.225	0.220	0.228
60GH/PVA/60Gly-2	0.328	0.290	0.282	0.300
60GH/PVA/60Gly-3	0.286	0.282	0.370	0.313
60GH/PVA/60Gly-4	0.255	0.252	0.250	0.252
60GH/PVA/60Gly-5	0.380	0.350	0.250	0.327
70GH/PVA/60Gly-1	0.410	0.415	0.371	0.399
70GH/PVA/60Gly-2	0.348	0.339	0.325	0.337
70GH/PVA/60Gly-3	0.232	0.318	0.280	0.277
70GH/PVA/60Gly-4	0.368	0.279	0.258	0.302
70GH/PVA/60Gly-5	0.690	0.390	0.390	0.490
80GH/PVA/60Gly-1	0.360	0.398	0.410	0.389
80GH/PVA/60Gly-2	0.400	0.412	0.412	0.408
80GH/PVA/60Gly-3	0.372	0.371	0.375	0.373
80GH/PVA/60Gly-4	0.395	0.339	0.339	0.358
80GH/PVA/60Gly-5	0.392	0.410	0.420	0.407
50GH/PVA/70Gly-1	0.320	0.330	0.336	0.329
50GH/PVA/70Gly-2	0.338	0.370	0.329	0.346
50GH/PVA/70Gly-3	0.240	0.250	0.290	0.260

Sample	Thickness (mm)			Average
	1	2	3	
50GH/PVA/70Gly-4	0.310	0.272	0.270	0.284
50GH/PVA/70Gly-5	0.295	0.306	0.342	0.314
60GH/PVA/70Gly-1	0.255	0.320	0.346	0.307
60GH/PVA/70Gly-2	0.340	0.400	0.430	0.390
60GH/PVA/70Gly-3	0.289	0.245	0.290	0.275
60GH/PVA/70Gly-4	0.275	0.296	0.331	0.301
60GH/PVA/70Gly-5	0.402	0.320	0.278	0.333
70GH/PVA/70Gly-1	0.370	0.285	0.271	0.309
70GH/PVA/70Gly-2	0.251	0.251	0.251	0.251
70GH/PVA/70Gly-3	0.320	0.312	0.369	0.334
70GH/PVA/70Gly-4	0.368	0.328	0.320	0.339
70GH/PVA/70Gly-5	0.325	0.309	0.370	0.335
80GH/PVA/70Gly-1	0.475	0.515	0.382	0.457
80GH/PVA/70Gly-2	0.392	0.330	0.320	0.347
80GH/PVA/70Gly-3	0.409	0.369	0.382	0.387
80GH/PVA/70Gly-4	0.372	0.339	0.269	0.327
80GH/PVA/70Gly-5	0.301	0.329	0.326	0.319

Table 3 Thickness of PVA/GH/Gly

GH	Volume (mL)	Thickness (mm)			Average
Content of filler (wt%)		1	2	3	
PVA/50GH/60Gly	3	0.072	0.121	0.110	0.101
PVA/50GH/60Gly	3	0.109	0.109	0.119	0.112
PVA/50GH/60Gly	3	0.121	0.101	0.130	0.117
PVA/50GH/60Gly	3	0.130	0.121	0.135	0.129
PVA/50GH/60Gly	3	0.125	0.129	0.120	0.125
PVA/60GH/60Gly	3	0.118	0.112	0.110	0.113
PVA/60GH/60Gly	3	0.109	0.092	0.112	0.104
PVA/60GH/60Gly	3	0.100	0.100	0.110	0.103
PVA/60GH/60Gly	3	0.130	0.100	0.130	0.120
PVA/60GH/60Gly	3	0.121	0.101	0.119	0.114
PVA/70GH/60Gly	3	0.095	0.119	0.130	0.115
PVA/70GH/60Gly	3	0.100	0.100	0.131	0.110
PVA/70GH/60Gly	3	0.131	0.101	0.121	0.118
PVA/70GH/60Gly	3	0.110	0.106	0.111	0.109
PVA/70GH/60Gly	3	0.131	0.112	0.110	0.118
PVA/80GH/60Gly	3	0.125	0.126	0.120	0.124
PVA/80GH/60Gly	3	0.130	0.110	0.120	0.120
PVA/80GH/60Gly	3	0.140	0.110	0.121	0.124
PVA/80GH/60Gly	3	0.130	0.105	0.119	0.118
PVA/80GH/60Gly	3	0.141	0.109	0.121	0.124
PVA/50GH/60Gly	4	0.110	0.105	0.105	0.107
PVA/50GH/60Gly	4	0.122	0.121	0.123	0.122
PVA/50GH/60Gly	4	0.120	0.120	0.121	0.120

GH Content of filler (wt%)	Volume (mL)	Thickness (mm)			Average
		1	2	3	
PVA/50GH/60Gly	4	0.190	0.127	0.121	0.146
PVA/50GH/60Gly	4	0.190	0.123	0.121	0.145
PVA/60GH/60Gly	4	0.198	0.101	0.121	0.140
PVA/60GH/60Gly	4	0.121	0.125	0.102	0.116
PVA/60GH/60Gly	4	0.119	0.126	0.100	0.115
PVA/60GH/60Gly	4	0.130	0.132	0.101	0.121
PVA/60GH/60Gly	4	0.110	0.105	0.149	0.121
PVA/70GH/60Gly	4	0.125	0.122	0.199	0.149
PVA/70GH/60Gly	4	0.130	0.130	0.129	0.130
PVA/70GH/60Gly	4	0.145	0.121	0.149	0.138
PVA/70GH/60Gly	4	0.108	0.121	0.142	0.124
PVA/70GH/60Gly	4	0.140	0.129	0.121	0.130
PVA/80GH/60Gly	4	0.120	0.131	0.128	0.126
PVA/80GH/60Gly	4	0.141	0.110	0.130	0.127
PVA/80GH/60Gly	4	0.140	0.115	0.109	0.121
PVA/80GH/60Gly	4	0.100	0.121	0.130	0.117
PVA/80GH/60Gly	4	0.129	0.102	0.152	0.128

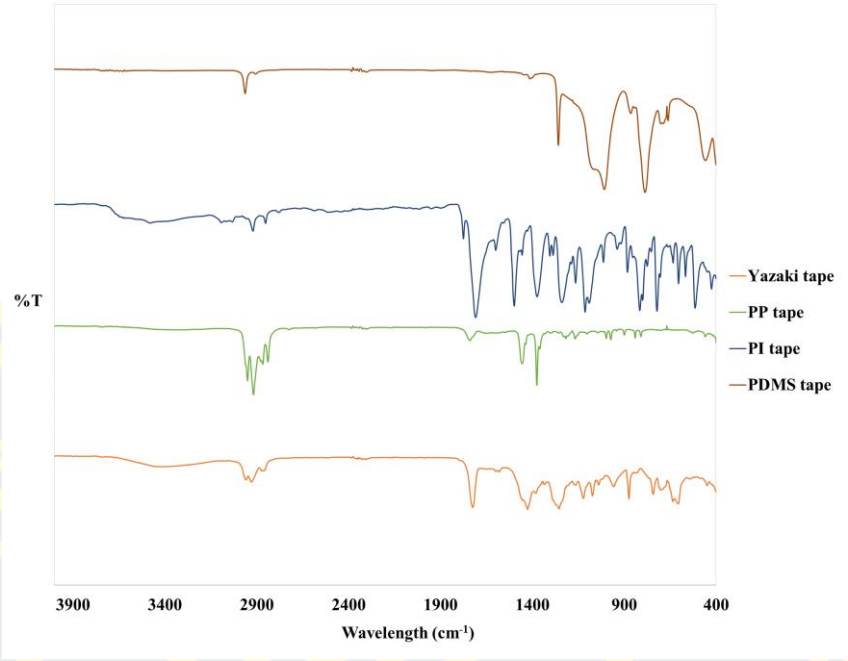

Figure 1 FTIR spectra of PI PDMS PP and PVC (Yazaki) tape

Table 4 Mechanical properties of the samples.

Sample	Elong at Break (%)	Stress at Break (N/mm^2)	Young Modulus (N/mm^2)
PVA/50GH/60Gly	435.63 ± 104.93	71264.04 ± 25504.84	1222140.54 ± 4950959.84
PVA/60GH/60Gly	251.23 ± 42.78	68933.17 ± 18295.11	1266048.05 ± 279478.13
PVA/70GH/60Gly	184.41 ± 48.37	61790.62 ± 18745.38	1382181.17 ± 239269.62
PVA/80GH/60Gly	108.23 ± 42.75	54722.22 ± 21364.01	1967404.71 ± 363233.64

Table 5 Thickness of PVA/GH/Gly

Sample	Volume (mL)	Thickness	Thickness Av	SD
PVA/50GH/60Gly-1	3	0.117		
PVA/50GH/60Gly-2	3	0.129		
PVA/50GH/60Gly-3	3	0.125	0.124	0.01
PVA/60GH/60Gly-1	3	0.113		
PVA/60GH/60Gly-2	3	0.104		
PVA/60GH/60Gly-3	3	0.103		
PVA/60GH/60Gly-4	3	0.120		
PVA/60GH/60Gly-5	3	0.114	0.111	0.01
PVA/70GH/60Gly-1	3	0.115		
PVA/70GH/60Gly-2	3	0.110		
PVA/70GH/60Gly-3	3	0.118		
PVA/70GH/60Gly-4	3	0.109		
PVA/70GH/60Gly-5	3	0.118	0.114	0.00
PVA/80GH/60Gly-1	3	0.124		
PVA/80GH/60Gly-2	3	0.120		
PVA/80GH/60Gly-3	3	0.124		
PVA/80GH/60Gly-4	3	0.118		
PVA/80GH/60Gly-5	3	0.124	0.122	0.00
PVA/50GH/60Gly-1	4	0.107		
PVA/50GH/60Gly-2	4	0.122		
PVA/50GH/60Gly-3	4	0.120		
PVA/50GH/60Gly-4	4	0.146		
PVA/50GH/60Gly-5	4	0.145	0.128	0.02
PVA/60GH/60Gly-1	4	0.140		
PVA/60GH/60Gly-2	4	0.116		
PVA/60GH/60Gly-3	4	0.115		
PVA/60GH/60Gly-4	4	0.121		
PVA/60GH/60Gly-5	4	0.121	0.123	0.01
PVA/70GH/60Gly-1	4	0.149		
PVA/70GH/60Gly-2	4	0.130		
PVA/70GH/60Gly-3	4	0.138		
PVA/70GH/60Gly-4	4	0.124		
PVA/70GH/60Gly-5	4	0.130	0.134	0.01
PVA/80GH/60Gly-1	4	0.126		
PVA/80GH/60Gly-2	4	0.127		
PVA/80GH/60Gly-3	4	0.121		
PVA/80GH/60Gly-4	4	0.117		
PVA/80GH/60Gly-5	4	0.128	0.124	0.00

Table 6 Thickness of the electroactive actuator.

ETA Sample	Calendaring	Layer 1 (µm)	Layer 2 (µm)	Layer 3 (µm)	Total (µm)
PVA50GH60Gly	Non-Calendaring	25.01	69.68	72.35	167.04
PVA60GH60Gly	Non-Calendaring	25.03	51.38	72.35	148.76
PVA70GH60Gly	Non-Calendaring	26.80	67.00	62.08	155.88
PVA80GH60Gly	Non-Calendaring	26.36	54.05	79.95	160.36
PVA50GH60Gly	Calendaring	16.10	90.21	41.56	147.87
PVA60GH60Gly	Calendaring	22.35	57.18	77.27	156.80
PVA70GH60Gly	Calendaring	18.33	87.54	56.73	162.60
PVA80GH60Gly	Calendaring	23.57	96.92	62.97	183.46

Table 7 The electrical resistivity and electrical conductivity values for each sample formula are as follows:

Sample Content of filler (wt%)	Volume (mL)	Volume resistivity, ρ (Ω.cm)	Conductivity, σ (S/m)
PVA/10GH/22Gly	15	1.3×10^{10}	7.85×10^{-9}
PVA/10GH/24Gly	15	4.6×10^{9}	2.15×10^{-8}
PVA/10GH/26Gly	15	1.4×10^{10}	7.03×10^{-9}
PVA/10GH/28Gly	15	5.3×10^{9}	1.88×10^{-8}
PVA/10GH/30Gly	15	1.0×10^{10}	1.33×10^{-8}
PVA/50GH/30Gly	15	2.68×10^{6}	9.96×10^{-6}
PVA/50GH/40Gly	15	1.73×10^{6}	5.84×10^{-5}
PVA/50GH/50Gly	15	1.21×10^{6}	8.96×10^{-5}
PVA/50GH/60Gly	15	8.27×10^{5}	1.76×10^{-4}
PVA/50GH/70Gly	15	2.70×10^{6}	4.07×10^{-5}
PVA/60GH/30Gly	15	1.46×10^{6}	1.79×10^{-4}
PVA/60GH/40Gly	15	6.57×10^{5}	2.34×10^{-4}
PVA/60GH/50Gly	15	5.63×10^{5}	2.42×10^{-4}
PVA/60GH/60Gly	15	3.41×10^{6}	5.81×10^{-5}
PVA/60GH/70Gly	15	2.99×10^{6}	5.16×10^{-5}
PVA/70GH/30Gly	15	8.46×10^{5}	1.49×10^{-4}
PVA/70GH/40Gly	15	3.46×10^{5}	3.61×10^{-4}
PVA/70GH/50Gly	15	1.67×10^{6}	6.43×10^{-5}
PVA/70GH/60Gly	15	1.37×10^{6}	1.04×10^{-4}
PVA/70GH/70Gly	15	9.27×10^{5}	3.39×10^{-4}
PVA/80GH/30Gly	15	2.48×10^{5}	4.15×10^{-4}
PVA/80GH/40Gly	15	4.51×10^{5}	2.38×10^{-4}
PVA/80GH/50Gly	15	1.75×10^{6}	1.20×10^{-4}
PVA/80GH/60Gly	15	4.17×10^{5}	3.14×10^{-4}
PVA/80GH/70Gly	15	2.97×10^{5}	3.57×10^{-4}

Table 8 Angle of Deviation for Each Sample Formula

Sample Content of filler (wt%)	Volume (mL)	Bending angle (◦)
PVA/10GH/22Gly	15	1.50
PVA/10GH/24Gly	15	5.00
PVA/10GH/26Gly	15	7.00
PVA/10GH/28Gly	15	3.00
PVA/10GH/30Gly	15	4.00
PVA/50GH/30Gly	15	2.75
PVA/50GH/40Gly	15	3.50
PVA/50GH/50Gly	15	7.83
PVA/50GH/60Gly	15	12.33
PVA/50GH/70Gly	15	4.80
PVA/60GH/30Gly	15	6.75
PVA/60GH/40Gly	15	8.25
PVA/60GH/50Gly	15	2.25
PVA/60GH/60Gly	15	5.00
PVA/60GH/70Gly	15	6.80
PVA/70GH/30Gly	15	4.20
PVA/70GH/40Gly	15	2.50
PVA/70GH/50Gly	15	5.90
PVA/70GH/60Gly	15	7.25
PVA/70GH/70Gly	15	5.40
PVA/80GH/30Gly	15	5.00
PVA/80GH/40Gly	15	7.63
PVA/80GH/50Gly	15	2.17
PVA/80GH/60Gly	15	2.40
PVA/80GH/70Gly	15	8.60

Table 9 The thickness of the actuator layers calendaring and non-calendaring at a magnification of 250x.

Sample	Non-Calendaring		Calendaring	
PVA/50GH/60Gly	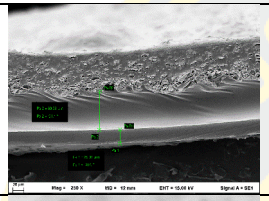	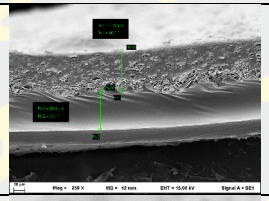	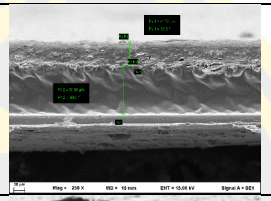	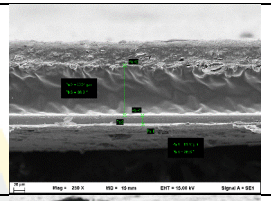
PVA/60GH/60Gly	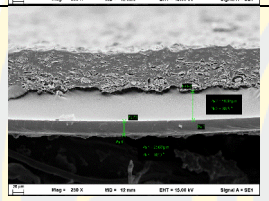	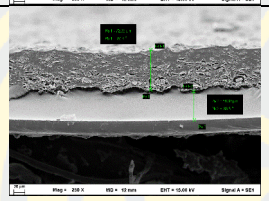	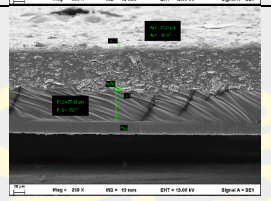	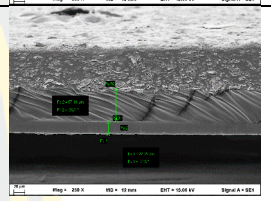
PVA/70GH/60Gly	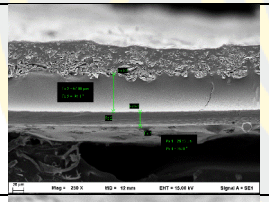	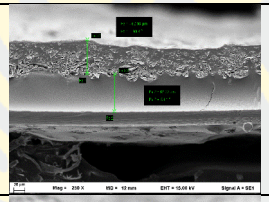	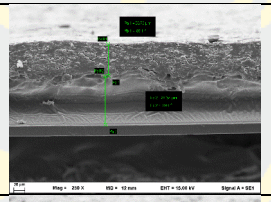	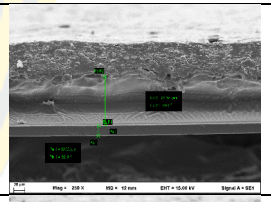
PVA/80GH/60Gly	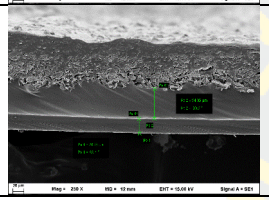	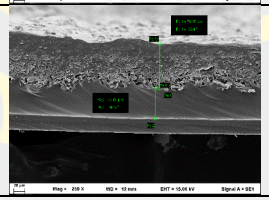	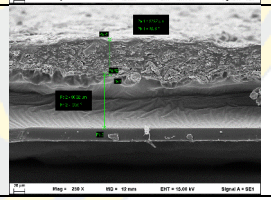	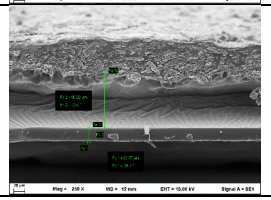

Comparisons for Stress @ Peak (N/mm2)

Tukey Pairwise Comparisons: Response = Stress @ Peak (N/mm2), Term = Sample

Grouping Information Using the Tukey Method and 95% Confidence

Sample	N	Mean	Grouping
PVA/50GH/Gly	12	71264.0	A
PVA/60GH/Gly	10	68933.2	A
PVA/70GH/Gly	10	61790.6	A
PVA/80GH/Gly	5	54722.2	A

Means that do not share a letter are significantly different.

Tukey Simultaneous 95% CIs

Figure 4 ANOVA Tukey Method analysis of stress@Peak (N/mm²)

Comparisons for Elong @ Break %

Tukey Pairwise Comparisons: Response = Elong @ Break %, Term = Sample

Grouping Information Using the Tukey Method and 95% Confidence

Sample	N	Mean	Grouping		
PVA/50GH/Gly	10	471.763	A		
PVA/60GH/Gly	10	255.030		B	
PVA/70GH/Gly	9	184.411		B	C
PVA/80GH/Gly	6	108.233			C

Means that do not share a letter are significantly different.

Figure 5 ANOVA Tukey Method analysis of Elongation at Break (%)

Comparisons for Young Modulus (N/mm2)

Tukey Pairwise Comparisons: Response = Young Modulus (N/mm2), Term = Sample

Grouping Information Using the Tukey Method and 95% Confidence

Sample	N	Mean	Grouping		
PVA/80GH/Gly	7	1857033	A		
PVA/70GH/Gly	7	1382181	A		B
PVA/60GH/Gly	8	1266048			B
PVA/50GH/Gly	11	1222141			B

Means that do not share a letter are significantly different.

Figure 6 ANOVA Tukey Method analysis of Young Modulus (N/mm^2)

Table 10 Electrical resistance and conductivity values of the samples

Sample Content of filler (wt%)	Volume (mL)	Volume resistivity, ρ (Ω.cm)	Conductivity, σ (S/m)
PVA/50GH/60Gly	8	1.348×10^{8}	6.78×10^{-7}
PVA/50GH/60Gly	8	2.89×10^{3}	3.46×10^{-2}
PVA/50GH/60Gly	8	1.39×10^{10}	7.13×10^{-7}
PVA/50GH/60Gly	9	1.16×10^{9}	8.62×10^{-8}
PVA/50GH/60Gly	9	2.23×10^{8}	4.47×10^{-7}
PVA/50GH/60Gly	9	6.64×10^{7}	1.51×10^{-6}
PVA/50GH/60Gly	15	2.94×10^{5}	3.40×10^{-4}
PVA/50GH/60Gly	15	9.00×10^{5}	1.11×10^{-4}
PVA/50GH/60Gly	15	3.92×10^{5}	2.55×10^{-4}
PVA/50GH/60Gly	15	1.00×10^{5}	9.98×10^{-5}
PVA/50GH/60Gly	15	3.64×10^{6}	2.75×10^{-4}

Table 11 Bending Angles of Each Sample

Sample Content of filler (wt%)	Volume (mL)	Voltage (V)	Bending angle (◦)
PVA/50GH/60Gly (Kapton)	8	6	5.5
PVA/50GH/60Gly (3M PVC)	8	6	6.3
PVA/50GH/60Gly (PVA Yazaki)	8	6	6.7
PVA/50GH/60Gly (Kapton)	8	21	5.0
PVA/50GH/60Gly (3M PVC)	8	21	5.7
PVA/50GH/60Gly (PVA Yazaki)	8	21	6.3
PVA/50GH/60Gly (Kapton)	8	30	6.3
PVA/50GH/60Gly (3M PVC)	8	30	6.5
PVA/50GH/60Gly (PVA Yazaki)	8	30	7.5
PVA/50GH/60Gly (Kapton)	9	6	4.0
PVA/50GH/60Gly (3M PVC)	9	6	4.3
PVA/50GH/60Gly (PVA Yazaki)	9	6	7.0
PVA/50GH/60Gly (Kapton)	9	21	5.0
PVA/50GH/60Gly (3M PVC)	9	21	6.0
PVA/50GH/60Gly (PVA Yazaki)	9	21	8.0
PVA/50GH/60Gly (Kapton)	9	30	2.0
PVA/50GH/60Gly (3M PVC)	9	30	7.3
PVA/50GH/60Gly (PVA Yazaki)	9	30	7.7
PVA/50GH/60Gly (Kapton)	15	6	7.8
PVA/50GH/60Gly (3M PVC)	15	6	8.0
PVA/50GH/60Gly (PVA Yazaki)	15	6	8.7
PVA/50GH/60Gly (Kapton)	15	21	8.7
PVA/50GH/60Gly (3M PVC)	15	21	9.4
PVA/50GH/60Gly (PVA Yazaki)	15	21	10.0
PVA/50GH/60Gly (Kapton)	15	30	6.2
PVA/50GH/60Gly (3M PVC)	15	30	12.8
PVA/50GH/60Gly (PVA Yazaki)	15	30	14.0

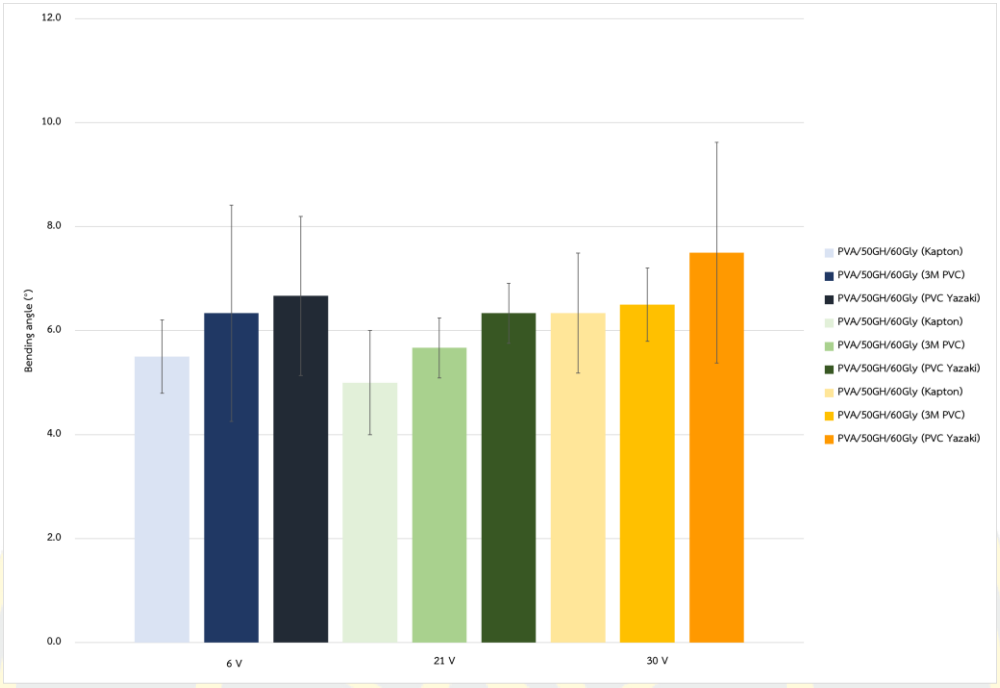

Figure 4.3 Bending angles of the PVA/50GH/60Gly sample with a volume of 8 mL using 3M Kapton Tape, PVC, and Yazaki PVC (Applied voltages: 6V, 21V, and 30V)

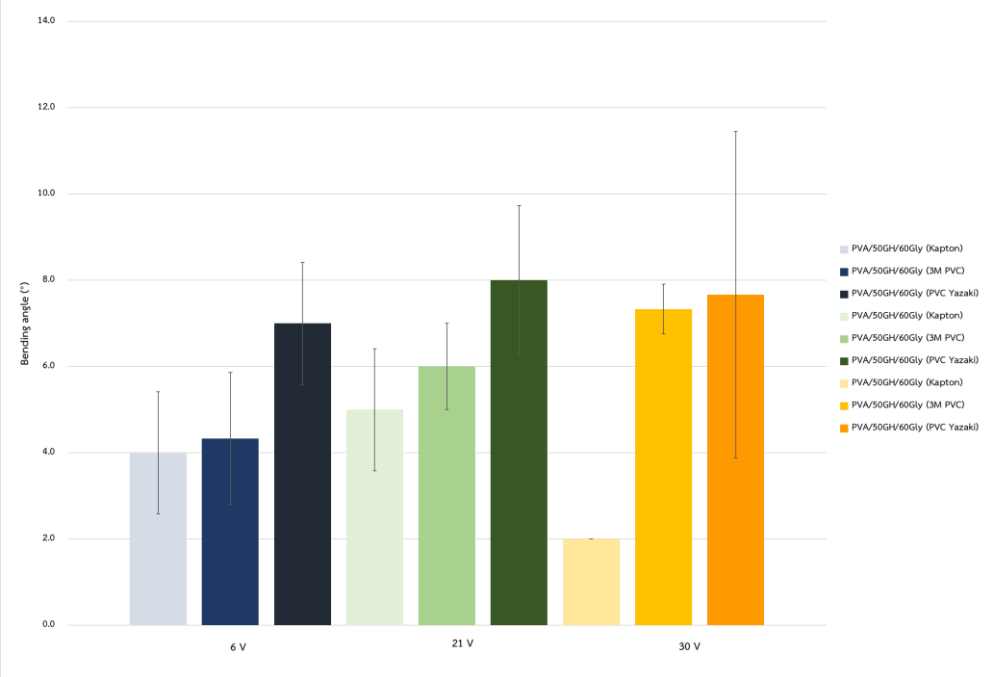

Figure 4.3 Bending angles of the PVA/50GH/60Gly sample with a volume of 9 mL using 3M Kapton Tape, PVC, and Yazaki PVC (Applied voltages: 6V, 21V, and 30V)

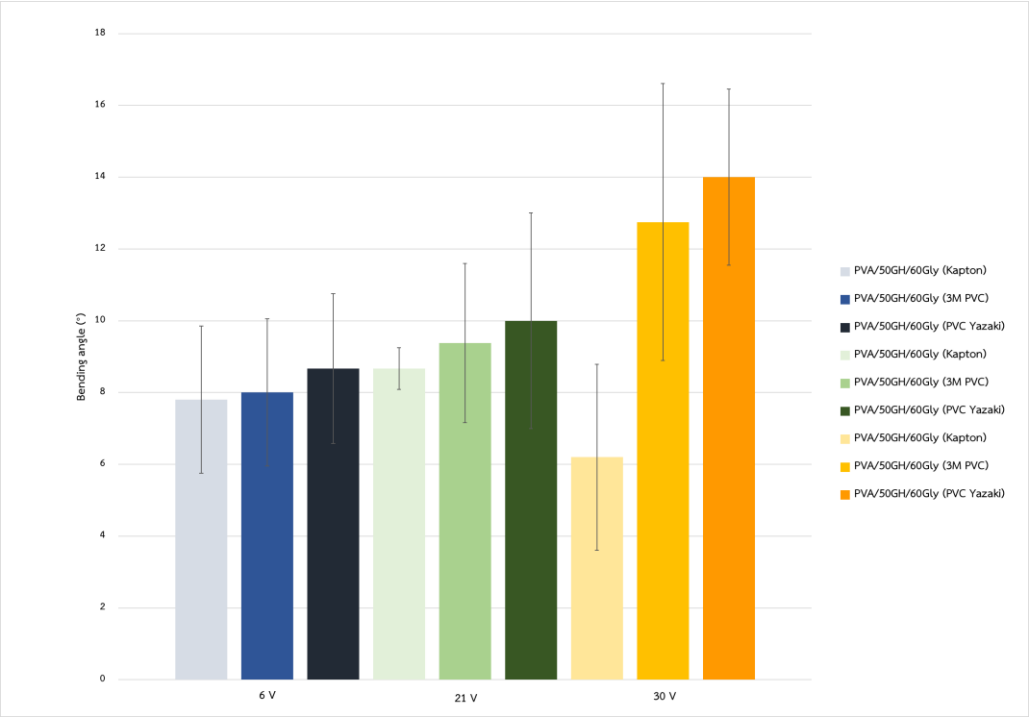

Figure 4.3 Bending angles of the PVA/50GH/60Gly sample with a volume of 15 mL using 3M Kapton Tape, PVC, and Yazaki PVC (Applied voltages: 6V, 21V, and 30V)

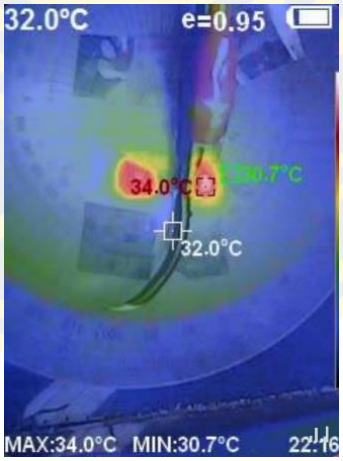

Figure 7 The thermal images of actuator

Table 12 Thickness of PVA/GH/Gly and ETA (Kapton tape)

GH	Volume (mL)	Thickness (mm)			Average		SD	Thickness of Kapton (mm)			Avg.	Thickness
Content of filler (wt%)		1	2	3				1	2	3		film (mm)
PVA/50GH/60Gly	3	0.072	0.121	0.110	0.101		0.101	0.054	0.058	0.054	0.055	0.046
PVA/50GH/60Gly	3	0.109	0.109	0.119	0.112		0.006	0.054	0.058	0.054	0.055	0.057
PVA/50GH/60Gly	3	0.121	0.101	0.130	0.117		0.015	0.054	0.058	0.054	0.055	0.062
PVA/50GH/60Gly	3	0.130	0.121	0.135	0.129		0.007	0.054	0.058	0.054	0.055	0.073
PVA/50GH/60Gly	3	0.125	0.129	0.120	0.125	0.110	0.005	0.054	0.058	0.054	0.055	0.069
PVA/60GH/60Gly	3	0.118	0.112	0.110	0.113		0.004	0.054	0.058	0.054	0.055	0.058
PVA/60GH/60Gly	3	0.109	0.092	0.112	0.104		0.011	0.054	0.058	0.054	0.055	0.049
PVA/60GH/60Gly	3	0.100	0.100	0.110	0.103		0.006	0.054	0.058	0.054	0.055	0.048
PVA/60GH/60Gly	3	0.130	0.100	0.130	0.120		0.017	0.054	0.058	0.054	0.055	0.065
PVA/60GH/60Gly	3	0.121	0.101	0.119	0.114	0.111	0.011	0.054	0.058	0.054	0.055	0.058
PVA/70GH/60Gly	3	0.095	0.119	0.130	0.115		0.018	0.054	0.058	0.054	0.055	0.059
PVA/70GH/60Gly	3	0.100	0.100	0.131	0.110		0.018	0.054	0.058	0.054	0.055	0.055
PVA/70GH/60Gly	3	0.131	0.101	0.121	0.118		0.015	0.054	0.058	0.054	0.055	0.062
PVA/70GH/60Gly	3	0.110	0.106	0.111	0.109		0.003	0.054	0.058	0.054	0.055	0.054
PVA/70GH/60Gly	3	0.131	0.112	0.110	0.118	0.114	0.012	0.054	0.058	0.054	0.055	0.062
PVA/80GH/60Gly	3	0.125	0.126	0.120	0.124		0.003	0.054	0.058	0.054	0.055	0.068
PVA/80GH/60Gly	3	0.130	0.110	0.120	0.120		0.010	0.054	0.058	0.054	0.055	0.065
PVA/80GH/60Gly	3	0.140	0.110	0.121	0.124		0.015	0.054	0.058	0.054	0.055	0.068
PVA/80GH/60Gly	3	0.130	0.105	0.119	0.118		0.013	0.054	0.058	0.054	0.055	0.063
PVA/80GH/60Gly	3	0.141	0.109	0.121	0.124	0.122	0.016	0.054	0.058	0.054	0.055	0.068
PVA/50GH/60Gly	4	0.110	0.105	0.105	0.107		0.107	0.054	0.058	0.054	0.055	0.051
PVA/50GH/60Gly	4	0.122	0.121	0.123	0.122		0.001	0.054	0.058	0.054	0.055	0.067
PVA/50GH/60Gly	4	0.120	0.120	0.121	0.120		0.001	0.054	0.058	0.054	0.055	0.065
PVA/50GH/60Gly	4	0.190	0.127	0.121	0.146		0.038	0.054	0.058	0.054	0.055	0.091
PVA/50GH/60Gly	4	0.190	0.123	0.121	0.145	0.128	0.039	0.054	0.058	0.054	0.055	0.089
PVA/60GH/60Gly	4	0.198	0.101	0.121	0.140		0.051	0.054	0.058	0.054	0.055	0.085
PVA/60GH/60Gly	4	0.121	0.125	0.102	0.116		0.012	0.054	0.058	0.054	0.055	0.061
PVA/60GH/60Gly	4	0.119	0.126	0.100	0.115		0.013	0.054	0.058	0.054	0.055	0.060
PVA/60GH/60Gly	4	0.130	0.132	0.101	0.121		0.017	0.054	0.058	0.054	0.055	0.066
PVA/60GH/60Gly	4	0.110	0.105	0.149	0.121	0.123	0.024	0.054	0.058	0.054	0.055	0.066
PVA/70GH/60Gly	4	0.125	0.122	0.199	0.149		0.044	0.054	0.058	0.054	0.055	0.093
PVA/70GH/60Gly	4	0.130	0.130	0.129	0.130		0.001	0.054	0.058	0.054	0.055	0.074
PVA/70GH/60Gly	4	0.145	0.121	0.149	0.138		0.015	0.054	0.058	0.054	0.055	0.083
PVA/70GH/60Gly	4	0.108	0.121	0.142	0.124		0.017	0.054	0.058	0.054	0.055	0.068
PVA/70GH/60Gly	4	0.140	0.129	0.121	0.130	0.134	0.010	0.054	0.058	0.054	0.055	0.075
PVA/80GH/60Gly	4	0.120	0.131	0.128	0.126		0.006	0.054	0.058	0.054	0.055	0.071
PVA/80GH/60Gly	4	0.141	0.110	0.130	0.127		0.016	0.054	0.058	0.054	0.055	0.072
PVA/80GH/60Gly	4	0.140	0.115	0.109	0.121		0.016	0.054	0.058	0.054	0.055	0.066
PVA/80GH/60Gly	4	0.100	0.121	0.130	0.117		0.015	0.054	0.058	0.054	0.055	0.062
PVA/80GH/60Gly	4	0.129	0.102	0.152	0.128	0.124	0.025	0.054	0.058	0.054	0.055	0.072

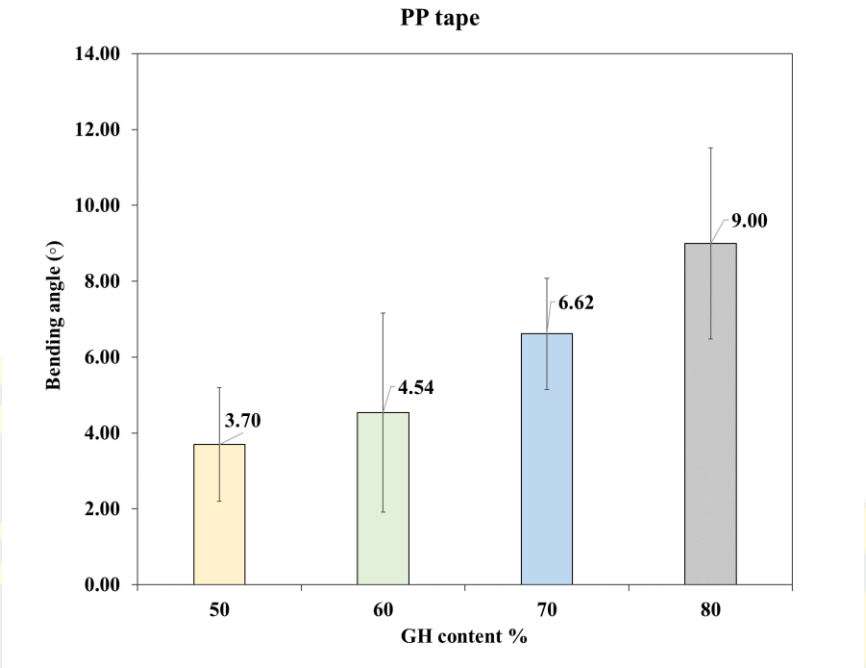

Figure 2 Bending angle of the actuator (PP tape)

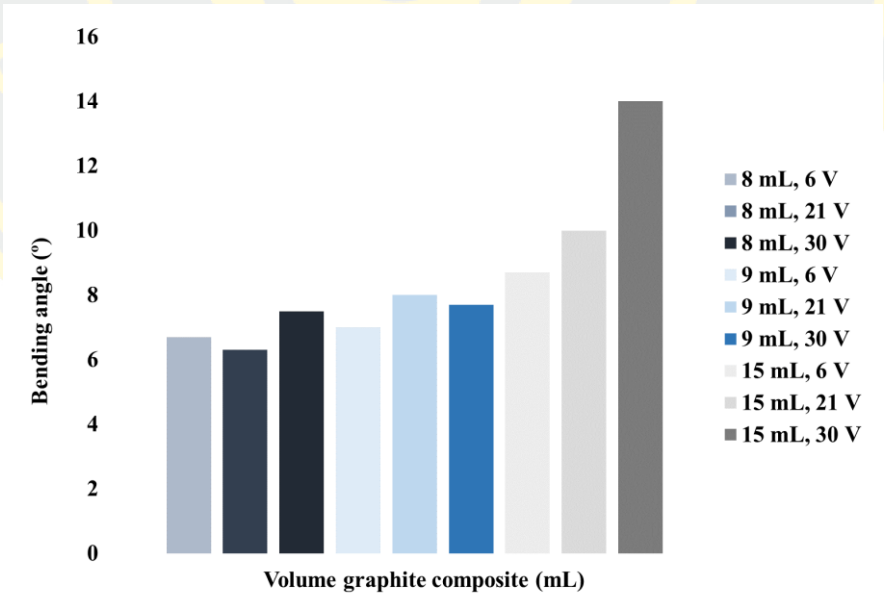

Figure 3 The bending angle of the actuator prepared with different solution volumes of 8 and 9 mL at voltages of 6, 21, and 30 v.

Table 13 Bending angles of each sample formula

Sample Content of filler (wt%)	Volume (mL)	Bending angle (◦)
PVA/10GH/22Gly	15	1.50
PVA/10GH/24Gly	15	5.00
PVA/10GH/26Gly	15	7.00
PVA/10GH/28Gly	15	3.00
PVA/10GH/30Gly	15	4.00
PVA/50GH/30Gly	15	2.75
PVA/50GH/40Gly	15	3.50
PVA/50GH/50Gly	15	7.83
PVA/50GH/60Gly	15	12.33
PVA/50GH/70Gly	15	4.80
PVA/60GH/30Gly	15	6.75
PVA/60GH/40Gly	15	8.25
PVA/60GH/50Gly	15	2.25
PVA/60GH/60Gly	15	5.00
PVA/60GH/70Gly	15	6.80
PVA/70GH/30Gly	15	4.20
PVA/70GH/40Gly	15	2.50
PVA/70GH/50Gly	15	5.90
PVA/70GH/60Gly	15	7.25
PVA/70GH/70Gly	15	5.40
PVA/80GH/30Gly	15	5.00
PVA/80GH/40Gly	15	7.63
PVA/80GH/50Gly	15	2.17
PVA/80GH/60Gly	15	2.40
PVA/80GH/70Gly	15	8.60

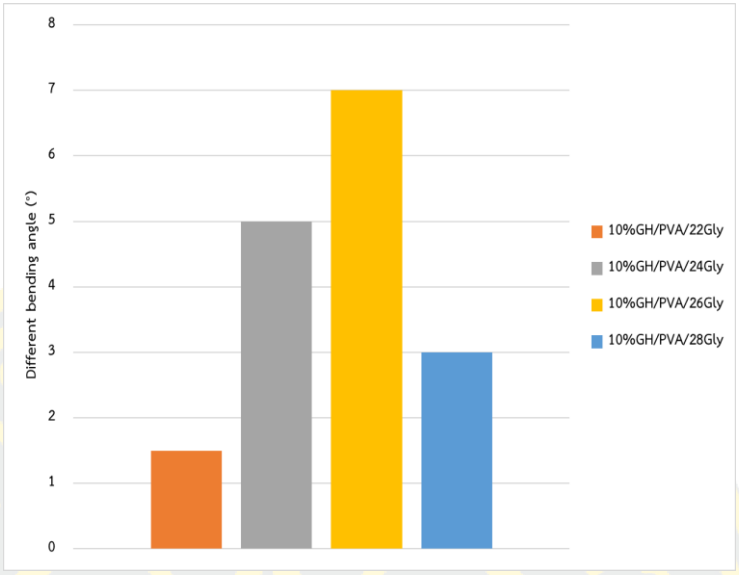

Figure 4.17 Bending Angles of the 10GH/PVA/22 24 26 28Gly Sample (Applied Voltage: 6V)

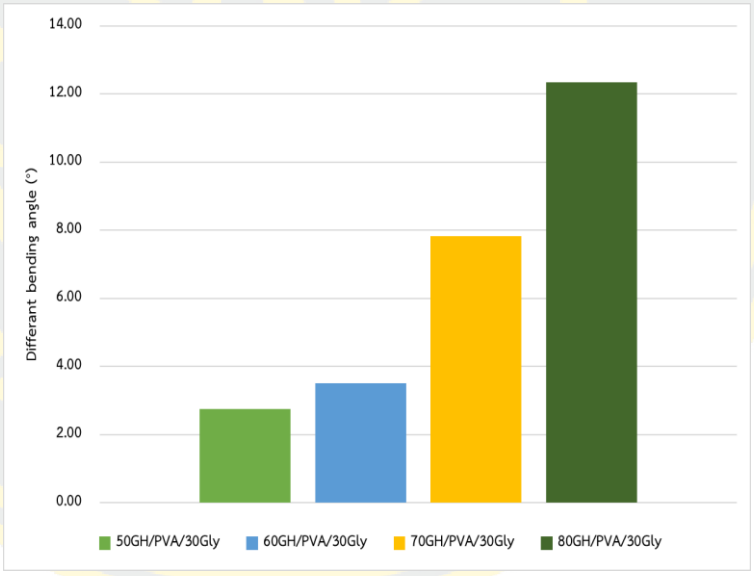

Figure 4.18 Bending Angles of the 50 60 70 80GH/PVA/30Gly Sample (Applied Voltage: 6V)

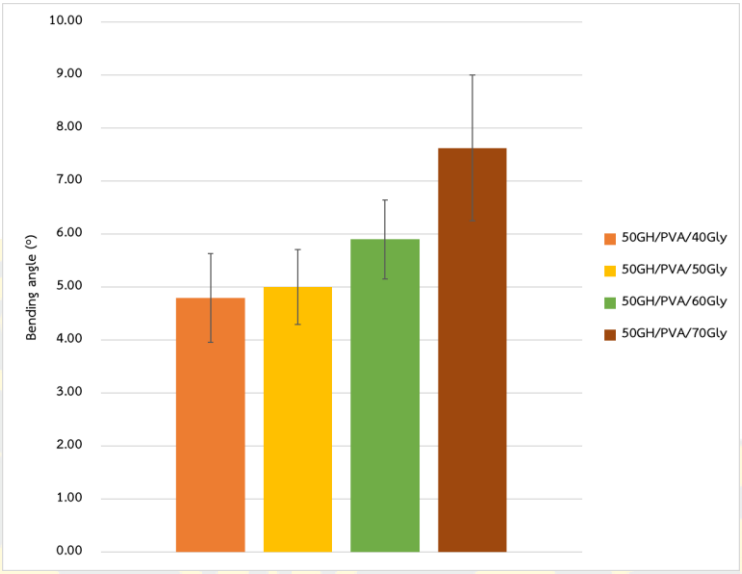

Figure 4.19 Bending Angles of the 50GH/PVA/40 50 60 70Gly Sample (Applied Voltage: 6V)

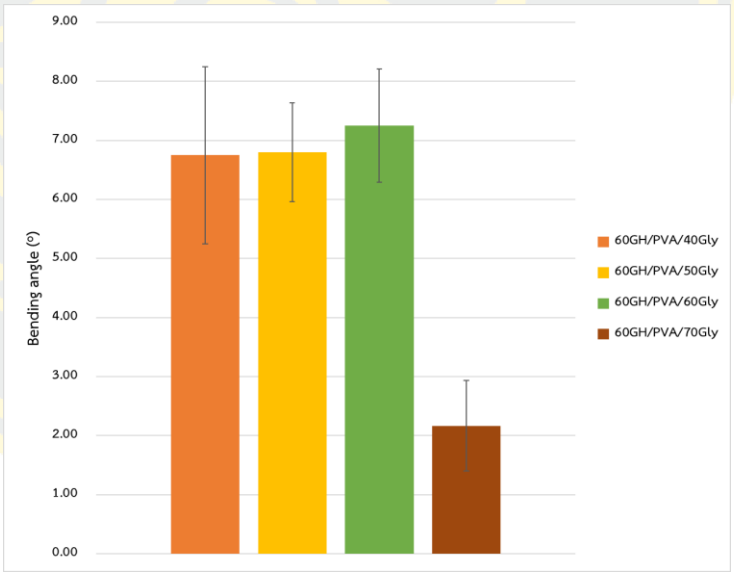

Figure 4.20 Bending Angles of the 60GH/PVA/40 50 60 70Gly Sample (Applied Voltage: 6V)

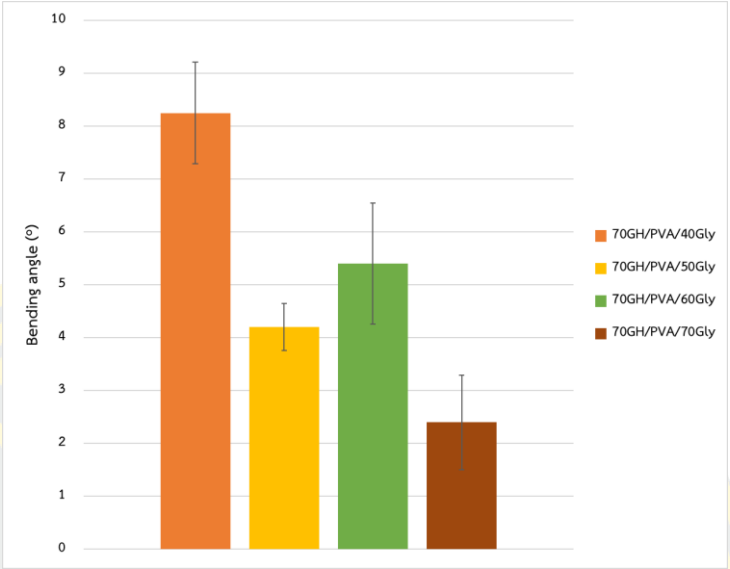

Figure 4.21 Bending Angles of the 70GH/PVA/40 50 60 70Gly Sample (Applied Voltage: 6V)

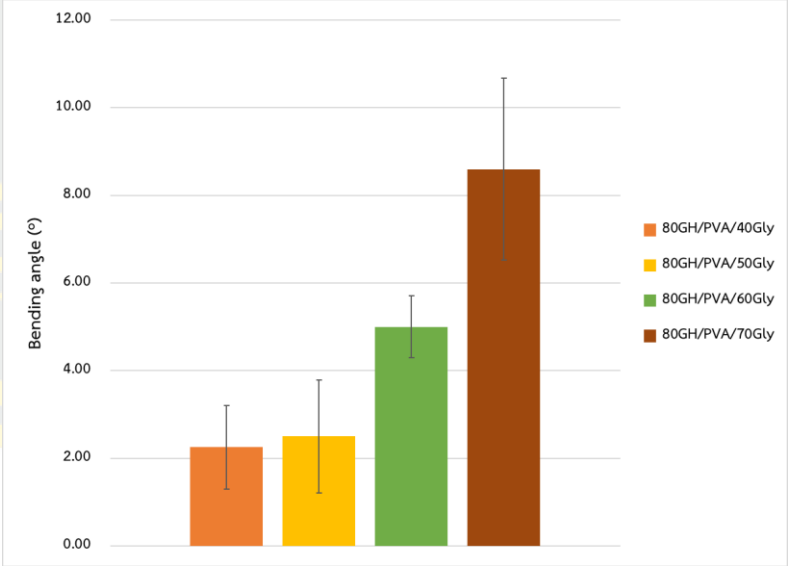

Figure 4.22 Bending Angles of the 80GH/PVA/40 50 60 70Gly Sample (Applied Voltage: 6V)

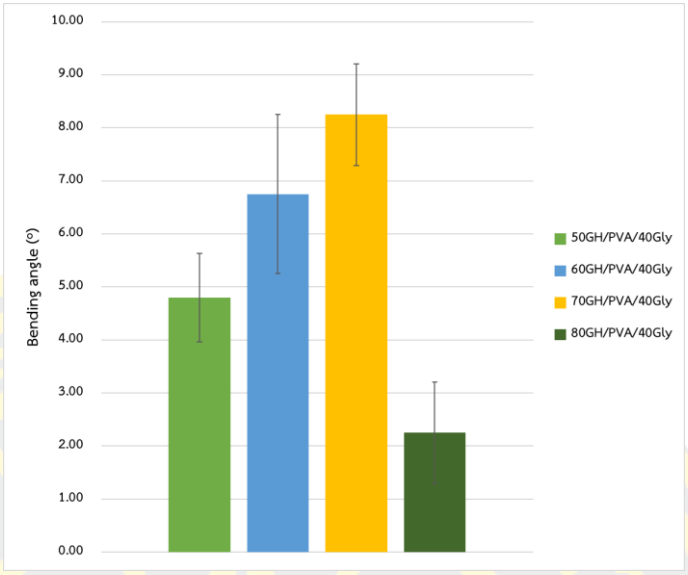

Figure 4.23 Bending Angles of the 50 60 70 80GH/PVA/40Gly Sample (Applied Voltage: 6V)

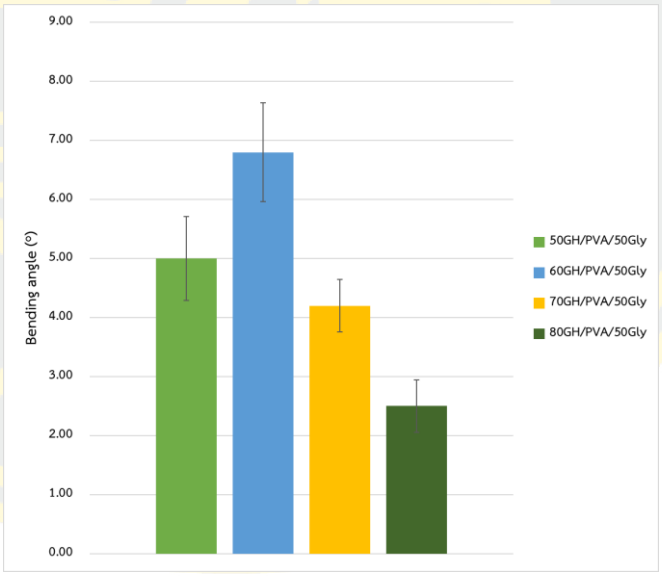

Figure 4.24 Bending Angles of the 50 60 70 80GH/PVA/50Gly Sample (Applied Voltage: 6V)

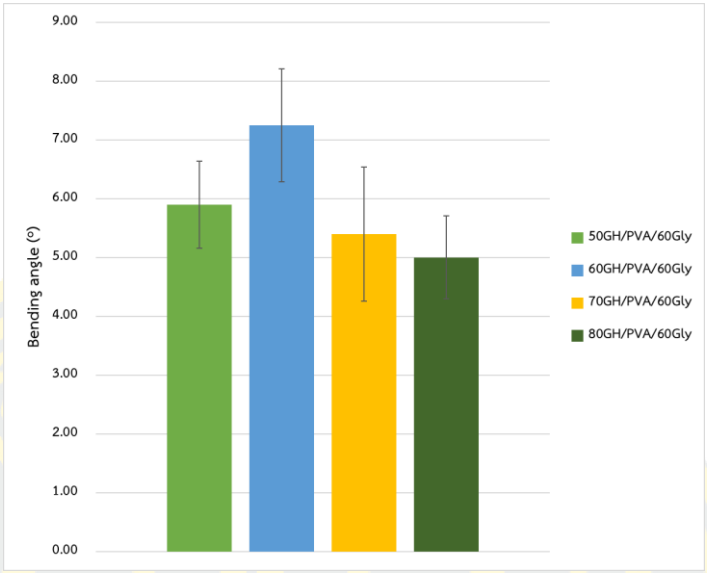

Figure 4.25 Bending Angles of the 50 60 70 80GH/PVA/60Gly Sample (Applied Voltage: 6V)

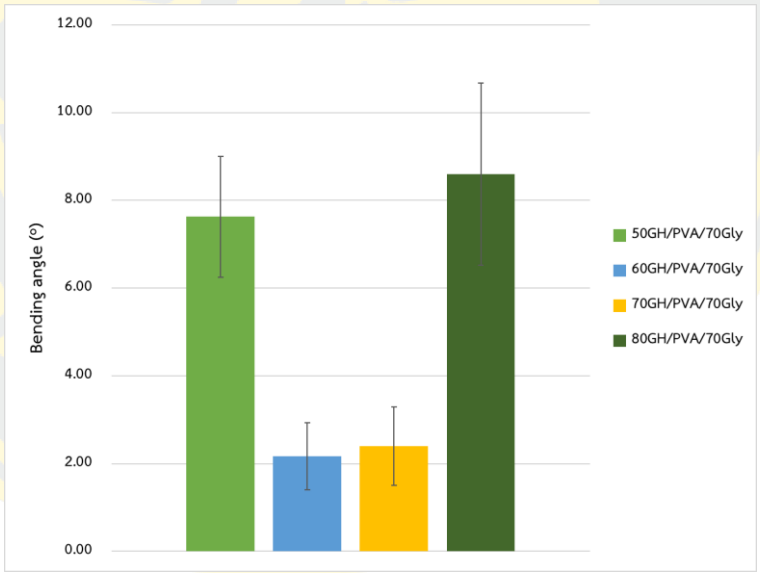

Figure 4.26 Bending Angles of the 50 60 70 80GH/PVA/70Gly Sample (Applied Voltage: 6V)

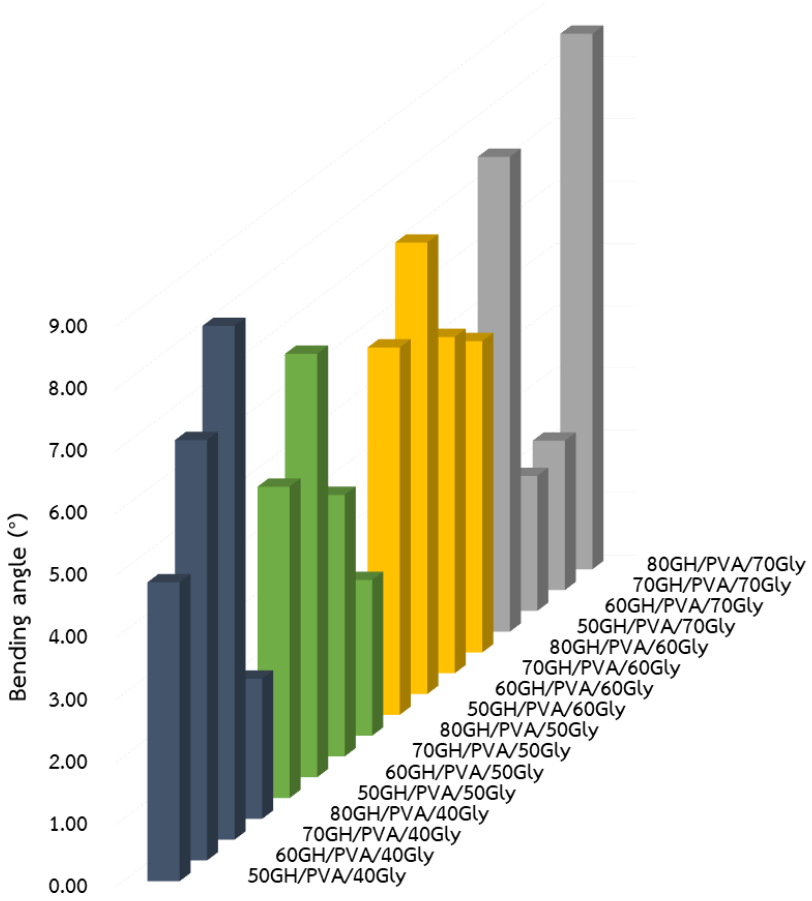

Figure 4.27 Bending Angles of Composite Films with Varying Concentrations of Graphite and Glycerol

Table 14 Blocking force of the actuator.

Time (s)	Force gripper (mN)			
	50GH	60GH	70GH	80GH
10	0.0275	0.0716	0.0127	0.0226
20	0.0412	0.0745	0.0255	0.0324
30	0.052	0.0814	0.0343	0.0451
40	0.0618	0.0853	0.0422	0.0490
50	0.0686	0.0863	0.0500	0.0569
60	0.0755	0.0873	0.0579	0.0637
70	0.0824	0.0892	0.0618	0.0726
80	0.0863	0.0922	0.0686	0.0824
90	0.0932	0.0951	0.0735	0.0892
100	0.099	0.0941	0.0784	0.0990
110	0.101	0.0941	0.0804	0.1118
120	0.1010	0.0912	0.0873	0.1216
130	0.0284	0.0922	0.0912	0.1255
140	0.0402	0.0922	0.0941	0.1353
150	0.0530	0.0912	0.0981	0.1461
160	0.0657	0.0902	0.1000	0.1530
170	0.0755	0.0892	0.1030	0.1579
180	0.0853	0.0883	0.1079	0.1677
190	0.0883	0.0892	0.1108	0.1755
200	0.0951	0.0863	0.1138	0.1746
210	0.0873	0.0863	0.1147	0.1775
220	0.0010	0.0863	0.1177	0.1863
230	0.0118	0.0863	0.1196	0.1873
240	0.0137	0.0853	0.1236	0.1873

APPENDIX B

Publications

1. (Proceedings) Preliminary study of low voltage activating, double layer electroactive actuator base on graphite composite

2. (Proceedings) Effect of calendaring on properties of electrothermal actuators based on graphite composite

PACCON KMITL 2022 "Frontiers in Chemical Sciences for Health, Energy, and Sustainability"

Preliminary study of low voltage activating, double layer electroactive actuator base on graphite composite

S. Thakasame[1], T. Nongnual[1], S. Kaewpirom[1*] and S. Boonsang[2]
[1]*Department of Chemistry, Faculty of Science, Burapha University, Chonburi 20131, Thailand.*
[2]*Department of Electrical Engineering, Faculty of Engineering, King Mongkut's Institute of Technology Ladkrabang, Bangkok 10520, Thailand.*

*Corresponding author: kaewpiro@go.buu.ac.th

Abstract:

This paper presents a flexible graphite composite/Kapton tape actuator as a U-shaped electroactive smart device, capable of changing shapes in direct response to electrical stimuli. A double layer actuator was designed and fabricated. It's composed of a conductive layer with high electrical and thermal conductivity, flexibility and hardness and a polymer layer with high coefficient of thermal expansion (CTE) and low modulus. A model system with a thickness in the range 0.30 and 0.39 mm, consisting of graphite composite and Kapton tape with high CTE of 10 ppm $°C^{-1}$, was chosen. The effect of graphite content on bending angle of the system was investigated. The graphite content was varied at 50, 60, 70 and 80%wt. Under a low driving voltage of 6 V by DC power supply, the actuator containing 60%wt of graphite showed a bending angle of 7° within 120 s. The results confirmed the possibility of the proposed graphite composite/Kapton tape system as a low voltage driven electroactive actuator. This could lead to a smart device that can convert electric energy in to mechanical energy under electrical stimulation. Once developed, this high-performance actuator can be used in a wide range of industries, e.g. robotic end effectors and grippers for material handling tasks.

Keywords: Graphite composite, Electroactive actuator, Low-voltage activating

1. Introduction

Electroactive actuators (ETA) that show reversible mechanical deformation in response to an electric field have received enormous interest in the era of biomimetic technology, including robotics.[1] Soft actuators can build interactions with humans and have attracted much interest in various applications, such as microfluidic channels, minimally invasive surgery devices, smart fabric, artificial muscles and soft robots.[2] Soft robots have been attracting significant attention because these robots have potential to bring a new era of robotics and be used in several real-world applications. Recent advances in soft robots have made them probable to grow complex functionalities that imitator the various motions of living creatures such as mobile, crawling, climbing and gripping.[3,4]

Polyvinyl alcohol (PVA) is a synthetic water-soluble biopolymer that is normally prepared by the saponification of polyvinyl acetate. PVA has received considerable attention due to its biodegradable character, transparency and good mechanical and thermal properties. Moreover, it has outstanding flexibility and recyclability and bio-tribological properties.[5,6]

U-shaped actuator double layer ETA structure consisting of a conductive layer with high electrical and thermal conductivity, flexibility and hardness and a polymer layer with high coefficient of thermal expansion (CTE) and low modulus. Those two materials own different CTE and the actuator can bend to the side with lesser CTE.[7] Among all thermal conductive fillers, graphite merits special attention not only due to its high thermal conductivity, but also high thermal stability, excellent chemical resistance and good mechanical properties. Moreover, graphite is a cheap material and performed better than other expensive conductive particles. Generally, the thermal conductivity growths nearly linearly with an increase in graphite content.[8] Besides, Kapton tape or polyimide (PI) film is a promising material due to its excellent mechanical properties and outstanding thermal stability at elevated temperatures as well as high CTE.[9]

In this study, a flexible graphite composite/Kapton tape actuator was developed. PI film with a CTE less than 10 ppm $°C^{-1}$ was used as a polymer layer and PVA/graphite composite was used as a conductive layer. The thickness of the model system and the effect of graphite content on bending angle of the model system were investigated as a function of graphite content (50, 60, 70 and 80%wt). The physical properties and the electrical conductivity of the model systems were also examined.

© The 2022 Pure and Applied Chemistry International Conference (PACCON 2022)

2. Materials and Methods

2.1 Materials

Extra pure graphite fine powder with the particle size < 50 µm and ≥ 99.5% purity was from Merck, Germany. Kapton tape with 5-mm width and 0.055-mm thickness were from 3M. Glutaraldehyde (1.2% w/v) was obtained from Fluka. Polyvinyl alcohol (PVA), Mw 89,000-98,000 g/mol, 99+% hydrolyzed, was from Sigma-Aldrich. Sulfuric acid (95-97%) and methanol (AR grade) were from QRëC. Acetic acid, (AR grade) was from Scharlan. Glycerol (92.09%), with the density of 1.2570 g/mL, analytical reagent, was from Ajax Finechem.

2.2 Preparation of graphite composite film

A 10%w/v polyvinyl alcohol solution was prepared using distilled water, stirred at 90 ºC for 2 h, and allowed to cool to room temperature. Into the prepared polymer solution (25 mL), glycerol 60%w/w with respect to PVA weight, was added and the solution was stirred for 2 min. Graphite was added at various concentrations (50, 60, 70 and 80%w/w), with continuous stirring for 10 minutes until homogeneous. Then, 2.8 mL of crosslink solution (methanol: acetic acid: glutaraldehyde: sulfuric acid with the volume ratio of 3:2:1:1) was added and the solution was stirred for 15 minutes. The solution was poured into a Petri dish. After pouring, the solution was sat at room temperature for 5 minutes to reduce air bubbles before being baked in a hot air oven at 70 ºC for 4 h. Later, the graphite film was removed. The film's thickness as well as the electrical conductivity were measured.

2.3 Electrical conductivity

Electrical conductivity measurement of the PVA/graphite composite films was performed with a digital multimeter (Agilent 34410) at room temperature, using copper electrode pads. The two 1.0×2.2 cm^2 copper sheets were placed on a 3.5×5.0 cm^2 PVA/graphite composite film, allowing a 1.5 cm space between the two pads. The red-black probe was pressed between the copper electrodes at a distance of 1.3 cm. Each measurement was performed for 50 s before the resistance was read. The volume resistivity (ρ_v) was calculated using equation (1), according to ASTM D257-90.[10] The corresponding volume conductivity (σ_v) was also calculated using equation (2).

$$\rho_v = \frac{A}{T} \times R_v \qquad (1),$$

where A = (a + g) (b + g)
R_v is the electrical resistivity (Ω),
A is the electrode surface area (cm^2),
T is the averaged thickness (cm),
g is the dimension of the digital multimeter probe (cm),
a, b are the lengths of the rectangular electrode (cm).

$$\sigma = \frac{1}{\rho} \qquad (2),$$

where ρ and σ are the resistivity (Ω·m) and the electrical conductivity (S/m), respectively.[11]

2.3 Characterization of graphite composite

The thickness of both the graphite composite and the model system was measured by a micrometer. DC power supply (Digital DRP-303D) was utilized to supply different voltages and activate the PVA/graphite composite film. Digital multimeter, Agilent 34410A (Agilent Technologies), was used to measure DC voltage and current. The resulted bending angle under applied voltages was recorded by a digital camera. The bending curvature of graphite composite/Kapton tape actuator was measured by a circle protractor (No.990 INCA).

3. Results & Discussion

3.1 Electroactive actuator mold systems

The proposed model system, consisting of graphite composite and Kapton tape is shown in Figure 1a. The set up and the bending test under a low driving voltage of 6 V, by a DC power supply, were shown in Figure 1b and 1c, respectively.

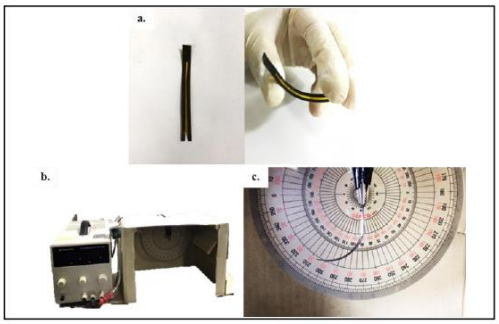

Figure 1. Physical appearance of an actuator model system (a), setting up device (b) for a bending test (c) of the actuator when an electric potential was applied.

The effect of graphite content on the thickness of PVA/graphite films and the model actuator systems is shown in Figure 2. The thickness of both actuator and composite film tends to increase with increasing graphite content. Comparable results were presented by

© The 2022 Pure and Applied Chemistry International Conference (PACCON 2022)

Umar et al.[12], who reported that SWCNT/ graphite films with various graphite mass fractions of 0, 50, 85 and 95 wt% showed the film thicknesses varied from ~100 to 500 µm. Graphite was uniformly distributed in most cases and orientated parallel to the plane of the films. However, in Figure 2, the film with 50%wt graphite is slightly thicker than that with 60%wt graphite. This may be due to the uneven distribution of graphite throughout the film, creating gaps in the film and causing the film to be thicker than usual.

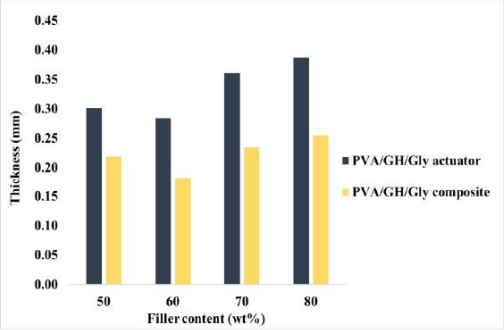

Figure 2. The thickness of graphite composite film and graphite composite/Kapton tape actuators.

3.2 Resistivity and conductivity

Figure 3a and 3b show the volume resistivity and volume conductivity of the PVA/graphite films as a function of graphite content, respectively.

From the results, it was found that volume resistivity reduced with the increased concentration of graphite. When the amount of graphite increased from 50%wt to 80%wt, the volume resistivity of the composites significantly decreased from 1.67×10^{6} Ω.cm. to 2.48×10^{5} Ω.cm. The results are in accordance with the results proposed by Dilhan et al.[13] that graphite composites, showed volume resistivity of 10^{6} Ω.cm to 10^{11} Ω.cm as the graphite content increased from 10%wt to 40%wt. Guo et al.[14] also showed that with the increase of graphite content, the volume resistivity of the graphite composites gradually decreased. Volume conductivity of the model system was shown in Figure 3b. With 50%wt graphite, the system showed the volume conductivity of 6.43×10^{-5} S/m. The value increased to 4.15×10^{-4} S/m when graphite content increased to 80%wt. Similar results were presented by Kim et al.[15], who reported that the volume conductivity of PE/graphite composites increased from 2.4×10^{-6} S/m to 8.0×10^{-4} S/m as the graphite content increased from 20%wt to 50%wt. With increasing graphite content, the electric current in the sample caused by the movement of electrons from the filler increased, resulting in the increased volume conductivity.[16] According to Abd-El Salam et al.[17], a slight change in the filler content of the composite changed its electrical conductivity.

From the results, it was found that each composite film formulation was conductive in its conductive layer. Hence, when the electric potential is applied, it was supposed to bend towards the conductive layer.

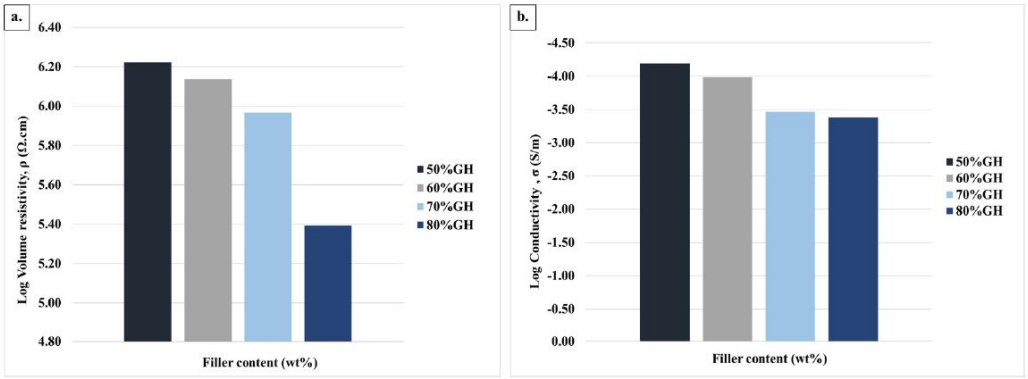

Figure 3. The volume resistivity (a) and volume conductivity (b) values of the composite films as a function of graphite content.

3.3 Bending angle of the model actuators

Figure 4 shows the bending angle of the model actuators, consisting of PVA/graphite composites with different graphite contents. With 50, 60, 70 and 80%w/w of graphite, the systems showed the bending angle of 5.90°, 7.25°, 5.40° and 5.00°, respectively. The actuator containing of 60%wt graphite showed the highest bending angle. This may be because at 60%wt graphite, the thickness of the actuator is the smallest, therefore, the actuator can be driven easiest at the low driving voltage of 6 V.[18]

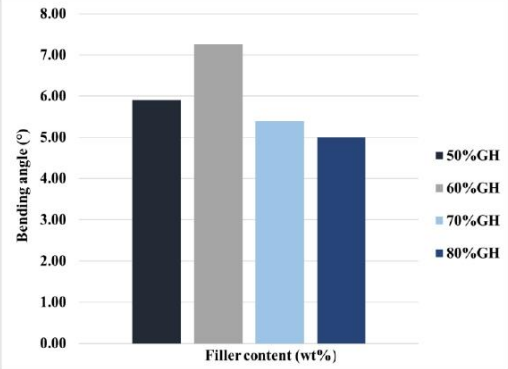

Figure 4. The bending angle of the proposed model actuators as a function of graphite content.

Table 1 summarized the performances of other soft actuator-based materials such as graphite oxide, carbon nanotube powder and multi-walled carbon nanotube in comparison with our proposed systems.

4. Conclusion

In this preliminary study, low voltage activating, double layer electroactive actuators base on graphite composite were successfully prepared. As the thickness of the model systems reduced, their volume conductivity increased relatively. The actuator containing 60%wt graphite exhibited bending angle of 7° at a low driving voltage of 6 V within 120 seconds. Therefore, ETAs bending deformation can be controlled by the driving voltage. After further improvement, this actuator could be used in a wide range of industries e.g. robotic end effectors and soft robotics grippers.

Table 1. Bending angles comparison with.

	Voltage (V)	Actuation*	Time (s)	References
CNT/KAPTON	100	300°	10	[19]
CNT/KAPTON	30	12 mm	~ 23	[6]
GO/PI film	65	270°	8	[20]
MWCNTs/WPU	7	28 mm	50	[21]
CNTF/PDMS	8	324°	12	[18]
GH/KAPTON	6	7°	120	This study

*Support information for bending angle and displacement comparison

Acknowledgements

This work was financially supported by Thailand Science and Research Innovation Fund and King Mongkut's Institute of Technology Ladkrabang Fund (RE-KRIS-016-64). Science Innovation Facility, Faculty of Science, Burapha University (SIF-IN-40100054) is also gratefully acknowledged.

References

1. Kim, O.; Shin, T. J.; Park, M. J. Fast low-voltage electroactive actuators using nanostructured polymer electrolytes. *Nature Communications*. **2013**, *4*.
2. Watanabe T.; Yokoyama Y.; Hayakawa T. Structurally isolated photoactuation of graphene-mixed temperature-responsive hydrogels in soft-rigid series structure. *Robomech Journal*. **2019**, *6*(1), 11

3. Kellaris, N.; Gopaluni Venkata, V.; Smith, Garrett M.; Mitchell, Shane K.; Keplinger, C. *Peano-HASEL* actuators: Muscle-mimetic, electrohydraulic transducers that linearly contract on activation. *Science Robotics*. **2018**, *3*(14)
4. Chellattoan, R.; Yudhanto, A.; Lubineau, G. Low-voltage-driven large-amplitude soft actuators based on phase transition. *Soft Robotics, soro.***2020**
5. Olalla A.L.; Sara L.I.; and Ricardo B. Academic editors: Florian J. Stadler and Alberto García-Peñas *Polymers*. **2021**, *13*(21), 3742
6. Amjadi, M., & Sitti, M., Self-Sensing Paper Actuators Based on Graphite-Carbon Nanotube Hybrid Films. *Advanced Science* **2018,** *5* (7), 1800239.
7. Fan, Q.; Miao, J.; Tian, M.; Zhao, H.; Zhu, S.; Liu, X., … Qu, L. Low-voltage driven flexible double-layer electrothermal actuator for smart human-machine interactions. *Sensors and Actuators A: Physical.* **2020**, 112352.
8. Mokhena, T.C.; Mochane, M.J.; Sefadi, J.S.; Motloung, S.V.; & Andala, D.M.; Thermal conductivity of graphite-based polymer composites. *Impact of Thermal Conductivity on Energy Technologies*. **2018**, 181-197.
9. Liu, F.; Liu, Z.; Gao, S.; You, Q.; Zou, L.; Chen, J.; Liu, J.; Liu, X. Polyimide film with low thermal expansion and high transparency by self-enhancement of polyimide/SiC nanofibers net. *RSC Advances*. **2018**, *8*(34), 19034–19040.
10. Anne L.S. Electromechanically Active Polymer (EAP) transducers & artificial muscles. EuroEAP 2016. *Biochemical and Chemical Engineering the Technical University of Denmark (DTU) 2800 Kgs Lyngby, Denmark.* **2016**.
11. Zainab R. *Standard test methods for DC resistance or conductance of insulating materials:* University of California Berkeley Library pursuant to License Agreement, June 2007.
12. Umar K.; Ian O.; Yurii K. G.; Jonathan N. C. The preparation of hybrid films of carbon nanotubes and nano-graphite/graphene with excellent mechanical and electrical properties. *Carbon* **2010,** *48* (10), 2825 – 2830.
13. Dilhan M.K.; Elvan B.; Rahmi Y.; Bahadir K.; Shawn W. Electrical properties of composites as affected by the degree of mixedness of the conductive filler in the polymer matrix. *Polymer engineering and science.* **2002**, *42*(7), 1609–1617.
14. Guo, R.; Ren, Z.; Bi, H.; Xu, M.; Cai, L. Electrical and thermal conductivity of polylactic Acid (PLA)-based biocomposites by Incorporation of Nano-graphite fabricated with fused deposition modeling. *Polymers*. **2019**, *11*(3), 549
15. Kim Y.H.; Kim D. H.; Kim J. M.; Kim S. H.; Kim W. N.; Lee H. S. Effects of filler characteristics and processing conditions on the electrical, morphological and rheological properties of PE and PP with conductive filler composites. **2009,** *17* (2), 110–115.
16. Rattanaweeranon S.; Limsuwan P.; Thongpool V.; Piriyawong V.; Asanithi P. Influence of Bulk Graphite Density on Electrical Conductivity, *Procedia Engineering*. **2012**, *32,* 1100–1106.
17. Abd-El Salam, M. H.; Elkomy, G. M.; Osman, H.; Nagy, M. R.; El- Sayed, F. Structure-electrical conductivity of polyvinylidene fluoride/graphite composites. *Journal of Reinforced Plastics and Composites*. **2012**, *31*(20),1342–1352
18. Aouraghe, M. A.; Mengjie, Z.; Qiu, Y.; & Fujun, X. Low-voltage activating, fast responding electro-thermal actuator based on carbon nanotube Film/PDMS composites. *Advanced Fiber Materials.* **2021**, *3*(1), 38–46.
19. Sachyani E.; Layani M.; Tibi G.; Avidan T.; Degani A.; Magdassi S. Enhanced movement of CNT-based actuators by a three-layered structure with controlled resistivity. *Sensors and Actuators B: Chemical* **2017,** *252*, 1071–1077.
20. Zhang T-Y.; Wang Q.; Deng N-Q.; Zhao H-M.; Wang D-Y.; Yang Z.; Liu Y.; Yang Y.; Ren T-L. A large-strain, fast-response, and easy-to-manufacture electrothermal actuator based on laser-reduced graphene oxide. *Applied Physics Letters* **2017,** *111* (12), 121901.
21. Zeng Z.; Jin H.; Zhang L.; Zhang H.; Chen Z.; Gao F; Zhang Z. Low-voltage and high-performance electrothermal actuator based on multi-walled carbon nanotube/polymer composites. *Carbon* **2015,** *84*, 327–334.

© The 2019 Pure and Applied Chemistry International Conference (PACCON 2019)

Chemical Diversity Towards Sustainable Development Goals
20 - 21 January 2023
A Celebration of Mae Fah Luang University 25th Anniversary
A Celebration of MFU 25th Anniversary
PACCON 2023
Pure and Applied Chemistry International Conference

Effect of calendaring on properties of electrothermal actuators based on graphite composite

Sarawadee Thakasame[1], Supranee Kaewpirom[1*] and Siridech Boonsang[2]
[1]*Department of Chemistry, Faculty of Science, Burapha University, Chonburi 20131, Thailand.*
[2]*Department of Electrical Engineering, Faculty of Engineering, King Mongkut's Institute of Technology Ladkrabang, Bangkok 10520, Thailand.*
**E-mail: kaewpiro@go.buu.ac.th*

Abstract:
In this study, a graphite composite/Kapton tape actuator was developed as a U-shaped flexible electroactive-driven material. With moderately difference in thermal expansion coefficients of graphite and Kapton tape and the excellent electrothermal property of graphite itself, the developed flexible double-layer electroactive actuator showed a driving performance at low applied voltages. The effect of calendaring on properties of the proposed actuator was examined in terms of conductivity, bending angle, and blocking force. The experimental results showed that under a low driving voltage of 6 V, by DC power supply, the actuators, containing 50%wt of graphite, with calendaring and non-calendaring, exhibited bending angles in the range 15 - 22º and 11 - 15 º, respectively within 120 seconds. The corresponding blocking forces were found in the range 0.001- 0.101 mN. Therefore, the proposed actuator could possibly use as electroactive actuators in many applications such as soft robotics and end effectors.

1. Introduction

Soft actuators are materials that can convert external stimuli into mechanical motion. Soft actuators operate by various physical, chemical, and optical stimulus such as electricity, heat, light, pressure, and humidity.[1,2] They have attracted much attention for use in many applications such as manufacturing related robots, artificial muscles, wearable devices, smart systems, and micromanipulators.[3] Electro-thermal flexible actuator (ETA) is a type of soft actuators, based on either thermal expansion of a single film or on the difference in thermal expansion between two layers.[4] The electrothermal system offers flexibility in the choice of materials, low-cost fabrication, and large displacement abilities.[5] ETAs can be activated under a relatively low voltage and do not require any fluids to produce large deformations.[6,7] A typical soft ETA driven by electric stimulus is composed of two layers: a polymer layer and a pivotal conductive layer, with different thermal expansion coefficient (CTE). [4,8] When voltages are applied, the conductive layer with a lower CTE generates the joule heat to heat up the whole ETA. Because of the difference in CTE, the substrate with higher CTE will expand more, producing a bending deformation to the lower-CTE layer.[9] The selected polymers are supposed to large CTE, low Young's modulus elasticity, good flexibility, chemical inertness, remarkable durability against repeated deformation, and resistance to high temperature, such as polydimethylsiloxane (PDMS) elastomer and polyimide (PI).[8]

Polyimide (PI) or Kapton has attracted growing interest with its unique temperature stability and excellent mechanical properties with T_g of 385 ºC and CTE less than 10 ppm $ºC^{-1}$. Moreover, the advantages of PI include high electrical insulation, low density, high toughness, temperature stability, flexibility, and mechanical stability.[10,11,12]

Conductivity layer can contract or expand when temperature changes. It has excellent electrical conductivity and thermal conductivity. [13] Graphite is one of the materials used to make conductive conductors. It has unique properties such as high thermal and electrical conductivity, low coefficient of thermal expansion, exceptional thermal resistance, high thermal shock resistance, and high stiffness and strength.[13]

In this study, graphite/polyvinyl alcohol (PVA) composite with the graphite content ranging from 50 to 80%wt was prepared and used as a conductive layer. Kapton tape was selected as a polymer layer. A graphite composite/Kapton tape bilayer material was then developed as a U-shaped flexible electroactive-driven actuator. The effect of calendaring on properties of the proposed actuator was investigated in terms of conductivity, bending angle, and blocking force.

© The 2023 Pure and Applied Chemistry International Conference (PACCON2023)

2. Materials and Methods

2.1 Materials

Extra pure graphite fine powder with the particle size < 50 µm, ≥ 99.5% purity, Mw 12.01 g/mol was from Merck, Germany. Kapton tape, 19 mm x 33m, with of 5 mm width and 0.055 mm thickness were from 3M. Glutaraldehyde was obtained from Fluka. Polyvinyl alcohol (PVA), Mw of 89,000-98,000 g/mol, 99+% hydrolyzed, was from Sigma-Aldrich, USA. Sulfuric acid (95-97%) and methanol (AR grade) were from QRëC. Acetic acid, (AR grade) was from Scharlan. Glycerol 99.5%, analytical reagent, was from QRëC, New Zealand.

2.2 Preparation of graphite composite film

Into 4 mL of the 10%w/v polyvinyl alcohol solution, glycerol (60%w/w with respect to PVA weight) was added and stirred for 2 h. Graphite was also added at various concentrations of 50, 60, 70, and 80%wt with continuous stirring for 10 min until homogeneous. Crosslink solution (methanol: acetic acid: glutaraldehyde: sulfuric acid with the volume ratio of 3:2:1:1) was then added and the mixture was stirred for 15 min. The mixture was poured into a plastic mold. After pouring, it was sat at room temperature for 5 min to reduce air bubbles before drying in a hot air oven at 60 ºC for 2 h. The film's thickness as well as the electrical conductivity were measured.

2.3 Preparation of U-shaped flexible ETA

The mixture of PVA solution/graphite composite was poured into a mold (0.5×5.0 cm^2) with a cello tape (0.1 ×4.0 cm^2) attached at the middle of the mold. A glass slide was brought to scrape off the excess composite mixture before drying in a hot air oven at 60 ºC for 2 h. After taken out of the oven, the cello tape was pull off. A U-shape PVA/graphite composite was obtained. Then the U-shape PVA/graphite composite was attached on the top of Kapton tape, creating a U-shaped flexible electroactive-driven actuator. (Fig. 1).

2.4 Electrical conductivity

Electrical conductivity measurement of the PVA/graphite composite films was performed with a digital multimeter at room temperature, using copper electrode pads. The two copper sheets (1.0×2.2 cm^2) were placed on a PVA/graphite composite film (3.5×5.0 cm^2), allowing a 1.5 cm space between the two pads. The red-black probe was pressed between the copper electrodes at a distance of 1.3 cm. The surface resistivity (ρ_v) was calculated using equation (1), according to ASTM D257-90.[14] The corresponding surface conductivity (σ_v) was also calculated using equation (2).

$$\rho_v = \frac{A}{T} \times R_v \qquad (1),$$

where A = (a + g) (b + g)
R_v = measured surface resistance (Ω),
A = the electrode surface area (cm^2),
T = the average thickness (cm),
g = the dimension of the digital multimeter probe (cm),
a, b = the length of the rectangular electrode (cm).

$$\sigma = \frac{1}{\rho} \qquad (2),$$

where ρ and σ are the resistivity (Ω·m) and the electrical conductivity (S/m), respectively.[15]

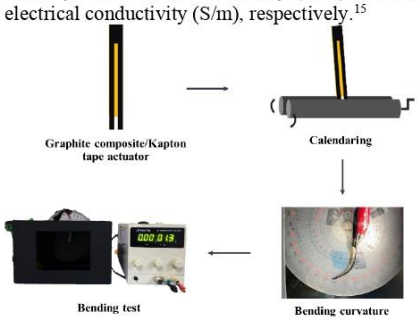

Figure 1. Schematic diagram presenting experimental procedure of bending for the electrothermal actuator with calendaring.

2.5 Thickness, bending angle, and blocking force measurements

Thickness of both the graphite composite and the model actuator system was measured by scanning electron microscopy. In order to perform bending angle measurement of the actuator model systems, DC power supply (Digital DRP-303D) was utilized to supply different voltages and stimulate the graphite composite/Kapton tape actuator. Digital multimeter, Agilent 34410A (Agilent Technologies), was used to measure the DC voltage. As soon as the voltage was applied, a video of the measurement was recorded by a digital camera. Pictures from the video were captured and printed out. Bending angle of the actuator was analyzed using a protractor. Straight lines along the curve at both ends of the actuator were drawn to the point of intersection of the two lines.

The bending angle at the intersection between the two tangent lines of electrothermal were measured by a circle protractor (No.990 INCA). [16]

Blocking force is a force at the tip of a bending actuator when the tip is fixed. Since the blocking force cannot be measured directly so that electronic balance is used to measure the blocking force indirectly.[12] In this study, blocking force of the model electro-active actuator was determined using a four-digit electronic balance. The measurement was conducted with DC electric fields. Both ends of the PVA/graphite composite surface of the actuator are connected to the DC power supply. The actuator was fixed during the measurement, and the PVA/graphite composite surface and the weighing area of the electronic balance are kept just out of contact (Fig. 2). The voltage of 6 V was applied to actuator for 2 min and the indication of the electronic balance was recorded to calculate the blocking force. After the voltage was removed, the blocking force measurement was also carried out for another 2 min with the same procedure.

2.6 Scanning Electron Microscopy

The U-shaped flexible ETA morphology and thickness were observed by a scanning electron microscope (SEM, LEO 1450 VP). Before the observation, the surfaces were coated with a thin layer of about 10 nm of gold via the sputter coating technique.

3. Results & Discussion

3.1 Electrothermal actuator model systems

The actuator model system consists of graphite composite and Kapton tape, which is characterized as a U-shaped flexible electroactive-driven is shown in Fig. 1. After calendaring by a dough sheeter machine, the actuator was subjected to the bending test. The setup and the bending test under a low driving voltage of 6 V, by a DC power thickness of the model actuator systems is shown in Figure 2. After calendaring, the thickness of the actuator with 50% graphite reduced, due to extrusion, which caused the material to expand and become tighter due to the actuator being extruded or compressed, which creates the thickness thinner. However, there was no significant changes in the thickness of the actuators containing 60−80 %wt of graphite. In addition, the thickness of the actuator increased with increased graphite content. This may be due to insufficient force exerted on the graphite. The results are in agreement with those presented by Fan et al.[12] They fabricated flexible double-layer ETAs from graphite paper and PI and reported that the spacing between the flexible graphite sheets becomes smaller after calendaring.

3.2 Resistivity and conductivity

Figure 3a and 3b show the surface resistivity and surface conductivity of the PVA/graphite composite films both non-calendaring and calendaring as a function of graphite content, respectively. When the concentration of graphite increased from 50 to 80%wt, volume resistivity of non-calendaring graphite composite film increased significantly with increasing graphite content from 2.16×10^{9} to 3.13×10^{9} Ω.cm. Besides, the corresponded volume conductivity decreased significantly with increasing graphite content from 4.63×10^{-12} to 3.20×10^{-12} S/m. This may be due to the poor distribution of graphite particles in PVA matrix as well as voids that hindered the electron movement. With calendaring, PVA/graphite composite film with 60%wt graphite showed the volume resistivity of 1.43×10^{9} Ω.cm. The value decreased to 1.11×10^{9} Ω.cm when graphite content increased to 80%wt. This was due to the voids and gaps between graphite particles reduced when the actuator was extruded and pressed. As a result, the graphite network was formed and the electron movement was enabled. Scanning electron micrographs in Fig. 4 confirm the reduction of voids and gaps after calendaring. Similar results were presented by Leng et al.[17] that the square resistance of the coating, containing 60 %wt graphite, was 829 kΩ and reduced to 14 kΩ when the graphite content reached 100 %wt.

The corresponding volume conductivity was also shown in Fig. 3b. Due to the relationship between resistivity and conductivity, a material that has a high conductivity will have a low resistivity, and vice versa.[17] The electrical conductivity of the composites increased when graphite content was increased. Hanif et al [18] showed that the conductivity of the composite films increased by two-order magnitude when graphite content increased from 15 %wt (2.44×10^{-6} S/cm) to 30 %wt. (9.44×10^{-5} S/cm). Moreover, Alo et al.[19] confirmed that the conductivity of PE/epoxy/graphite composites increased from 0.20 Scm^{-1} at 30 %wt graphite to 4.12 Scm^{-1} at 80 %wt graphite. In this present study, when calendaring was applied, the composite containing 50%wt graphite showed the lowest electrical resistivity of 8.03×10^{8} Ω.cm and

the highest conductivity of 1.24×10^{-11} S/m. The high conductivity may be caused by the well scattering of graphite particles PVA matrix.[20] By extruding, graphite particles in the composites got denser, which resulted in better electrical conductivity.[21]

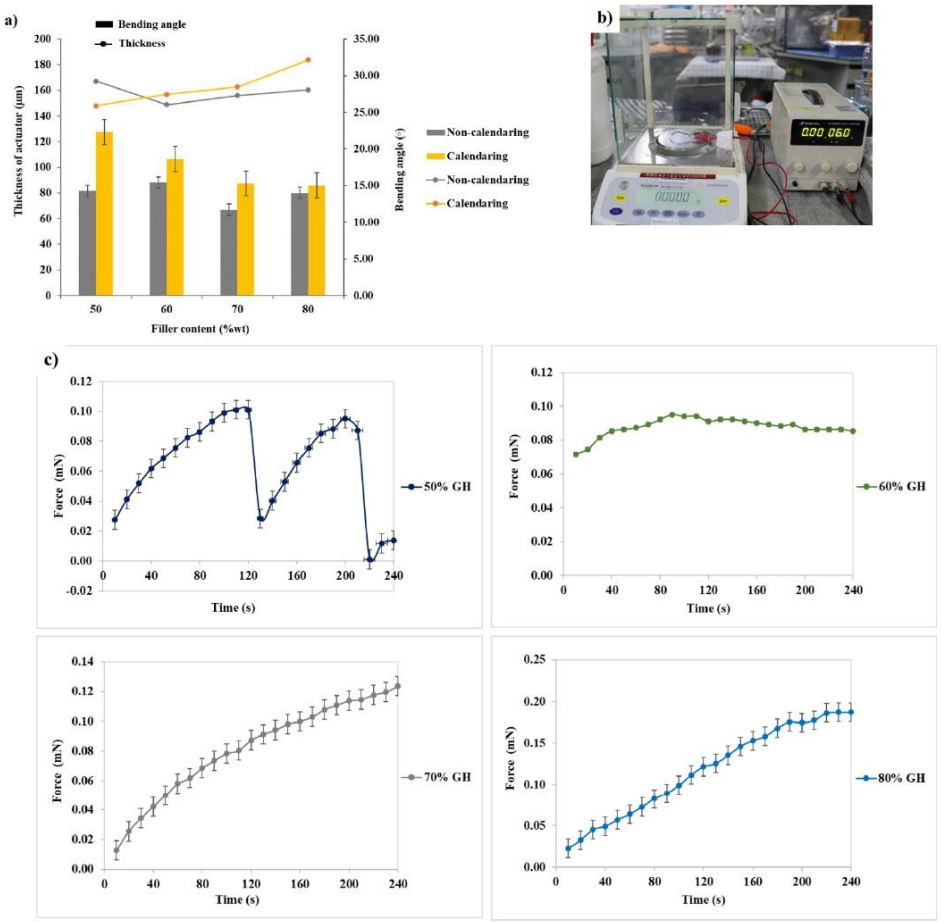

Figure 2. Bending angle and blocking force measurements: (a) thickness and bending angle for non-calendaring and calendaring actuators at 6 V, (b) experimental set up for blocking force measurement and (c) blocking force of the calendaring actuator when power is on (2 min) and off (2 min) at 6 V.

3.3 Bending angle and blocking force

Figure 2a shows relationship between thickness and bending angle of actuators under low voltage of 6 V. With graphite content of 50, 60, 70 and 80%wt, non-calendaring systems showed the bending angle of 14.30°, 15.40°, 11.70°, and 14.00°, respectively. The bending angle of calendaring systems is 22.30°, 18.60°, 15.30°, and 15.00°, respectively. Obviously, the actuator with 50%wt

graphite exhibited the greatest bending angle of 22.30° after calendaring. This corresponds to the actuator thickness of 147.87 µm, which is the thinnest. Therefore, calendaring may narrow the gap between conductive layer and Kapton tape, making the two layers attach to each other tightly, resulting in a high bending angle. Besides, calendaring probably lead to porosity loss in PVA/graphite composite, resulting in decreased pores that is small enough for electricity to flow through.

According to the above experimental results, the bending angle of the actuator with calendaring was greater than non-calendaring actuator. Therefore, only the actuator with calendaring was taken to blocking force test. The image of the experimental set up is shown in Figure 2b.

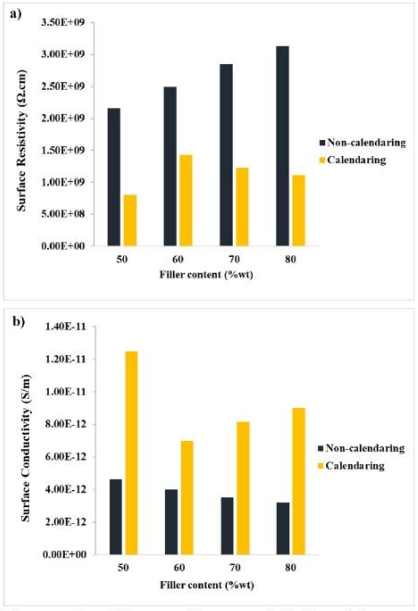

Figure 3. The surface resistivity (a) and conductivity (b) values of the composite films with and without calendaring.

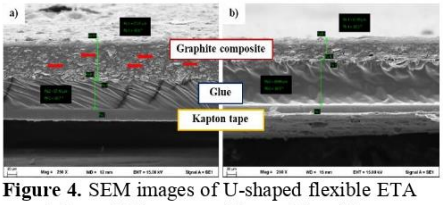

Figure 4. SEM images of U-shaped flexible ETA containing 50%wt graphite with (a) non-calendaring and (b) calendaring. Voids and gaps are pointed by arrows.

Since, the blocking force cannot be evaluated directly so that electronic balance was used to evaluate the blocking force indirectly, followed the procedure described by Fan et al.[13] During the measurement, both ends of the graphite composite film of the actuator were connected to a DC power supply. So that the electric current stimulated the displacement or bend, then the bent depressed to the surface of the weighing floor in the electronic balance. When the electric potential was applied for 2 min minutes, the maximum indication of the electronic balance was recorded can and converted to blocking force. Figure. 2c shows blocking force of calendaring actuator containing graphite contents of 50, 60, 70, and 80%wt. With applied voltage, the blocking force of the actuator containing 50%wt graphite increased with increasing time until reached the maximum value of 0.101 N. After the applied voltage was taken off, the blocking force suddenly dropped to 0.025 N and increased constantly after that. According to Tian et al.[8] when a voltage was applied, the conductive layer with a lower CTE generated the joule heat to heat up the whole ETA. Because of the difference in CTE, the substrate with higher CTE expanded more, yielding a bending deformation to the lower-CTE layer. The deformation here was generally expressed in bending curvature and angular of ETA. When the electric potential was taken off, there was no joule heat to heat up the system. As a result, the bending curvature ceased. However, in this present study there was a gradual increase in bending curvature from 130 s to 220 s (Fig. 2c). With 60, 70 and 80%wt of graphite, the actuator systems showed the gradually increased blocking force with time, even if the applied voltage was removed. This may be due to the residue strain found in the actuator caused by the stiffness of graphite. Further investigation is needed to be carried out to prove this hypothesis.

© The 2023 Pure and Applied Chemistry International Conference (PACCON2023)

4. Conclusion

A graphite composite/Kapton tape actuator was developed successfully. The volume conductivity and the thickness of the actuators increased with increasing graphite content. With moderate difference in thermal expansion coefficients of graphite and Kapton tape, the developed actuator showed a low bending performance in the range 11.70° − 15.40° when a low voltage of 6 V was applied. However, after calendaring, bending angle of the actuator increased to 15.00° − 22.30°, with the maximum blocking force of 0.101 N. This preliminary study showed the possibility of using graphite composite/Kapton tape system as electroactive actuators, which could be applied in broad application prospects. However, further investigation is needed to be carried on.

Acknowledgements

This work was financially supported by Thailand Science and Research Innovation Fund (10F640206). Science Innovation Facility, Faculty of Science, Burapha University (SIF-IN-64910181) is also gratefully acknowledged.

References

1. Kim, H.; Lee, H.; Ha, I.; Jung, J.; Won, P.; Cho, H.; Ko, S. H. *Adv. Funct. Mater*. **2018**, *28*(32), 1801847.
2. Zhang, X.; Tian, M.; Raza, T.; Zhao, H.; Wang, J.; Du, X.; Qu, L. *Compos. B. Eng.* **2021**, *223*, 109099.
3. Ahn, J.; Jeong, Y.; Zhao, Z.; Hwang, S.; Kim, K.; Ko, J.; Park, I. *Adv. Mater. Technol.* **2019**, *5*(2), 1900997.
4. Tibi, G.; Sachyani Keneth, E.; Layani, M.; Magdassi, S.; Degani, A. *Soft Robot.* **2020**, *7*(5), 649-662.
5. Potekhina, A., & Wang, C. *Actuators*. **2019**, *8*(4), 69.
6. Chen, S.; Tan, M.; W. M.; Gong, X.; & Lee, P. S. *Adv. Intell. Syst.* **2022**, *4*(2), 2100075.
7. Hu, Y.; Wang, G.; Tao, X.; & Chen, W. *Macromol. Chem. Phys*. **2011**, *212*(15), 1671–1676.
8. Tian, Y.; Li, Y.-T.; Tian, H.; Yang, Y.; Ren, T.-L. *Soft Robot*. **2021**, *8*(3), 241-250.
9. Qian, G.; Chen, H.; Song, G.; Dai, F.; Chen, C.; Yao, J. (2020). *Polym. J.* **2020**, *196*, 122482.
10. Sezer Hicyilmaz, A., & Celik Bedeloglu, A. *SN Appl. Sci*. **2021**, *3*(3), 1-22.
11. Liu, F.; Liu, Z.; Gao, S.; You, Q. Zou, L.; Chen, J.; Liu, X. *RSC Adv*. **2018**, *8*(34), 19034–19040.
12. Fan, Q.; Miao, J.; Tian, M.; Zhao, H.; Zhu, S.; Liu, X.; Qu, L. *Sens. Actuator A Phys*. **2020**, *315*, 112352.
13. Mokhena, T. C.; Mochane, M. J.; Sefadi, J. S.; Motloung, S. V.; Andala, D. M. (2018). Impact of thermal conductivity on energy technologies. **2018**, *181*.
14. Anne L.S. Electromechanically Active Polymer (EAP) transducers & artificial muscles. EuroEAP 2016. *BEng, BSc, MSc*. **2016**.
15. Zainab R. *Standard test methods for DC resistance or conductance of insulating materials*: University of California Berkeley Library pursuant to License Agreement, June **2007**.
16. Aouraghe, M. A.; Mengjie, Z.; Qiu, Y.; Fujun, X. *Advanced Fiber Materials*. **2021**, *3*(1), 38-46.
17. Leng, Z.; Li, T.;Wang, X.;Zhang, S.; Zhou, J. *Coat*. **2022**, *12*, 434.
18. Hanif, M. P. M.; Jalilah, A. J.; Badrul, F.; Nuraqmar, S. M. S. (2019, December). *IOP Conf. Ser.: Mater. Sci. Eng.* (Vol. 701, No. 1, p. 012015). IOP Publishing.
19. Alo1 O. A.; Otunniyi I. O.; HCvZ Pienaar. (2020). *AIP Conf. Proc* (Vol. 2289, No. 1, p. 020007). AIP Publishing LLC.
20. Wilka, M. Alterung sowie weiterer anwendungsrelevanter Eigenschaften. **2014**, (Doctoral dissertation, Universität Ulm).
21. Hille, L.; Toepper, H. C.; Schriever, C.; Kriegler, J.; Keilhofer, J.; Noecker, M. P.; Zaeh, M. F. *J. Electrochem. Soc*. **2022**, *169*(6), 060518.

© The 2023 Pure and Applied Chemistry International Conference (PACCON2023)

A.L., S. (2016). Electromechanically Active Polymer (EAP) transducers & artificial muscles. *6th international conference*

Alo, O. A., & Otunniyi, I. O. (2020). Graphite-Filled Polyethylene/Epoxy Blend for High-Conductivity Applications: The Immiscibility Edge. *Polymer-Plastics Technology and Materials, 60*(1), 105-116. doi:10.1080/25740881.2020.1793195

Amjadi, M., & Sitti, M. (2016). High-Performance Multiresponsive Paper Actuators. *ACS Nano, 10*(11), 10202-10210. doi:10.1021/acsnano.6b05545

Aouraghe, M. A., Mengjie, Z., Qiu, Y., & Fujun, X. (2021). Low-Voltage Activating, Fast Responding Electro-thermal Actuator Based on Carbon Nanotube Film/PDMS Composites. *Advanced Fiber Materials, 3*(1), 38-46. doi:10.1007/s42765-020-00060-w

Arham, R., Salengke, S., Metusalach, M., & Mulyati, M. T. (2018). Optimization of agar and glycerol concentration in the manufacture of edible film. *nternational Food Research Journal, 25*(5), 1845-1851.

Bera, M., Gupta, P., & Maji, P. K. (2018). Facile One-Pot Synthesis of Graphene Oxide by Sonication Assisted Mechanochemical Approach and Its Surface Chemistry. *J Nanosci Nanotechnol, 18*(2), 902-912. doi:10.1166/jnn.2018.14306

Catalog, Y. THAI Yazaki

Cobos, M., Fernandez, M. J., & Fernandez, M. D. (2018). Graphene Based Poly(Vinyl Alcohol) Nanocomposites Prepared by In Situ Green Reduction of Graphene Oxide by Ascorbic Acid: Influence of Graphene Content and Glycerol Plasticizer on Properties. *Nanomaterials (Basel), 8*(12). doi:10.3390/nano8121013

Davis, G. (2003). Durability of Adhesive Joints. In *Handbook of Adhesive Technology, Revised and Expanded*.

Du, F. P., Tang, C. Y., Xie, X. L., Zhou, X. P., & Tan, L. (2009). Carbon nanotube enhanced gripping in polymer-based actuators. *The Journal of Physical Chemistry C, 113*(7), 7223-7226.

DuPont™. (2022). DuPont™ Kapton®.

Fahmy Taha, M., Ashraf, H., & Caesarendra, W. (2020). A Brief Description of Cyclic Voltammetry Transducer-Based Non-Enzymatic Glucose Biosensor Using Synthesized Graphene Electrodes. *Applied System Innovation, 3*(3). doi:10.3390/asi3030032

Fan, Q., Miao, J., Tian, M., Zhao, H., Zhu, S., Liu, X., . . . Qu, L. (2020). Low-voltage driven flexible double-layer electrothermal actuator for smart human-machine interactions. *Sensors and Actuators A: Physical, 315*. doi:10.1016/j.sna.2020.112352

Georgiou, K., Koutsioukis, A., & Georgakilas, V. (2021). Transparent conductive film of polyvinyl alcohol: reduced graphene oxide composite. *Journal of Materials Science, 56*(30), 17028-17039. doi:10.1007/s10853-021-06386-z

Gong, Z., Cheng, J., Chen, X., Sun, W., Fang, X., Hu, K., . . . Wen, L. (2018). A Bio-inspired Soft Robotic Arm: Kinematic Modeling and Hydrodynamic Experiments. *Journal of Bionic Engineering, 15*(2), 204-219. doi:10.1007/s42235-018-0016-x

Hanif, M. P. M., Jalilah, A. J., Badrul, F., & Nuraqmar, S. M. S. (2019). The influence of graphite on conductivity, crystallinity and tensile properties of hydroxyethyl cellulose (hec)/graphite composite films. *In IOP Conference Series: Materials Science and Engineering, 701*, 012015.

He, Y., Wang, X., Wu, D., Gong, Q., Qiu, H., Liu, Y., . . . Gao, J. (2013). Biodegradable amylose films reinforced by graphene oxide and polyvinyl alcohol. *Materials Chemistry and Physics, 142*(1), 1-11. doi:10.1016/j.matchemphys.2013.05.036

Heaney, M. B. (2003). Electrical conductivity and resistivity. *Electrical measurement, signal processing, and displays, 7*(1).

Immanuel, S., & Sivasubramanian, R. (2020). Fabrication of two-dimensional chemically reduced graphene oxide nanosheets for the electrochemical determination of epinephrine. *Bulletin of Materials Science, 43*(1). doi:10.1007/s12034-019-2034-7

J.Boylan. (1996). Carbon - Graphite Materials. *Materials World, 4*(12), 707-708.

Jamali, A. R., Shaikh, A. A., & Chandio, A. D. (2023). doi:10.20944/preprints202307.0618.v1

Jing, Y., Wang, Z., Chen, W., Liang, Y., Yang, Z., Zheng, C., . . . Zhang, Z. (2021). Preparation of Polyvinyl Alcohol/Graphene Oxide Composite Film with "Sandwich" Structure and High Toughness. *Polymer Science, Series A, 63*(6), 822-827. doi:10.1134/s0965545x21060067

Keeling, J. (2017). Graphite: properties, uses and South Australian resources. *MESA J, 84*(3), 28-41.

Lee, T.-I., Kim, M. S., & Kim, T.-S. (2016). Contact-free thermal expansion measurement of very soft elastomers using digital image correlation. *Polymer Testing, 51*, 181-189. doi:10.1016/j.polymertesting.2016.03.014

Leng, Z., Li, T., Wang, X., Zhang, S., & Zhou, J. (2022). Effect of Graphite Content on the Conductivity, Wear Behavior, and Corrosion Resistance of the Organic Layer on Magnesium Alloy MAO Coatings. *Coatings, 12*(4). doi:10.3390/coatings12040434

Liew, C.-W., Ramesh, S., & Arof, A. K. (2014). Good prospect of ionic liquid based-poly(vinyl alcohol) polymer electrolytes for supercapacitors with excellent electrical, electrochemical and thermal properties. *International Journal of Hydrogen Energy, 39*(6), 2953-2963. doi:10.1016/j.ijhydene.2013.06.061

Ma, P.-C., Siddiqui, N. A., Marom, G., & Kim, J.-K. (2010). Dispersion and functionalization of carbon nanotubes for polymer-based nanocomposites: A review. *Composites Part A: Applied Science and Manufacturing, 41*(10), 1345-1367. doi:10.1016/j.compositesa.2010.07.003

Manousi, N., Rosenberg, E., Deliyanni, E., Zachariadis, G. A., & Samanidou, V. (2020). Magnetic Solid-Phase Extraction of Organic Compounds Based on Graphene Oxide Nanocomposites. *Molecules, 25*(5). doi:10.3390/molecules25051148

Mission, E. G., Quitain, A. T., Hirano, Y., Sasaki, M., Cocero, M. J., & Kida, T. (2018). Integrating reduced graphene oxide with microwave-subcritical water for cellulose depolymerization. *Catalysis Science & Technology, 8*(21), 5434-5444. doi:10.1039/c8cy00953h

Mohan, V. B., Brown, R., Jayaraman, K., & Bhattacharyya, D. (2015). Characterisation of reduced graphene oxide: Effects of reduction variables on electrical conductivity. *Materials Science and Engineering: B, 193*, 49-60. doi:10.1016/j.mseb.2014.11.002

Morimoto, N., Kubo, T., & Nishina, Y. (2016). Tailoring the Oxygen Content of Graphite and Reduced Graphene Oxide for Specific Applications. *Sci Rep, 6*, 21715. doi:10.1038/srep21715

Nemet, N., Soso, V., & Lazic, V. (2010). Effect of glycerol content and pH value of film-forming solution on the functional properties of protein-based edible films. *Acta Periodica Technologica*(41), 57-67. doi:10.2298/apt1041057n

Ozdemir, O., Karakuzu, R., Sarikanat, M., Akar, E., Seki, Y., Cetin, L., . . . Mermer, O. (2015). Effects of PEG loading on electromechanical behavior of cellulose-based electroactive composite. *Cellulose, 22*(3), 1873-1881. doi:10.1007/s10570-015-0581-7

Pei, S., & Cheng, H.-M. (2012). The reduction of graphene oxide. *Carbon, 50*(9), 3210-3228. doi:10.1016/j.carbon.2011.11.010

Phuchaduek, W., Jamnongkan, T., Rattanasak, U., Boonsang, S., & Kaewpirom, S. (2015). Improvement in physical and electrical properties of poly(vinyl alcohol) hydrogel conductive polymer composites. *Journal of Applied Polymer Science, 132*(28). doi:10.1002/app.42234

Ramesh, A., Prakash, J. N., Gowda, A. S. S., & Appaiah, S. (2009). Comparison of the mechanical properties of AL6061/albite and AL6061/graphite metal matrix composites. Journal of Minerals and Materials Characterization and Engineering. *8*, *02*(93).

Razi-Asrami, M., Ghasemi, J. B., Amiri, N., & Sadeghi, S. J. (2017). Simultaneous spectrophotometric determination of crystal violet and malachite green in water samples using partial least squares regression and central composite design after preconcentration by dispersive solid-phase extraction. *Environ Monit Assess, 189*(4), 196. doi:10.1007/s10661-017-5898-2

Ruidíaz-Martínez, M., Álvarez, M. A., López-Ramón, M. V., Cruz-Quesada, G., Rivera-Utrilla, J., & Sánchez-Polo, M. (2020). Hydrothermal Synthesis of rGO-TiO2 Composites as High-Performance UV Photocatalysts for Ethylparaben Degradation. *Catalysts, 10*(5). doi:10.3390/catal10050520

Sachyani, E., Layani, M., Tibi, G., Avidan, T., Degani, A., & Magdassi, S. (2017). Enhanced movement of CNT-based actuators by a three-Layered structure with controlled resistivity. *Sensors and Actuators B: Chemical, 252*, 1071-1077. doi:10.1016/j.snb.2017.06.104

Salavagione, H. J., Gómez, M. A., & Martínez, G. (2009). Polymeric Modification of Graphene through Esterification of Graphite Oxide and Poly(vinyl alcohol). *Macromolecules, 42*(17), 6331-6334. doi:10.1021/ma900845w

Salim, E., Hany, W., Elshahawy, A. G., & Oraby, A. H. (2022). Investigation on optical, structural and electrical properties of solid-state polymer nanocomposites electrolyte incorporated with Ag nanoparticles. *Sci Rep, 12*(1), 21201. doi:10.1038/s41598-022-25304-0

Sieradzka, M., Ślusarczyk, C., Biniaś, W., & Fryczkowski, R. (2021). The Role of the Oxidation and Reduction Parameters on the Properties of the Reduced Graphene Oxide. *Coatings, 11*(2). doi:10.3390/coatings11020166

Song, J., Zhang, J., Lin, C., & Chen, G. (2013). Influence of Graphene Oxide on the Tribological and Electrical Properties of PMMA Composites. *Journal of Nanomaterials, 2013*(1). doi:10.1155/2013/846102

Srihata, W., Jamnongkan, T., Rattanasak, U., Boonsang, S., & Kaewpirom, S. (2016). Enhanced electrostatic dissipative properties of chitosan/gelatin composite films filled with reduced graphene oxide. *Journal of Materials Science: Materials in Electronics, 28*(1), 999-1010. doi:10.1007/s10854-016-5620-0

Suma, S. B., & Sangappa, Y. (2024). Physical, optical and electrical properties of polyvinyl alcohol-graphene oxide nanocomposite films. *Indian Journal of Physics*. doi:10.1007/s12648-024-03314-0

Tan, M. W. M., Wang, H., Gao, D., Huang, P., & Lee, P. S. (2024). Towards high performance and durable soft tactile actuators. *Chem Soc Rev, 53*(7), 3485-3535. doi:10.1039/d3cs01017a

Tian, Y., Li, Y. T., Tian, H., Yang, Y., & Ren, T. L. (2021). Recent Progress of Soft Electrothermal Actuators. *Soft Robot, 8*(3), 241-250. doi:10.1089/soro.2019.0164

Xing, W., Wu, J., Huang, G., Li, H., Tang, M., & Fu, X. (2014). Enhanced mechanical properties of graphene/natural rubber nanocomposites at low content. *Polymer International, 63*(9), 1674-1681. doi:10.1002/pi.4689

Xu, C., Faul, C. F. J., Taghavi, M., & Rossiter, J. (2023). Electric Field-Driven Dielectrophoretic Elastomer Actuators. *Advanced Functional Materials, 33*(13). doi:10.1002/adfm.202208943

Yao, S., Cui, J., Cui, Z., & Zhu, Y. (2017). Soft electrothermal actuators using silver nanowire heaters. *Nanoscale, 9*(11), 3797-3805. doi:10.1039/c6nr09270e

Zainab, S. M., Junaid, M., Xu, N., & Malik, R. N. (2020). Antibiotics and antibiotic resistant genes (ARGs) in groundwater: A global review on dissemination, sources, interactions, environmental and human health risks. *Water Res, 187*, 116455. doi:10.1016/j.watres.2020.116455

Zhang, Z., & Fang, X. (2006). Study on paraffin/expanded graphite composite phase change thermal energy storage material. *Energy Conversion and Management, 47*(3), 303-310. doi:10.1016/j.enconman.2005.03.004

REFERENCES

A.L., S. (2016). Electromechanically Active Polymer (EAP) transducers & artificial muscles. *6th international conference*

Abdullah, N. M., Kamarudin, M. S., Rus, A. Z. M., & Abdullah, M. F. L. . (2017). Preparation of Conductive Polymer Graphite (PG) Composites. *IOP Conference Series: Materials Science and Engineering, 226*, 012181. doi:doi:10.1088/1757-899x/226/1/012181

Alo, O. A., & Otunniyi, I. O. (2020). Graphite-Filled Polyethylene/Epoxy Blend for High-Conductivity Applications: The Immiscibility Edge. *Polymer-Plastics Technology and Materials, 60*(1), 105-116. doi:10.1080/25740881.2020.1793195

Amjadi, M., & Sitti, M. (2016). High-Performance Multiresponsive Paper Actuators. *ACS Nano, 10*(11), 10202-10210. doi:10.1021/acsnano.6b05545

Amjadi, M., & Sitti, M. (2018). Self-Sensing Paper Actuators Based on Graphite-Carbon Nanotube Hybrid Films. *Adv Sci (Weinh), 5*(7), 1800239. doi:10.1002/advs.201800239

Ansar Khan, C. S. M. (2016). Journal of Polymer & Composites PVC Pipe Designer Furniture. *Journal of Polymer & Composites, 4*(2).

Aouraghe, M. A., Mengjie, Z., Qiu, Y., & Fujun, X. (2021). Low-Voltage Activating, Fast Responding Electro-thermal Actuator Based on Carbon Nanotube Film/PDMS Composites. *Advanced Fiber Materials, 3*(1), 38-46. doi:10.1007/s42765-020-00060-w

Arachchige, D. D. K., Chen, Y., Walker, I. D., & Godage, I. S. (2021). *A Novel Variable Stiffness Soft Robotic Gripper*. Paper presented at the 2021 IEEE 17th International Conference on Automation Science and Engineering (CASE).

Arham, R., Salengke, S., Metusalach, M., & Mulyati, M. T. (2018). Optimization of agar and glycerol concentration in the manufacture of edible film. *nternational Food Research Journal, 25*(5), 1845-1851.

Bar-Cohen, Y. (2007). Electroactive polymers as an enabling materials technology. Proceedings of the Institution of Mechanical Engineers. *Part G: Journal of Aerospace Engineering, 221*(4), 553–564. doi:doi:10.1243/09544100jaero141

Bar-Cohen, Y., & Anderson, I. A. (2019). Electroactive polymer (EAP) actuators—background review. *Mechanics of Soft Materials, 1(1)*. doi:doi:10.1007/s42558-019-0005-1

Bera, M., Gupta, P., & Maji, P. K. (2018). Facile One-Pot Synthesis of Graphene Oxide by Sonication Assisted Mechanochemical Approach and Its Surface Chemistry. *J Nanosci Nanotechnol, 18*(2), 902-912. doi:10.1166/jnn.2018.14306

Cao, Y., & Dong, J. (2021). Programmable soft electrothermal actuators based on free-form printing of the embedded heater. *Soft Matter, 17*(9), 2577-2586. doi:10.1039/d0sm02062a

Chen, G., Yang, Z., Wang, W., Bi, L., Chen, L., Peng, Y., & Ye, C. (2020). Electrothermal Actuators with Ultrafast Response Speed and Large Deformation. *Advanced Intelligent Systems, 2*(8). doi:10.1002/aisy.202000036

Chen, M., Frueh, J., Wang, D., Lin, X., Xie, H., & He, Q. (2017). Polybenzoxazole Nanofiber-Reinforced Moisture-Responsive Soft Actuators. *Sci Rep, 7*(1), 769. doi:10.1038/s41598-017-00870-w

Chuayjuljit, S., Thongraar, R., & Saravari, O. (2008). Preparation and Properties of PVC/EVA/ Organomodified Montmorillonite Nanocomposites. *Journal of Reinforced Plastics and Composites, 27*(4), 431-442. doi:10.1177/0731684407084124

Clingerman, M. L., King, J. A., Schulz, K. H., & Meyers, J. D. (2002). Evaluation of electrical conductivity models for conductive polymer composites. *Journal of Applied Polymer Science, 83*(6), 1341-1356. doi:10.1002/app.10014

Cobos, M., Fernandez, M. J., & Fernandez, M. D. (2018). Graphene Based Poly(Vinyl Alcohol) Nanocomposites Prepared by In Situ Green Reduction of Graphene Oxide by Ascorbic Acid: Influence of Graphene Content and Glycerol Plasticizer on Properties. *Nanomaterials (Basel), 8*(12). doi:10.3390/nano8121013

Dai, C.-A., Chang, C.-J., Kao, A.-C., Tsai, W.-B., Chen, W.-S., Liu, W.-M., . . . Ma, C.-C. (2009). Polymer actuator based on PVA/PAMPS ionic membrane: Optimization of ionic transport properties. *Sensors and Actuators A: Physical, 155*(1), 152-162. doi:10.1016/j.sna.2009.08.002

Davis, G. (2003). Durability of Adhesive Joints. In *Handbook of Adhesive Technology, Revised and Expanded*.

DeMerlis, C. C., & Schoneker, D. R. (2003). Review of the oral toxicity of polyvinyl alcohol (PVA). *Food and Chemical Toxicology, 41*(3), 319-326. doi:10.1016/s0278-6915(02)00258-2

Dimiev, A., Kosynkin, D. V., Alemany, L. B., Chaguine, P., & Tour, J. M. (2012). Pristine graphite oxide. *J Am Chem Soc, 134*(5), 2815-2822. doi:10.1021/ja211531y

Dow. (1995-2024). PDMS ®™ Trademark of Dow or an affiliated company.

Dr. Gurumurthy.B. R and Dinesh Bhatia, D. R. K. P. (2017). Structural analysis of merino wool, pashmina and angora fibers using analytical instruments like scanning electron microscope and infra-red spectroscopy. *International Journal of Engineering Technology Science and Research, 4*(8).

Du, F.-P., Tang, C.-Y., Xie, X.-L., Zhou, X.-P., & Tan, L. (2009). Carbon Nanotube Enhanced Gripping in Polymer-Based Actuators. *The Journal of Physical Chemistry C 113(17)*, 7223–7226. doi:doi:10.1021/jp807707m

Du, F. P., Tang, C. Y., Xie, X. L., Zhou, X. P., & Tan, L. (2009). Carbon nanotube enhanced gripping in polymer-based actuators. *The Journal of Physical Chemistry C, 113*(7), 7223-7226.

Duangkhaetita Kanjanasopa, B. P., Suraphon Thitithanakul and Suwaluk Wisunthorn. (2018). Biodegradation of Polyvinyl Alcohol by Thai Indigenous Mixed Microbial Culture. *Walailak J Sci & Tech, 17*(7), 698-707.

DuPont™. (2022). DuPont™ Kapton®.

Ernesto Hernández-Hernández, P. J. H.-B., Mónica A. Ceniceros-Reyes, Oliverio S. Rodríguez-Fernández and Pablo González-Morones. (2020). Graphite Oxide: A Simple and Reproducible Synthesis Route. *Licensee IntechOpen*.

facstaff.bucknell.edu. (2014). Introduction to the Agilent 34401A Digital Multimeter. . Retrieved from https://www.yumpu.com/en/document/view/19647653/introduction-to-the-agilent-34401a-digital-multimeter.

Fadlelmoula, A., Pinho, D., Carvalho, V. H., Catarino, S. O., & Minas, G. (2022).

Fourier Transform Infrared (FTIR) Spectroscopy to Analyse Human Blood over the Last 20 Years: A Review towards Lab-on-a-Chip Devices. *Micromachines (Basel), 13*(2). doi:10.3390/mi13020187

Fahmy Taha, M., Ashraf, H., & Caesarendra, W. (2020). A Brief Description of Cyclic Voltammetry Transducer-Based Non-Enzymatic Glucose Biosensor Using Synthesized Graphene Electrodes. *Applied System Innovation, 3*(3). doi:10.3390/asi3030032

Fan, Q., Miao, J., Tian, M., Zhao, H., Zhu, S., Liu, X., . . . Qu, L. (2020). Low-voltage driven flexible double-layer electrothermal actuator for smart human-machine interactions. *Sensors and Actuators A: Physical, 315*. doi:10.1016/j.sna.2020.112352

Feldman, D. (2020). Poly(Vinyl Alcohol) Recent Contributions to Engineering and Medicine. *Journal of Composites Science, 4*(4). doi:10.3390/jcs4040175

Gaaz, T. S., Sulong, A. B., Akhtar, M. N., Kadhum, A. A., Mohamad, A. B., & Al-Amiery, A. A. (2015). Properties and Applications of Polyvinyl Alcohol, Halloysite Nanotubes and Their Nanocomposites. *Molecules, 20*(12), 22833-22847. doi:10.3390/molecules201219884

Georgiou, K., Koutsioukis, A., & Georgakilas, V. (2021). Transparent conductive film of polyvinyl alcohol: reduced graphene oxide composite. *Journal of Materials Science, 56*(30), 17028-17039. doi:10.1007/s10853-021-06386-z

Gong, Z., Cheng, J., Chen, X., Sun, W., Fang, X., Hu, K., . . . Wen, L. (2018). A Bio-inspired Soft Robotic Arm: Kinematic Modeling and Hydrodynamic Experiments. *Journal of Bionic Engineering, 15*(2), 204-219. doi:10.1007/s42235-018-0016-x

Gracheva, E., Lambard, G., Samitsu, S., Sodeyama, K., & Nakata, A. (2021). Prediction of the coefficient of linear thermal expansion for the amorphous homopolymers based on chemical structure using machine learning. *Science and Technology of Advanced Materials: Methods, 1*(1), 213-224. doi:10.1080/27660400.2021.1993729

Granberg, M. G. a. H. (2021). Graphitic carbon –Production from biomass? *Digital Cellulose Center (digitalcellulosecenter.se).*

Graphite Powder. (2022). Retrieved from https://www.ebay.com/itm/251919624773.

Gürsel, H. (2022). What is the Difference Between Graphene Oxide and Reduced Graphene Oxide. Retrieved from https://nanografi.com/blog/what-is-the-difference-between-graphene-oxide-and-reduced-graphene-oxide/.

Hanif, M. P. M., Jalilah, A. J., Badrul, F., & Nuraqmar, S. M. S. (2019). The influence of graphite on conductivity, crystallinity and tensile properties of hydroxyethyl cellulose (hec)/graphite composite films. *In IOP Conference Series: Materials Science and Engineering, 701*, 012015.

He, W., Hao, W., Meng, X., Zhang, P., Sun, X., & Shen, Y. (2021). Influence of Graphite Powder on the Mechanical and Acoustic Emission Characteristics of Concrete. *Buildings, 12*(1). doi:10.3390/buildings12010018

He, Y., Wang, X., Wu, D., Gong, Q., Qiu, H., Liu, Y., . . . Gao, J. (2013). Biodegradable amylose films reinforced by graphene oxide and polyvinyl alcohol. *Materials Chemistry and Physics, 142*(1), 1-11. doi:10.1016/j.matchemphys.2013.05.036

Heaney, M. B. (2003). Electrical conductivity and resistivity. *Electrical measurement, signal processing, and displays, 7*(1).

Immanuel, S., & Sivasubramanian, R. (2020). Fabrication of two-dimensional chemically reduced graphene oxide nanosheets for the electrochemical determination of epinephrine. *Bulletin of Materials Science, 43*(1). doi:10.1007/s12034-019-2034-7

Introduction to Fourier Transform Infrared Spectrometry. (2001). Retrieved from https://www.chem.uci.edu/~dmitryf/manuals/Fundamentals/FTIR%20principles.pdf.

J.Boylan. (1996). Carbon - Graphite Materials. *Materials World, 4*(12), 707-708.

Jamali, A. R., Shaikh, A. A., & Chandio, A. D. (2023). doi:10.20944/preprints202307.0618.v1

Jing, Y., Wang, Z., Chen, W., Liang, Y., Yang, Z., Zheng, C., . . . Zhang, Z. (2021). Preparation of Polyvinyl Alcohol/Graphene Oxide Composite Film with "Sandwich" Structure and High Toughness. *Polymer Science, Series A, 63*(6), 822-827. doi:10.1134/s0965545x21060067

Kaur, R. (2018). Carbon Nanotubes: A Review Article. *International Journal for Research in Applied Science and Engineering Technology, 6*(4), 5075-5079. doi:10.22214/ijraset.2018.4827

Keeling, J. (2017). Graphite: properties, uses and South Australian resources. *MESA Journal, 84*(3).

Keeling, J. (2017). Graphite: properties, uses and South Australian resources. *MESA J, 84*(3), 28-41.

Kim-Rui Henga, A. S. A., Milan Shresthaa, and Gih-Keong Laua,. (2017). *Strong dielectric-elastomer grippers with tension arch flexures*. Paper presented at the Electroactive Polymer Actuators and Devices (EAPAD).

Lee, T.-I., Kim, M. S., & Kim, T.-S. (2016). Contact-free thermal expansion measurement of very soft elastomers using digital image correlation. *Polymer Testing, 51*, 181-189. doi:10.1016/j.polymertesting.2016.03.014

Leng, Z., Li, T., Wang, X., Zhang, S., & Zhou, J. (2022). Effect of Graphite Content on the Conductivity, Wear Behavior, and Corrosion Resistance of the Organic Layer on Magnesium Alloy MAO Coatings. *Coatings, 12*(4). doi:10.3390/coatings12040434

Li, Y., Chen, Y., Yang, Y., & Li, Y. (2019). Soft Robotic Grippers Based on Particle Transmission. *IEEE/ASME Transactions on Mechatronics, 24*(3), 969-978. doi:10.1109/tmech.2019.2907045

Liew, C.-W., Ramesh, S., & Arof, A. K. (2014). Good prospect of ionic liquid based-poly(vinyl alcohol) polymer electrolytes for supercapacitors with excellent electrical, electrochemical and thermal properties. *International Journal of Hydrogen Energy, 39*(6), 2953-2963. doi:10.1016/j.ijhydene.2013.06.061

Lim, H., & Hoag, S. W. (2013). Plasticizer effects on physical-mechanical properties of solvent cast Soluplus(R) films. *AAPS PharmSciTech, 14*(3), 903-910. doi:10.1208/s12249-013-9971-z

Lin, Y., He, D., Hu, H., Yi, P., Liu, X., Huang, J., . . . Li, G. (2019). Preparation and Properties of Polydimethylsiloxane (PDMS)/Polyethylene Glycol (PEG)-Based Amphiphilic Polyurethane Elastomers. *ACS Appl Bio Mater, 2*(10), 4377-4384. doi:10.1021/acsabm.9b00605

Liu, F., Liu, Z., Gao, S., You, Q., Zou, L., Chen, J., . . . Liu, X. (2018). Polyimide film with low thermal expansion and high transparency by self-enhancement of

polyimide/SiC nanofibers net. *RSC Adv, 8*(34), 19034-19040. doi:10.1039/c8ra02479k

Ma, P.-C., Siddiqui, N. A., Marom, G., & Kim, J.-K. (2010). Dispersion and functionalization of carbon nanotubes for polymer-based nanocomposites: A review. *Composites Part A: Applied Science and Manufacturing, 41*(10), 1345-1367. doi:10.1016/j.compositesa.2010.07.003

Manousi, N., Rosenberg, E., Deliyanni, E., Zachariadis, G. A., & Samanidou, V. (2020). Magnetic Solid-Phase Extraction of Organic Compounds Based on Graphene Oxide Nanocomposites. *Molecules, 25*(5). doi:10.3390/molecules25051148

Michael S. Reid, Y. M., and Antion M. Kofranek. (1981). Epinasty of Poinsettias-the Role of Auxin and Ethylene. *Plant Physiol., 67*(5), 950-952. doi:doi:10.1104/pp.67.5.950

Mission, E. G., Quitain, A. T., Hirano, Y., Sasaki, M., Cocero, M. J., & Kida, T. (2018). Integrating reduced graphene oxide with microwave-subcritical water for cellulose depolymerization. *Catalysis Science & Technology, 8*(21), 5434-5444. doi:10.1039/c8cy00953h

Miura, R., Sekine, T., Wang, Y. F., Hong, J., Watanabe, Y., Ito, K., . . . Tokito, S. (2020). Printed Soft Sensor with Passivation Layers for the Detection of Object Slippage by a Robotic Gripper. *Micromachines (Basel), 11*(10). doi:10.3390/mi11100927

Mohan, V. B., Brown, R., Jayaraman, K., & Bhattacharyya, D. (2015). Characterisation of reduced graphene oxide: Effects of reduction variables on electrical conductivity. *Materials Science and Engineering: B, 193*, 49-60. doi:10.1016/j.mseb.2014.11.002

Mohd Radzuan, N. A., Sulong, A. B., & Sahari, J. (2017). A review of electrical conductivity models for conductive polymer composite. *International Journal of Hydrogen Energy, 42*(14), 9262-9273. doi:10.1016/j.ijhydene.2016.03.045

Morimoto, N., Kubo, T., & Nishina, Y. (2016). Tailoring the Oxygen Content of Graphite and Reduced Graphene Oxide for Specific Applications. *Sci Rep, 6*, 21715. doi:10.1038/srep21715

Naficy, S., & Garmabi, H. (2007). Study of the effective parameters on mechanical and electrical properties of carbon black filled PP/PA6 microfibrillar composites. *Composites Science and Technology, 67*(15-16), 3233-3241. doi:10.1016/j.compscitech.2007.04.001

Narkis, M., Lidor, G., Vaxman, A., & Zuri, L. (1999). New injection moldable electrostatic dissipative (ESD) composites based on very low carbon black loadings. *Journal of Electrostatics, 47*(4), 201–214. doi: doi:10.1016/s0304-3886(99)00041-8

Nemet, N., Soso, V., & Lazic, V. (2010). Effect of glycerol content and pH value of film-forming solution on the functional properties of protein-based edible films. *Acta Periodica Technologica*(41), 57-67. doi:10.2298/apt1041057n

Ozdemir, O., Karakuzu, R., Sarikanat, M., Akar, E., Seki, Y., Cetin, L., . . . Mermer, O. (2015). Effects of PEG loading on electromechanical behavior of cellulose-based electroactive composite. *Cellulose, 22*(3), 1873-1881. doi:10.1007/s10570-015-0581-7

Pei, S., & Cheng, H.-M. (2012). The reduction of graphene oxide. *Carbon, 50*(9), 3210-3228. doi:10.1016/j.carbon.2011.11.010

Perabo, C. (2013). Volume Resistivity vs. Volume Conductivity vs. Surface Resistivity. . Retrieved from https://www.caplinq.com/blog/linqstat-volume-resistivity-vs-volume-conductivity-vs-surface-resistivity_267/.

Phuchaduek, W., Jamnongkan, T., Rattanasak, U., Boonsang, S., & Kaewpirom, S. (2015). Improvement in physical and electrical properties of poly(vinyl alcohol) hydrogel conductive polymer composites. *Journal of Applied Polymer Science, 132*(28). doi:10.1002/app.42234

Pirahmadi, P., Kokabi, M., & Alamdarnejad, G. (2020). Polyvinyl alcohol/chitosan/carbon nanotubes electroactive shape memory nanocomposite hydrogels. *Journal of Applied Polymer Science, 138*(11). doi:10.1002/app.49995

Priyanka. Curves: Definition and Types. *Engineeringenotes*. Retrieved from https://www.engineeringenotes.com/surveying/curves/curves-definition-and-types-curves-surveying/14477

Prof. Tushar S Kulkarni, P. A. K. J. (2012). Thermo mechanical analysis of polypropylene/calcium carbonate nano composite using Thermo Mechanical Analyzer. *Journal of Engineering, 2*(12). doi:10.9790/3021-021243237

Raheem, Z. (2007). Standard test methods for DC resistance or conductance of insulating materials. *University of California Berkeley Library pursuant to License Agreement*.

Ramesh, A., Prakash, J. N., Gowda, A. S. S., & Appaiah, S. (2009). Comparison of the mechanical properties of AL6061/albite and AL6061/graphite metal matrix composites. Journal of Minerals and Materials Characterization and Engineering. *8, 02*(93).

Razaq, A., Bibi, F., Zheng, X., Papadakis, R., Jafri, S. H. M., & Li, H. (2022). Review on Graphene-, Graphene Oxide-, Reduced Graphene Oxide-Based Flexible Composites: From Fabrication to Applications. *Materials (Basel), 15*(3). doi:10.3390/ma15031012

Razi-Asrami, M., Ghasemi, J. B., Amiri, N., & Sadeghi, S. J. (2017). Simultaneous spectrophotometric determination of crystal violet and malachite green in water samples using partial least squares regression and central composite design after preconcentration by dispersive solid-phase extraction. *Environ Monit Assess, 189*(4), 196. doi:10.1007/s10661-017-5898-2

Resistance Measurement Considerations. Retrieved from https://rfmw.em.keysight.com/bihelpfiles/Truevolt/WebHelp/US/Content/__F_Tutorial/Tutorial%2003%20Resistance.htm

Ridwan, R., Prabowo, A. R., Muhayat, N., Putranto, T., & Sohn, J. M. (2020). Tensile analysis and assessment of carbon and alloy steels using FE approach as an idealization of material fractures under collision and grounding. *Curved and Layered Structures, 7*(1), 188-198. doi:10.1515/cls-2020-0016

Rodriguez, F. (1982). Principles of Polymer Systems (2nd ed.). *Singapore: McGraw-Hill book.*

.

Ruidíaz-Martínez, M., Álvarez, M. A., López-Ramón, M. V., Cruz-Quesada, G., Rivera-Utrilla, J., & Sánchez-Polo, M. (2020). Hydrothermal Synthesis of rGO-TiO2 Composites as High-Performance UV Photocatalysts for Ethylparaben Degradation. *Catalysts, 10*(5). doi:10.3390/catal10050520

Sachyani, E., Layani, M., Tibi, G., Avidan, T., Degani, A., & Magdassi, S. (2017).

Enhanced movement of CNT-based actuators by a three-Layered structure with controlled resistivity. *Sensors and Actuators B: Chemical, 252*, 1071-1077. doi:10.1016/j.snb.2017.06.104

Salavagione, H. J., Gómez, M. A., & Martínez, G. (2009). Polymeric Modification of Graphene through Esterification of Graphite Oxide and Poly(vinyl alcohol). *Macromolecules, 42*(17), 6331-6334. doi:10.1021/ma900845w

Salavagione, H. J., Martínez, G., & Gómez, M. A. (2009). Synthesis of poly(vinyl alcohol)/reduced graphite oxide nanocomposites with improved thermal and electrical properties. *Journal of Materials Chemistry, 19*(28). doi:10.1039/b904232f

Salim, E., Hany, W., Elshahawy, A. G., & Oraby, A. H. (2022). Investigation on optical, structural and electrical properties of solid-state polymer nanocomposites electrolyte incorporated with Ag nanoparticles. *Sci Rep, 12*(1), 21201. doi:10.1038/s41598-022-25304-0

Seo, H., Ahn, S., Kim, J., Lee, Y. A., Chung, K. H., & Jeon, K. J. (2014). Multi-resistive reduced graphene oxide diode with reversible surface electrochemical reaction induced carrier control. *Sci Rep, 4*, 5642. doi:10.1038/srep05642

Shazia Shaikh, N. A., Ramesh Manza. (2019). Current trends in the application of thermal imaging in medical condition analysis. *International Journal of Innovative Technology and Exploring Engineering (IJITEE), 8*(8).

Shintake, J., Cacucciolo, V., Floreano, D., & Shea, H. (2018). Soft Robotic Grippers. *Adv Mater*, e1707035. doi:10.1002/adma.201707035

Shirasu, K., Yamamoto, G., Inoue, Y., Ogasawara, T., Shimamura, Y., & Hashida, T. (2017). Development of large-movements and high-force electrothermal bimorph actuators based on aligned carbon nanotube reinforced epoxy composites. *Sensors and Actuators A: Physical, 267*, 455-463. doi:10.1016/j.sna.2017.10.051

Sieradzka, M., Ślusarczyk, C., Biniaś, W., & Fryczkowski, R. (2021). The Role of the Oxidation and Reduction Parameters on the Properties of the Reduced Graphene Oxide. *Coatings, 11*(2). doi:10.3390/coatings11020166

Skov, A. L. (2016). Electromechanically Active Polymer (EAP) transducers & artificial muscles. . *EuroEAP 2016*.

Song, J., Zhang, J., Lin, C., & Chen, G. (2013). Influence of Graphene Oxide on the Tribological and Electrical Properties of PMMA Composites. *Journal of Nanomaterials, 2013*(1). doi:10.1155/2013/846102

Srihata, W., Jamnongkan, T., Rattanasak, U., Boonsang, S., & Kaewpirom, S. (2016). Enhanced electrostatic dissipative properties of chitosan/gelatin composite films filled with reduced graphene oxide. *Journal of Materials Science: Materials in Electronics, 28*(1), 999-1010. doi:10.1007/s10854-016-5620-0

Suma, S. B., & Sangappa, Y. (2024). Physical, optical and electrical properties of polyvinyl alcohol-graphene oxide nanocomposite films. *Indian Journal of Physics*. doi:10.1007/s12648-024-03314-0

Sun, Y. C., Leaker, B. D., Lee, J. E., Nam, R., & Naguib, H. E. (2019). Shape programming of polymeric based electrothermal actuator (ETA) via artificially induced stress relaxation. *Sci Rep, 9*(1), 11445. doi:10.1038/s41598-019-47949-0

Swapp. (2017). Scanning Electron Microscopy (SEM). Retrieved from

https://serc.carleton.edu/research_education/geochemsheets/techniques/SEM.html.

Tan, M. W. M., Wang, H., Gao, D., Huang, P., & Lee, P. S. (2024). Towards high performance and durable soft tactile actuators. *Chem Soc Rev, 53*(7), 3485-3535. doi:10.1039/d3cs01017a

Tian, Y., Li, Y. T., Tian, H., Yang, Y., & Ren, T. L. (2021). Recent Progress of Soft Electrothermal Actuators. *Soft Robot, 8*(3), 241-250. doi:10.1089/soro.2019.0164

Wang, D., Wu, X., Zhang, J., & Du, Y. (2021). A Pneumatic Novel Combined Soft Robotic Gripper with High Load Capacity and Large Grasping Range. *Actuators, 11*(1). doi:10.3390/act11010003

Wang, H., Chen, J., Lau, H. Y. K., & Ren, H. (2016). Motion Planning Based on Learning From Demonstration for Multiple-Segment Flexible Soft Robots Actuated by Electroactive Polymers. *IEEE Robotics and Automation Letters, 1*(1), 391-398. doi:10.1109/lra.2016.2521384

Wang, Z.-H., Chen, X., Yang, H.-X., Zhao, J., & Yang, S.-Y. (2018). The In-plane Orientation and Thermal Mechanical Properties of the Chemically Imidized Polyimide Films. *Chinese Journal of Polymer Science, 37*(3), 268-278. doi:10.1007/s10118-019-2173-8

Wes W Tooley, S. F., Sangyoon J Han, Junlan Wang and Nathan J Sniadecki. (2011). Thermal fracture of oxidized polydimethylsiloxane during soft lithography of nanopost arrays. *Journal of Micromechanics and Microengineering, 21*(5), 054013. doi:doi:10.1088/0960-1317/21/5/054013

Xing, W., Wu, J., Huang, G., Li, H., Tang, M., & Fu, X. (2014). Enhanced mechanical properties of graphene/natural rubber nanocomposites at low content. *Polymer International, 63*(9), 1674-1681. doi:10.1002/pi.4689

Xu, C., Faul, C. F. J., Taghavi, M., & Rossiter, J. (2023). Electric Field-Driven Dielectrophoretic Elastomer Actuators. *Advanced Functional Materials, 33*(13). doi:10.1002/adfm.202208943

Yao, S., Cui, J., Cui, Z., & Zhu, Y. (2017). Soft electrothermal actuators using silver nanowire heaters. *Nanoscale, 9*(11), 3797-3805. doi:10.1039/c6nr09270e

Yin, R., Yang, B., Ding, X., Liu, S., Zeng, W., Li, J., . . . Tao, X. (2020). Wireless Multistimulus-Responsive Fabric-Based Actuators for Soft Robotic, Human–Machine Interactive, and Wearable Applications. *Advanced Materials Technologies, 5*(8). doi:10.1002/admt.202000341

Young Hoon Jo, C. H. L. a. J. H. Y. (2013). Study on applicability of passive infrared thermography analysis for blistering detection of stone cultural heritage. *Journal of Conservation Science, 29*, 55-67. doi:http://dx.doi.org/10.12654/JCS.2013.29.1.06

Yuan, N. Y., Ma, F. F., Fan, Y., Liu, Y. B., & Ding, J. N. (2012). High conductive ethylene vinyl acetate composites filled with reduced graphene oxide and polyaniline. *Composites Part A: Applied Science and Manufacturing, 43*(12), 2183-2188. doi:10.1016/j.compositesa.2012.06.003

Zaidi, S., Maselli, M., Laschi, C., & Cianchetti, M. (2021). Actuation Technologies for Soft Robot Grippers and Manipulators: A Review. *Current Robotics Reports, 2*(3), 355-369. doi:10.1007/s43154-021-00054-5

Zainab. (2007). Standard test methods for DC resistance or conductance of insulating

materials.
Zainab, S. M., Junaid, M., Xu, N., & Malik, R. N. (2020). Antibiotics and antibiotic resistant genes (ARGs) in groundwater: A global review on dissemination, sources, interactions, environmental and human health risks. *Water Res, 187*, 116455. doi:10.1016/j.watres.2020.116455
Zhang, W., Dehghani-Sanij, A. A., & Blackburn, R. S. . (2007). Carbon based conductive polymer composites. *Journal of Materials Science, 42(10)*, 3408–3418. doi:doi:10.1007/s10853-007-1688-5
Zhang, Z., & Fang, X. (2006). Study on paraffin/expanded graphite composite phase change thermal energy storage material. *Energy Conversion and Management, 47*(3), 303-310. doi:10.1016/j.enconman.2005.03.004
Zhou, X., Majidi, C., & O'Reilly, O. M. . (2015). Soft hands: An analysis of some gripping mechanisms in soft robot design. *International Journal of Solids and Structures, 64-65*, 155–165. doi:doi:10.1016/j.ijsolstr.2015.03.021
Zhuang, Y., Seong, J. G., & Lee, Y. M. (2019). Polyimides containing aliphatic/alicyclic segments in the main chains. *Progress in Polymer Science, 92*, 35-88. doi:10.1016/j.progpolymsci.2019.01.004

ต้นฉบับไม่ปรากฏหน้านี้